

**Evaluation and Optimization of Dedicated  
Breast Nuclear Medicine Based Imaging  
Systems for the Early Detection and  
Diagnosis of Breast Cancer**

---

A Dissertation

Presented to

the faculty of the School of Engineering and Applied Science

University of Virginia

---

in partial fulfillment  
of the requirements for the degree

Doctor of Philosophy

by

Andrew Michael Polemi

December 2018

## APPROVAL SHEET

This Dissertation  
is submitted in partial fulfillment of the requirements  
for the degree of  
Doctor of Philosophy

Author Signature: 

This Dissertation has been read and approved by the examining committee:

Advisor: Mark B. Williams, PhD

Committee Member: John A. Hossack, PhD

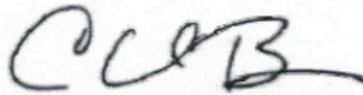
Committee Member: Stuart S. Berr, PhD

Committee Member: Luke Lancaster, MD

Committee Member: Frederick Epstein, PhD

Committee Member: \_\_\_\_\_

Accepted for the School of Engineering and Applied Science:



Craig H. Benson, School of Engineering and Applied Science

December 2018

## Abstract

Breast cancer continues to be the second most frequently diagnosed cancer among US women, coming second only to skin cancers. The current standard for breast cancer screening is x-ray mammography (XRM), however XRM sensitivity and specificity decrease with increasingly radiodense breasts. Imaging modalities such as ultrasound (US) and magnetic resonance (MRI) are utilized as effective supplements for mammography, however, used as stand-alone screening modalities US and MRI suffer from high false positive rates. This dissertation evaluates two unique nuclear medicine (NM) based imaging systems developed with the goal of improving the detection and characterization of breast abnormalities.

The first system is a dual modality tomosynthesis (DMT) imaging system. This system includes two integrated components, an x-ray digital breast tomosynthesis (DBT) system and a novel NM system for molecular breast tomosynthesis (MBT). DBT and MBT are performed on a shared gantry, allowing for a spatially co-registered hybrid set of 3D x-ray transmission and gamma ray emission images. A human study was performed to assess the value of adding functional 3D MBT images to the current standard of combined 3D DBT plus 2D XRM. In this study 94 subjects, all scheduled for biopsies, were imaged. Of these, actual biopsies and full image sets were obtained for 75. A total of 83 lesions were biopsied with 21 found to be malignant and 62 benign. A NM radiologist first interpreted the MBT images alone localizing any findings and rating them on a linear suspicion scale from 1-5, with 5 being definitely malignant. The findings from the NM radiologist were then used as a consult report for a breast radiologist who interpreted the images for each case (both breasts independently) in the following sequence: 1) DBT alone, 2) DBT + XRM, 3) DMT (=DBT+MBT) + XRM, 4) DMT + XRM + consult report. Updated suspicion scores were provided as each additional type of information was added. Reader interpretation results for each modality were then compared in terms of the area under the receiver operating characteristic (ROC) curve (AUC), using the biopsy results as ground truth. Compared to the reference imaging standard of DBT+XRM (AUC = 0.74), all modalities, DMT + XRM (AUC = 0.93), MBT (AUC = 0.90), and DBT (AUC = 0.58), are all shown to be significantly different. Both DMT +XRM (difference in AUC – 0.19, 95% confidence limits – 0.075 to 0.302, p-value 0.0011) and MBT alone (difference – 0.16, 95% confidence limits – 0.028 to 0.293, p-value 0.0177) showed a significant improvement in diagnostic accuracy, while DBT alone (difference – -0.17, 95% confidence limits – 0.283 to 0.048, p-value 0.0056) showed a significant decrease in diagnostic accuracy using 0.05 as an indicator for significance.

To allow for timely evaluation and optimization of system and protocol improvements to the DMT system a computational model observer, based on the channelized Hotelling observer (CHO), is under development. Two versions of the CHO will be developed; one for DBT and one for MBT. To get the large image sets necessary to generate the ensemble covariance matrices required to inform the model observer regarding the statistical noise properties of each imaging task, sets of synthetic DBT and MBT images were created. The synthetic images were created using principle component analysis (PCA) and a subset of the available human DMT data sets, resulting in a set of eigenvectors, which we call eigenDMT images. A variety of synthetic training images were formed via weighted sums of the eigenDMT images plus a mean (averaged over eigenDMT images) breast image. We demonstrated that synthetic images generated from the eigenimage basis set using weighting factors selected for similarity to any particular human image matched that image voxel-by-voxel with a mean square error analysis showing a negligible difference of  $4e^{-8}$ . Synthetic images generated using randomly selected weighting factors were compared to those from the original human DMT images by comparing their power spectral densities. The metric used for quantifying the similarity was the power-law exponent obtained by fitting the power spectral density estimates with a power law of form  $P(f) = A/f^\beta$ ,

where  $f$  is radial spatial frequency. A two-tailed paired Student's  $t$ -test, with an assumed statistical significance level of  $p < 0.05$ , was then used to determine if the  $\beta$ -values differ significantly or not. The  $\beta$ -values of the synthetic DBT and MBT images were shown to not differ significantly from those of the human images. The synthetic images are thus thought to be suitable to be used as a viable and realistic training set for the model observer under development.

A new low-profile (LP) gamma camera, for use in the DMT system, was designed with the goals of increasing the field of view (FOV) and overall imaging performance compared to the DMT gamma camera used to that point. Like the previous camera, the new camera has a NaI(Tl) pixelated scintillation crystal and uses position sensitive photomultiplier tubes (PSPMTs) with a custom-designed electronic readout. Compared to the original camera a higher sensitivity collimator was designed and fabricated. The performance of the two cameras was compared using the following metrics: energy resolution, sensitivity, intrinsic and extrinsic spatial resolution. A breast phantom with simulated lesions was created to compare the signal-to-noise ratio (SNR) of the two cameras under realistic conditions. An improvement in energy resolution was seen (LP camera – 10.8%, original camera – 13.5%). The intrinsic spatial resolution was measured to be similar between cameras;  $\sim 2.3$  mm FWHM. The LP camera demonstrated a 1.7x increase in sensitivity relative to the original camera. The SNR experiment showed that the lesion SNR was a minimum of 1.7x higher for the LP camera.

The second imaging system is a dedicated breast ring PET (BRPET) scanner. The scanner contains a single ring of 12 small detector modules that surround the pendant breast, while the patient lies prone on a positioning table. Current dedicated breast PET systems have been shown to miss breast cancers near the chest wall. To overcome this limitation the detectors on the BRPET system have a unique slanted light guide designed to allow the system to obtain better images of the subject's chest wall. The photon counting rate capability of the system was improved via an optimization process that tested multiple coincidence pair selections and timing window settings. This resulted in a peak noise equivalent count rate of 5.33 kcps, compared to 2.15 kcps prior to optimization. This was followed by a complete evaluation of imaging performance and the completion of a pilot human study testing the clinical viability of the system. To characterize the basic imaging performance of the BRPET system the measurements detailed by the National Electrical Manufacturers Association (NEMA) NU-4 2008 protocol were adapted. The scanner's spatial resolution at the center of the FOV was measured to be 1.8, 1.7, and 1.9 mm FWHM in the axial, radial, and tangential directions, respectively. A total system sensitivity of 19.3% was observed. In addition, a set of unique tests was created to measure the system's ability to reliably image close to the top of the examination table, i.e. to visualize posterior regions of the breast. The tests showed that the scanner ring can image up to a minimum distance of 6.25 mm from the top of the examination table under high contrast conditions. The pilot human study included 10 subjects who also underwent clinical contrast-enhanced MRI scans. There was a total of 11 biopsied lesions with 7 malignancies and 4 benign findings. The PET images were interpreted by two blinded NM radiologists while the clinical MRI images were interpreted by a blinded breast radiologist. The study results showed an average sensitivity and specificity of 92.5% and 100% respectively for BRPET, while the sensitivity and specificity for CE-MRI were 100% and 25% respectively. The pilot clinical evaluation of the system suggests it is a clinically viable system with the potential capability improve upon the specificity of current breast cancer imaging systems.

## Acknowledgements

I would like to thank Dr. Mark B. Williams, my advisor, for all of his guidance over the years. His passion for and expertise in dedicated imaging research greatly helped drive me to the completion of my dissertation. I would like to thank Dr. Stan Majewski for his continued support and expertise on all of these projects as well. I greatly appreciate the support and guidance of my committee members, Dr. John Hossack, Dr. Stuart Berr, Dr. Luke Lancaster, and Dr. Frederick Epstein. I also want to thank Dr. Patricia Collins and Allen Goode for the support and many conversations they gave me over the last several years.

I would like to thank my parents, Rosemarie and Dean, my sister Katelyn, and my aunt Donna who supported and encouraged me to attain all my goals in life. It was from my early exposure to cancer through my mom and my uncle, Alvin Gates, that I drew motivation to work in the field of cancer detection. Lastly, I would like to thank my wife Danae for her support, encouragement, and patience over the past 5 years.

## Table of Contents

Cover Page .....	i
Approval Sheet .....	ii
Abstract.....	iii
Acknowledgements .....	v
Table of Contents .....	vi
List of Figures .....	ix
List of Tables.....	xii
List of Abbreviations .....	xiv
1. Introduction .....	1
1.1. Prevalence of Breast Cancer.....	1
1.2. Current Breast Imaging Techniques and Technology .....	2
1.2.1. Mammography .....	4
1.2.2. X-ray Tomosynthesis .....	5
1.2.3. Ultrasound.....	7
1.2.4. Magnetic Resonance Imaging.....	7
1.2.5. Nuclear Medicine .....	8
1.2.5.1. Single Gamma Breast Imaging.....	9
1.2.5.2. Positron Emission Breast Imaging .....	10
1.2.6. Dissertation Systems.....	10
1.2.6.1. Dual Modality Tomosynthesis.....	10
1.2.6.2. Brest Ring Positron Emission Tomography .....	12
2. Nuclear Medicine Systems and Theory .....	19
2.1. Radiopharmaceuticals.....	19
2.2. Detector Setup.....	23
2.2.1. Scintillators .....	23
2.2.2. Photomultipliers .....	25
2.2.3. Electronics .....	26
2.2.4. Collimators.....	27
2.3. Detector and Image Characteristics in Nuclear Medicine.....	31
2.3.1. Image Quality.....	31
2.3.2. Calibration .....	32
2.3.3. Energy Resolution .....	33
2.3.4. System Sensitivity .....	35
2.3.5. Geometric Linearity and Intrinsic Uniformity.....	36
2.3.6. System Spatial Resolution .....	37
3. Dual Modality Tomosynthesis Human Study.....	40
3.1. Introduction.....	40
3.2. Materials and Methods.....	41
3.2.1. System Description .....	41
3.2.2. Subjects and Imaging Protocol .....	42
3.2.3. Observer Study Design .....	44
3.2.4. Data Analysis.....	44
3.3. Results.....	45

3.4. Discussion.....	47
4. Synthesized DMT Images.....	53
4.1. Motivation.....	53
4.1.1. Image Formation and Model Observers.....	53
4.2. Creation of Synthetic Images.....	55
4.2.1. Theory of Principal Component Analysis.....	55
4.2.2. Eigenimages and Synthesized Images for DMT Study.....	56
4.3. Synthesized Image Background Analysis.....	59
4.3.1. Methods.....	59
4.3.2. Results and Discussion.....	62
4.4. Addition of Lesions to Synthesized Images.....	63
4.5. Conclusion.....	68
5. Characterization of Low Profile 20 X 25 cm NaI(Tl) Gamma Camera for Dedicated Breast Tomosynthesis.....	71
5.1. Introduction.....	71
5.2. Methods.....	72
5.2.1. Camera Design.....	72
5.2.2. Energy Resolution.....	74
5.2.3. Intrinsic Uniformity.....	75
5.2.4. Intrinsic Geometric Linearity.....	76
5.2.5. Spatial Resolution.....	76
5.2.5.1. Intrinsic.....	76
5.2.5.2. Extrinsic.....	77
5.2.6. System Sensitivity.....	77
5.2.7. SNR Experiment.....	77
5.3. Results.....	78
5.4. Discussion.....	83
6. Characterization and Pilot In-Human Trial of Dedicated Breast Ring PET System.....	88
6.1. Introduction.....	88
6.2. Methods.....	90
6.2.1. System Design.....	90
6.2.2. Energy Resolution.....	91
6.2.3. Spatial Resolution.....	91
6.2.4. System Sensitivity.....	92
6.2.5. Count Rate and Scatter Fraction.....	92
6.2.6. Image Quality for Posterior Tissue Imaging.....	95
6.2.7. Pilot Human Study.....	97
6.3. Results.....	99
6.3.1. Energy Resolution.....	99
6.3.2. Spatial Resolution.....	99
6.3.3. System Sensitivity.....	101
6.3.4. Count Rate and Scatter Fraction.....	102
6.3.5. Image Quality for Posterior Tissue Imaging.....	103
6.3.6. Pilot Human Study.....	106
6.4. Discussion.....	107

7. Conclusions and Future Works .....	113
7.1. Conclusions.....	113
7.2. Future Works .....	114
7.2.1. Dual Modality Tomosynthesis and LP Gamma Camera .....	114
7.2.2. Synthetic DMT Images.....	115
7.2.3. Dedicated Breast Ring PET.....	115
Appendix A.....	116
Appendix B.....	121
Appendix C .....	128
Appendix D.....	131

## List of Figures

Figure 1-1: Anatomy of a female breast .....	1
Figure 1-2: Absorption spectra of breast tissue .....	3
Figure 1-3: BIRADS Assessment Categories .....	3
Figure 1-4: Example of a clinical mammogram .....	4
Figure 1-5: DBT system schematic and definition of the coordinate system.....	5
Figure 1-6: Comparison between a 2D mammographic and 3D tomosynthesis .....	6
Figure 1-7: Example of a contrast enhanced breast MRI image .....	8
Figure 1-8: Breast images acquired using dedicated nuclear medicine breast scanners.....	9
Figure 1-9: Dual Modality Tomosynthesis (DMT) system .....	12
Figure 2-1: Positron annihilation and acollinearity .....	20
Figure 2-2: Basic Gamma Camera System Setup.....	23
Figure 2-3: Crystal Lattice Band Gap .....	24
Figure 2-4: Basic Photomultiplier Tube Design .....	25
Figure 2-5: Gamma Camera Photon Position Logic .....	26
Figure 2-6: Parallel hole collimator with hexagonal holes.....	28
Figure 2-7: Example of different gamma ray interactions in a collimated detector .....	28
Figure 2-8: Collimator Path Length .....	30
Figure 2-9: Collimator Types.....	31
Figure 2-10: Raw image of a pixelated NaI(Tl) gamma camera .....	33
Figure 2-11: Example of energy histogram of point source .....	34
Figure 2-12: Scatter vs no scatter energy histogram.....	35
Figure 2-13: Nonparalyzable vs paralyzable systems downtime.....	36
Figure 2-14: Flood correction .....	37
Figure 3-4: Dual Modality Tomosynthesis system (DMT) .....	42

Figure 3-5: Examples of DMT Image Sets .....	46
Figure 3-3: ROC curve for all modality sets.....	46
Figure 4-1: A scatter plot of 33 data points of 2 variables with a positive relationship.....	56
Figure 4-2: Image masking .....	57
Figure 4-3: Example masked images.....	58
Figure 4-4: Example of a ROI in a DBT slice.....	60
Figure 4-5: An example of a 1D NPS plot from a human DBT image .....	61
Figure 4-6: Log-log plot of 1D NPS data with a fitted linear regression .....	61
Figure 4-7: Depicts the areas the ROIs were selected for each modality .....	62
Figure 4-8: Reconstructed Flood slices.....	63
Figure 4-9: Workflow for creating signal present synthetic MBT images.....	64
Figure 4-10: Displays different slices of the reconstructed lesion phantoms.....	65
Figure 4-11: Synthetic MBT image with inserted lesion.....	65
Figure 4-12: Different sized inserted lesions in MBT .....	66
Figure 4-13: Workflow for creating signal present synthetic DBT images.....	67
Figure 4-14: Displays a human tumor isolated via pixel thresholding .....	67
Figure 4-15: Isolated tumors inserted in synthetic DBT .....	68
Figure 5-6: Dual Modality Tomosynthesis system (DMT).....	72
Figure 5-7: Customized circuit boards.....	73
Figure 5-8: Resistive row and column setup .....	73
Figure 5-9: Raw flood image used for crystal mapping.....	74
Figure 5-10: Combined and corrected for non-uniformity energy spectrum.....	75
Figure 5-11: Raw image of the slit before crystal mapping.....	76
Figure 5-12: Gelatin phantom breast mold.....	78
Figure 5-13: Deviation from linear fit of the image of the slit.....	79
Figure 5-14: Results of extrinsic resolution .....	79

Figure 5-15: Surface plots for two of the differential non-uniformity experiments.....	80
Figure 5-16: Images LP and original camera projection views .....	82
Figure 5-17: Images LP and original camera reconstructed central slice.....	82
Figure 5-18: Comparison of extrinsic resolution .....	84
Figure 5-19: Profiles taken through raw data of flood image .....	84
Figure 6-20: Illustration of Slanted Light Guides.....	89
Figure 6-2: BRPET ring.....	91
Figure 6-3: Count rate phantom dimensions .....	93
Figure 6-4: Depicts a couple detector configurations allowed by the Mesytec MCFD-16.....	94
Figure 6-5: Experimental set up of two high contrast vertical position experiments .....	96
Figure 6-6: SNR phantom experiment images .....	96
Figure 6-7: Depicts the ROIs used to calculate the SNR.....	97
Figure 6-8: Average corrected energy histogram .....	99
Figure 6-9: Example spatial resolution image .....	100
Figure 6-10: Resolution vs position graphs .....	101
Figure 6-11: Axial absolute sensitivity along z-direction of BRPET scanner.....	101
Figure 6-12: Counting rate performance plot.....	102
Figure 6-13: NEC curve comparisons .....	103
Figure 6-14: Capillary tube experiment images .....	104
Figure 6-15: Capillary tube experiment profiles .....	104
Figure 6-16: SNR values for each lesion and LBR pair .....	105
Figure 6-17: BRPET scan of subject's right breast with a known malignancy.....	106
Figure 6-18: Single slice example image of a benign subjects BRPET study.....	107

## List of Tables

Table 2-1: Commonly used Radiopharmaceuticals and their Properties .....	22
Table 2-2: Common Inorganic Scintillators and their Properties.....	25
Table 3-1: Histologic Results for 83 Biopsied Lesions.....	43
Table 3-2: Resulting AUCs for the ROC curves for each modality .....	47
Table 3-3: AUC contrast values for each modality set.....	47
Table 3-4: Resulting sensitivity, specificity, PPV, and NPV for each modality set based off of suspicious ratings $\geq 4$ .....	47
Table 4-1: Compares the $\beta$ values for first 10 human images with the first 10 synthetic images for each modality.....	62
Table 5-1: Results obtained for energy resolution, intrinsic uniformity, intrinsic spatial resolution, and system sensitivity .....	78
Table 5-2: SNR values and SNR ratios for LP camera vs original camera 2D projection views.....	81
Table 5-3: SNR values and SNR ratios for LP camera vs original camera.....	81
Table 5-4: Comparison of thicker gamma camera and LP gamma camera dimensions and collimator parameters .....	83
Table 5-5: Comparison of imaging characteristics of the current thicker gamma camera and the new LP gamma camera.....	83
Table 6-1: Depicts the axial resolution at the center of the FOV of several dedicated breast PET scanners .....	89
Table 6-2: Mesytev MCFD-16 configurations tested.....	95
Table 6-35: Activity Concentrations Used in SNR Experiments.....	97
Table 6-4: Histological Results of Lesion Biopsies for BRPET Subjects.....	98
Table 6-5: Injected Activity, Ring Position, and Scan Times for BRPET Subjects .....	99
Table 6-6: Spatial resolution measurements .....	100
Table 6-7: Comparison of peak count rates.....	102

Table 6-8: Depth of Highest Detectable Lesion .....	105
Table 6-9: Performance Metrics for BRPET .....	106
Table 6-10: BRPET vs commercial systems spatial resolution.....	107

## List of Abbreviations

2D – Two Dimensional  
3D – Three Dimensional  
ACS – American Cancer Society  
ACR – American College of Radiology  
ADC – Analog to Digital Converter  
BIO – Bayesian Ideal Observer  
BIRADS – Breast Imaging Reporting and Data System  
BRPET – Breast Ring Positron Emission Tomography  
BSGI – Breast Specific Gamma Imaging  
Bq – Becquerel  
CAD – Computer Aided Diagnosis  
CC – Cranial Caudal  
CEMRI – Contrast Enhanced Magnetic Resonance Imaging  
CHO – Channelized Hotelling Observer  
Ci – Curie  
COG – Center of Gravity  
CT – Computed Tomography  
DMT – Dual Modality Tomosynthesis  
Dps – disintegrations per second  
EC – Electron Capture  
eV – Electron Volt  
FDG – 2-deoxy-2-[<sup>18</sup>F]fluoro-D-glucose  
FOV – Field of View  
FWHM – Full Width Half Max  
HO – Hotelling Observer  
HVL – Half Value Layer  
IT – Isomeric Transition  
kVp – Peak Kilo-voltage  
MBI – Molecular Breast Imaging  
MIBI – <sup>99m</sup>Tc-methoxyisobutylisonitrile  
MLO – Mediolateral-oblique  
MM – Mammography  
MRI – Magnetic Resonance Imaging  
NaI – Sodium Iodine  
NaI(Tl) – Thallium activated Sodium Iodine  
NEMA – National Electrical Manufacturers Association  
NPS – Noise Power Spectrum  
NPV – Negative Predictive Value  
PC – Principal Component  
PCA – Principal Component Analysis  
PEM – Positron Emission Mammography  
PET – Positron Emission Tomography  
PMT – Photomultiplier Tube  
PPV – Positive Predictive Value

PSPMT – Position-Sensitive Photomultiplier Tube

$\rho$  – Density

ROI – Region of Interest

SBI – Society of Breast Imaging

SI – Systeme International

SPECT – Single Photon Emission Computed Tomography

SNR – Signal to Noise Ratio

TPF – True Positive Fraction (Sensitivity)

US – Ultrasound

$\mu$  – Linear Attenuation Coefficient

VOV – Volume of View

WBPET – Whole Body Positron Emission Tomography

XBT – X-ray Breast Tomosynthesis

XRM – X-Ray Mammography

# Chapter 1

## Introduction

### 1.1 Prevalence of Breast Cancer

Breast cancer continues to be the most commonly diagnosed cancer in women <sup>1,2</sup>. In general, cancer results from the uncontrolled growth of cells, which is caused by genetic defects due to the deregulation of cell division and apoptosis (programmed cell death) <sup>3</sup>. The progression of normal tissue to malignant tissue requires the mutation or deletion of all three of the following gene types: 1) Proto-oncogenes, which are positive growth regulators; 2) Tumor suppressor genes, which are negative growth regulators; and 3) DNA stability genes, which monitor and maintain DNA integrity in the cell <sup>3</sup>. Although all types of cancer develop from cells that have genetic mutations leading to uncontrolled growth, the type of cancer depends on the cell class that has mutated. The three main cell class types of cancers are: carcinomas, which begin in epithelial cells; sarcomas, which begin in connective or supportive tissue; and leukemia, which begins in blood forming tissue <sup>4</sup>. Breast cancers are most commonly categorized as carcinomas, more specifically they tend to be adenocarcinomas, originating in the ducts or lobules (glandular tissue) (Fig. 1-1) <sup>2,5</sup>. When the cancer has not spread past the layer of cells it began in, it is referred to as “in situ”. However, once the cancer has invaded nearby tissues, it is known as “invasive”. It has been shown that women with denser breasts (larger percentage of glandular tissue) have a higher risk of developing breast cancer compared to those with mostly fatty breasts. Breast density, and the challenges it presents for diagnosing breast cancer, will be discussed in subsequent sections <sup>6,7</sup>.

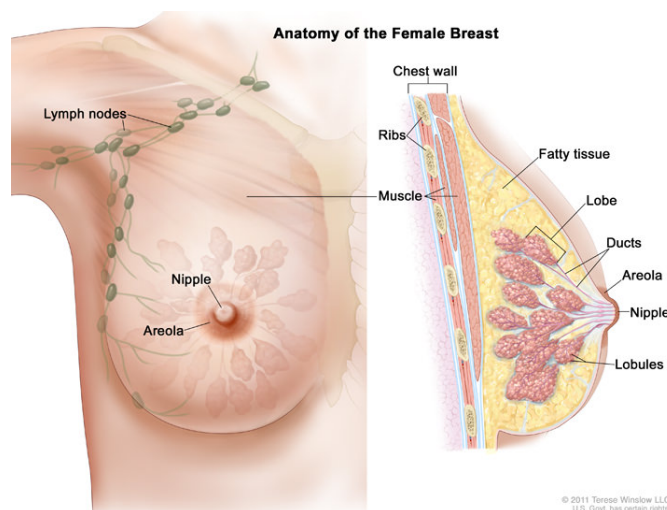


Figure 1-1: Anatomy of a female breast.

Based on the most recent data, the American Cancer Society (ACS) predicts that 1 in 8 women in the United States will be diagnosed with breast cancer in their lifetime. In 2018 alone, the ACS estimates 63,960 women will be diagnosed with in situ breast cancer while another 266,120 women will be diagnosed with an invasive type. Although the mortality rate for breast cancer has declined over the last 30 years <sup>2</sup>, it is estimated that breast cancer will account for approximately 40,920 deaths in 2018 <sup>1</sup>. The decline in the mortality rate can be attributed to

many factors, including improvement in and availability of more personalized treatment options, as well as improved ways to identification of high risk populations. Early detection is one of the most important factors in the reduction breast cancer mortality, as described in more detail below<sup>8,9</sup>.

## 1.2 Current Breast Imaging Techniques and Technology

The most common way that breast cancer is detected is via a screening process. Here the patient is imaged without any known symptom of breast cancer, with the goal of detecting a cancer as early as possible. Currently the ACS, along with the Society of Breast Imaging (SBI) and the American College of Radiology (ACR), recommend annual screening for women starting at 40 years of age<sup>8-10</sup>. Since 1990, there has been nearly a 38% decrease in breast cancer mortality through 2014. This decrease is in part attributed to breast cancer screening<sup>8-11</sup>. During screening, the imaging systems typically used are x-ray mammography and x-ray tomosynthesis (these and other imaging systems subsequently mentioned will be described in more detail later on). However, other screening modalities such as whole breast ultrasound or MRI may be recommended for women with dense breasts and/or designated as high-risk patients.

As illustrated by figure 1.1, breasts largely consist of two tissue types: fatty tissue and glandular (lobules and ducts) tissue. The amount of glandular tissue present in the breast dictates the radiodensity of the breast. The amount of x-ray energy a tissue absorbs is a function of the x-ray attenuation coefficient of the tissue, which depends on the energy of the x-rays. In the case of glandular and cancerous tissues of the breast, the x-ray attenuation coefficients are very similar for the range of photon energies used in mammography, making distinguishing between the two challenging (Fig. 1-2)<sup>12</sup>. The attenuation differences are maximized at lower x-ray energies, which is one reason for the specialized equipment used in breast imaging.

Due to natural variability from patient to patient in breast density, during screening each breast is typically assigned a BIRADS (Breast Imaging Reporting and Data System) density index level. There are 4 index categories: Category A- mostly entirely fatty (less than 10% dense tissue), Category B- scattered areas of fibroglandular density (10-49% dense tissue), Category C- heterogeneously dense (49-90% dense tissue), and Category D- extremely dense (>90% dense tissue)<sup>13,14</sup>. Patients with BIRADS density index levels of 4 are typically advised to undergo further screening with other modalities such as ultrasound or magnetic resonance imaging (MRI). Annual MRIs are also recommended for women considered to have a high risk of breast cancer. These are women who either carry a BRCA1/BRCA2 gene mutation, have a cancer risk greater than 20%, or have received radiation treatment for prior cancers between the ages 10-30<sup>15</sup>.

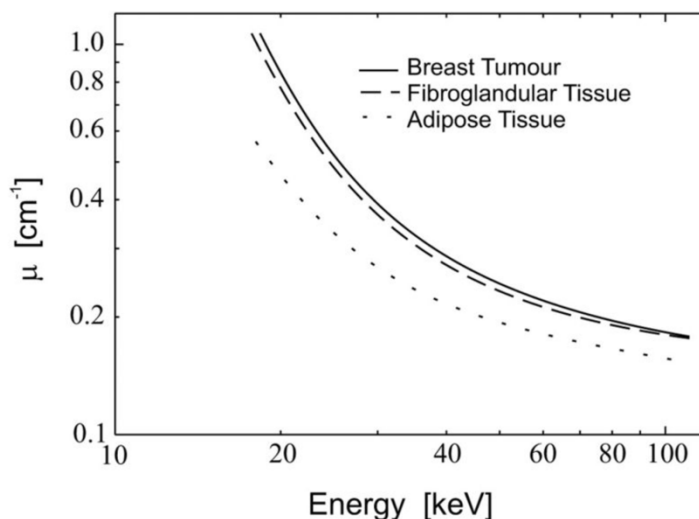


Figure 1-2: Absorption spectra of healthy breast tissue, adipose and glandular, compared to cancerous breast tissue <sup>12</sup>. Notice the close similarity between the linear attenuation coefficients of fibroglandular tissue and breast tumor.

In addition to the four BIRADS density categories there is an additional set of BIRADS categories that pertains to the diagnostic assessment for breast cancer of the mammographic or tomosynthesis images. The assessment categories rank from 0 to 6. Descriptions of each category can be found in Figure 1-3. Patients whose images result in a BIRADS category of 1 or 2 are advised to continue with routine annual screening <sup>14</sup>. If a patient's images result in a BIRADS category of either 0 or 3 and greater, they will be called back for a diagnostic evaluation. This evaluation usually starts with diagnostic imaging, which can include a diagnostic mammogram, breast MRI, and ultrasound. To a lesser extent, nuclear medicine systems are used. The resultant images from the diagnostic evaluation are read and the BIRADS categories are re-assessed. If the findings under review are still suspicious, a breast biopsy is taken. Here a sample of the tissue is acquired, and a pathology report is obtained to determine if there are malignant cells present. If the sample is determined to be cancerous then a treatment plan is created.

Currently, x-ray mammography, x-ray tomosynthesis, ultrasound, MRI, and to a lesser extent nuclear medicine play important roles in the screening and diagnosis of breast cancer. A more in-depth description of each follows.

BIRADS Assessment Categories						
0	1	2	3	4	5	6
Need additional Imaging Evaluation	Negative: Nothing to comment on	Benign Finding	Probably Benign Finding	Suspicious Abnormality	Highly Suggestive of Malignancy	Known Biopsy – Proven Malignancy

Figure 1-3: BIRADS Assessment Categories. This is a universal scaling system to allow radiologists to assess breast images. It is recommended to continue screening as normal for patients with categories 1 and 2 assessments. Patients with category 3 assessments should get a follow-up scan in 6 months. Patients with category 4 or 5 assessments will get biopsies and will be treated based on biopsy reports.

### 1.2.1 Mammography

X-ray mammography (XRM) is currently the most common imaging modality used for breast cancer screening. XRM is a two-dimensional (2D) imaging technique performed by taking a low-energy x-ray projection (15 – 30 keV) while compressing the breast between a detector and compression paddle with the patient in an upright position. The breast compression is dual purpose. First, it immobilizes the breast, reducing motion artifacts in the image. Second, it reduces the path length of x-rays traveling through the breast allowing for a reduction in patient dose and an improvement in image quality<sup>16</sup>. Although necessary, compression can be a source of patient discomfort.

As discussed above, XRM is used for both screening and diagnostic imaging. A typical screening scan includes one cranial caudal (CC) projection image and one mediolateral-oblique (MLO) projection image per breast (Fig. 1-4). For diagnostic imaging, additional images are taken to inspect the suspicious area, including magnification or spot views. XRM has been proven to be an effective screening technique with a high sensitivity of 71 – 96% averaged over all breast types<sup>11</sup>. However, the sensitivity of XRM varies greatly with breast density.

The sensitivity change with radiodensity occurs in part because of the 2D nature of XRM. In 2D x-ray imaging a three-dimensional (3D) volume is projected onto a 2D plane, which leads to a superposition of tissue in the image. In radiodense breasts, superposition of normal glandular tissue can obscure the visualization of cancerous tissue or create patterns that resemble cancer<sup>17-19</sup>. XRM sensitivity ranges from 78 – 96% for fatty breasts to 68% for women with radiodense breasts<sup>11,20,21</sup>. Furthermore, XRM has a low specificity of 20 – 30% for women with radiodense breasts<sup>11,20,21</sup>. In a study averaging data over 44 participating sites, the positive predictive value (PPV) for XRM was found to be 4.1%, where the PPV is defined as the proportion of screens that were associated with a breast cancer diagnosis within a one year follow-up period among those with a BIRADS 3, 4, or 5 lesion assessment classification<sup>22</sup>. This outcome suggests that a large portion of the screening population were subjected to additional diagnostic procedures, such as lesion biopsies.

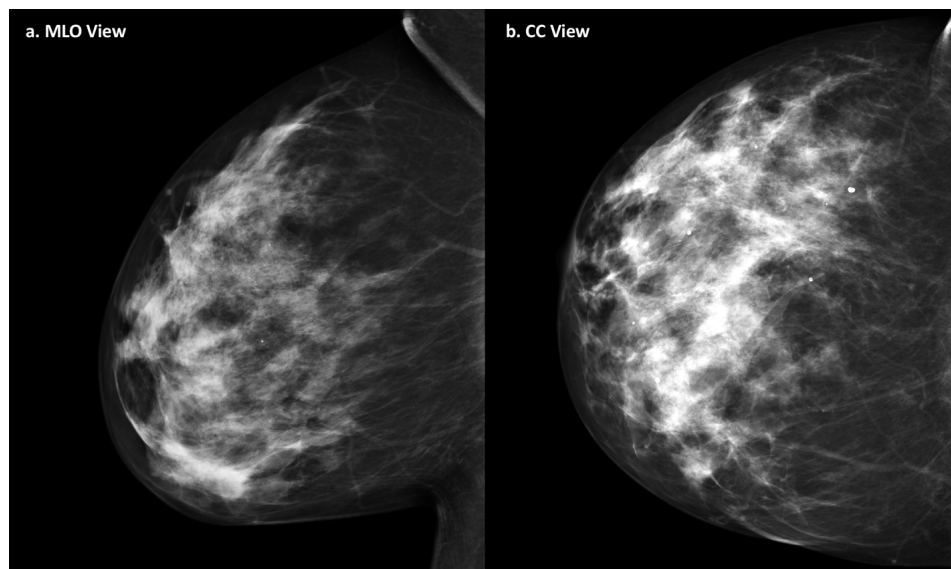


Figure 1-4: Example of a clinical mammogram of a right breast where a) is a mediolateral-oblique projection view and b) is a cranial caudal mammographic projection view.

## 1.2.2 X-ray Tomosynthesis

Digital x-ray breast tomosynthesis (XBT) was developed to overcome some of the limitations of XRM. It takes the next step from 2D XRM to a limited angle 3D image. Over the last 10-15 years, x-ray tomosynthesis has been developed by both academic and commercial entities and has become increasingly used for breast cancer screening<sup>23-28</sup>. XBT uses the same equipment and upright configuration as XRM, however, in XBT, the x-ray tube is rotated through a limited angle arc (up to  $\pm 25^\circ$ ) during which a series of projection images (usually 15) are taken of a compressed breast. These projection images are then input to an iterative reconstruction algorithm that calculates a 3D attenuation map, similar to x-ray CT (computed tomography). Unlike CT, XBT is not capable of rendering a true 3D volume due to the limited angular sampling of the projection images. As a result, XBT have lower spatial resolution and artifacts along the direction of compression (the z-dimension) compared to the x and y dimensions (Fig. 1-5). However, despite the resolution difference, the addition of angular information aids in reducing the amount of superimposed breast tissue present in each slice of the reconstructed volume, thus improving lesion visibility compared to traditional XRM systems. The volumetric image set also allows for the possibility of depth localization of lesions within the volume. Figure 1-6 compares an XRM image of a right breast with multiple slices of an XBT image set of the same breast, where the lesion is circled in red. It can be seen that the reduction in the superimposed tissue allows for an increase in lesion visibility.

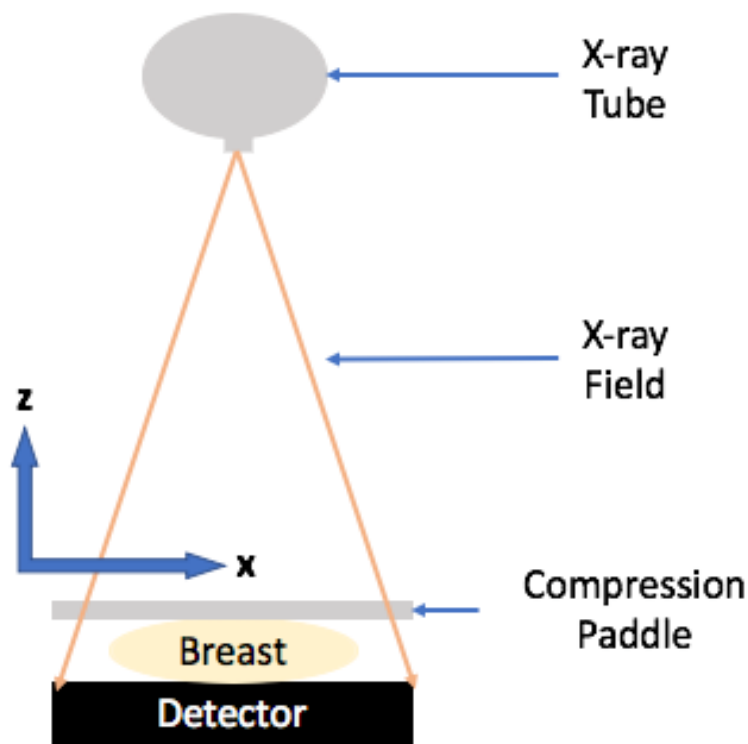


Figure 1-5: DBT system schematic and definition of the coordinate system used here. Note the z-axis is parallel to the direction of breast compression. The y-axis goes into the page.

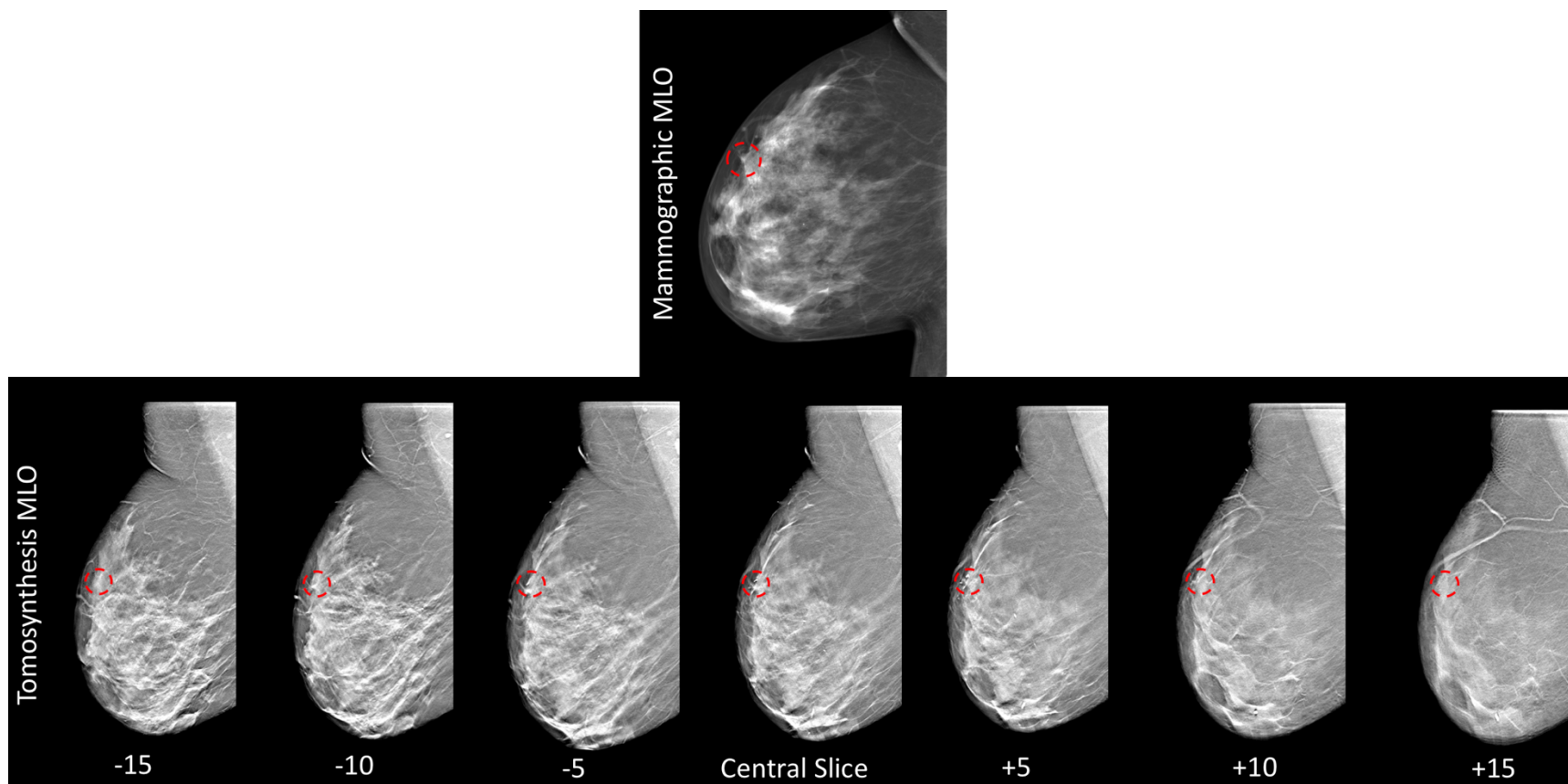


Figure 1-6: Comparison between a 2D mammographic image and several slices of a 3D tomosynthesis reconstruction (images take at University of Virginia). The lesion was identified as an architectural distortion which can be difficult to see in the 2D image due to the dense breast tissue. The architectural distortion can be seen more clearly in the tomosynthesis slices. The central slice of the lesion is where it is most in focus and it can be seen that the further away (in either direction) from the central slice the more obscure the lesion becomes.

Experiments have shown an increase in sensitivity of XBT over XRM systems along with improved lesion characterization<sup>29-31</sup>. In a 2013 study of 12631 patients, a 15% decrease in false positives was seen when XBT was added to mammography<sup>32</sup>. A separate 2013 study by Rose et al. showed that the addition of XBT to XRM increased cancer detection rates and decreased recall rates from 8.7% to 5.5%<sup>33</sup>. Although XBT has improved upon XRM systems, the images contain artifactual smearing of the images of tissue, calcifications, or other objects into adjacent slices. This is caused by the limited angle reconstruction and limited spatial resolution along the direction of compression.

### 1.2.3 Ultrasound

Ultrasound (US) has been shown to be an effective supplemental imaging system to XRM and is typically used for diagnosis and biopsy guidance. US systems use an acoustic transducer to generate repetitive bursts of high frequency sound that travel through the target tissue and are reflected back to the transducer. The transducer analyzes the reflected sound and uses the time of return and the intensity of the reflected wave to distinguish between tissue types as well as to discern tissue/object borders. When added to XRM, US has been shown to increase both sensitivity and specificity for dense breasts, with sensitivity ranging from 76 – 94% and specificity ranging from 74 – 84%<sup>34</sup>. Yet, even when XRM and US are used together, the false positive rate is high. A study comparing XRM with US versus XRM alone found a large improvement in sensitivity, going from 50% with XRM only to 81% when US is added, but with no significant change in specificity, PPV and negative predictive value (NPV). The study also showed that 42.7% of the 51 lesions were considered false positives<sup>35</sup>.

### 1.2.4 Magnetic Resonance Imaging (MRI)

MRI is an anatomical imaging system that detects the relaxation of proton spins after radiofrequency pulses are used to manipulate the spin alignments of the protons in a strong static magnetic field. It is mainly used as a diagnostic system but is also used to screen high risk patients and patients with radiodense breasts<sup>36,37</sup>. Breast imaging patients typically undergo a contrast enhanced MRI (CEMRI) where the subject is injected with the extracellular contrast agent gadolinium, which relies on the increased angiogenesis and vascular permeability for lesion enhancement<sup>38,39</sup>. Figure 1-7 shows a typical CEMRI of the breast. It has been widely validated as an effective method for high risk screening<sup>40,41</sup>. MRI has been proven to be a useful system for breast cancer detection, due to its high sensitivity, but has shown to vary greatly in specificity. In a 2005 study of 529 subjects with 43 breast cancers, comparing mammography, ultrasound, and MRI, Kuhl et al. showed that MRI was superior in both sensitivity (90.7%) and specificity (97.2%) when compared to mammography (sensitivity – 32.6%; specificity – 96.8%) and mammography plus ultrasound (sensitivity – 48.8%; specificity – 89.0%)<sup>41</sup>. Although this is a compelling result, a similar study of 821 subjects with 404 breast cancers imaged with CEMRI resulted in an overall sensitivity of 88.1% and a specificity of only 67.4%. Although the sensitivity of CEMRI has consistently been shown to be high (88 – 99%), there has been mixed results in its reported specificity, with some reporting a specificity as low as 37%<sup>42-45</sup>. However, with its superior sensitivity, especially for radiodense breasts, CEMRI has a clear advantage over XRM. Yet even with its advantages, MRI has not been utilized more due to its high cost, long procedure time, and limited availability across the country<sup>46</sup>.

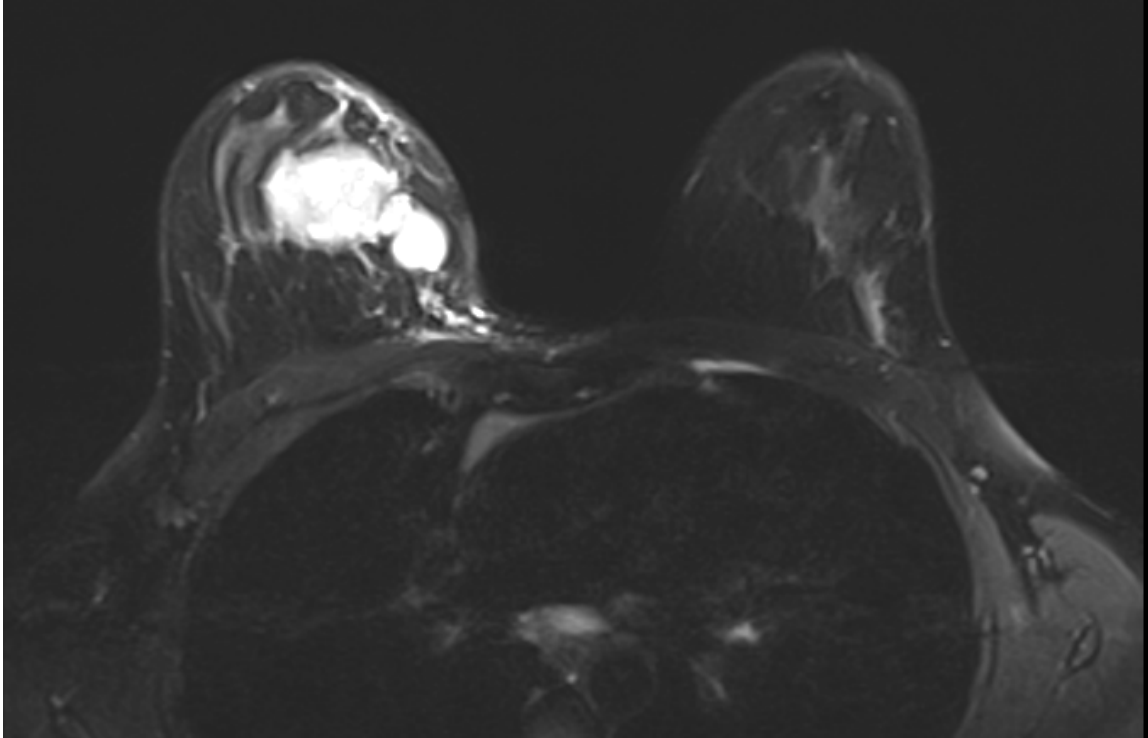


Figure 1-7: Example of a contrast enhanced breast MRI image. A gadolinium-based contrast agent was used. The subject was diagnosed with an invasive ductal carcinoma in the right breast (which can be seen in the breast on the left side of the image).

### 1.2.5 Nuclear Medicine

Nuclear medicine imaging is a unique modality that provides functional information rather than the anatomical information provided by modalities such as XRM, US, and MRI. These differences can be seen by comparing Figure 1-8, examples of gamma and positron emission tomography (PET) images, with the anatomical images of Figures 1-6 and 1-7. Nuclear medicine works by imaging an intravenously injected radiotracer that emits either gamma rays or positrons. Radiotracers are biologically significant molecules that have been modified by chemically attaching a radioactive element. In breast imaging, there are currently only two FDA approved nuclear medicine imaging agents. For single-gamma imaging (also known as molecular breast imaging – MBI or breast specific gamma imaging – BSGI),  $^{99m}\text{Tc}$ -methoxyisobutylisonitrile ( $^{99m}\text{Tc}$ -sestamibi or MIBI) is used, while for positron emission imaging 2-deoxy-2- $^{18}\text{F}$ fluoro-D-glucose (FDG) is used. These tracers will be discussed more in-depth in the next chapter.

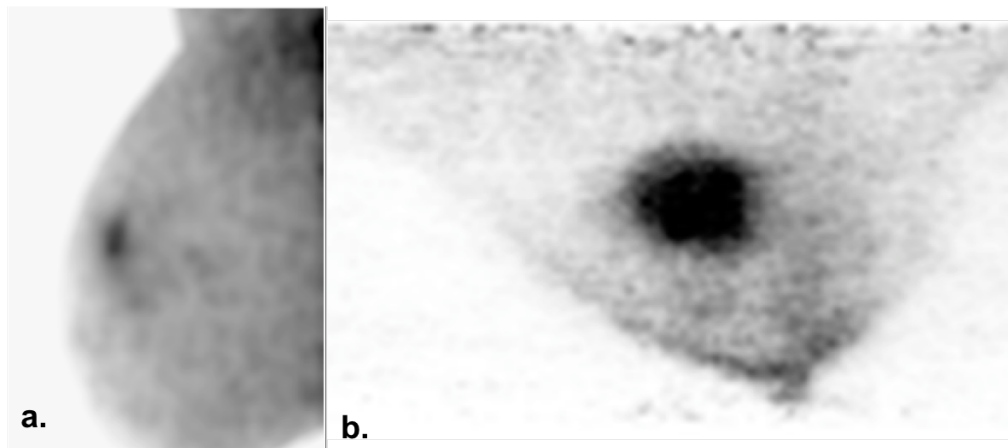


Figure 1-8: Images a and b are examples of breast images acquired using dedicated nuclear medicine breast scanners. Image a is an example of a single gamma image, and b is an example of a positron image.

### 1.2.5.1 Single Gamma Breast Imaging

The higher energy gamma rays of  $^{99m}\text{Tc}$ -sestamibi, with an energy of 140 keV, are attenuated less by the fibroglandular tissue than the 20 – 30 keV x-rays used in mammography. Due to the potential benefits of single gamma imaging for women with radiodense breasts,  $^{99m}\text{Tc}$ -sestamibi scintigraphy was investigated in the late 1990s as a supplemental screening modality<sup>47</sup>. Early nuclear medicine-based breast studies were accomplished with general purpose, large field of view (FOV) gamma cameras. The patients lay prone with their breasts hanging pendant through holes in the table. This was termed scintimammography. Studies showed that when combined with XRM, scintimammography provided complimentary diagnostic information, but displayed poor spatial resolution for deep lesions and low sensitivity for lesions less than 1 cm in size<sup>48–51</sup>.

The poor spatial resolution and low lesion detection sensitivity of scintimammography was largely a result of geometric constraints. Specifically, the large physical size of the cameras coupled with large inactive borders made positioning the patient's breast close to the parallel hole collimator surface challenging and often impossible. This resulted in large lesion-to-collimator distances and substantial geometric collimator blur, causing the counts from small (<1 cm) and deeply positioned lesions to be blurred out over a large area in the image, thereby lowering the image contrast of the lesions and decreasing lesion detectability<sup>49,52–55</sup>. The lack of resolution and sensitivity with large-camera scintimammography led to the development of dedicated breast gamma cameras with a small FOV and reduced inactive borders. These dedicated systems allow the cameras to be placed near or in direct contact with the breast, vastly decreasing the lesion-to-collimator distance and permitting more reliable detection of lesions less than 1 cm in diameter<sup>56–59</sup>.

Compared to earlier scintimammography studies using large FOV gamma cameras, recent studies using dedicated, compact single gamma systems have demonstrated higher sensitivity for small lesions<sup>60–62</sup>. Brem et al. completed two cancer specific studies comparing the sensitivities of BSGI, mammography, and MRI. The first study looked at ductal carcinoma in situ and showed a sensitivity of 91% for single gamma BSGI imaging and sensitivities of 82% and 88% for mammography and MRI, respectively<sup>58</sup>. The second study focused on invasive lobular carcinoma and showed sensitivities of 93%, 79%, and 83% for single gamma imaging,

mammography, and MRI, respectively<sup>63</sup>. More recently, Park et al. completed a study comparing the sensitivity and specificity of BSGI, mammography and ultrasound. For BSGI with semi-quantitative analysis (which is defined as a lesion to background count ratio from measured regions of interest (ROIs)), the sensitivity was found to be 76.2%, compared to 57.1% for mammography and 97.6% for ultrasound. The corresponding specificities were found to be 92.1%, 81.6%, and 61.8% respectively<sup>64</sup>.

### 1.2.5.2 Positron Emission Breast Imaging

Akin to the large FOV cameras used in early single gamma breast imaging, whole body PET (WBPET) scanners have also shown similar limitations regarding spatial resolution and tumor sensitivity for tumors less than 1 cm in size<sup>65,66</sup>. For these reasons, dedicated breast PET systems have been developed in an effort to improve performance. Higher spatial resolution in the dedicated breast PET scanners is achieved in part by positioning the scintillation crystals closer to the breast, which minimizes the effect of acollinearity of the annihilation photons. The first systems used two opposing flat detectors between which the compressed breast was positioned. The available lines of coincidence with this geometry resulted in limited angle acquisition, and the technique was dubbed positron emission mammography (PEM)<sup>67,68</sup>. PEM showed an increased sensitivity for detection of small lesions when compared to WBPET<sup>69,70</sup>; however, it suffered from poor spatial resolution in the direction parallel to the direction of breast compression, had poor signal-to-noise ratio for regions of the breast near the chest wall, and could not image large breasts adequately<sup>71</sup>. In a multicenter study including 388 women with newly diagnosed breast cancer, PEM was compared with MRI and showed a comparable sensitivity for detecting additional cancer in the ipsilateral breast but a higher specificity than MRI<sup>71,72</sup>.

To improve upon the spatial resolution of the PEM system, newer full ring dedicated PET systems have been created. Two examples are the prone MAMMI system by Oncovision and a semi-prone dedicated breast PET system by Shimadzu<sup>73,74</sup>. These systems have a ring made from 8-12 smaller PET detector modules, allowing for full 3-D imaging and improved spatial resolution in all dimensions<sup>73-75</sup>. In a recent study of 230 subjects, the MAMMI system had a lesion detection sensitivity of 88.9%, however, when tumors outside the scanner's FOV (near the chest wall) were excluded, the sensitivity increased to 98.6%<sup>76</sup>. This study highlights the still present difficulty for positron breast imaging of visualizing the tissue in the posterior region of the breast. More extensive human studies with the MAMMI system are ongoing.

## 1.2.6 Dissertation Systems

To improve upon some of the limitations of current dedicated breast imaging systems, our lab has developed two new imaging systems, both of which are briefly described below. The purpose of this work is to optimize and evaluate the following systems, including conducting human studies to help discern their utility for breast cancer detection in terms of sensitivity and specificity. The optimization, evaluation and human studies of the systems will be discussed in the subsequent chapters.

### 1.2.6.1 Dual Modality Tomosynthesis (DMT)

One drawback to dedicated breast nuclear medicine systems is the lack of anatomical information, such as that obtained from mammography, ultrasound, and MRI. This leads to difficulty in accurately correlating nuclear medicine findings to those of the anatomical modalities. One reason for this difficulty is the unescapable difference in breast positioning and

breast shape when moving from one type of imaging system to another. This issue was also seen with whole body nuclear medicine systems and led to the advent of dual modality scanners. These systems combine an anatomical imaging system with a functional imaging system. The two most widely used examples of such hybrid systems are whole body PET/CT and SPECT/CT systems. Although not yet widely used, several PET/MRI systems have become clinically available. Several trials comparing WBPET only versus WBPET/CT have demonstrated the value of adding high-resolution anatomical information to molecular imaging for reducing localization ambiguities in tracer uptake distribution and improving attenuation correction in the PET images<sup>77-79</sup>. Furthermore, clinical trials using hybrid systems for the characterization of disease and the evaluation of treatments for the disease have produced encouraging results for cervical cancer<sup>80</sup>, lymphoma<sup>81</sup>, pulmonary disease<sup>82</sup>, and cardiovascular disease<sup>83</sup>.

As discussed earlier, these whole-body systems have inadequate spatial resolution for early breast cancer detection. Currently, there are several developmental dual modality systems being investigated for dedicated breast imaging. Two noteworthy systems are a dedicated breast SPECT/CT system from Tornai et al. at Duke University and a dedicated breast PET/CT from Bowen et al. at UC-Davis<sup>84,85</sup>. In the SPECT/CT system, the subject lies prone with their uncompressed breast hanging pendant through a hole in a specialized table. Below the table is a quasi-monochromatic cone beam CT system and a CZT-based gamma camera. The gamma camera is mounted on a goniometer to permit 3-dimensional camera orbits. The PET/CT system, similar to the SPECT/CT system, has the subject lie prone with their uncompressed breast hanging pendant through a hole. It utilizes a cone beam CT system and two opposing planar PET detectors. Cone beam CT is acquired over 360 degrees, followed by a PET scan in which the two PET detectors rotate 180 degrees in a step-and-shoot motion.

Over the last ten years, our group at UVa has been developing a limited angle, dual modality tomosynthesis system (DMT)<sup>86</sup>. The DMT system was built in collaboration with Dexela Inc. (London, UK) and Jefferson Lab (Newport News, VA). It is a unique dual modality system permitting XBT and molecular breast imaging tomosynthesis (MBIT) to be performed in rapid succession using a common breast compression, leading to structural and functional volumetric images that are inherently spatially correlated (Fig. 1-9). As discussed above, XBT has become widely accepted clinically and is in the process of replacing planar mammography. The addition of a small FOV gamma camera for MBIT to the existing XBT gantries could be relatively inexpensive and could potentially be made available as an accessory during purchasing. Since planar breast scintigraphy using a gamma camera is already an FDA approved modality it is possible for this type of system to move to the clinic quickly.



Figure 1-9: Dual Modality Tomosynthesis (DMT) system. X-ray tube, gamma camera, and x-ray detector are on a single gantry arm, which rotates around an independent breast compression system.

### 1.2.6.2 Breast Ring Positron Emission Tomography (BRPET)

Although it is not a dual modality system, the dedicated breast ring PET (BRPET) was designed to provide some advantages over current WBPET, MBI and PEM systems. First, the BRPET system utilizes a full detector ring around the breast allowing for fully 3-D images, similar to those of whole body CT and MRI, to be obtained. Compared to limited angle tomography (i.e. PEM), imaging over larger angles (360 degrees in this case) results in more isotropic spatial resolution and fewer under-sampling artifacts. Second, with the goal of improving visualization of posterior breast tissue close to the chest wall each detector in the PET ring has a slanted light guide, thereby permitting the ring of detector crystals to be positioned inside the table hole rather than below it. Visualization of posterior breast tissue (i.e. tissue near the chest wall) has been shown to be an issue not only for PEM systems but also newer dedicated PET systems<sup>87-90</sup>, due to the inherent difficulty of forming an adequate number of lines of response intersecting that region. In most prone systems the thickness of the table places the detector crystals below the table, thereby creating a non-imageable region near the chest wall. In a recent study of 236 lesions a dedicated PET system missed 23 lesions because they were outside the field of view due to their proximity to the chest wall<sup>76</sup>.

## References

- 1 What are the key statistics about breast cancer?. American Cancer Society. n.d. URL: <http://www.cancer.org/cancer/breastcancer/detailedguide/breast-cancer-key-statistics> (Accessed 3 November 2016).
- 2 *Cancer Facts & Figures 2016* | American Cancer Society. n.d. URL: <http://www.cancer.org/research/cancerfactsstatistics/cancerfactsfigures2016/> (Accessed 21 March 2016).
- 3 Hall EJ, Giaccia AJ. *Radiobiology for the Radiologist*. Lippincott Williams & Wilkins; 2006.
- 4 Alberts B, Johnson A, Lewis J, Raff M, Roberts K, Walter P. *Molecular Biology of the Cell*. 4th ed. Garland Science; 2002.
- 5 Andersson I. Invasive Breast Cancer. *Radiologic-Pathologic Correlations from Head to Toe*. Springer, Berlin, Heidelberg; 2005. p. 757–66.
- 6 Boyd NF, Guo H, Martin LJ, Sun L, Stone J, Fishell E, *et al*. Mammographic Density and the Risk and Detection of Breast Cancer. *New England Journal of Medicine* 2007;**356**:227–36. <https://doi.org/10.1056/NEJMoa062790>.
- 7 Harvey JA, Bovbjerg VE. Quantitative Assessment of Mammographic Breast Density: Relationship with Breast Cancer Risk. *Radiology* 2004;**230**:29–41. <https://doi.org/10.1148/radiol.2301020870>.
- 8 Berry DA, Cronin KA, Plevritis SK, Fryback DG, Clarke L, Zelen M, *et al*. Effect of Screening and Adjuvant Therapy on Mortality from Breast Cancer. *New England Journal of Medicine* 2005;**353**:1784–92. <https://doi.org/10.1056/NEJMoa050518>.
- 9 Lee CH, Dershaw DD, Kopans D, Evans P, Monsees B, Monticciolo D, *et al*. Breast Cancer Screening With Imaging: Recommendations From the Society of Breast Imaging and the ACR on the Use of Mammography, Breast MRI, Breast Ultrasound, and Other Technologies for the Detection of Clinically Occult Breast Cancer. *Journal of the American College of Radiology* 2010;**7**:18–27. <https://doi.org/10.1016/j.jacr.2009.09.022>.
- 10 Monticciolo DL, Newell MS, Hendrick RE, Helvie MA, Moy L, Monsees B, *et al*. Breast Cancer Screening for Average-Risk Women: Recommendations From the ACR Commission on Breast Imaging. *Journal of the American College of Radiology* 2017;**14**:1137–43. <https://doi.org/10.1016/j.jacr.2017.06.001>.
- 11 Humphrey LL. Breast Cancer Screening: A Summary of the Evidence for the U.S. Preventive Services Task Force. *Annals of Internal Medicine* 2002;**137**:347. [https://doi.org/10.7326/0003-4819-137-5\\_Part\\_1-200209030-00012](https://doi.org/10.7326/0003-4819-137-5_Part_1-200209030-00012).
- 12 Johns PC, Yaffe MJ. X-ray characterisation of normal and neoplastic breast tissues. *Phys Med Biol* 1987;**32**:675. <https://doi.org/10.1088/0031-9155/32/6/002>.
- 13 Balleyguier C, Ayadi S, Nguyen KV, Vanel D, Dromain C, Sigal R. BIRADS™ classification in mammography. *European Journal of Radiology* 2007;**61**:192–4. <https://doi.org/10.1016/j.ejrad.2006.08.033>.
- 14 Bevers TB, Anderson BO, Bonaccio E, Buys S, Daly MB, Dempsey PJ, *et al*. Breast Cancer Screening and Diagnosis. *J Natl Compr Canc Netw* 2009;**7**:1060–96. <https://doi.org/10.6004/jnccn.2009.0070>.
- 15 Saslow D, Boetes C, Burke W, Harms S, Leach MO, Lehman CD, *et al*. American Cancer Society Guidelines for Breast Screening with MRI as an Adjunct to Mammography. *CA: A Cancer Journal for Clinicians* 2007;**57**:75–89. <https://doi.org/10.3322/canjclin.57.2.75>.
- 16 Nightingale JM, Murphy FJ, Robinson L, Newton-Hughes A, Hogg P. Breast compression – An exploration of problem solving and decision-making in mammography. *Radiography* 2015;**21**:364–9. <https://doi.org/10.1016/j.radi.2014.11.004>.
- 17 Tabár L, Dean PB. Mammographic Parenchymal Patterns: Risk Indicator for Breast Cancer? *JAMA* 1982;**247**:185–9. <https://doi.org/10.1001/jama.1982.03320270023016>.

- 18 Sickles E. Mammographic features of 300 consecutive nonpalpable breast cancers. *American Journal of Roentgenology* 1986;**146**:661–3. <https://doi.org/10.2214/ajr.146.4.661>.
- 19 Jackson VP, Hendrick RE, Feig SA, Kopans DB. Imaging of the radiographically dense breast. *Radiology* 1993;**188**:297–301. <https://doi.org/10.1148/radiology.188.2.8327668>.
- 20 Rosenberg RD, Hunt WC, Williamson MR, Gilliland FD, Wiest PW, Kelsey CA, *et al*. Effects of age, breast density, ethnicity, and estrogen replacement therapy on screening mammographic sensitivity and cancer stage at diagnosis: review of 183,134 screening mammograms in Albuquerque, New Mexico. *Radiology* 1998;**209**:511–8. <https://doi.org/10.1148/radiology.209.2.9807581>.
- 21 Kolb TM, Lichy J, Newhouse JH. Comparison of the Performance of Screening Mammography, Physical Examination, and Breast US and Evaluation of Factors that Influence Them: An Analysis of 27,825 Patient Evaluations. *Radiology* 2002;**225**:165–75. <https://doi.org/10.1148/radiol.2251011667>.
- 22 Taplin S, Abraham L, Barlow WE, Fenton JJ, Berns EA, Carney PA, *et al*. Mammography Facility Characteristics Associated With Interpretive Accuracy of Screening Mammography. *JNCI J Natl Cancer Inst* 2008;**100**:876–87. <https://doi.org/10.1093/jnci/djn172>.
- 23 Niklason LT, Christian BT, Niklason LE, Kopans DB, Castleberry DE, Opsahl-Ong BH, *et al*. Digital tomosynthesis in breast imaging. *Radiology* 1997;**205**:399–406. <https://doi.org/10.1148/radiology.205.2.9356620>.
- 24 Tingberg A. X-Ray Tomosynthesis: A Review of Its Use for Breast and Chest Imaging. *Radiat Prot Dosimetry* 2010;ncq099. <https://doi.org/10.1093/rpd/ncq099>.
- 25 Wu T, Stewart A, Stanton M, McCauley T, Phillips W, Kopans DB, *et al*. Tomographic mammography using a limited number of low-dose cone-beam projection images. *Medical Physics* 2003;**30**:365–80. <https://doi.org/10.1118/1.1543934>.
- 26 Sechopoulos I, Suryanarayanan S, Vedantham S, D’Orsi C, Karellas A. Computation of the glandular radiation dose in digital tomosynthesis of the breast. *Medical Physics* 2007;**34**:221–32. <https://doi.org/10.1118/1.2400836>.
- 27 Zhao B, Zhao W. Three-dimensional linear system analysis for breast tomosynthesis. *Medical Physics* 2008;**35**:5219–32. <https://doi.org/10.1118/1.2996014>.
- 28 Mainprize JG, Bloomquist AK, Kempston MP, Yaffe MJ. Resolution at oblique incidence angles of a flat panel imager for breast tomosynthesis. *Medical Physics* 2006;**33**:3159–64. <https://doi.org/10.1118/1.2241994>.
- 29 Andersson I, Ikeda DM, Zackrisson S, Ruschin M, Svahn T, Timberg P, *et al*. Breast tomosynthesis and digital mammography: a comparison of breast cancer visibility and BIRADS classification in a population of cancers with subtle mammographic findings. *Eur Radiol* 2008;**18**:2817–25. <https://doi.org/10.1007/s00330-008-1076-9>.
- 30 Svahn TM, Chakraborty DP, Ikeda D, Zackrisson S, Do Y, Mattsson S, *et al*. Breast tomosynthesis and digital mammography: a comparison of diagnostic accuracy. *BJR* 2012;**85**:e1074–82. <https://doi.org/10.1259/bjr/53282892>.
- 31 Noroozian M, Hadjiiski L, Rahnama-Moghadam S, Klein KA, Jeffries DO, Pinsky RW, *et al*. Digital Breast Tomosynthesis Is Comparable to Mammographic Spot Views for Mass Characterization. *Radiology* 2012;**262**:61–8. <https://doi.org/10.1148/radiol.11101763>.
- 32 Skaane P, Bandos AI, Gullien R, Eben EB, Ekseth U, Haakenaasen U, *et al*. Comparison of Digital Mammography Alone and Digital Mammography Plus Tomosynthesis in a Population-based Screening Program. *Radiology* 2013;**267**:47–56. <https://doi.org/10.1148/radiol.12121373>.
- 33 Rose SL, Tidwell AL, Bujnoch LJ, Kushwaha AC, Nordmann AS, Sexton R. Implementation of Breast Tomosynthesis in a Routine Screening Practice: An Observational Study. *American Journal of Roentgenology* 2013;**200**:1401–8. <https://doi.org/10.2214/AJR.12.9672>.

- 34 Berg WA, Zhang Z, Lehrer D, Jong RA, Pisano ED, Barr RG, *et al.* Detection of Breast Cancer With Addition of Annual Screening Ultrasound or a Single Screening MRI to Mammography in Women With Elevated Breast Cancer Risk. *JAMA* 2012;**307**:1394–404. <https://doi.org/10.1001/jama.2012.388>.
- 35 Kelly KM, Dean J, Lee S-J, Comulada WS. Breast cancer detection: radiologists' performance using mammography with and without automated whole-breast ultrasound. *Eur Radiol* 2010;**20**:2557–64. <https://doi.org/10.1007/s00330-010-1844-1>.
- 36 Morrow M, Waters J, Morris E. MRI for breast cancer screening, diagnosis, and treatment. *The Lancet* 2011;**378**:1804–11. [https://doi.org/10.1016/S0140-6736\(11\)61350-0](https://doi.org/10.1016/S0140-6736(11)61350-0).
- 37 Sardanelli F, Giuseppetti GM, Panizza P, Bazzocchi M, Fausto A, Simonetti G, *et al.* Sensitivity of MRI Versus Mammography for Detecting Foci of Multifocal, Multicentric Breast Cancer in Fatty and Dense Breasts Using the Whole-Breast Pathologic Examination as a Gold Standard. *American Journal of Roentgenology* 2004;**183**:1149–57. <https://doi.org/10.2214/ajr.183.4.1831149>.
- 38 Heywang-Köbrunner SH, Viehweg P, Heinig A, Küchler C. Contrast-enhanced MRI of the breast: accuracy, value, controversies, solutions. *European Journal of Radiology* 1997;**24**:94–108. [https://doi.org/10.1016/S0720-048X\(96\)01142-4](https://doi.org/10.1016/S0720-048X(96)01142-4).
- 39 Caravan P, Ellison JJ, McMurry TJ, Lauffer RB. Gadolinium(III) Chelates as MRI Contrast Agents: Structure, Dynamics, and Applications. *Chem Rev* 1999;**99**:2293–352.
- 40 Holbrook AI, Newell MS. Magnetic Resonance Imaging of the Breast. *Clinical Obstetrics and Gynecology* 2016;**59**:394–402. <https://doi.org/10.1097/GRF.0000000000000189>.
- 41 Kuhl CK, Schradang S, Leutner CC, Morakkabati-Spitz N, Wardelmann E, Fimmers R, *et al.* Mammography, Breast Ultrasound, and Magnetic Resonance Imaging for Surveillance of Women at High Familial Risk for Breast Cancer. *JCO* 2005;**23**:8469–76. <https://doi.org/10.1200/JCO.2004.00.4960>.
- 42 Teifke A, Hlawatsch A, Beier T, Werner Vomweg T, Schadmand S, Schmidt M, *et al.* Undetected Malignancies of the Breast: Dynamic Contrast-enhanced MR Imaging at 1.0 T. *Radiology* 2002;**224**:881–8. <https://doi.org/10.1148/radiol.2243010547>.
- 43 Bluemke DA, Gatsonis CA, Chen MH, DeAngelis GA, DeBruhl N, Harms S, *et al.* Magnetic Resonance Imaging of the Breast Prior to Biopsy. *JAMA* 2004;**292**:2735–42. <https://doi.org/10.1001/jama.292.22.2735>.
- 44 *Prospective Comparison of Standard Triple Assessment and Dyn... : Annals of Surgery*. LWW. n.d. URL: [http://journals.lww.com/annalsofsurgery/Fulltext/1999/11000/Prospective\\_Comparison\\_of\\_Standard\\_Triple.10.aspx](http://journals.lww.com/annalsofsurgery/Fulltext/1999/11000/Prospective_Comparison_of_Standard_Triple.10.aspx) (Accessed 4 November 2016).
- 45 Fischer U, Kopka L, Grabbe E. Breast Carcinoma: Effect of Preoperative Contrast-enhanced MR Imaging on the Therapeutic Approach. *Radiology* 1999;**213**:881–8. <https://doi.org/10.1148/radiology.213.3.r99dc01881>.
- 46 Moore SG, Shenoy PJ, Fanucchi L, Tumej JW, Flowers CR. Cost-effectiveness of MRI compared to mammography for breast cancer screening in a high risk population. *BMC Health Services Research* 2009;**9**:9. <https://doi.org/10.1186/1472-6963-9-9>.
- 47 Taillefer R, Robidoux A, Lambert R, Turpin S, Laperrière J. Technetium-99m-sestamibi prone scintimammography to detect primary breast cancer and axillary lymph node involvement. *J Nucl Med* 1995;**36**:1758–65.
- 48 F S, O S, W U, K N, R C, G DV, *et al.* A three center study on the diagnostic accuracy of 99mTc-MIBI scintimammography. *Anticancer Res* 1996;**17**:1631–4.
- 49 Cinti MN, Pani R, Pellegrini R, Bonifazzi C, Scafe R, Vincentis GD, *et al.* Tumor SNR analysis in scintimammography by dedicated high contrast imager. *IEEE Transactions on Nuclear Science* 2003;**50**:1618–23. <https://doi.org/10.1109/TNS.2003.817345>.

- 50 Buscombe JR, Cwikla JB, Holloway B, Hilson AJW. Prediction of the Usefulness of Combined Mammography and Scintimammography in Suspected Primary Breast Cancer Using ROC Curves. *J Nucl Med* 2001;**42**:3–8.
- 51 Moadel RM. Breast Cancer Imaging Devices. *Seminars in Nuclear Medicine* 2011;**41**:229–41. <https://doi.org/10.1053/j.semnuclmed.2010.12.005>.
- 52 More MJ, Goodale PJ, Majewski S, Williams MB. Evaluation of Gamma Cameras for Use in Dedicated Breast Imaging. Presented at the 2004 IEEE Nuclear Science Symposium Conference Record.
- 53 Hruska CB, O'Connor MK. Effect of Collimator Selection on Tumor Detection for Dedicated Nuclear Breast Imaging Systems. *IEEE Transactions on Nuclear Science* 2006;**53**:2680–9. <https://doi.org/10.1109/TNS.2006.879824>.
- 54 Majewski S, Kieper D, Curran E, Keppel C, Kross B, Palumbo A, *et al.* Optimization of dedicated scintimammography procedure using detector prototypes and compressible phantoms. *IEEE Transactions on Nuclear Science* 2001;**48**:822–9. <https://doi.org/10.1109/23.940170>.
- 55 Pani R, Bennati P, Cinti MN, Pellegrini R, Betti M, Ridolfi S, *et al.* Imaging Characteristics Comparison of Compact Pixellated Detectors for Scintimammography. Presented at the 2004 IEEE Nuclear Science Symposium Conference Record.
- 56 Berg WA. Nuclear Breast Imaging: Clinical Results and Future Directions. *J Nucl Med* 2016;**57**:46S–52S. <https://doi.org/10.2967/jnumed.115.157891>.
- 57 Brem RF, Rapelyea JA, Zisman G, Mohtashemi K, Raub J, Teal CB, *et al.* Occult Breast Cancer: Scintimammography with High-Resolution Breast-specific Gamma Camera in Women at High Risk for Breast Cancer. *Radiology* 2005;**237**:274–80. <https://doi.org/10.1148/radiol.2371040758>.
- 58 Brem RF, Fishman M, Rapelyea JA. Detection of Ductal Carcinoma in Situ with Mammography, Breast Specific Gamma Imaging, and Magnetic Resonance Imaging: A Comparative Study. *Academic Radiology* 2007;**14**:945–50. <https://doi.org/10.1016/j.acra.2007.04.004>.
- 59 Hruska CB, Phillips SW, Whaley DH, Rhodes DJ, O'Connor MK. Molecular Breast Imaging: Use of a Dual-Head Dedicated Gamma Camera to Detect Small Breast Tumors. *AJR Am J Roentgenol* 2008;**191**:. <https://doi.org/10.2214/AJR.07.3693>.
- 60 O'Connor MK, Tourassi G, Orton CG. Molecular breast imaging will soon replace x-ray mammography as the imaging modality of choice for women at high risk with dense breasts. *Medical Physics* 2009;**36**:1463–6. <https://doi.org/10.1118/1.3098126>.
- 61 Rechtman LR, Lenihan MJ, Lieberman JH, Teal CB, Torrente J, Rapelyea JA, *et al.* Breast-Specific Gamma Imaging for the Detection of Breast Cancer in Dense Versus Nondense Breasts. *American Journal of Roentgenology* 2014;**202**:293–8. <https://doi.org/10.2214/AJR.13.11585>.
- 62 Weigert JM, Bertrand ML, Lanzkowsky L, Stern LH, Kieper DA. Results of a Multicenter Patient Registry to Determine the Clinical Impact of Breast-Specific Gamma Imaging, a Molecular Breast Imaging Technique. *American Journal of Roentgenology* 2012;**198**:W69–75. <https://doi.org/10.2214/AJR.10.6105>.
- 63 Brem RF, Ioffe M, Rapelyea JA, Yost KG, Weigert JM, Bertrand ML, *et al.* Invasive Lobular Carcinoma: Detection with Mammography, Sonography, MRI, and Breast-Specific Gamma Imaging. *American Journal of Roentgenology* 2009;**192**:379–83. <https://doi.org/10.2214/AJR.07.3827>.
- 64 Park KS, Chung HW, Yoo YB, Yang J-H, Choi N, So Y. Complementary Role of Semiquantitative Analysis of Breast-Specific Gamma Imaging in the Diagnosis of Breast Cancer. *American Journal of Roentgenology* 2014;**202**:690–5. <https://doi.org/10.2214/AJR.13.11324>.

- 65 Wu D, Gambhir SS. Positron Emission Tomography in Diagnosis and Management of Invasive Breast Cancer: Current Status and Future Perspectives. *Clinical Breast Cancer* 2003;**4**, **Supplement 1**:S55–63. <https://doi.org/10.3816/CBC.2003.s.016>.
- 66 Avril N, Adler LP. F-18 Fluorodeoxyglucose-Positron Emission Tomography Imaging for Primary Breast Cancer and Loco-Regional Staging. *Radiologic Clinics of North America* 2007;**45**:645–57. <https://doi.org/10.1016/j.rcl.2007.05.004>.
- 67 Thompson CJ, Murthy K, Weinberg IN, Mako F. Feasibility study for positron emission mammography. *Medical Physics* 1994;**21**:529–38. <https://doi.org/10.1118/1.597169>.
- 68 Raylman RR, Majewski S, Wojcik R, Weisenberger AG, Kross B, Popov V, *et al.* The potential role of positron emission mammography for detection of breast cancer. A phantom study. *Medical Physics* 2000;**27**:1943–54. <https://doi.org/10.1118/1.1287439>.
- 69 Kalinyak JE, Berg WA, Schilling K, Madsen KS, Narayanan D, Tartar M. Breast cancer detection using high-resolution breast PET compared to whole-body PET or PET/CT. *Eur J Nucl Med Mol Imaging* 2014;**41**:260–75. <https://doi.org/10.1007/s00259-013-2553-1>.
- 70 Eo JS, Chun IK, Paeng JC, Kang KW, Lee SM, Han W, *et al.* Imaging sensitivity of dedicated positron emission mammography in relation to tumor size. *The Breast* 2012;**21**:66–71. <https://doi.org/10.1016/j.breast.2011.08.002>.
- 71 Berg WA, Madsen KS, Schilling K, Tartar M, Pisano ED, Larsen LH, *et al.* Breast Cancer: Comparative Effectiveness of Positron Emission Mammography and MR Imaging in Presurgical Planning for the Ipsilateral Breast. *Radiology* 2011;**258**:59–72. <https://doi.org/10.1148/radiol.10100454>.
- 72 Berg WA, Madsen KS, Schilling K, Tartar M, Pisano ED, Larsen LH, *et al.* Comparative Effectiveness of Positron Emission Mammography and MRI in the Contralateral Breast of Women With Newly Diagnosed Breast Cancer. *American Journal of Roentgenology* 2012;**198**:219–32. <https://doi.org/10.2214/AJR.10.6342>.
- 73 Hernández TG, González AV, Rebolleda JF, Jurado RS, Ferrando JR, González LB, *et al.* Performance evaluation of a high resolution dedicated breast PET scanner. *Medical Physics* 2016;**43**:2261–72. <https://doi.org/10.1118/1.4945271>.
- 74 Miyake KK, Matsumoto K, Inoue M, Nakamoto Y, Kanao S, Oishi T, *et al.* Performance Evaluation of a New Dedicated Breast PET Scanner Using NEMA NU4-2008 Standards. *J Nucl Med* 2014;**55**:1198–203. <https://doi.org/10.2967/jnumed.113.131565>.
- 75 Moliner L, González AJ, Soriano A, Sánchez F, Correcher C, Orero A, *et al.* Design and evaluation of the MAMMI dedicated breast PET. *Medical Physics* 2012;**39**:5393–404. <https://doi.org/10.1118/1.4742850>.
- 76 Teixeira SC, Rebolleda JF, Koolen BB, Wesseling J, Jurado RS, Stokkel MPM, *et al.* Evaluation of a Hanging-Breast PET System for Primary Tumor Visualization in Patients With Stage I–III Breast Cancer: Comparison With Standard PET/CT. *American Journal of Roentgenology* 2016;**206**:1307–14. <https://doi.org/10.2214/AJR.15.15371>.
- 77 Ben-Haim S, Eil P. 18F-FDG PET and PET/CT in the Evaluation of Cancer Treatment Response. *J Nucl Med* 2009;**50**:88–99. <https://doi.org/10.2967/jnumed.108.054205>.
- 78 Sung YM, Lee KS, Kim B-T, Choi JY, Chung MJ, Shim YM, *et al.* 18F-FDG PET versus 18F-FDG PET/CT for Adrenal Gland Lesion Characterization: a Comparison of Diagnostic Efficacy in Lung Cancer Patients. *Korean Journal of Radiology* 2008;**9**:19–28. <https://doi.org/10.3348/kjr.2008.9.1.19>.
- 79 Tatsumi M, Miller JH, Wahl RL. 18F-FDG PET/CT in Evaluating Non-CNS Pediatric Malignancies. *J Nucl Med* 2007;**48**:1923–31. <https://doi.org/10.2967/jnumed.107.044628>.
- 80 Magné N, Chargari C, Vicenzi L, Gillion N, Messai T, Magné J, *et al.* New trends in the evaluation and treatment of cervix cancer: The role of FDG–PET. *Cancer Treatment Reviews* 2008;**34**:671–81. <https://doi.org/10.1016/j.ctrv.2008.08.003>.
- 81 Kuo PH, Carlson KR, Christensen I, Girardi M, Heald PW. FDG-PET/CT for the Evaluation of Response to Therapy of Cutaneous T-cell Lymphoma to Vorinostat

- (Suberoylanilide Hydroxamic Acid, SAHA) in a Phase II Trial. *Mol Imaging Biol* 2008;**10**:306–14. <https://doi.org/10.1007/s11307-008-0161-4>.
- 82 Jeong SY, Lee KS, Shin KM, Bae YA, Kim B-T, Choe BK, *et al*. Efficacy of PET/CT in the characterization of solid or partly solid solitary pulmonary nodules. *Lung Cancer* 2008;**61**:186–94. <https://doi.org/10.1016/j.lungcan.2007.12.021>.
- 83 Neglia D, Rimoldi O, Kaufmann PA, Camici PG. Radionuclide PET and PET/CT in coronary artery disease. *Curr Pharm Des* 2008;**14**:1798–814.
- 84 Madhav P, Crotty DJ, McKinley RL, Tornai MP. Initial Development of a Dual-Modality SPECT-CT System for Dedicated Mammotomography. Presented at the 2006 IEEE Nuclear Science Symposium Conference Record.
- 85 Bowen SL, Wu Y, Chaudhari AJ, Fu L, Packard NJ, Burkett GW, *et al*. Initial Characterization of a Dedicated Breast PET/CT Scanner During Human Imaging. *J Nucl Med* 2009;**50**:1401–8. <https://doi.org/10.2967/jnumed.109.064428>.
- 86 More MJ, Li H, Goodale PJ, Zheng Y, Majewski S, Popov V, *et al*. Limited Angle Dual Modality Breast Imaging. *IEEE Transactions on Nuclear Science* 2007;**54**:504–13. <https://doi.org/10.1109/TNS.2007.897828>.
- 87 Murthy K, Aznar M, Thompson CJ, Loutfi A, Lisbona R, Gagnon JH. Results of Preliminary Clinical Trials of the Positron Emission Mammography System PEM-I: A Dedicated Breast Imaging System Producing Glucose Metabolic Images Using FDG. *J Nucl Med* 2000;**41**:1851–8.
- 88 Rosen EL, Turkington TG, Soo MS, Baker JA, Coleman RE. Detection of Primary Breast Carcinoma with a Dedicated, Large-Field-of-View FDG PET Mammography Device: Initial Experience. *Radiology* 2005;**234**:527–34. <https://doi.org/10.1148/radiol.2342040654>.
- 89 Berg WA, Weinberg IN, Narayanan D, Lobrano ME, Ross E, Amodei L, *et al*. High-Resolution Fluorodeoxyglucose Positron Emission Tomography with Compression (“Positron Emission Mammography”) is Highly Accurate in Depicting Primary Breast Cancer. *The Breast Journal* 2006;**12**:309–23. <https://doi.org/10.1111/j.1075-122X.2006.00269.x>.
- 90 MacDonald L, Edwards J, Lewellen T, Haseley D, Rogers J, Kinahan P. Clinical Imaging Characteristics of the Positron Emission Mammography Camera: PEM Flex Solo II. *J Nucl Med* 2009;**50**:1666–75. <https://doi.org/10.2967/jnumed.109.064345>.

## Chapter 2

### Nuclear Medicine Systems and Theory

Nuclear medicine is an imaging procedure that allows visualization and characterization of cellular function within the body. Due to its unique ability to observe cellular function nuclear medicine is considered a functional imaging system, differing from more traditional imaging techniques such as CT and MRI, which are structural (anatomical) imaging techniques. A nuclear medicine procedure has two main components: 1) a radiopharmaceutical and 2) a detector system. The radiopharmaceutical (also called radiotracer) is typically a biologically significant molecule that has been modified to have a radionuclide attached to it. The radiopharmaceutical is injected (usually intravenously) into the subject and the resulting distribution of the tracer within the body is imaged by the detector. This chapter will describe the basics of the radiopharmaceuticals, including the description of the ones used for breast cancer imaging, the typical design of the detectors, and common system evaluation techniques used to characterize these systems.

#### 2.1 Radiopharmaceuticals

Radiopharmaceuticals are the imaging agents that make nuclear medicine possible. They typically consist of two parts, the first a radionuclide and the second a biologically relevant pharmaceutical.

A radionuclide is an atom whose nucleus contains unstable grouping of protons and neutrons. The radioactive nucleus (referred to as the parent) emits either high energy charged particles or gamma rays in order to reach a stable state (with the resulting nucleus called the daughter). This process is called radioactive decay. Although there are several different modes of decay, there are only three that are relevant to medical imaging. They are: 1) isomeric transition, 2) electron capture, and 3) positron decay. Isomeric transition (IT) occurs when a metastable daughter nucleus of a radioactive parent releases energy in the form of a gamma ray to get to a stable state. Metastable atoms with long half-lives have been proven to be useful for medical imaging<sup>1,2</sup>. The half-life is defined as the amount of time it takes for the total number of nuclides,  $N$ , to decay to  $N/2$  nuclides. An example of an isomeric transition is:



Some fraction of the emitted gamma rays will interact with the atom's shell electrons. During this interaction the gamma ray's energy is transferred to the electron giving it enough energy to break free of the atom; this electron is called a conversion electron. For imaging purposes, nuclides that produce small conversion electron to gamma ray ratios are chosen. This helps minimize the extra radiation dose the subject receives from the conversion electrons. The most common metastable radionuclide used for imaging is currently Tc-99m (see Table 2-1).

Electron capture (EC) occurs when an unstable nucleus absorbs (captures) an orbital electron, which then combines with a positron to create a neutron, with simultaneous release of a neutrino. The resulting nucleus can release excess energy in the form of characteristic x-rays created as the vacant inner orbital electron shell is filled by an outer shell electron<sup>1,2</sup>. The decay of a parent nuclide via EC can lead to a daughter nuclide in an excited state. These daughter nuclides quickly decay to a stable state via a separate gamma emission; this is typically represented as (EC, $\gamma$ ) decay. Some EC nuclides emit characteristic x-rays that are sufficient

energetic for use in medical imaging (for example I-125, with x-ray energy of 31.7 keV). For others the gamma rays created during the (EC, $\gamma$ ) process are imaged.

The last decay mode is positron decay. Here a positron ( $\beta^+$ ) is created by the decay of a proton into a neutron. An example of a positron emitting radionuclide is:



where  $\nu$  is a neutrino. A positron is the antiparticle of an electron, meaning it is the same mass but opposite charge of an electron. When the two particles meet they undergo a process called annihilation, where the masses of the two particles are converted into energy. This creates two photons of equal energy emitted at approximately 180 degrees from each other (Figure 2-1a). Since the mass-energy equivalent of each particle is 511 keV the emitted photons each have an energy of 511 keV. An electron volt (eV) is defined as the amount of energy gained when an electron accelerates through a potential of 1 volt<sup>1</sup>. It is important to note that the angle between the two photons is not typically exactly 180 degrees. This is because the positron-electron pair typically has non-zero total momentum, and this momentum is carried away by the annihilation photons. The difference in emission angle from 180 degrees is called acollinearity and can be seen in Figure 2-1b.

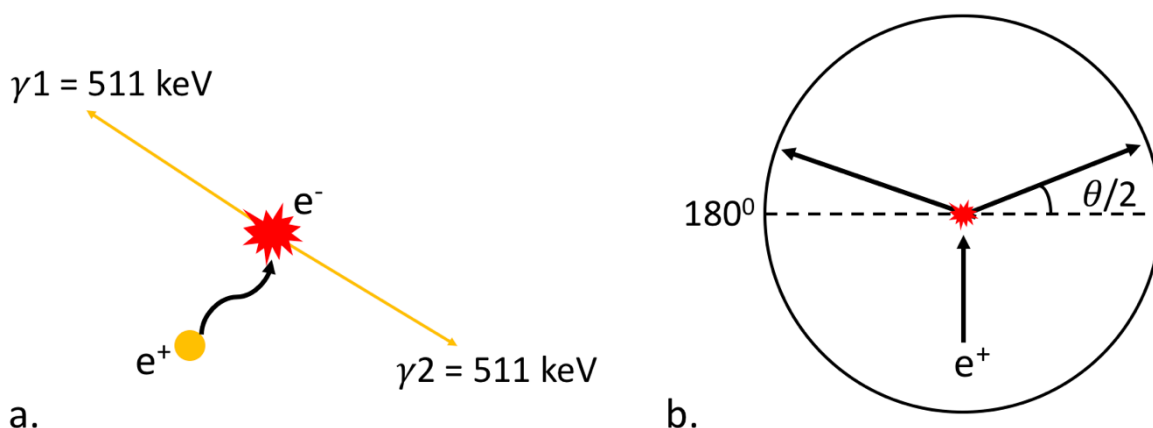


Figure 2-1: a) Illustrates positron annihilation. b) Illustrates the acollinearity effect caused by the non-zero momentum of the positron-electron pair.

In nuclear medicine, images of the biodistribution of a radiopharmaceutical are created through the detection of the photons released via the decay modes above. So, to ensure quality images, along with minimizing the radiation dose to the subject, the radionuclides chosen should ideally have the following three main characteristics: 1) a balanced half-life, 2) appropriate energy photons, and 3) a single decay mode. First, the nuclide should have a balanced half-life. This means the half-life should be long enough for the radiopharmaceutical to accumulate in the target area, but short enough to minimize radiation dose to the subject. If the number of undecayed isotope atoms is  $N_0$ , then after a time  $t$  the number is:

$$N(t) = N_0 e^{-\lambda t} \quad (2-3)$$

Equation 2-3 defines the number of undecayed nuclei left after the original number of nuclides decays for a time,  $t$ . Here  $\lambda$ , known as the decay factor, is defined by:

$$\frac{dN}{dt} = -\lambda N \quad (2-4)$$

Equation 2-3 is originally derived from equation 2-4. The half-life,  $T_{1/2}$ , of a nuclide is defined as the time it takes for the number of original nuclides to decay by  $1/2$ . From equation 2-3, a following relationship can be derived:  $\lambda = 0.693/T_{1/2}$ . Because the number of radioactive nuclides decay exponentially over time short-lived radionuclide can be injected and left to decay away helping keep the radiation dose to the patient low. The half-life of typical radionuclides used in imaging can be seen in Table 2-1. It is important to note that once a radionuclide is attached to a pharmaceutical the effective half-life, which determines the radiation dose, becomes dependent on both the radionuclide's half-life,  $T_p$ , and the biological half-life of the molecule,  $T_b$ . The effective half-life or  $T_e$  is given by.

$$T_e = \frac{T_p * T_b}{T_p + T_b} \quad (2-5)$$

Since the number of radioactive atoms in a sample cannot be easily measured, the quantity of a sample is measured by its activity, or decay rate,  $A = \Delta N/\Delta t = \lambda N$ . It has Systeme International (SI) units of disintegrations per second (dps), known as a becquerel (Bq). However, the traditional unit, which is still widely used is the curie (Ci), which is defined as  $3.7 \times 10^{10}$  dps, the activity of 1 gram of Ra-226.

Second, the radionuclide must emit photons with energies that can penetrate the soft tissue and bone that they will have to travel through to get to the detectors. Each tissue a photon goes through will attenuate the photon differently; this is what allows us to differentiate organs in conventional x-ray imaging. The linear attenuation coefficient ( $\mu$ ) is defined as the probability of interaction per unit length (Eqn. 2-6).

$$\frac{dI}{dt} = -\lambda I \quad (2-6)$$

More specifically  $\mu$  relates the attenuation per cm of an absorber for a discrete photon energy <sup>2,3</sup>. The coefficient is dependent on both the density ( $\rho$ ) of the absorbing material and the energy of the photon <sup>3</sup>. It increases linearly with increasing density and generally decreases with increasing photon energy. Similarly to equation 2-4, the equation that defines the transmission of a monoenergetic photon beam through a single absorber can be derived from equation 2-6:

$$I = I_0 e^{-\mu x} \quad (2-7)$$

Where  $I_0$  is the intensity of the incident photon beam and  $x$  is the thickness of the absorbing material.

Typical photon energies associated with nuclear imaging agents are between 60 – 511 keV <sup>2</sup>. Over this energy range, the value of  $\mu$  for biological tissue is sufficiently low to permit a large fraction of emitted gamma rays to escape the body, but  $\mu$  for available detector materials is high enough to ensure detection of a significant fraction of gammas. In transmission x-ray imaging, the goal is to measure the difference in x-ray attenuation along various lines through the body. In that case differences in  $\mu$  values for different tissue types are maximized at somewhat lower energy, and the x-ray energy range is ~25 – 140 keV, depending on the part of the body being imaged. A metric commonly used to quantify photon beam energy is the half value layer (HVL), which is the thickness of a standard absorber (usually aluminum) needed to reduce the photon beam intensity to half of that of the incident beam. From 2-7, the HVL is given by

$$HVL = \frac{0.693}{\mu} \quad (2-8)$$

In current breast tomosynthesis systems, x-ray tubes usually have tube voltages set between 25 and 50 kVp (peak kilo-voltage), which results in x-ray spectra with maximum photon energy given by the electron charge times the tube voltage setting <sup>4</sup>. For example, a 30 kVp tube voltage will result in a max energy of 30 keV. The HVL of water at 140 keV, a typical photon energy for nuclear medicine, is 4.3 cm, while at 30 keV it is 1.9 cm. It is important to note that the mean x-ray energy tends to be much less than the maximum energy, meaning the effective HVL is actually less than 1.9 cm. Water is used here because its linear attenuation coefficient is similar to that of soft tissue <sup>5</sup>.

Finally, the radionuclide should not have multiple decay modes, with only one being used for imaging and the others contributing only radiation dose. This is important to ensure the radiation dose to the patient is kept to a minimum. An example of an isotope with multiple decay modes is Au-138, which produces beta-particles and gamma rays. Although, we could produce images through positron or gamma ray emission, the subject would attain a large radiation dose from the nuclide's beta particles. Therefore, nuclides such as Tc-99m or F-18 are preferable (see Table 2-1 for several commonly used single gamma and positron isotopes).

Table 2-1: Commonly used Radiopharmaceuticals and their Properties

Modality	Nuclide	Decay Mode	Primary Energy	Half-Life	Pharmaceutical	Target Imaged
Gamma	Tc-99m	IT	140	6 hr.	Sestamibi (MIBI)	Cardiac, Breast, Parathyroid
					MAA	Lung Perfusion
					per technetate	Thyroid
					DTPA	Lung Ventilation
					MDP	Bone
	In-111	EC	173, 247	2.81 d.	Pentetreotide	Brain
I-123	EC	159	13 hr.	Sodium Iodide	Thyroid	
TI-201	EC	167	3.05 d.	Chloride	Heart	
PET	F-18	$\beta^+$	511	110 min.	FDG	Glucose Metabolism
					Sodium Fluoride	Bone
	C-11	$\beta^+$	511	20.3 min.	Choline	Prostate
	O-15	$\beta^+$	511	2.07 min.	O <sub>2</sub>	Blood Flow

With the knowledge of the specific radionuclides that can be used, pharmaceuticals or biologically significant molecules with biological pathways of interest to the imagers are chosen for attachment. A process called radiochemistry is used to bond the nuclide and pharmaceutical to create the radiopharmaceutical. There are many available radiopharmaceuticals available with a large range of physiological targets. Some examples can be seen in Table 2-1. For the purpose of breast imaging there are only two FDA approved imaging agents that can be used specifically for breast imaging <sup>6</sup>. They are Tc-99m MIBI and F-18 FDG.

Tc-99m MIBI is a lipophilic cation that reversibly accumulates in a cell's cytoplasm and mitochondria in both normal and malignant cells. It is passively transported into the cell due to the largely negatively charged plasma and mitochondrial membranes <sup>7,8</sup>. This occurs until an equilibrium potential has been reached. MIBI has been shown to reflect the increase in the negative charge of the plasma membranes, along with the increase of vascularity around the tumor <sup>7-11</sup>.

FDG is a glucose analog, which is readily taken up by cells with high metabolic rates, such as brain cells, heart cells, and malignant tumors. It enters the cell via GLUT transporters in the cell's plasma membrane. Once in the cell, the FDG begins the process of glycolysis, as glucose would. However, because it is an analog, once the FDG has undergone

phosphorylation via hexokinase the molecule becomes stuck (or trapped) in the cell because the phosphorylated FDG is not a viable substrate for glucose-6-phosphate isomerase and it cannot be transported out of the cell. Due to the trapping of FDG in the cells a long post-injection uptake time is given to the patients prior to imaging, allowing for greater accumulation of FDG in the cells. This improves lesion to background ratios.

## 2.2 Detector Setup

Currently there are three main types of nuclear medicine detectors being used: scintillation cameras with photomultiplier tubes (PMTs) or position sensitive photomultiplier tubes (PSPMTs) (see section 2.2.2), scintillation cameras with silicon photomultipliers (SiPMs), and solid state direct-conversion semiconductor cameras. The scintillation camera with PMTs is currently the most common detector type and is most relevant to this project; therefore, this section will focus on the typical design of a scintillation camera with PSPMTs. The other two camera designs along with the reason we chose to go with the PSPMT will be explained more in chapter 5.

For both gamma and PET imaging the overall camera design is very similar. The cameras can be split into three components: 1) scintillators, 2) photomultipliers, and 3) electronic components. The basic design of a gamma camera can be seen in Figure 2-2. A fourth component, the collimator, must be added to gamma cameras used to image single gammas in order to obtain a coherent image.

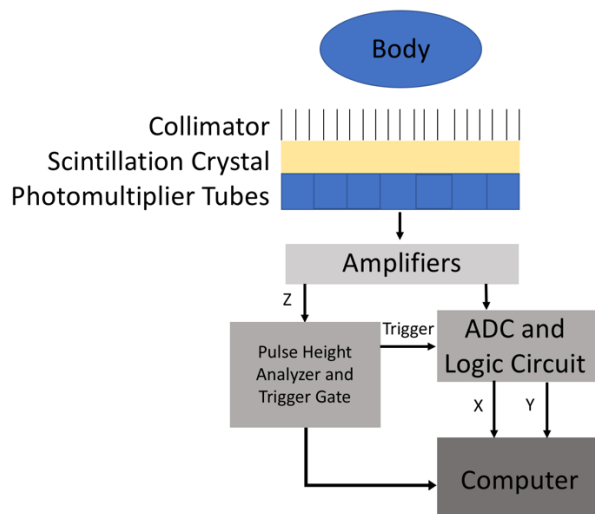


Figure 2-2: Basic Gamma Camera System Setup

### 2.2.1 Scintillators

When radiation interacts with matter it deposits energy causing the ionization and/or excitation of the material's atoms. As the excited atoms relax back to their stable state energy is released. Depending on the material, the energy can be released as heat and/or characteristic x-rays. In some cases, the energy is released in the form of visible light. The class of materials where visible light is released due to interaction with radiation is called scintillators. There are two different types of scintillators, inorganic or organic. Inorganic scintillators are crystal lattices

where the visible light created after interaction with ionizing radiation is a characteristic of the crystal lattice. This differs from organic scintillators where the visible light created is characteristic to the specific molecule <sup>2,12</sup>. The most widely used type scintillator for nuclear medicine imaging is inorganic.

The crystal structure of inorganic scintillators ensures there are only discrete energy bands between which electrons can move <sup>12</sup>. The valance band is the low energy or ground state of the lattice and represents the energies of electrons that are bound at lattice sites (Fig. 2-3) <sup>12</sup>. When an electron has sufficient energy to break free of the valance band they migrate to the conduction band. As high energy electrons de-excite and fall back to the more favorable valance band the excess energy is released in the form of electromagnetic radiation. Typically, the de-excitation of electrons in a pure crystal can be inefficient and result in wavelengths outside the visible range. To ensure visible light is created, impurities known as activators are added to the crystal lattice. The activators modify the allowed energy levels for an excited or ground state electron. So, when an electron de-excites from the activator's excited state and drops down to the modified ground level visible light is created. An example of the importance of an activator is seen when looking at one of the most used inorganic crystals, sodium iodine (NaI). A pure NaI crystal will not scintillate at room temperature; however, by adding a thallium (Tl) activator the resulting crystal lattice NaI(Tl) will emit light with a spectrum whose peak wave length is 415 nm at room temperature. Note that in the scintillator name activators are usually denoted in parenthesis or following a colon.

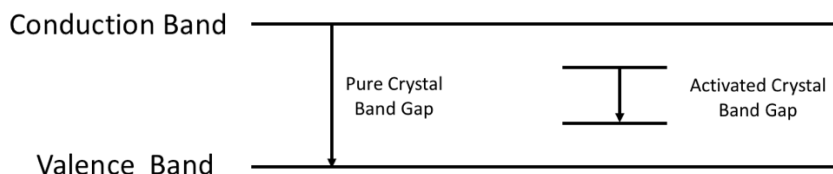


Figure 2-3: Depiction of how the addition of activators into a crystal lattice shrinks the band gap allowing for more productive and reliable scintillators.

Table 2-2 shows several common inorganic scintillators and their properties. As depicted by the table there are several important characteristics beyond the creation visible light that determine the usefulness of scintillating crystals. The differences in the characteristics make some scintillators better than others for certain applications. The density of the scintillator one of the primary factors determining its stopping power for radiation absorption. For higher energy applications a denser scintillator may be desired. The decay time describes the time it takes for an excited electron to de-excite back to its ground state. Scintillators with slower decay times can cause an “afterglow” effect, where residual phosphorescence builds up due to overlap of scintillation light from multiple interactions. Photon yield describes how many photons are created per keV of radiation energy absorbed. Crystals with high photon yields are more efficient scintillators. The peak emission wavelength is important when choosing a PMT to pair with the scintillator. A PMT that is most sensitive to the peak wavelength emitted by the scintillator is desired to maximize the net number of PMT photoelectrons per unit of absorbed incident photon energy. Last, it is important to know if the crystal is hygroscopic or not. Working with a hygroscopic crystal can prove difficult if it is not properly sealed. If the crystal is exposed to moisture it can lead to discoloration of the crystal, reduction in photon yield, and reduced scintillation light transmission.

Table 2-2: Common Inorganic Scintillators and their Properties

Modality	Scintillator	Density (g/cm <sup>3</sup> )	Peak Wavelength Emission (nm)	Photon Yield (per keV)	Decay Time (nsec)	Hygroscopic
Gamma	NaI(Tl)	3.67	415	38	230	yes
	CsI(Tl)	4.51	540	65	680	no
	CsI(Na)	4.51	420	39	460	no
	LaBr <sub>3</sub> (Ce)	5.3	358	61	350	yes
PET	BGO	7.13	480	8.2	300	no
	LSO(Ce)	7.4	420	25	47	no
	LYSO	7.1	420	27.6	45	no

## 2.2.2 Photomultipliers

Scintillators are connected to PMTs via an optical grease/glue or via a plastic light guide. The PMT is a vacuum sealed tube that produces a pulse of electrical current in reaction to a photon signal. A basic schematic of a scintillator/PMT pair can be seen in Figure 2-4.

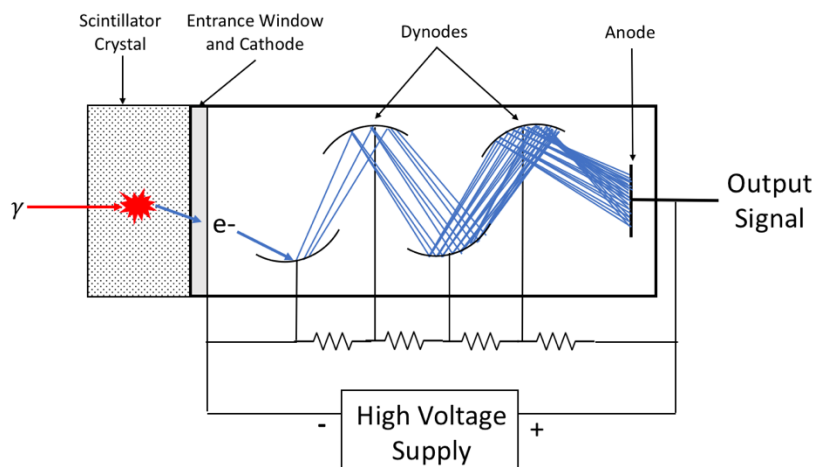


Figure 2-4: Basic Photomultiplier Tube Design

As stated in the last section, an incident gamma ray absorbed by a scintillator creates a pulse of visible light. The light enters the PMT through an entrance window that has a semi-transparent alkali photocathode coated on its rear surface. A fraction of the scintillation photons will interact with the photocathode to produce photoelectrons. Photoelectrons are electrons with sufficient energy to escape the photocathode surface into the vacuum of the PMT. The free photoelectrons are then accelerated toward the back of the PMT via a large potential created by a high voltage supply between a photocathode behind the entry window and an anode at the back of the PMT. The cathode-anode voltage can range from 300 to 1300 V<sup>2</sup>. To increase the output signal, a series of metal plates with an increasing voltage called dynodes are placed between the cathode and anode. Electrons from more negative dynodes are accelerated towards the next dynode stage, where a subsequent collision emits secondary electrons. The number of electrons is typically multiplied by 3 to 6 times at each dynode stage

depending on the dynode. Following the last dynode stage, the resulting group of electrons is collected by the anode. A single anode charge pulse can contain  $10^5$ - $10^7$  electrons depending on the PMT gain<sup>12</sup>. The design of the PMT allows for proportionality to be maintained throughout the PMT, meaning the output current is proportional to the amount of light input.

Position sensitive photomultiplier tubes (PSPMTs) were created to improve upon photon localization and energy resolution compared to the classic PMT<sup>13-15</sup>. To do this, new types of dynodes were created to ensure the path electrons take from the cathode to the anode does not change the coordinates from the original interaction at the cathode<sup>14,15</sup>. In this work the Hamamatsu H8500 model PSPMT is utilized (Hamamatsu, Japan). The H8500 PSPMT specifically uses a metal channel dynode with an 8 x 8 array anode<sup>14</sup>. So, in the case of a PSPMT scintillated light would hit the photocathode creating a shower of electrons which travel down a small set of the metal channel toward the anodes outputting a proportional and position accurate electronic pulse.

Once the electronic pulse has been created, the signal is amplified by a series of pre-amplifiers and amplifiers. It then continues on to a positioning circuit.

### 2.2.3 Electronics

To this point the discussion has been on how a photon is detected and how the subsequent electronic pulse is created. The question now becomes, how is the position of the interaction of the original incident photon at the detector input surface known? Conventional gamma cameras use single large crystals optically coupled to an array of smaller PMTs (Fig. 2-5). Light generated in the scintillator is emitted isotropically, and its spatial distribution expands in the space between the point of absorption and the input surface of the PMT array. Thus the light is shared by multiple PMTs, and the relative PMT anode pulse amplitudes can be used to calculate the 2-dimensional position of absorption in the crystal.

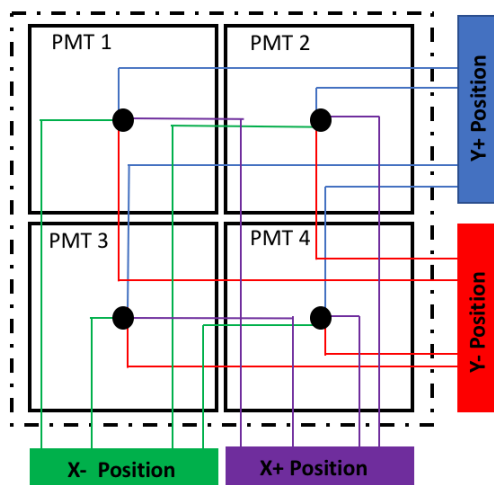


Figure 2-5: The dotted line around the perimeter represents the scintillation crystal above the tiled PMTs.

The amplified PMT electronic signals are analyzed to determine the center of the light distribution in the scintillator. To do this the PMT anodes are connected using a resistor network, X<sup>-</sup>, X<sup>+</sup>, Y<sup>-</sup>, Y<sup>+</sup> (Fig. 2-5). To calculate the X- and Y-positions of the interaction, the following equations are used:

$$X = \frac{(X^+ - X^-)}{(X^+ + X^-)} \quad (2-9)$$

$$Y = \frac{(Y^+ - Y^-)}{(Y^+ + Y^-)} \quad (2-10)$$

The differences of  $X^-$ ,  $X^+$  and  $Y^-$ ,  $Y^+$  are normalized by the total X and Y signals so the position is not dependent on the pulse height <sup>2</sup>.

A fifth component, Z, is added by summing the other 4 components. As opposed to the other 4 components, which are used to find the position of the interaction, the magnitude of Z is proportional to the total amount of light produced by the scintillator and therefore proportional to the energy deposited in the crystal by the incident photon. Comparison of the value of Z for each interaction allows events to be retained or rejected on their deposited energy. An event whose Z value is substantially less than that corresponding to deposition of the full energy of the photon produced by the isotope is rejected since there has been one or more Compton scatter interaction, thereby making the position of interaction in the crystal meaningless. Scattered photons give false positional information that degrades the quality of the image.

The description above discusses the use of analog charge division for position calculation. In newer digital systems, the individual PMT outputs are digitized and the COG calculations are done in software, which allows the use of more sophisticated algorithms. These algorithms can take into account sensitivity non-linearities, such as sensitivity loss at PMT borders and in areas between PMTs, in the PMT tube response <sup>2</sup>.

## 2.2.4 Collimators

When imaging radiotracer tagged with single gamma ray emitting isotopes, collimators must be used to determine the direction from which each detected photon came. Collimators are photon absorbing grids or apertures positioned between the object being imaged and the input surface of the scintillator crystal. They are used to differentiate incident photons based on their direction of travel. By absorbing photons whose incident path does not align with the desired direction, the collimator allows for an accurate projection of the source's distribution onto the detector surface. However, due to the photon absorbing characteristic of the collimators a large fraction of emitted photons are impeded from reaching the detector. This results in a low absolute sensitivity. Where sensitivity is the gamma ray detection efficiency of a detector, which will be discussed further in section 2.3.4.

There are four main types of collimators used. They are 1) parallel hole, 2) pinhole, 3) converging, and 4) diverging.

The parallel hole collimator is the most common collimator type and the most relevant to this project. As eluded to by the name, a parallel hole collimator is made of an array of parallel round, hexagonal, or square holes with lead walls called septa. The width and height of the septa are chosen to maximize photon transmission while achieving adequate spatial resolution. Parallel hole collimators offer no form of magnification or minification. Figure 2-6 shows a close up of a parallel hole collimator and figure 2-7 depicts a cut-away schematic of a gamma camera with a parallel hole collimator along with a source.

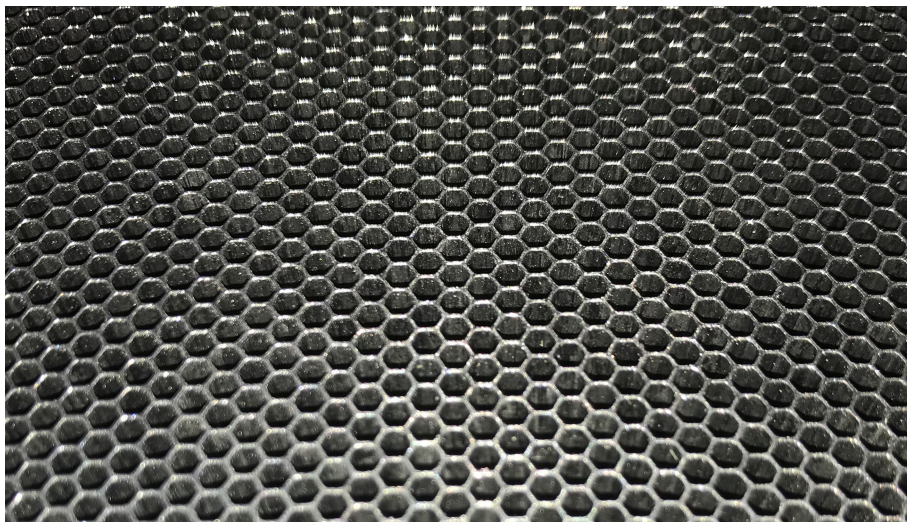


Figure 2-6: Parallel hole collimator with hexagonal holes.

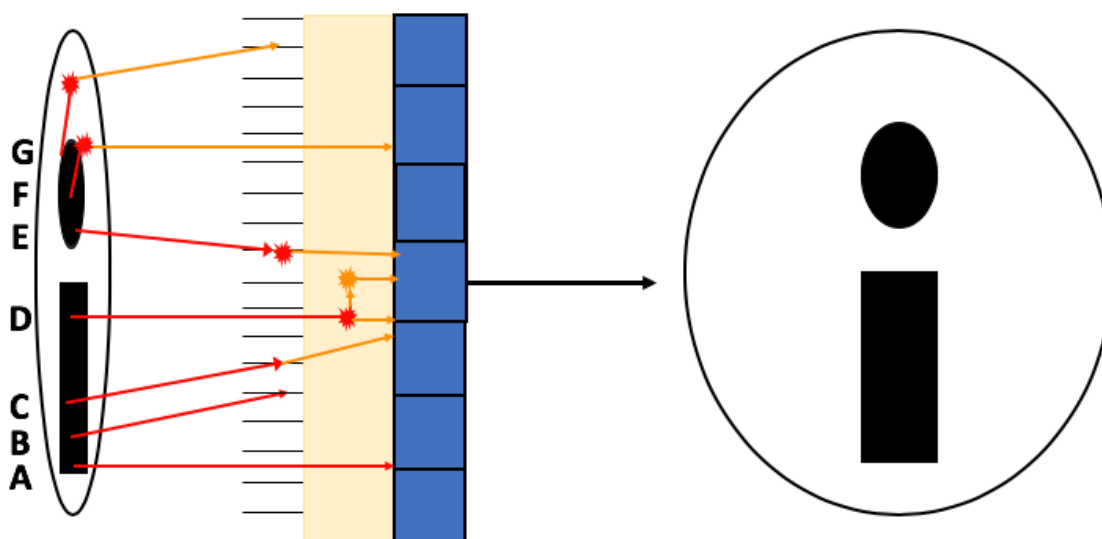


Figure 2-7: Example of different gamma ray interactions in a collimated detector. Red depicts the original energy photon, while orange depicts a lower energy photon caused by a scatter event (depicted by colored stars). A) is a true event, B) shows a gamma ray with non-normal incident direction being absorbed by the collimator, C) is a septal penetration, D) is an event that travels unimpeded by the collimator but scatters in the crystal, E) is a photon that scatters while interacting with the collimator, F) is an event that scattered in the source and because of its normal incidence traveled unimpeded to the detector, and G) is an event that scattered in the source and because of its non-normal incident direction was absorbed by the collimator.

Figure 2-7 demonstrates the seven possible photon interactions with a collimated detector. Photons A through C illustrate different type of non-scattered photon interactions, while photons D through G illustrate possible scattered photon interactions. Photon A is an unscattered, normally incident, detected gamma ray. In this case the gamma ray is emitted parallel to the gamma camera's holes and arrives at the scintillator unobstructed where all of the photon's energy is deposited in a single location. Photon B shows a photon entering the collimator at an oblique angle where it is subsequently absorbed by the collimator. Photon C

depicts septal penetration. This is where a photon passes through a collimator septum and the photon's energy is deposited into the crystal. Such events degrade spatial resolution. Photon D is a gamma ray that is emitted parallel to the collimator but scatters in the scintillator. Here the photon's energy is partially deposited in the crystal through Compton scattering and the rest is either absorbed in another interaction or escapes the crystal. Photon E depicts an obliquely incident photon scattering during interaction with the collimator. Photon F shows a photon scattering in the phantom or body and the subsequent scattered photon passes through the collimator while Photon G shows a photon scattered in the subject but not passing through the collimator.

In each case in which a scattered photon makes it through the collimator the photon energy has been reduced. Using the energy discrimination of the Z component (total energy deposited) allows the rejection of many of these photons; however, when a scattered photon deposits energy in the crystal and is not rejected it leads to the mispositioning of the origin of the event. This leads to blurring of the image resulting in a loss of resolution and contrast.

For the reasons above, the collimator has an important effect on the system sensitivity and resolution. The thickness of the collimator's septa plays an important role in the probability of septal penetration in the collimator. To determine what the septa's thickness should be, one must first know what the shortest path length a photon can take through the septa. This is determined by knowing the diameter of the collimator hole,  $d$ , and maximum angle of acceptance (determined by the length of the septa,  $l$ ) would be for a photon passing through a septum and striking the scintillator on the other side. If the path length through the septum is  $w$  (Fig. 2-8), the thickness of the septum can be determined by eqn. 2-11<sup>2</sup>.

$$t = \frac{2wl}{(l-w)} \quad (2-11)$$

Ideally, the septa thickness would prevent any penetration, however, as the thickness of the septa increase the useable surface area of the detector will decrease. So, it has become common to allow 5% septal penetration<sup>2</sup>. This improves the sensitivity of the system but decreases the resolution.

The collimator resolution,  $R_{col}$ , is determined by the characteristics of the collimator holes, including, the hole diameter,  $d$ , and septa length,  $l$ . It is described by the following equation (with variables illustrated in figure 2-8)<sup>2</sup>:

$$R_{col} = \frac{d(l_{eff}+b)}{l_{eff}} \quad (2-12)$$

Where  $b$  is the distance from the source to the collimator surface and the effective length,  $l_{eff} = l - 2 \cdot \mu^{-1}$ . The effective length is used to account for possible septal penetration and depends on the material used to make the collimator and the energy of photons used in the study. It is important to note that the spatial resolution is dependent on the source-to-collimator distance meaning objects closer to the collimator will be better resolved than distant ones and objects will

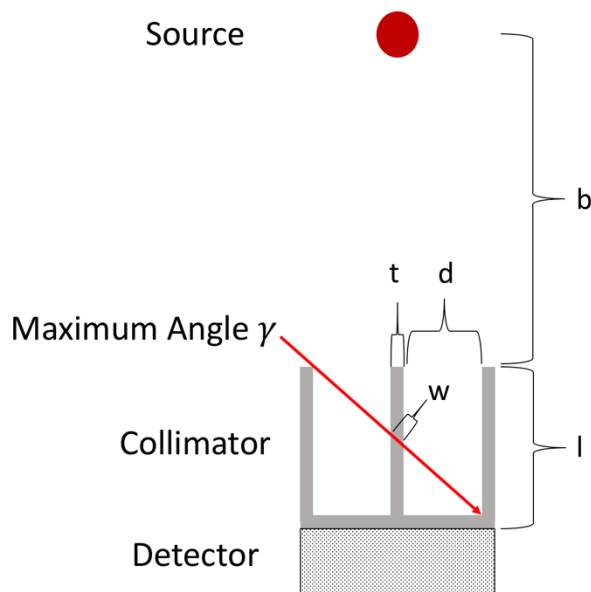


Figure 2-8: The minimum path length of a photon,  $w$ , through a collimator septum is at the maximum acceptance angle of the collimator based off of the length,  $l$ , diameter of the collimator holes,  $d$ , and the septal thickness,  $t$ . Also represented here is  $b$ , the source-to-collimator distance.

blur as the object-collimator distance increases.

The collimator efficiency,  $g$ , is defined as the ratio of the number of photons allowed to pass through the collimator per unit time to the number of photon emitted per unit time by a point source (Eqn. 2-13)<sup>2</sup>. The efficiency depends on not only the hole diameter, length, and septal thickness, but also on the shape of the holes.

$$g = \left( \frac{Kd^2}{l_{eff}(d+t)} \right)^2 \propto \left( \frac{d}{l_{eff}} \right)^2 \quad (2-13)$$

Where  $K$  is a constant depending on the hole shape. This equation exemplifies the relationship between high resolution collimators (i.e. collimators with small  $d$  and/or large  $l$ ) and high sensitivity collimators (i.e. collimators with large  $d$  and/or small  $l$ ).

There is a variation on the parallel hole collimator called a slant hole collimator. The holes in this type of collimator are still parallel but are not perpendicular to the scintillator's surfaces. They are instead slanted by a small angle. Slanting the collimator can be advantageous when the object being scanned is beyond or near the edge of the detector.

The three collimators shown in Figure 2-9 result in magnification or minimization of the image of objects compared to the actual object size. Converging collimators have builds similar to a parallel hole collimator, however all the holes are focused on a single point in front of the camera a specified distance away (Fig. 2-9b). The image of any object placed within the focus point is magnified onto the detector surface. Diverging collimators are designed in a similar fashion as the converging collimators. The main difference is that the focal point is set at a

specified distance behind the detector (Fig. 2-9c). This causes objects placed in front of the collimator to be minified.

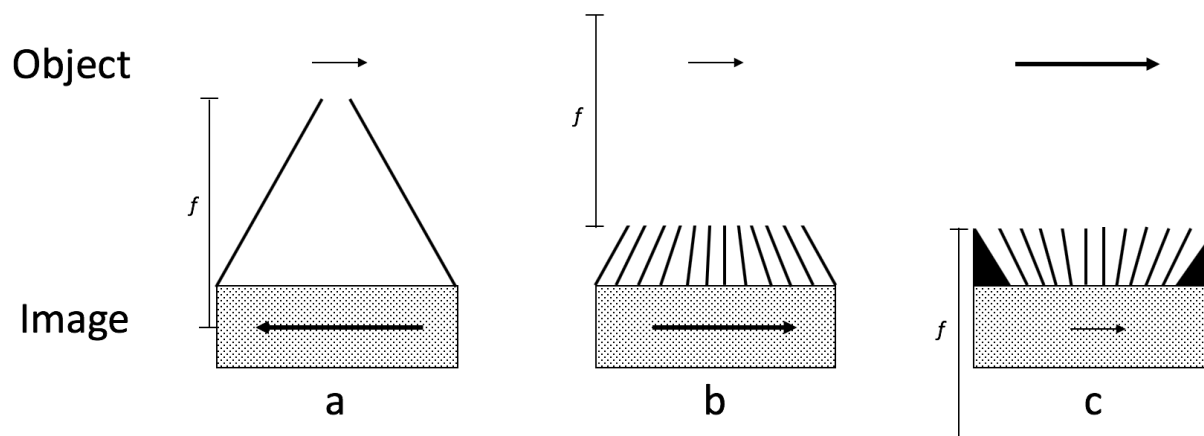


Figure 2-9: The three other collimator types. A) Pinhole collimator. B) Converging collimator. C) Diverging collimator. The focal length ( $f$ ) and magnification for each collimator is illustrated.

The pinhole collimator contains single or multiple apertures in a high attenuation material (lead, tungsten, gold, etc.) (Fig. 2-9a). The pinhole camera causes an inversion of the object being imaged. The object is magnified when the object-to-pinhole distance is smaller than the pinhole-to-detector distance and minified if the object-to-pinhole distance is larger. A single pinhole can be used or an array of pinholes.

## 2.3 Detector and Image Characteristics in Nuclear Medicine

In this section, the basic image characteristics of nuclear medicine systems will be discussed. These quantities are often evaluated in quality control protocols that have been developed and published by groups such as the National Electrical Manufacturers Association (NEMA). The following characteristics described are relevant to both single gamma and PET systems.

### 2.3.1 Image Quality

Image quality is defined as the reliability with which an image recreates the object<sup>2</sup>. Three main characteristics are used to evaluate the images quality in nuclear medicine. The first is spatial resolution, which will be discussed in detail in section 2.3.6. The next two are contrast and noise. Contrast is the difference in average count densities (counts per area) between an object and its surrounding area, compared to the average count density of the surrounding area (Eqn. 2-14). The surrounding area is typically referred to as the background<sup>2</sup>.

$$C = \frac{(N_l - N_{bg})}{N_{bg}} \quad (2-14)$$

Where  $N_l$  is the average count density of the lesion and  $N_{bg}$  is the average count density of the background. As can be seen in equation 2-16, the contrast relies on the how much of the radionuclide is taken up in the target of interest versus how much is taken in the background

area. For example, if a radionuclide has a great affinity for tumor tissue and a poor affinity for healthy tissue the ratio between the two will be larger giving a high contrast, but if the nuclide is taken up more equally between the two the contrast will be small.

There are two types of noise to be considered. The first is structural noise. This strictly speaking is not noise, since it is variations of count density that are caused by actual variations in radiotracer concentration within the imaged object. It is referred to as noise only insofar as it creates a nonuniform background in the image within which small objects must be detected. Structural noise is caused by uneven uptake of the radiopharmaceutical in different regions of the object, and overlap of different tissue types in projection images<sup>2</sup>. The second noise type is random noise. As discussed in section 2.3.1, random noise is inherent to gamma ray production and detection. Random noise is present everywhere in a nuclear medicine image and can greatly impair the detectability of an object<sup>2</sup>. A useful figure of merit to evaluate image quality is called the signal-to-noise ratio (SNR)<sup>1,2,16</sup>.

$$SNR = \frac{(N_I - N_{bg})}{\sigma_{bg}} \quad (2-15)$$

CNR is used to determine the detectability of an object in background. It is widely accepted that a ratio with a value of 3 and up is considered detectable<sup>1,2,16</sup>. This is called the Rose criterion.

### 2.3.2 Calibration

Before evaluation of a system can begin the system must be properly calibrated. Calibration is dependent on the type of scintillator crystal used. The calibration of a system starts with mapping the true crystal locations to specific pixels in the 2D histogram the image will be placed. This ensures the 2D image is a reliable representation of where the gamma interaction occurred in the crystal (Figure 2-10). After the crystals have been mapped an energy calibration is performed. Here the pulse height spectrum of each crystal is analyzed and a record of the peak location (channel number) of each pulse height spectrum is recorded ensuring the energy histogram from each pixel is correctly binned. This can be very important due to the gain of the PMTs. A PMT is most efficient in the center and decreases moving toward the edge. For this reason, the pulse height spectra can look vastly different when comparing centrally located events versus those on the edge.

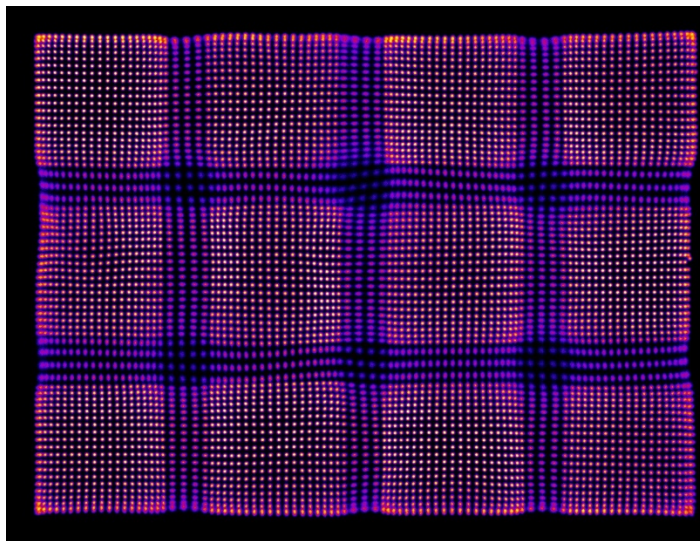


Figure 2-10: Shows a raw image of a pixelated NaI(Tl) gamma camera. Note the linear distortions in the crystal rows and columns.

Once the crystals have been mapped and the energy correction has been made a full field flood image must be acquired to correct for sensitivity nonuniformities caused by the junctions between PMTs. A flood image is obtained using a uniform gamma fluence from a radioactive source that covers the face of the entire detector. This flood is then used to correct image nonuniformities, which will be discussed in section 2.3.4.

After sensitivity nonuniformity correction, the only pixel-to-pixel fluctuations in a uniform flood image should ideally be due to random statistical noise related to the emission of the gamma rays. Emission and detection of gamma rays are random (stochastic) processes governed by Poisson statistics<sup>1,2,12</sup>. The Poisson distribution describes the probability of obtaining a specific result  $N$  when the true value (or mean) is  $m$ <sup>2</sup>.

$$P(N; m) = \frac{m^N e^{-m}}{N!} \quad (2-16)$$

The variance,  $\sigma^2$ , of a Poisson distribution is equal to the mean,  $m$ ; therefore, the standard deviation,  $\sigma = \sqrt{m} = \sqrt{N}$ . The standard deviation is used to determine the uncertainty of a measurement within a detector pixel<sup>2</sup>.

### 2.3.3 Energy Resolution

Energy resolution measures how precisely a detector can identify the energy of the interacting photon. In an ideal system, the true energy of a photon would be correctly identified for every interaction. For example, if several unscattered 140 keV Tc-99m photons interacted with an ideal detector the pulse height spectrum would contain a single narrow peak at 140 keV (Fig. 2-11). In reality, however, spectral blurring occurs due to random statistical variations occurring in the detection and amplification processes and impurities in the crystal<sup>2</sup>. These effects cause photon-to-photon differences in the Z-component amplitude, which in turn causes broadening of the spectral peak. The peak corresponding to the photon energy is defined as the photopeak. Beyond the broadening of the 140 keV peak other peaks are broadened by the same processes (Fig. 2-11). The two lower energy peaks in Fig. 2-11 are caused by characteristic x-rays caused by the excitation of electrons in the crystal and lead shielding of the

detector. Energy resolution of a nuclear medicine spectroscopic or imaging system depends on the energy of the radiation it is measuring, with higher resolution at higher energy. It is typically quantified at a particular photon energy by the Full Width at Half Maximum of the photopeak (Eqn. 2-17) <sup>2</sup>.

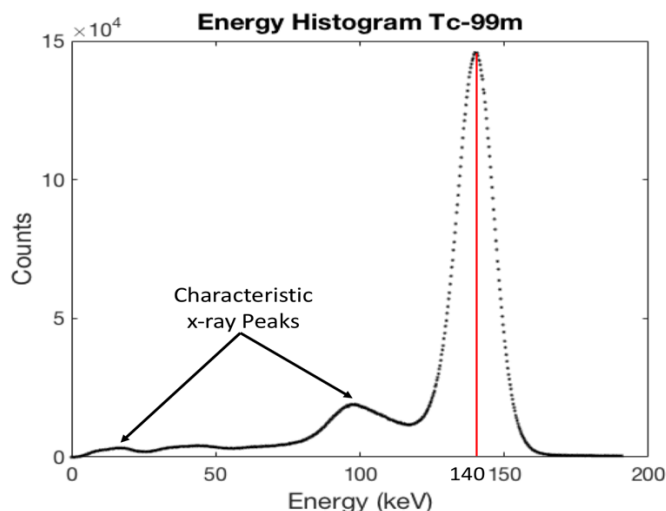


Figure 2-11: Example of energy histogram of point source. The peak centered at 140 keV is the 99m-Tc primary gamma emission photopeak. The red vertical line represents the response of an ideal detector, while the spectrum in black shows the response of a real detector. Two characteristic x-rays from photon interactions in the crystal and lead shielding are also visible.

$$FWHM(\%) = \frac{\Delta E}{E_\gamma} * 100\% \quad (2-17)$$

Where  $\Delta E$  is the width of the peak at half height and  $E_\gamma$  is the maximum energy in the peak. A smaller FWHM denotes better energy resolution, and better the ability to resolve the energies of two photons with similar energy. Current NaI(Tl) detectors typically have energy resolutions of 9-15% <sup>2,12,17,18</sup>.

Good energy resolution becomes important when imaging humans because it allows for better scatter rejection. During human imaging, the detectors are flooded with a wide range of photon energies. This is due to photons undergoing Compton scattering within the body. Compton scattering is the process of a photon interacting with an outer shell electron of an atom and imparting part of its energy to the electron. The photon loses energy in the collision and is diverted to a new direction. The photon energy change is described by equation 2-18 <sup>2</sup>.

$$E_c = \frac{E_0}{\left[1 + \left(\frac{E_0}{0.511}\right)(1 - \cos \theta)\right]} \quad (2-18)$$

Where  $E_c$  is the energy of the scattered photon,  $E_0$  is the energy of the incoming photon, and  $\theta$  is the photon's angle of deflection after the collision. All energies are expressed in keV. With this equation it can be seen that depending on the angle of deflection it is possible to have scattered photons with energies near that of the original photon or energies much less than the original photon, depending on the scattering angle. Figure 2-12 depicts an energy spectrum of a combination of primary (unscattered) and scattered 99m-Tc photons. The inclusion of detected Compton scattered photons in the image degrades image quality since the change in the photon's direction causes its point of origin to be estimate incorrectly (see Fig. 2-7). To minimize

the effect of scatter on the image electronic collimation, called an energy window, is used to discriminate between desired energy photons and lower energy scattered photons. The windows are typically set at 15-20% <sup>2</sup>. Meaning for a Tc-99m source with a 20% window, any detected photon with energy less than 90% or greater than 110% of 140 keV will be excluded.

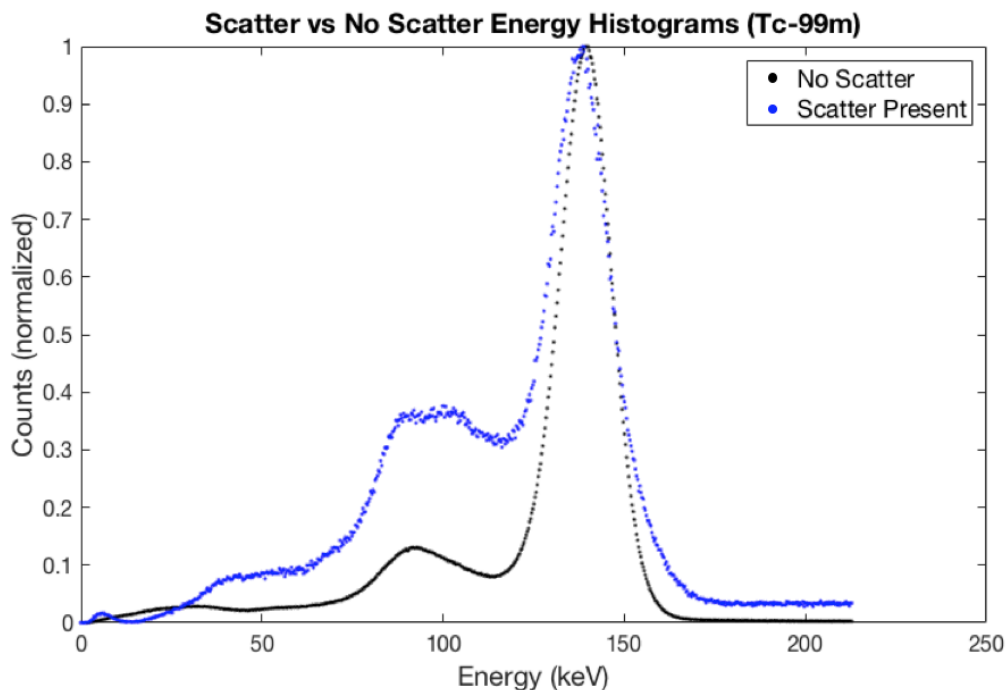


Figure 2-12: Comparison of pulse height spectra of a 99m-Tc source with scatter (blue) and a source with no scatter (black). Note the broadening of the 140 keV photopeak and the increase of lower energy photons caused by Compton scattering.

### 2.3.4 System Sensitivity

System sensitivity defines the gamma ray detection efficiency of a detector and is reported in counts per second per unit of activity. It is typically measured by placing a source of known activity in front of the detector and imaging for a specified time. The total number of events recorded are counted and divided by the scan time and activity used.

In nuclear medicine imaging a limited amount of radiotracer is used to minimize radiation dose, acquisition times are limited for pharmacokinetic and clinical workflow reasons, and detectors typically subtend a relatively small total solid angle about the patient. Therefore, the total number of detected photons is much less than that in typical x-ray based imaging modalities. In fact, many limitations of nuclear medicine derive from insufficient count densities in the image. To ensure useful counting statistics, a procedure may require a long scan time or a higher radiation dose, therefore to limit scan time and dose a high sensitivity system is preferable. There are several factors affecting sensitivity: the collimator efficiency, absorption efficiency of the crystal and the width of the energy window. As discussed in section 2.2.4 the collimator's effect on a system's sensitivity is due to its geometry. For example, a detector with a single pinhole collimator will typically have less sensitivity than that of a parallel hole collimator. System's with a low absorption efficiency lowers the systems sensitivity. The energy window

can also have a great effect on the system sensitivity. Narrowing the energy window will reject more counts dropping the sensitivity. So, before measuring sensitivity it is important to optimize the energy window for the imaging task to reduce scatter with minimal loss of sensitivity.

A potentially important cause of sensitivity loss is system dead time,  $\tau$ . Dead time is defined as the time needed to process individual detected events <sup>1,2</sup>. There are two types of dead time: paralyzable or nonparalyzable. In a paralyzable system, if an event occurs within the dead time of a preceding event, the second event is not counted but causes a new dead time <sup>2</sup>. In a nonparalyzable system, events occurring during the deadtime of a preceding event are ignored with no effect on the pre-existing dead time <sup>2</sup>. So, in a very high-count rate situation, a nonparalyzable system will continue to count events at a lower rate, while a paralyzable system will cease to count if the time between events is shorter than the system's dead time. As illustrated by figure 2-13 systems with nonparalyzable dead time have a greater system sensitivity. Typical scintillation based systems have deadtimes between 0.5 - 5  $\mu\text{sec}$  <sup>2</sup>.

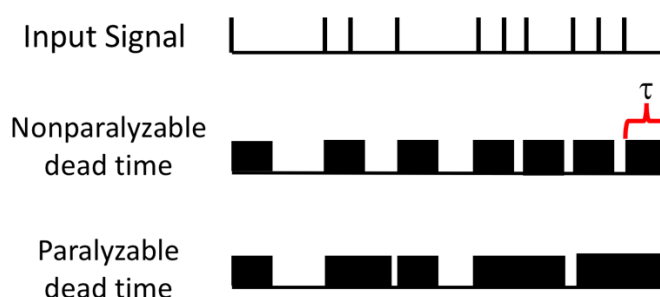


Figure 2-13: Compares the output of nonparalyzable and paralyzable systems given the input signal above. The time period  $\tau$  is the dead time. Note the nonparalyzable system is more efficient because it has fewer count losses at higher count rates.

### 2.3.5 Geometric Linearity and Intrinsic Uniformity

When a straight object appears distorted in an image this is called geometric nonlinearity. The primary source of geometric nonlinearity in detectors with tiled PMTs is biasing of the measured scintillator light centroid position due to the way the scintillation light is shared between more than one PMT near PMT edges. Additional distortions are caused by truncation of the amplified charge pulse near the PMT perimeters.

A related issue to image nonlinearity is image nonuniformity. When a sensitivity nonuniformity correction is performed for an ideal detector uniform flood irradiation would produce a perfectly flat and uniform image. However, due to sensitivity differences across the face of the detector a flood-field image will produce an image where the PMT tile pattern can be seen (Fig. 2-14). These nonuniformities arise for two main reasons. The first, is due to the nonlinearities described above. The second, is due to the nonuniform detection efficiency of the PMTs. More specifically differences in the pulse height spectrum of neighboring PMTs <sup>2</sup>. The differences in pulse height spectrums can be caused by differences in tube gains providing the differing amplitude signals across the surface of the detector. Poor calibration can also lead to image nonuniformities. If the crystals are incorrectly mapped the positioning of the incident photon will be misplaced causing spatial distortion.

Both geometric nonlinearities and sensitivity nonuniformities can be corrected. On the hardware level, the detector gains can be modified to ensure equal amplitude outputs on the PMTs, while proper system calibration will help minimize positioning artifacts. Even with proper calibration nonuniformities will be seen due to the loss of sensitivity at PMT edges. Correction

images are used to correct for these nonuniformities. Here a high-count flood field image, called a sensitivity correction image, is created and each image taken afterwards is corrected on a pixel-by-pixel basis by the following equation.

$$F(i, j) = \left( \frac{I(i, j)}{CI(i, j)} \right) * \text{mean}(CI) \quad (2-19)$$

Where  $F$  is the final corrected image,  $I$  is the original image,  $CI$  is the correction image, and  $i$  and  $j$  are pixel co-ordinates. An example of a corrected image can be seen in figure 2-13b. Flood correction images are typically acquired every day the camera is used to correct for any small changes that could occur in the electronics.

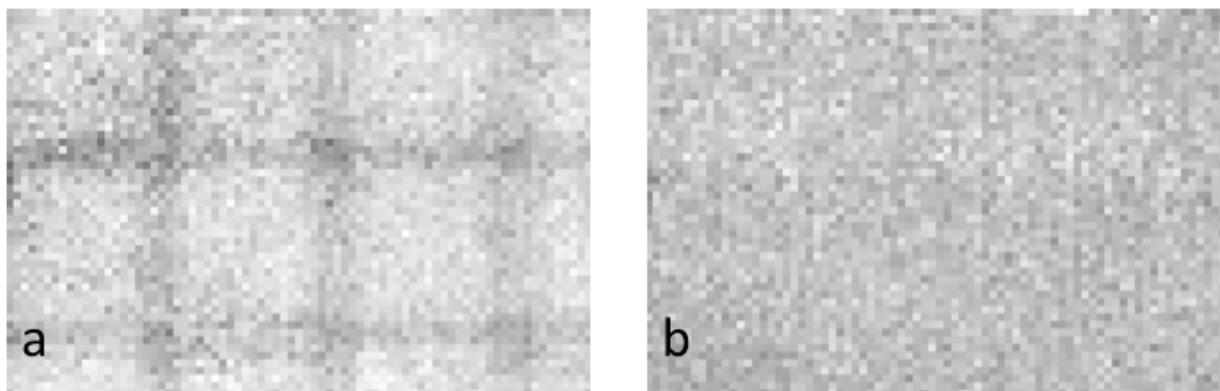


Figure 2-14: a) depicts an uncorrected image of a uniform gamma flood. The tiling of the PMTs can clearly be seen. b) shows the corrected flood.

### 2.3.6 System Spatial Resolution

Spatial resolution is the ability of an imaging system to discern two individual but closely spaced objects from one another<sup>1</sup>. So, the higher the resolution of a system the smaller the objects it can reliably resolve. Nuclear medicine systems typically have poor spatial resolution; ~4-8 mm for whole body systems, compared to that of anatomical systems such as x-ray mammography, which is on the order of tens of microns<sup>1</sup>. System resolution,  $R_{sys}$ , is defined as the resolution of the entire camera and readout electronics, including effects from reconstruction algorithms. The camera spatial resolution depends on two main terms: the intrinsic (detector) resolution,  $R_{int}$ , and the resolution of the collimator,  $R_{col}$ <sup>2</sup>.  $R_{col}$  for parallel collimators is discussed in section 2.2.4. The spatial resolutions of the detector and collimator sum in quadrature to yield the camera spatial resolution:

$$R_{sys} = \sqrt{R_{int}^2 + R_{col}^2} \quad (2-20)$$

The intrinsic resolution describes the spatial resolution of the detector for gamma input directly onto its surface. It is equal to the camera resolution in the limit of perfect collimation. There are several factors that affect the intrinsic resolution. First, the resolution is highly affected by gamma photon and visible photon scattering occurring within the crystal<sup>2</sup>. A gamma photon scattering within a crystal can lead to energy being deposited in multiple positions. Determination of the centroid of these locations would not necessarily provide an accurately

representation of the true position of the object and would lead to blurring in the image. The light output of the crystal is dependent not only on the crystal type, but also on the crystal thickness. As the volume where the photon can deposit its energy increases the larger the variation in scintillation light patterns. Figure 2-14 demonstrates how the cone of light produced from an interaction at the top of the pixel versus an interaction at the bottom of a crystal differ. While thin crystals can provide a good intrinsic resolution, the volume in which gamma interactions can occur is small. To improve upon intrinsic resolution while keeping the photon interaction volume larger, some crystals are pixelated to form an array of smaller crystals. In such arrays the scintillation light produced in any given crystal is largely confined to that crystal as it propagates. Thus, the light incident on the photodetector is confined to a smaller area than it would be with a single crystal. The spatial resolution of crystal arrays can be no better than the size of the crystal pitch. The crystal pitch is defined as the center-to-center distance between crystals.

System spatial resolution, also known as extrinsic spatial resolution, describes the spatial resolution with the collimator attached. The addition of the collimator introduces a dependence of spatial resolution on the source-to-collimator distance. Recall from equation 2-9, the collimator spatial resolution degrades as the object moves further from the collimator surface.

## References

- 1 Prince JL, Links JM. *Medical Imaging : Signals and Systems*. CERN Document Server. 2006. URL: <http://cds.cern.ch/record/1116811> (Accessed 22 April 2018).
- 2 Cherry SR, Sorenson J, Phelps ME, Methé BM. Physics in Nuclear Medicine. *Med Phys* 2004;**31**:2370–1. <https://doi.org/10.1118/1.1776595>.
- 3 Martin JE. *Physics for Radiation Protection: A Handbook*. John Wiley & Sons; 2006.
- 4 Feng SSJ, Sechopoulos I. Clinical Digital Breast Tomosynthesis System: Dosimetric Characterization. *Radiology* 2012;**263**:35–42. <https://doi.org/10.1148/radiol.11111789>.
- 5 Richard Hammerstein G, Miller DW, White DR, Ellen Masterson M, Woodard HQ, Laughlin JS. Absorbed Radiation Dose in Mammography. *Radiology* 1979;**130**:485–91. <https://doi.org/10.1148/130.2.485>.
- 6 *Molecular Imaging Agents for Breast Cancer*. Society of Breast Imaging. n.d. URL: <https://www.sbi-online.org/RESOURCES/WhitePapers/TabId/595/ArtMID/1617/ArticleID/640/Molecular-Imaging-Agents-for-Breast-Cancer.aspx> (Accessed 19 June 2018).
- 7 Vecchio SD, Salvatore M. 99mTc-MIBI in the evaluation of breast cancer biology. *Eur J Nucl Med Mol Imaging* 2004;**31**:S88–96. <https://doi.org/10.1007/s00259-004-1530-0>.
- 8 Delmon-Moingeon LI, Piwnica-Worms D, Abbee AD, den, Holman BL, Davison A, Jones AG. Uptake of the Cation Hexakis(2-methoxyisobutylisonitrile)-Technetium-99m by Human Carcinoma Cell Lines in Vitro. *Cancer Res* 1990;**50**:2198–202.
- 9 Fowler AM. A Molecular Approach to Breast Imaging. *J Nucl Med* 2014;**55**:177–80. <https://doi.org/10.2967/jnumed.113.126102>.
- 10 Maublant J, de Latour M, Mestas D, Clemenson A, et al. Technetium-99m-sestamibi uptake in breast tumor and associated lymph nodes. *The Journal of Nuclear Medicine* 1996;**37**:922–5.
- 11 Carvalho PA, Chiu ML, Kronauge JF, Kawamura M, Jones AG, Holman BL, et al. Subcellular distribution and analysis of technetium-99m-MIBI in isolated perfused rat hearts. *J Nucl Med* 1992;**33**:1516–22.
- 12 Knoll GF. *Radiation Detection and Measurement*. John Wiley & Sons; 2010.
- 13 Kume H, Muramatsa S, Iida M. Position Sensitive Photomultiplier Tubes for scintillation imaging. *IEEE Transactions on Nuclear Science* 1986;**NS-33**:vp.
- 14 Pani R, Pellegrini R, Cinti MN, Trotta C, Trotta G, Garibaldi F, et al. Flat Panel PMT for photon emission imaging. *Nuclear Instruments and Methods in Physics Research Section A: Accelerators, Spectrometers, Detectors and Associated Equipment* 2003;**505**:590–4. [https://doi.org/10.1016/S0168-9002\(03\)01154-9](https://doi.org/10.1016/S0168-9002(03)01154-9).
- 15 Pani R, Pellegrini R, Cinti MN, Mattioli M, Trotta C, Montani L, et al. Recent advances and future perspectives of position sensitive PMT. *Nuclear Instruments and Methods in Physics Research Section B: Beam Interactions with Materials and Atoms* 2004;**213**:197–205. [https://doi.org/10.1016/S0168-583X\(03\)01571-4](https://doi.org/10.1016/S0168-583X(03)01571-4).
- 16 Rose A. Vision: Human and Electronic. *Applied Solid State Physics*. Springer, Boston, MA; 1970. p. 79–160.
- 17 Williams MB, Goode AR, Galbis-Reig V, Majewski S, Weisenberger AG, Wojcik R. Performance of a PSPMT based detector for scintimammography. *Phys Med Biol* 2000;**45**:781. <https://doi.org/10.1088/0031-9155/45/3/315>.
- 18 Long Z, Connors AL, Hunt KN, Hruska CB, O'Connor MK. Performance characteristics of dedicated molecular breast imaging systems at low doses. *Medical Physics* 2016;**43**:3062–70. <https://doi.org/10.1118/1.4950873>.

# Chapter 3

## Dual Modality Tomosynthesis Human Study

### 3.1 Introduction

As discussed in Chapter 1, mammography (MM) is considered the current clinical standard for breast cancer screening and diagnosis. Mammography has been shown to have a sensitivity ranging from 71 – 96% averaged over all breast density types, however, this can be misleading. For women who have radiologically dense breasts (heterogeneously or extremely dense) the sensitivity drops to 68%, and if they have extremely dense breasts the sensitivity drops further to 48%<sup>1,2</sup>. In the US, around half of the women who undergo mammographic screening will have heterogeneously dense or extremely dense breasts<sup>3,4</sup>. The loss of sensitivity in mammographic imaging of radiodense breasts can be caused by the superposition of normal tissue obscuring cancerous tissue. Similarly, superposition of normal tissue can create patterns mimicking cancerous tissue, leading to false positives<sup>5-7</sup>.

Over the last several years, x-ray breast tomosynthesis, also called digital breast tomosynthesis (DBT) has become more prevalent in breast cancer diagnostic imaging. DBT obtains multiple low-exposure mammographic images of the breast at various angles by moving the x-ray tube in an arc. The resulting 2D projection images are then fed to a reconstruction algorithm to produce a 3D image. Image slices parallel to the breast support are individually interpreted. The fact that each slice contains much less breast tissue than a full thickness 2D mammogram reduces the amount of superimposed breast tissue in each viewed image, thereby decreasing the amount of obscuration of potential lesions. In several recent studies, both the sensitivity and specificity for the detection of breast cancer were shown to increase with DBT over MM alone<sup>8-10</sup>. However, in several large studies (Gilbert et al. with 7060 subjects and Michell et al. with 738 subjects) the specificity of MM + DBT is under 80%. The current clinical standard practice is to use MM and DBT together, either by acquiring both types of images, or by calculating a 2D projection image from the DBT projection images. Both MM and DBT provide only anatomical information; however, the addition of a complimentary functional imaging system may be a desirable path to improve the specificity of MM+DBT or DBT alone.

Nuclear medicine imaging is a way to add functional information to the anatomical information given by the DBT systems. Breast specific gamma imaging (BSGI), also called molecular breast imaging (MBI), uses one or more compact gamma cameras to obtain 2D scintigraphic images of the distribution within the breast of an intravenously injected radiotracer. BSGI using the single gamma ray emitting radiotracer <sup>99m</sup>Tc-sestamibi (MIBI), which preferentially accumulates in breast tumors compared to normal breast tissue, has been shown to have sensitivity comparable to that of MM, while improving upon specificity, when used in a diagnostic cohort<sup>11-13</sup>.

Because BSGI is performed separately from mammographic imaging, it can be difficult to correlate BSGI findings with those of MM or DBT. To investigate the potential of improving sensitivity and specificity in breast cancer detection by combining DBT with nuclear medicine imaging, our lab at the University of Virginia, Charlottesville, developed a breast imaging system designed to acquire x-ray tomosynthesis and nuclear medicine tomosynthesis images in succession with the breast in a single configuration. The dual modality tomosynthesis (DMT) system combines the anatomical x-ray component (tube and x-ray detector) and the functional

gamma ray component (gamma camera) on a single upright gantry. The breast is immobilized using a breast support structure that is independent of the rotating gantry arm and located close to the arm's axis of rotation (AOR). DBT is performed right after MIBI injection, followed immediately by tomosynthetic gamma emission imaging of the tracer in the breast. The resulting DBT image slices can be viewed alongside the corresponding slices of the molecular breast tomosynthesis (MBT) scan. A detailed description of this system will be provided in the next section.

The DMT system was evaluated in a pilot study enrolling women scheduled for breast biopsy<sup>14</sup>. The study included 17 women (mean age 53; age range 44 to 67) with a total of 21 biopsied lesions. Subjects were scanned prior to biopsy under an IRB-approved protocol at UVA. A reader study was performed to determine the diagnostic value for lesion detection and characterization of adding MBT to DBT. Results of the reader study were compared to histopathological results. Of the 21 lesions, 7 were determined by biopsy to be malignant and 14 were determined to be benign. The sensitivity, specificity, positive predictive value, negative predictive value and accuracy of DMT (DBT+MBT) scanning were 86%, 100%, 100%, 93% and 95%, respectively, compared to 86%, 57%, 50%, 89%, and 67% for DBT alone. In one case DMT was able to detect DCIS that went originally undetected by the subject's clinical mammography/US workup. These results suggested that DMT scanning is a feasible and accurate method for breast cancer detection and diagnosis and that specificity and positive predictive value can be improved through the addition of MBT to DBT.

Based on the results of the pilot study, a larger trial comparing DBT, DBT plus MM, and DMT was completed to investigate whether or not DMT provides a statistically significant improvement in sensitivity and specificity over the other modalities.

## **3.2 Materials and Methods**

### **3.2.1 System Description**

The DMT system has one gantry arm where both the x-ray and gamma components are attached, with a breast support and compression mechanism attached independently near the axis of rotation of the gantry arm (Fig. 3-1). The x-ray scanner uses fully isocentric motion, in which both the x-ray and gamma subsystems rotate together around a common axis. The DBT component was developed in collaboration with Dexela Inc. (London, UK). The x-ray tube is a Varian RAD 70, which is a high-output, oil-cooled tube with a tungsten target and a 50 micron thick rhodium filter (Varian Medical Systems, Palo Alto, California). The 2923MAM CsI-CMOS detector (Perkin-Elmer/Dexela) has a 3888 x 3072 matrix of 75 micron detector elements. It has an overall sensitive area of 29 x 23 cm. With no pixel binning the system has a frame rate of 17 frames per second. DBT image reconstruction is performed using a statistically based iterative algorithm developed by Dexela that prevents overfitting of the noise in the data.



Figure 3-1: Dual Modality Tomosynthesis (DMT) scanner. X-ray tube, gamma camera, and x-ray detector are on a single gantry arm, which rotates around an independent breast immobilization system. In this photo the gamma camera has been pulled away from the gantry arm so that its posterior edge aligns with that of the breast support. This posterior position is used for MBT scanning, but with the camera lowered to be as close as possible to the compression paddle.

The gamma camera and readout electronics were provided by Jefferson Laboratory (Newport News, VA). The gamma camera contains a 20 cm x 15 cm pixelated NaI(Tl) scintillation crystal coupled to a 3 x 4 array of H8500 position-sensitive photomultiplier tubes (PSPMTs) (Hamamatsu Photonics, Hamamatsu City, Japan). The crystal array has a crystal size of 2.0 mm with a crystal pitch of 2.2 mm and a crystal thickness of 6 mm. A parallel-hole lead-foil collimator with hexagonal holes is attached to the camera and has dimensions of 21.5 mm, 1.85 mm, and 0.3 mm for the hole length, hole diameter, and septal thickness respectively. During MBT scanning the gamma camera is positioned above the breast and below the x-ray tube. It is attached to a pair of parallel motorized linear translation stages via two parallel aluminum slide stages. This allows the camera to be positioned close to the gantry arm, out of the x-ray cone beam during x-ray imaging and then repositioned for MBT scanning. During the MBT scan the posterior (chest wall) edge of the camera is aligned with the posterior edge of the breast support, and the distance between the camera and the compression paddle is minimized.

### 3.2.2 Subjects and Imaging Protocol

Women who were over the age of 18, not pregnant, and scheduled for a breast biopsy were recruited for a DMT scan prior to their biopsy under the approval of an institutional review board from the University of Virginia Human Investigations Committee. Every subject provided informed consent. All subject information was handled in compliance with the rules and regulations of the Health Insurance Portability and Accountability Act. Seventy-five subjects were recruited in this study with a total of 83 biopsied lesions, 21 of which were malignant while 62 were benign. The histologic description of the lesions can be seen in Table 3-1.

Table 3-1: Histologic Results for 83 Biopsied Lesions

<b>Biopsy Histological Results</b>	
<b>Benign</b>	<b>Number of Biopsied Lesions</b>
Bland vascular proliferation	1
Cyst	1
Ductal hyperplasia	3
Fat necrosis	1
Fibroadenoma	10
Fibrocystic changes	34
Lobular carcinoma in situ	2
Papilloma	3
Pseudoangiomatous stromal hyperplasia	1
Radial scar	2
No abnormality	4
<b>malignant</b>	
Ductal carcinoma in situ	11
Infiltrating ductal carcinoma	4
Intracystic carcinoma	2
Poorly differentiated carcinoma	3
Sarcamotoid pleomorphic spindle cell neoplasm	1

At the beginning of their scanning session each subject was intravenously injected with approximately 22 mCi (814 MBq) of  $^{99m}\text{Tc}$ —sestamibi resulting in an absorbed radiation dose of approximately 3 mGy to the breast tissue and a total body effective dose of 6.9 mSv. Immediately following tracer injection, the suspicious breast was mildly compressed using a mediolateral oblique (MLO) compression orientation and scanned first with DBT and immediately thereafter with MBT without modifying the compression. For each scan type only MLO compression was used (no cranio-caudad compression images were acquired).

During DBT scans thirteen equally spaced views were acquired over an angular range of  $24^\circ$  ( $\pm 12^\circ$  centered along the direction of breast compression). Tube voltage and current-time product were selected to result in a total mean glandular dose (MGD) equal to or less than two times that of the MLO image of the subject's most recent clinical mammographic exam, either MM or DBT. In this study, for which the average compressed breast thickness was 6.7 cm, the DBT MGD was typically 3 to 4 mGy.

MBT scanning used five evenly spaced views spanning an angular range of  $40^\circ$  ( $\pm 20^\circ$  centered along the compression direction). At each of the five positions, the radial distance between the MBT camera and the subject's breast was minimized and the perpendicular distance between the collimator and the AOR was noted for reconstruction purposes. The acquisition time for each projection view was 120 seconds. This scan time was chosen to result in a total MBT scan time of 10 minutes, equal to that used in clinical MBI/BSGI imaging. MBT scans were reconstructed using an expectation maximization algorithm developed at UVA<sup>15</sup>.

After the first breast was scanned, the second breast was positioned using the MLO compression orientation and scanned with the same acquisition protocol as used for the first breast. The total scan time per breast was approximately 12 minutes; ~30 seconds for the DBT scan and ~11.5 minutes for the MBT scan, including positioning time.

### 3.2.3 Observer Study Design

Our primary goal in the observer study was to assess the value of the addition of MBT to the current clinical standard of DBT plus MM. To do this, board-certified, MQSA-certified breast radiologists were asked to review the DMT images in a sequence similar to the one most likely to be used clinically. At the time of this thesis a single reader has completed their review while a second reader has started, results of the first reader are presented here. Images were viewed in the following sequence, in which successively more image information was added: 1) DBT alone, 2) add MM, and 3) add MBT<sup>16-18</sup>. Since only 3D scans were obtained with the DMT scanner, for the MM image the subject's most recent clinical MLO mammogram was used. At each of the three steps readers were first asked to rate the quality of the image (1 – not adequate, 2 – barely adequate, 3 – adequate, 4 – good, 5 – excellent) and the breast positioning (1 – poor, 2 – adequate, 3 – good). Readers then recorded the location and type of all findings, up to a maximum of three findings per modality. DBT and MM findings were described using the established BI-RADS assessment terminology put forth by the American College of Radiology<sup>19</sup>. MBT findings were categorized using the feature analysis lexicon described by Narayanan *et al* for PEM<sup>20</sup>. Readers scored each finding in terms of the likelihood of malignancy using a 5-point Likert scale as follows: (1 – definitely benign, 2 – probably benign, 3 – indeterminate, 4 – probably malignant, 5 – definitely malignant)<sup>9</sup>. Readers also provided for each finding a percent 'confidence' rating ranging from 0 to 100 indicating their subjective assessment of their confidence in their malignancy suspicion score for that finding. Each reader was trained using a set of 30 DMT image sets from a separate human study that enrolled BIRADS 5 and 6 patients. The readers were blinded to all clinical information, including the biopsy report. All observer sessions were performed using a mammographic workstation certified for primary interpretation (reads were completed on a Carestream Vue PACS version 12.2.0.1007 workstation with 2 MQSA approved BARCO MDCG-5221 Monitors).

Readers participating in the above 3-step sequence had extensive experience interpreting MM, DBT, breast MRI, and breast ultrasound scans but limited experience with nuclear breast imaging of any type. DMT is a new hybrid imaging procedure that combines an established mammographic modality (DBT) with a new nuclear medicine modality (MBT). As was the case for early SPECT-CT and PET-CT, expert observers with experience in both modalities of the hybrid scan do not exist. Furthermore, it is not reasonable to expect a breast radiologist who does not routinely interpret nuclear medicine images to feel entirely comfortable interpreting MBT studies or to expect them to fully utilize the information therein, even after some amount of initial training in MBT. In order to measure the performance of a reader skilled in nuclear medicine interpretation, a board-certified nuclear medicine radiologist with over 20 years' experience, who was also blinded to all clinical information, was asked to independently interpret the entire set of MBT scans, without access to the DBT or MM images. The same 5-point suspicion scale was applied to all findings, and images were scored for overall image quality and breast positioning. The results of this MBT interpretation by the nuclear medicine radiologist were supplied as an expert consult report on a case-by-case basis to the breast radiologist readers after they completed their sequential 3-step evaluation. At that time, they were asked to provide final suspicion scores for all of their findings, including any that were also identified in the nuclear medicine consult report.

### 3.2.4 Data Analysis

Receiver operating characteristic (ROC) curves were generated for each reader for each of the three stages in the reading sequence (DBT, DBT+MM, DBT+MM+MBT), again following the addition of the expert nuclear medicine review (DBT+MM+MBT+ expert MBT consult), and lastly for the nuclear medicine review by itself<sup>21</sup>. Biopsy results were used as ground truth for

each lesion. A decision threshold was established in the reader malignancy suspicion scale such that scores below the threshold were considered to be negative calls and those above were considered positive calls. Combining biopsy and reader results established true positive, false positive, true negative, and false negative classifications for each biopsied lesion. Only reader findings that were determined to be in the location of a biopsied lesion were considered. Positive biopsied lesions not identified (and thus not scored) by a reader were considered false negatives irrespective of image quality. Negative biopsied lesions not identified by a reader were scored as true negatives only if the image was rated by the reader as having adequate or better (scores of 3 or higher) image quality. Of the 450 images (75 subjects x 2 breast x 3 image types) used in the study, a total of only 13 were given an image quality score of 'not adequate'. In one case the biopsied lesion was out of the field of view of the MBT system because of the somewhat limited size (15 cm x 20 cm) of the gamma camera.

This analysis was repeated for each of the six possible threshold locations along the 5-point Likert scale. Combining the lesion classifications for all 83 lesions the resulting true positive fraction (sensitivity) is plotted versus the false positive fraction (1-specificity) for each threshold value to form the ROC curves.

For each of the five ROC curves the area under the curve (AUC), denoted here as denoted  $A_z$ , was calculated using trapezoidal integration<sup>22-25</sup>. The AUC is a commonly used metric to indicate overall accuracy and gives the probability of correctly classifying a lesion<sup>21,26,27</sup>.

The  $A_z$  value for each of the reading stages were compared to that of DBT+MM, which we are considering as the current standard of care. Comparison was made in terms of the AUC contrast, which is the difference between  $A_z$  values. AUC contrast values were analyzed for statistical significance using a pairwise 2-tailed t-test. All analyses were performed using SAS version 9.4 software (SAS Institute Inc., NC, USA).

### 3.3 Results

Figure 3-2 shows an example of a positive (disease present) DMT scan and a negative (disease absent) DMT scan. The ROC curves for all the three reading stages, DMT + MM + expert consult, and MBT alone are shown in Figure 3-3. Table 3-2 lists the resulting  $A_z$  value for each state. Differences in the  $A_z$  for all reading stages, along with DMT + MM + expert consult, and MBT alone compared to DBT+MM can be seen in Table 3-3.

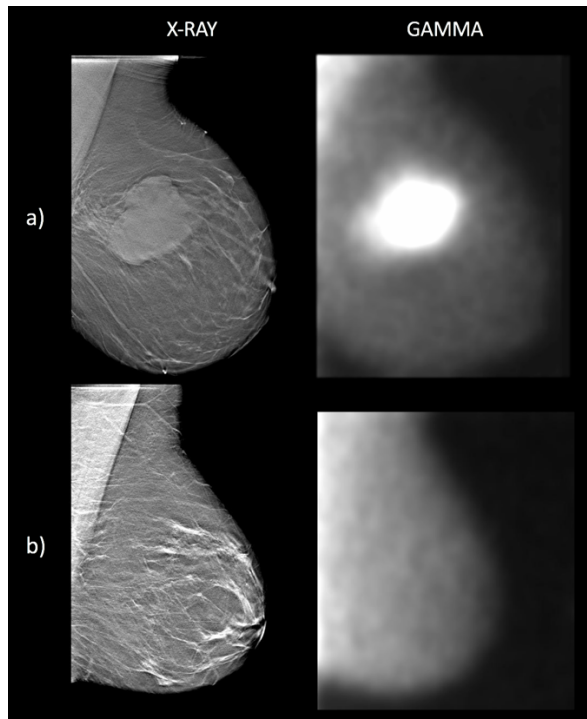


Figure 3-2: Example DMT images: a) shows positive DMT study; b) shows negative DMT study.

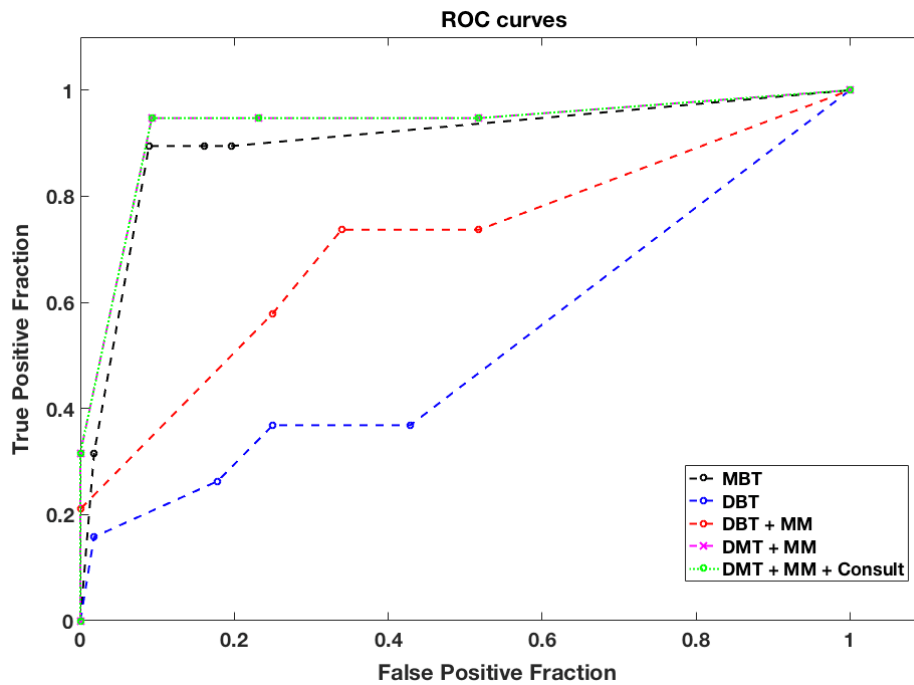


Figure 3-3: ROC curves for each of the stages of the reading sequence. Note that DMT = DBT+MBT. The curves for DMT+MM and DMT+MM+NM Consult are superimposed on each other.

Table 3-2: AUCs for the ROC curves of Figure 3-3.

Method	MBT	DBT	DBT + MM	DMT + MM	DMT + MM + Consult
ROC, Az	0.9	0.61	0.74	0.93	0.93

Table 3-3: AUC contrast values, along with their associated confidence limits and p-values

ROC Contrast Estimation and Testing Results by Row						
Contrast	Estimate	Standard Error	95% Confidence Limits		Chi-Square	P-value
MBT - (DBT + MM)	0.1605	0.0677	0.2791	0.2931	5.6283	0.0177
DBT - (DBT + MM)	-0.1659	0.0598	-0.2832	-0.0486	7.6856	0.0056
(DMT + MM) - (DBT + MM)	0.1886	0.0579	0.0751	0.302	10.6191	0.0011
(DMT + MM + Consult) - (DBT + MM)	0.1886	0.0579	0.0751	0.302	10.6191	0.0011

A p-value of less than 0.05 was considered statistically significant. As shown in Table 3-3, a statistically significant difference in  $A_z$  value was seen between DBT + MM and all other stages in the reading sequence including, DMT + MM + Consult and MBT alone. The AUCs of DMT, DMT + MM + Consult, and MBT alone were all significantly higher than that of DBT + MM, while the  $A_z$  value of DBT alone was significantly lower. It is notable that the addition of the expert nuclear medicine consult report had no measurable effect on the ROC shape or  $A_z$  value of the breast radiologist given DBT+ MM+ MBT. Also notable is that even using only MBT, the nuclear medicine radiologist performed significantly better than DBT + MM, and nearly as well as DBT+ MM+ MBT.

Table 3-4 shows the sensitivities and specificities calculated using a decision threshold that defined suspicion ratings of 4 or more as positive calls and 3 or less as negative calls.

Table 3-4: Sensitivity and specificity, positive predictive value (PPV), and negative predictive value (NPV) when the decision threshold is placed between suspicion scores of 3 and 4.

	MBT	DBT	DBT + MM	DMT + MM	DMT + MM + Consult
Sensitivity	0.86	0.29	0.62	0.95	0.95
Specificity	0.92	0.82	0.76	0.9	0.9
PPV	0.75	0.38	0.50	0.77	0.77
NPV	0.95	0.75	0.84	0.98	0.98

### 3.4 Discussion

The results of this study show that, for the cohort of women scheduled for breast biopsy, the addition of the MBT to the combination of DBT and mammography results in significant improvement in diagnostic performance as measured by the area under the ROC curve. With the malignancy decision threshold between scores of 3 and 4, the addition of MBT to DBT+MM resulted in improvements in sensitivity, specificity, PPV, and NPV. As an indicator of overall accuracy,  $A_z$  significantly increased with the addition of MBT to MBT + MM. This suggests that functional imaging could be a useful adjunct for structural breast imaging, particularly when it is performed with an integrated hybrid scanner so that structural and functional images have a high degree of spatial correlation.

The expert breast radiologist reader whose results are reported here had minimal nuclear medicine experience prior to this study. The lack of any measurable difference between

his AUC before and after the opinion of the nuclear medicine expert became available suggests that the breast radiologist was able to effectively utilize the information available in the MBT scans and provides encouragement that the addition of MBT to DBT would not require separate radiographic and nuclear medicine interpretations. The ability to have a single breast radiologist effectively interpret both the DBT and MBT images would greatly facilitate the clinical adoption of DMT. Compared to DBT interpretation, MBT interpretation is also much quicker to perform, so overall interpretation time would not be substantially lengthened.

A remarkable and somewhat unanticipated result of the study was the excellent performance obtained using MBT alone, which for this subject cohort was nearly as good as the performance using the full DMT+MM image set.

This study used only MLO compression rather than the more commonly used combination of MLO plus CC. The rationale is that the use of two compressions, while useful in 2D mammography for ruling out false positives due to superposition of breast tissue, may not be necessary with tomosynthesis breast imaging. The MLO compression permits both the breast and axillary regions to be imaged, so is the preferred choice if a single compression is used. The use of single-compression DBT also approximately halves the overall radiation dose, as well as the total scan time. Svahn et al. found no statistically significant performance difference between single compression DBT and 2-compression MM, although single compression DBT was slightly superior in terms of  $A_z$  value (0.81 for 1cDBT vs 0.76 for 2cMM)<sup>27</sup>. A recent study by Rodriguez-Ruiz et al. showed that single compression DBT is not statistically inferior to either 2-compression MM or to 2-compression MM plus 2-compression DBT<sup>18</sup>. In the Malmo Breast Tomosynthesis Screening Trial (MBTST), whose main goal was to investigate the accuracy of single compression (MLO) DBT in population screening compared with standard two-compression digital mammography, approximately 15,000 women were enrolled. The results of the study, recently published in *Lancet*, showed that 'Breast cancer screening by use of one-view digital breast tomosynthesis with a reduced compression force has higher sensitivity at a slightly lower specificity for breast cancer detection compared with two-view digital mammography and has the potential to reduce the radiation dose and screen-reading burden required by two-view digital breast tomosynthesis with two-view digital mammography.'<sup>28</sup>

In this study the  $A_z$  value measured for DBT+MM ( $A_z = 0.74$ ) was lower than that documented in the recent DBT literature. For example in a study comparing DBT+MM to MRI+MM and MM alone, Svahn et al. measured  $A_z \sim 0.83$  for single view (MLO) DBT+ single view (CC) MM compared to  $A_z \sim 0.76$  for MM alone<sup>22</sup>. When comparing single view (MLO) DBT+ single view (CC) MM to 2-view DBT+MM Rodriguez-Ruiz et al. measured  $A_z$  values of 0.82 and 0.83 for single- and double-compression, respectively<sup>18</sup>. However, they also noted readers with experience reading single view DBT performed better while readers inexperienced with reading single view DBT underperformed when compared to their 2 view MM scores<sup>18</sup>. Ohashi et al. reported  $A_z \sim 0.94$  for single view (MLO) DBT+ 2 view MM compared to  $A_z \sim 0.92$  for MM alone<sup>29</sup>.

The underperformance of the DBT alone modality set may have a few causes. First, the reader was inexperienced with single compression DBT. As mentioned above, it has been noted by Rodriguez-Ruiz et al. that this could detrimentally affect the reads<sup>18</sup>. Since the study, currently, has only a single reader it is difficult to determine how much affect this had on the study. Second, is the capability of DBT to identify malignancies presented by calcifications. In this study 4 out of the 21 malignancies were originally detected in clinical MM images as calcifications. Three out of the 4 calcification malignancies were missed in the DBT alone study, while those same 3 malignancies were seen on MM. The question if calcifications are well

depicted on DBT is still under investigation. Poplack et al. showed in their study out of 14 cases with microcalcifications 8 (57%) were only seen on MM<sup>30</sup>. In a larger study, Spangler et al. showed 90% of microcalcification clusters were identified on MM, while 80% were identified in DBT<sup>31</sup>. While these studies showed an advantage for identification of calcifications using MM, some studies suggest little difference between MM's and DBT's ability to identify calcifications<sup>32,33</sup>.

For breast scintigraphy using <sup>99m</sup>Tc-sestamibi the injected radiotracer activity recommended by the Society of Nuclear Medicine and Molecular Imaging, the European Association of Nuclear Medicine, and the tracer manufacturer is 740 – 1110 MBq (20 – 30 mCi)<sup>34-36</sup>. Investigators at Mayo Clinic have performed human studies showing that for 2-dimensional breast scintigraphy using opposing planar gamma cameras the injected activity can be substantially lower (296 MBq or 8 mCi) without compromising the detection of small breast cancers<sup>37</sup>. Studies at UVA are underway to investigate the impact of lower injected <sup>99m</sup>Tc-sestamibi activity on tomographic breast imaging studies such as MBT.

#### Limitations:

1) These results are from a single reader. A multi-reader study would be more desirable, due to the ability to increase the statistical power and to generalize the results over a larger reader population<sup>26</sup>. As seen in the ROC AUC ranges given above by Svahn *et al* the AUC's from different readers can greatly vary. The addition of more readers would allow for the averaging of the ROC curve to gain a smoother and better fitting representation of each modality sets ability.

2) The MM images used in the observer study were the subject's most recent clinical MM images. Therefore, they were acquired using a mammographic system other than the DMT scanner. Ideally all images would be acquired using the same scanner.

## References

- 1 Rosenberg RD, Hunt WC, Williamson MR, Gilliland FD, Wiest PW, Kelsey CA, *et al.* Effects of age, breast density, ethnicity, and estrogen replacement therapy on screening mammographic sensitivity and cancer stage at diagnosis: review of 183,134 screening mammograms in Albuquerque, New Mexico. *Radiology* 1998;**209**:511–8. <https://doi.org/10.1148/radiology.209.2.9807581>.
- 2 Kolb TM, Lichy J, Newhouse JH. Comparison of the Performance of Screening Mammography, Physical Examination, and Breast US and Evaluation of Factors that Influence Them: An Analysis of 27,825 Patient Evaluations. *Radiology* 2002;**225**:165–75. <https://doi.org/10.1148/radiol.2251011667>.
- 3 Stomper PC, D'Souza DJ, DiNitto PA, Arredondo MA. Analysis of parenchymal density on mammograms in 1353 women 25-79 years old. *American Journal of Roentgenology* 1996;**167**:1261–5. <https://doi.org/10.2214/ajr.167.5.8911192>.
- 4 Liberman L, Menell JH. Breast imaging reporting and data system (BI-RADS). *Radiologic Clinics of North America* 2002;**40**:409–30. [https://doi.org/10.1016/S0033-8389\(01\)00017-3](https://doi.org/10.1016/S0033-8389(01)00017-3).
- 5 Tabár L, Dean PB. Mammographic Parenchymal Patterns: Risk Indicator for Breast Cancer? *JAMA* 1982;**247**:185–9. <https://doi.org/10.1001/jama.1982.03320270023016>.
- 6 Sickles E. Mammographic features of 300 consecutive nonpalpable breast cancers. *American Journal of Roentgenology* 1986;**146**:661–3. <https://doi.org/10.2214/ajr.146.4.661>.
- 7 Jackson VP, Hendrick RE, Feig SA, Kopans DB. Imaging of the radiographically dense breast. *Radiology* 1993;**188**:297–301. <https://doi.org/10.1148/radiology.188.2.8327668>.
- 8 Gilbert FJ, Tucker L, Gillan MGC, Willsher P, Cooke J, Duncan KA, *et al.* Accuracy of Digital Breast Tomosynthesis for Depicting Breast Cancer Subgroups in a UK Retrospective Reading Study (TOMMY Trial). *Radiology* 2015;**277**:697–706. <https://doi.org/10.1148/radiol.2015142566>.
- 9 Michell MJ, Iqbal A, Wasan RK, Evans DR, Peacock C, Lawinski CP, *et al.* A comparison of the accuracy of film-screen mammography, full-field digital mammography, and digital breast tomosynthesis. *Clinical Radiology* 2012;**67**:976–81. <https://doi.org/10.1016/j.crad.2012.03.009>.
- 10 Bernardi D, Ciatto S, Pellegrini M, Tuttobene P, Fanto' C, Valentini M, *et al.* Prospective study of breast tomosynthesis as a triage to assessment in screening. *Breast Cancer Res Treat* 2012;**133**:267–71. <https://doi.org/10.1007/s10549-012-1959-y>.
- 11 Brem RF, Fishman M, Rapelyea JA. Detection of Ductal Carcinoma in Situ with Mammography, Breast Specific Gamma Imaging, and Magnetic Resonance Imaging: A Comparative Study. *Academic Radiology* 2007;**14**:945–50. <https://doi.org/10.1016/j.acra.2007.04.004>.
- 12 Brem RF, Ioffe M, Rapelyea JA, Yost KG, Weigert JM, Bertrand ML, *et al.* Invasive Lobular Carcinoma: Detection with Mammography, Sonography, MRI, and Breast-Specific Gamma Imaging. *American Journal of Roentgenology* 2009;**192**:379–83. <https://doi.org/10.2214/AJR.07.3827>.
- 13 Park KS, Chung HW, Yoo YB, Yang J-H, Choi N, So Y. Complementary Role of Semiquantitative Analysis of Breast-Specific Gamma Imaging in the Diagnosis of Breast Cancer. *American Journal of Roentgenology* 2014;**202**:690–5. <https://doi.org/10.2214/AJR.13.11324>.
- 14 Williams MB, Judy PG, Gunn S, Majewski S. Dual-Modality Breast Tomosynthesis. *Radiology* 2010;**255**:191–8. <https://doi.org/10.1148/radiol.09091160>.
- 15 Gong Z, Klanian K, Patel T, Sullivan O, Williams MB. Implementation and evaluation of an expectation maximization reconstruction algorithm for gamma emission breast tomosynthesis. *Medical Physics* 2012;**39**:7580–92. <https://doi.org/10.1118/1.4764480>.

- 16 Beiden SV, Wagner RF, Doi K, Nishikawa RM, Freedman M, Lo S-CB, *et al.* Independent versus Sequential Reading in ROC Studies of Computer-Assist Modalities: Analysis of Components of Variance. *Academic Radiology* 2002;**9**:1036–43. [https://doi.org/10.1016/S1076-6332\(03\)80479-8](https://doi.org/10.1016/S1076-6332(03)80479-8).
- 17 Sahiner B, Chan H-P, Hadjiiski LM, Roubidoux MA, Paramagul C, Bailey JE, *et al.* Multi-modality CADx: ROC Study of the Effect on Radiologists' Accuracy in Characterizing Breast Masses on Mammograms and 3D Ultrasound Images. *Academic Radiology* 2009;**16**:810–8. <https://doi.org/10.1016/j.acra.2009.01.011>.
- 18 Rodriguez-Ruiz A, Gubern-Merida A, Imhof-Tas M, Lardenoije S, Wanders AJT, Andersson I, *et al.* One-view digital breast tomosynthesis as a stand-alone modality for breast cancer detection: do we need more? *Eur Radiol* 2018;**28**:1938–48. <https://doi.org/10.1007/s00330-017-5167-3>.
- 19 Rao AA, Feneis J, Lalonde C, Ojeda-Fournier H. A Pictorial Review of Changes in the BI-RADS Fifth Edition. *RadioGraphics* 2016;**36**:623–39. <https://doi.org/10.1148/rg.2016150178>.
- 20 Narayanan D, Madsen KS, Kalinyak JE, Berg WA. Interpretation of Positron Emission Mammography: Feature Analysis and Rates of Malignancy. *American Journal of Roentgenology* 2011;**196**:956–70. <https://doi.org/10.2214/AJR.10.4748>.
- 21 Metz CE. Receiver Operating Characteristic Analysis: A Tool for the Quantitative Evaluation of Observer Performance and Imaging Systems. *Journal of the American College of Radiology* 2006;**3**:413–22. <https://doi.org/10.1016/j.jacr.2006.02.021>.
- 22 Svahn T, Andersson I, Chakraborty D, Svensson S, Ikeda D, Förnvik D, *et al.* The diagnostic accuracy of dual-view digital mammography, single-view breast tomosynthesis and a dual-view combination of breast tomosynthesis and digital mammography in a free-response observer performance study. *Radiat Prot Dosimetry* 2010;**139**:113–7. <https://doi.org/10.1093/rpd/ncq044>.
- 23 Lewin JM, Hendrick RE, D'Orsi CJ, Isaacs PK, Moss LJ, Karellas A, *et al.* Comparison of Full-Field Digital Mammography with Screen-Film Mammography for Cancer Detection: Results of 4,945 Paired Examinations. *Radiology* 2001;**218**:873–80. <https://doi.org/10.1148/radiology.218.3.r01mr29873>.
- 24 Giger ML, Inciardi MF, Edwards A, Papaioannou J, Drukker K, Jiang Y, *et al.* Automated Breast Ultrasound in Breast Cancer Screening of Women With Dense Breasts: Reader Study of Mammography-Negative and Mammography-Positive Cancers. *American Journal of Roentgenology* 2016;**206**:1341–50. <https://doi.org/10.2214/AJR.15.15367>.
- 25 Zanca F, Hillis SL, Claus F, Ongeval CV, Celis V, Provoost V, *et al.* Correlation of free-response and receiver-operating-characteristic area-under-the-curve estimates: Results from independently conducted FROC/ROC studies in mammography. *Medical Physics* n.d.;**39**:5917–29. <https://doi.org/10.1118/1.4747262>.
- 26 Chakraborty DP, Berbaum KS. Observer studies involving detection and localization: Modeling, analysis, and validation. *Medical Physics* 2004;**31**:2313–30. <https://doi.org/10.1118/1.1769352>.
- 27 Svahn TM, Chakraborty DP, Ikeda D, Zackrisson S, Do Y, Mattsson S, *et al.* Breast tomosynthesis and digital mammography: a comparison of diagnostic accuracy. *BJR* 2012;**85**:e1074–82. <https://doi.org/10.1259/bjr/53282892>.
- 28 Zackrisson S, Lång K, Rosso A, Johnson K, Dustler M, Förnvik D, *et al.* One-view breast tomosynthesis versus two-view mammography in the Malmö Breast Tomosynthesis Screening Trial (MBTST): a prospective, population-based, diagnostic accuracy study. *The Lancet Oncology* 2018;**19**:1493–503. [https://doi.org/10.1016/S1470-2045\(18\)30521-7](https://doi.org/10.1016/S1470-2045(18)30521-7).
- 29 Ohashi R, Nagao M, Nakamura I, Okamoto T, Sakai S. Improvement in diagnostic performance of breast cancer: comparison between conventional digital mammography alone

- and conventional mammography plus digital breast tomosynthesis. *Breast Cancer* 2018;**25**:590–6. <https://doi.org/10.1007/s12282-018-0859-3>.
- 30 Poplack SP, Tosteson TD, Kogel CA, Nagy HM. Digital Breast Tomosynthesis: Initial Experience in 98 Women with Abnormal Digital Screening Mammography. *American Journal of Roentgenology* 2007;**189**:616–23. <https://doi.org/10.2214/AJR.07.2231>.
- 31 Spangler ML, Zuley ML, Sumkin JH, Abrams G, Ganott MA, Hakim C, *et al.* Detection and Classification of Calcifications on Digital Breast Tomosynthesis and 2D Digital Mammography: A Comparison. *American Journal of Roentgenology* 2011;**196**:320–4. <https://doi.org/10.2214/AJR.10.4656>.
- 32 Good WF, Abrams GS, Catullo VJ, Chough DM, Ganott MA, Hakim CM, *et al.* Digital Breast Tomosynthesis: A Pilot Observer Study. *American Journal of Roentgenology* 2008;**190**:865–9. <https://doi.org/10.2214/AJR.07.2841>.
- 33 Teertstra HJ, Loo CE, van den Bosch MAAJ, van Tinteren H, Rutgers EJT, Muller SH, *et al.* Breast tomosynthesis in clinical practice: initial results. *Eur Radiol* 2010;**20**:16–24. <https://doi.org/10.1007/s00330-009-1523-2>.
- 34 Bombardieri E, Aktolun C, Baum RP, Bishof-Delaloye A, Buscombe J, Chatal JF, *et al.* Breast scintigraphy: procedure guidelines for tumour imaging. *Eur J Nucl Med Mol Imaging* 2003;**30**:BP107-114.
- 35 Bristol-Myers Squibb Medical Imaging. *Miraluma drug datasheet*. 2009.
- 36 Goldsmith SJ, Parsons W, Guiberteau MJ, Stern LH, Lanzkowsky L, Weigert J, *et al.* SNM Practice Guideline for Breast Scintigraphy with Breast-Specific  $\gamma$ -Cameras 1.0. *J Nucl Med Technol* 2010;**38**:219–24. <https://doi.org/10.2967/jnmt.110.082271>.
- 37 Hruska CB, Weinmann AL, Tello Skjerseth CM, Wagenaar EM, Connors AL, Tortorelli CL, *et al.* Proof of concept for low-dose molecular breast imaging with a dual-head CZT gamma camera. Part II. Evaluation in patients. *Med Phys* 2012;**39**:3476–83.

# Chapter 4

## Synthesized DMT Images

### 4.1 Motivation

Since the late 80's and early 90's, model observers have been under development and have become important tools in the assessment of imaging devices<sup>1-4</sup>. They can be utilized as a device test and improve the system before images are given to human observers for interpretation. They are also used as support for human observers, these models are then called computer-aided diagnosis (CAD) systems.

The observer, when used for DMT studies, would allow for timely testing of new imaging protocols and reconstructions before lengthy human observer clinical trials are pursued. Currently, a model observer is under development in our lab. For the model observer to function properly prior information is needed. This information is used to "train" the observer and must be a large data set realistically representing the type of images that will be assessed by the observer. This chapter will focus on the basics of model observers and the creation and verification of clinically-based synthetic breast images need for the training of the model observer.

Note, throughout this chapter the notation will be denoted as follows: vectors will be bold lowercase letters, matrices will be bold uppercase letters, and scalar values will be represented by non-bolded letters. The transpose operation is denoted by a superscript uppercase t.

#### 4.1.1 Image Formation and Model Observers

An imaging system can be considered as a continuous-to-discrete mapping operator,  $\mathbf{H}$ , that maps a continuous object,  $\mathbf{f}$ , to a discrete digital image,  $\mathbf{g}$ <sup>4</sup>. Therefore, the formation of an image can be described as follows:

$$\mathbf{g} = \mathbf{H}\mathbf{f} + \mathbf{n} , \quad (4-1)$$

where  $\mathbf{n}$  is additive noise coming from the Poisson nature of photon counting and the Gaussian nature of electronic noise arising from the detector and signal amplifiers<sup>4</sup>. In the case of medical imaging the object is an area of interest on a human subject and the operator is the imaging system used (i.e. CT, MRI, etc.).

The object can be further broken down into two components, a signal component,  $\mathbf{f}_s$ , and a background component,  $\mathbf{f}_b$ <sup>4-6</sup>. Such that a binary detection task to determine if a signal is present in an image or if no signal is present in an image. These tasks create the two hypotheses,  $H_0$  and  $H_1$ , used for a model observer<sup>3-5</sup>.

$$H_0: \mathbf{g} = \mathbf{H}\mathbf{f}_b + \mathbf{n} \quad (4-2)$$

$$H_1: \mathbf{g} = \mathbf{H}(\mathbf{f}_b + \mathbf{f}_s) + \mathbf{n} \quad (4-3)$$

Model observers used in image assessment have the same basic form, where a decision to accept a hypothesis is based off of a scalar test statistic,  $t$ <sup>4</sup>. Where  $t$  is defined as:

$$t = T(\mathbf{g}) , \quad (4-4)$$

$\mathbf{g}$  is the raw or processed image and  $T(\mathbf{g})$  is the observer's decision function<sup>3,4</sup>. A threshold must be placed on the test statistic to determine if the desired hypothesis is accepted or not.

There are two main categories of model observers typically used for medical imaging: nonlinear and linear<sup>4</sup>. Each of these categories can be broken into optimal and suboptimal classes<sup>4</sup>. The optimal class is usually preferred when testing image quality, while suboptimal observers are preferred when trying to mimic the response of human observers to the image sets. This discussion will focus on the optimal observers. The main nonlinear, optimal observer is the Bayesian Ideal Observer (BIO). It is the ideal observer because it minimizes the cost of a decision task, while maximizing the sensitivity or true positive fraction (TPF) of the binary detection task<sup>4</sup>. Where TPF is defined as the number of tests that are called a disease that actually have a disease divided by total number of images that have the disease. The test statistic for the BIO is the likelihood ratio,  $\Lambda(\mathbf{g})$ <sup>4</sup>.

$$\Lambda(\mathbf{g}) = \frac{pr(\mathbf{g}|H_1)}{pr(\mathbf{g}|H_0)} \quad (4-5)$$

The BIO has been shown to work well with well-defined Gaussian backgrounds and in cases where the signal is known exactly (SKE) cases, but if there are variable signals and/or non-Gaussian background the calculation of the likelihood ratio, which requires full knowledge of the probability density, becomes intensive<sup>4</sup>.

In many cases the desired task is to find random/variable signals in random background noise. This leads to the use of linear observers. One of the most common is the Hotelling Observer (HO), which uses the mean and covariance of the data to define its test statistic<sup>4</sup>. The HO test statistic is defined as:

$$t = \mathbf{w}^T \mathbf{g} \quad , \quad (4-6)$$

where  $\mathbf{w}^T$  is the  $M \times 1$  "data space" template<sup>4</sup>. The data space template for the HO is

$$\mathbf{w}^T = \mathbf{K}_g^{-1} \Delta \bar{\mathbf{g}} \quad , \quad (4-7)$$

where  $\mathbf{K}_g$  is the average of the signal present and signal absent covariance matrices and  $\Delta \bar{\mathbf{g}}$  is the difference between the average signal present and signal absent images<sup>4</sup>.

$$\Delta \bar{\mathbf{g}} = \bar{\mathbf{g}}_1 - \bar{\mathbf{g}}_0 \quad (4-8)$$

$$\mathbf{K}_g = \frac{1}{2} (\mathbf{K}_{g|H_0} + \mathbf{K}_{g|H_1}) \quad (4-9)$$

$$\mathbf{K}_{g|H_j} = \langle (\mathbf{g} - \bar{\mathbf{g}}_j)(\mathbf{g} - \bar{\mathbf{g}}_j)^T \rangle \quad \text{for } j = 0 \text{ or } 1 \quad (4-10)$$

Here, it is important to note that each image,  $\mathbf{g}$ , tested is compared to an ensemble average of similar signal present and signal absent images<sup>4</sup>. The ensemble data is also called the observer's training set. These training sets must be large and representative of the background and signal being evaluated by the HO to ensure reliable results. The creation and testing of this training set will be discussed in the following sections.

Depending on the data set,  $\mathbf{K}_g$  can be very large causing the inverse to be computationally unattainable<sup>4</sup>. To reduce the size of the data set linear observers can be channelized<sup>4</sup>. Channelization is typically coupled with the HO and is called the Channelized Hotelling Observer (CHO). In a CHO a linear transform,  $\mathbf{U}$ , is applied to the original image,  $\mathbf{g}$ , giving a reduced output,  $\mathbf{v}$ <sup>4</sup>.

$$\mathbf{v} = \mathbf{U}\mathbf{g} \quad (4-11)$$

There are many different transforms used. Some examples are the Laguerre-Gauss function, Singular Vector Channels, and Partial Least Squares<sup>3</sup>. The reduced image,  $\mathbf{v}$ , is then used in the same way the original image is in the HO, with equation 4-7 and 4-6 becoming:

$$\mathbf{w}_v^T = \mathbf{K}_g^{-1} \Delta \bar{\mathbf{v}}, \quad (4-12)$$

$$t = \mathbf{w}_v^T \mathbf{v}. \quad (4-13)$$

Due to the dimensionality (DBT: 2007 x 1120 x 66 voxels; MBT: 90 x 66 x 66 voxels) and variability in signal and background of the DMT images, it seems that a CHO will be the most viable choice. However, before observers can be tested and compared, a training set needs to be created. A large training set is preferred allowing for better estimates of background structure and signal structure. This can require hundreds of images, which have the same background noise structure as the DMT images. Unfortunately, the number of human images available are too few to create a training set. To remedy this issue, new synthetic images that mimic the structure of both the x-ray and single gamma human images were created (Section 4.2).

## 4.2 Creation of Synthetic Images

To fulfill the needs of the model observers, both 'signal present' and 'signal absent' synthetic images are needed. Signal absent images are created first using principal component analysis (PCA) to create a base set of eigenimages from the set of signal absent (no tumor present) human images. By using eigenimages based off of human images, a database of synthetic images with similar background noise structure can be created. Once the background synthetic images are created, tumors can be added to simulate signal present images. The next few sections detail the creation and testing of these images.

### 4.2.1 Theory of Principal Component Analysis

PCA is a dimension-reduction tool, which extracts important information from large correlated data sets and reduces them to a set of uncorrelated orthogonal variables called principal components (PC)<sup>7,8</sup>. PCA focuses on the variances of the data or the spread of the data in specific directions (Fig. 4-1). The first PC represents the direction (axis) in which the most variation is in the data (Fig. 4-1)<sup>7,8</sup>. Each subsequent PC will have less variation than that of the PC preceding it<sup>7</sup>. For a data set with N variables a total of N PCs can be found giving rise to a N-dimensional space<sup>7</sup>. The first few PCs have a large variation depicting the main differences in the data, while the last few PCs will have little variation identifying the similarities in the data<sup>7</sup>.

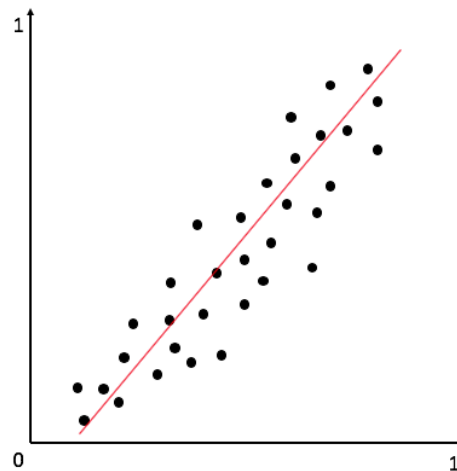


Figure 4-1: A scatter plot of 33 data points of 2 variables with a positive relationship. The red line represents the first principal component representing the largest variance within the data set.

To find the PCs of a data set, the data must first be presented as a square matrix<sup>7</sup>. The data set is not typically a square matrix, for example a data set  $\mathbf{A}$  can have  $N$  variables and  $V$  trials. To get around this the asymmetry in the data, a covariance matrix  $\mathbf{C}$  can be created. This covariance matrix describes the relationships between each variable. The diagonal elements of the matrix represent the variance in each variable, while the off-diagonal elements represent the covariance between specific variables. The covariance between variables is calculated as follows<sup>9</sup>.

$$cov = \frac{1}{N-1} \sum_{i=1}^N (x_i - \bar{x})(y_i - \bar{y}) \quad (4-14)$$

With the creation of the covariance matrix the PCs are the matrix's  $N$  eigenvectors,  $\mathbf{v}$ , where

$$\mathbf{Cv} = \lambda \mathbf{v}, \quad (4-15)$$

and  $\lambda$  is the eigenvector's corresponding eigenvalue<sup>7</sup>. By looking at the eigenvalues, the order of eigenvectors which represent the PC with the most variance to the least can be determined<sup>7</sup>. Generally speaking, the largest eigenvalue corresponds to the first PC and the next largest eigenvalues corresponds to the second PC and so on<sup>7</sup>. Once a set of PCs has been created these can then be used to further analyze the data or, in the case of this dissertation, be used to create synthetic images.

## 4.2.2 Eigenimages and Synthesized Images for DMT Study

In 1987, Sirovich and Kirby developed a new technique where they used PCA on a set of cropped face images to gain a set of eigenvectors which they dubbed eigenpictures. They showed that with a small set of eigenpictures any set of faces could be classified as a weighted linear combination of the eigenpictures<sup>10</sup>. Several years later, this concept was built on by Turk and Pentland, who proved eigenpictures could be used for facial recognition<sup>11</sup>. Over the next 20 to 25 years eigenimages started to be used as a tool to create statistical appearance models of 2D mammograms and masses<sup>12,13</sup>. More recently, Sturgeon et al. showed that unique digital

breast phantoms could be created using linear combinations of eigenimages from a 3D breast data set by selecting unique vector weights <sup>14</sup>.

Based off of the work done in the past, it was believed that a set of synthetic breast tomosynthesis images could be created from the clinical DMT data sets <sup>11,14</sup>. This set of synthetic images would not be a set of phantoms which could be used to get projection views from, but a set of reconstructed DBT and MBT images that have a similar background structure as the true human DMT images. This set of synthetic DBT and MBT images could then be used as a training set for a model observer. To our knowledge, this is the first time that eigenimages have been used to synthesize new tomosynthesis volumes, in x-ray and gamma images.

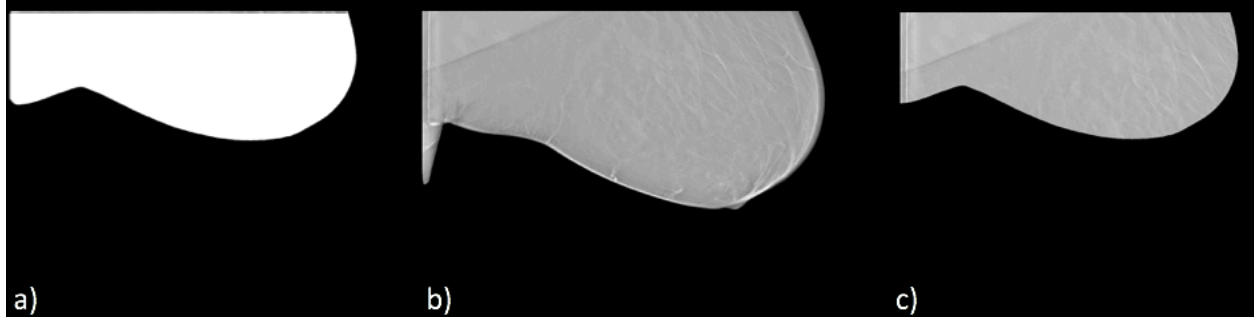


Figure 4-2: a) depicts the central slice of the image mask. Here all the values within the breast volume are 1, while the exterior values are 0. b) is the central slice of a human DBT image which is masked by a) to create c) the final masked human DBT image.

The creation of synthesized DBT and MBT images is a multi-step process. First, it is important to note, the original images must have the same size and shape to create a reliable data set of synthetic images. If the images are not the same size and shape, those features become the most dominant structures in the resulting principle components. To mask the images, a masking template was created by using an edge finding function in MATLAB to find the edges of one of the trial's smaller breast volumes, which fit into most other breast volumes. Once the mask was created, all breasts that had larger volumes were masked with the template, taking only values within the masking template's volume (Fig. 4-2a). Using the masked images, an average breast image,  $\Psi$ , was created for each modality (Fig. 4-2 b,c). If we have set of N breast tomosynthesis images,  $\Gamma_i$  for  $i = 1, 2, \dots, N$ , then

$$\Psi = \frac{1}{N} \sum_{i=1}^N \Gamma_i, \quad (4-16)$$

and it follows that each breast image then differs from the average image by the vector <sup>11</sup>

$$\Phi_i = \Gamma_i - \Psi. \quad (4-17)$$

Each  $\Phi$  is put into vector form,  $\phi$ , and a data matrix of the difference images is created such that  $\mathbf{A} = [\phi_1, \phi_2, \dots, \phi_N]$  <sup>11</sup>. The matrix  $\mathbf{A}$  becomes the data matrix that undergoes PCA. The covariance matrix of  $\mathbf{A}$  is calculated, and the eigenvectors and eigenvalues are acquired. These eigenvectors are then the eigenimages which we will refer to as eigenDBT for DMT x-ray tomosynthesis images and eigenMBT for DMT gamma tomosynthesis images. We will refer to the generic (non-modality specific) eigenimages as eigenBT,  $u_i$  (eigenbreast tomosynthesis image).

A set of unique synthetic breast images,  $\mathbf{s}_i$ , can then be created by summing a set of weighted eigenBTs and adding the sum to a mean of the breast images <sup>11</sup>.

$$\mathbf{s}_i = \boldsymbol{\Psi} + \sum_{l=1}^{N-1} w_l^i \mathbf{u}_l \quad (4-18)$$

Where the  $w_l$  are weighting factors. The weights are found in two steps. First, each image used to create the eigenBTs is decomposed into its eigenBT components, as described by Turk et al.

$$w_l = \mathbf{u}_l^T \boldsymbol{\Phi} \quad (4-19)$$

With a newly created set of N weights for each eigenBT, the mean,  $\mu$ , and standard deviation,  $\sigma$ , for each set are found and new weights for each eigenBT are randomly selected using a random number generator over the range of  $(\mu-\sigma)$  to  $(\mu+\sigma)$  <sup>14</sup>. The sets of new weights created are then used in equation 4-18 to obtain the synthesized images. Figure 4-3 depicts a human DBT and MBT image and examples of synthetic DBT and MBT images.

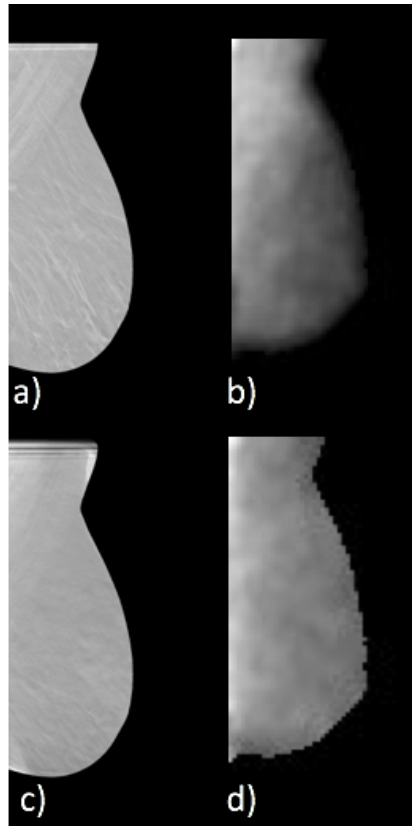


Figure 4-3: a) and b) display the central slices of masked human images. c) and d) display the central slices of synthetic breast images.

To create the DMT synthetic images, all the human x-ray and gamma images were evaluated and only the images of breasts with no lesions, skin tags, and/or biopsy clips were selected. Of these, only the breasts large enough to be masked were utilized. The matrix sizes for the DBT images are 1120 X 2007 X 66 pixels and 66 X 90 X 66 pixels for the MBT images. A thickness of 66 was chosen to ensure the central area of each human image was selected. This

ensures that there is no added noise from the reconstruction artifacts and the shrinking amount of breast tissue toward either edge of the image. The masking resulted in a total of 46 x-ray and 48 gamma human images leading to 45 eigenDBTs and 47 eigenMBTs. The images were created using a program written in MALAB (Version R2007b, Math Works, Natick, MA, USA) and can be reviewed in Appendix B. Following the above method, a total of 2000 synthetic breast images for each modality were created.

For the synthetic images to be useful as a training set in a model observer, the background structure needs to be similar to that of the human images. To ensure the new synthetic images were in fact similar in background structure to the human images, a noise power analysis was completed to test the similarity.

### 4.3 Synthesized Image Background Analysis

To test if the background structure of the synthetic images reliably recreates that of the human DMT images, analysis of the 1D power spectral density (PSD) was conducted. The PSD is a tool that provides characterization of the statistical variance of fluctuations in an image<sup>15</sup>. As stated in chapter 2, noise in an image is created by the quantum noise from x-ray or gamma ray detection and electronic noise within the detector's electronics. Over the past 15 – 20 years, it has been shown that the 1D PSD of anatomical noise in 2D and 3D mammographic images can be modeled by a power law of the form  $P(f) = A/f^\beta$ <sup>14,16–18</sup>. Here  $f$  represents the radial spatial frequency. The power,  $\beta$ , has been used as a metric to compare breast phantom noise characteristics with that of human breast images<sup>17,19,20</sup>.  $\beta$  has been shown to have a values near 3 for 2D mammography and around 1.7 for 3D data x-ray sets<sup>16,18</sup>.

#### 4.3.1 Methods

Calculation of  $\beta$  starts with the calculation of the PSD of the data set. In this case, a data set is considered a 3D DBT or MBT image. The 1D PSD is defined as the square modulus of the Fourier transform of the data itself<sup>15</sup>,

$$PSD(u) = \lim_{L \rightarrow \infty} \frac{1}{L} |P(u)|^2, \quad (4-20)$$

where  $P(u)$  is the Fourier transform of the data itself ( $FT\{p(x)\}$ ), and  $L$  is the length of the data vector. This can be expanded into 2D such that

$$PSD(u, v) = \lim_{X, Y \rightarrow \infty} \frac{1}{XY} |P(u, v)|^2, \quad (4-21)$$

where  $X$  and  $Y$  are the lengths in each direction and  $P(u, v)$  is the Fourier transform of the 2D image data<sup>15</sup>. For a discrete dataset, like those from imaging systems, the continuous object is sampled at regular intervals of  $\Delta x$  and  $\Delta y$ <sup>15</sup>. The lengths of  $X$  and  $Y$  are then described by  $X = N\Delta x$  and  $Y = M\Delta y$ , where  $N$  and  $M$  are the number of pixels (samples) in each direction<sup>15</sup>. Thus, equation 4-21 becomes<sup>15</sup>

$$PSD(u, v) = \lim_{X, Y \rightarrow \infty} \frac{1}{N\Delta x} \frac{1}{M\Delta y} |\Delta x \Delta y P(u, v)|^2 = \lim_{X, Y \rightarrow \infty} \frac{\Delta x \Delta y}{N M} |P(u, v)|^2. \quad (4-22)$$

Equation 4-22 can be solved by using the Fast Fourier transform (FFT) in MATLAB. Accurate spectral analysis requires the data to be statistically stationary; meaning, the noise

samples must be obtained from spatial uniform images and there is no added fixed correlated noise from the detector <sup>4,15</sup>. Both these requirements do not hold true for x-ray or gamma breast images. To account for variations in the image, regions of interest (ROIs) are selected in the regions of the breast that are similar. These regional ROIs allow the assumption that noise fluctuations within the selected area is statistically stationary and allow for the exclusion of known artifacts and non-uniformities caused by the detector and electronics <sup>15,21</sup>. The size and number of ROIs can have a significant effect on the variability in the PSD <sup>21</sup>. The size of the ROI affects the spatial frequency resolution, while the number of ROIs allow for the averaging of the PSD, creating a more statistically stable result <sup>4,15,21</sup>. There is an inverse correlation between the size and number of ROIs; Dolly et. al. explain, as the size of the ROI increases the resolution in spatial frequency increases, but this means that fewer ROIs are possibly leading to higher statistical fluctuations in the PSD <sup>21</sup>.

Before the PSD is calculated, the zero-frequency (DC component estimation) of the ROI should be subtracted. This is done to help reduce the effect of low-frequency trends <sup>15</sup>. This is done by subtracting the average pixel intensity from the ROI. The 2D PSD of an ROI is then calculated by utilizing MATLAB's Fast Fourier transform (FFT) function <sup>15,21</sup>:

$$PSD(u, v) = \lim_{X, Y \rightarrow \infty} \frac{\Delta x \Delta y}{N M} \left| \text{FFT}\{p_{roi}(x, y) - \overline{p_{roi}(x, y)}\} \right|^2. \quad (4-23)$$

Due to the properties of the FT, the resulting frequency data is symmetrical <sup>4</sup>. Thus, it is possible to analyze 1D NPS selections from the resulting 2D PSD from equation 4-23. To get the most reliable trend, several 1D segments are taken from the 2D PSD and averaged <sup>15</sup>. Each of the 1D PSD segments taken were off of the central axes to avoid any residual zero-frequency (Fig. 4-4). A final 1D PSD is calculated by averaging the results from all ROIs (Fig. 4-5).

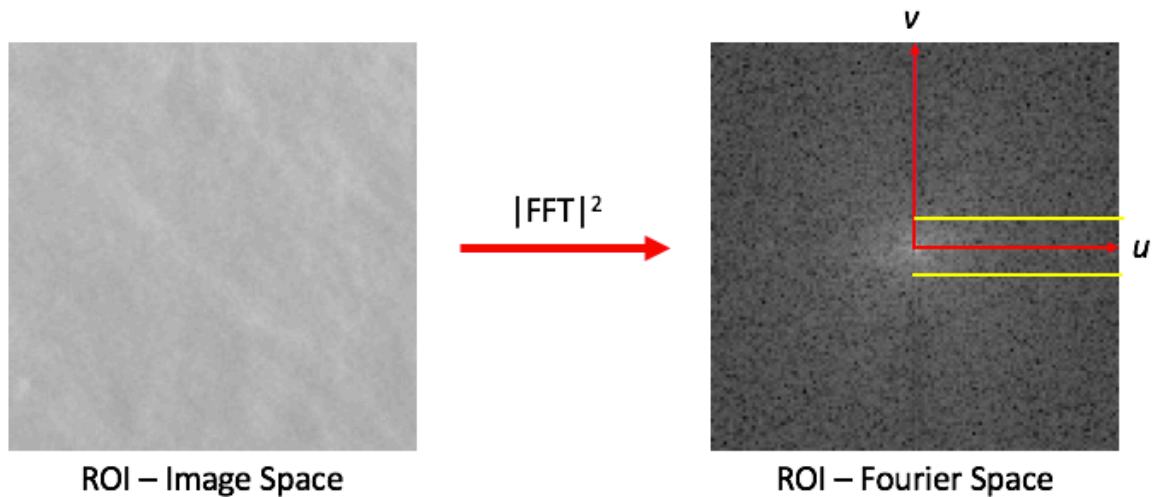


Figure 4-4: The image to the left an example of a ROI in a DBT slice. The data within the ROI undergoes a 2D FFT resulting in the Fourier space image to the right. The yellow lines represent the area the profiles for the 1D PSD were taken. The profiles are only taken over half of the Fourier space due to the symmetry of the image.

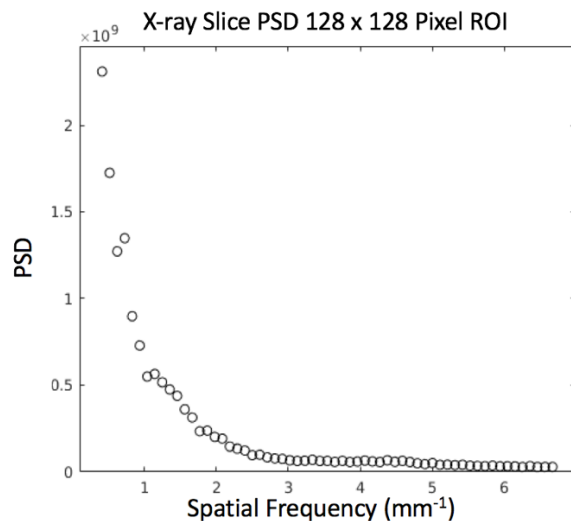


Figure 4-5: An example of a 1D PSD plot from a human DBT image. The ROI size was 128 x 128.

With the 1D PSD in hand, the  $\beta$  value can be calculated via curve fitting<sup>16</sup>. Recall, the power law is defined as:  $P(f) = A/f^\beta$ . Therefore, by replotting the PSD on a log-log plot the power law becomes  $\log(P) = \log(A) - \beta * \log(f)$  and  $\beta$  can be solved for using a simple linear regression (Fig 4-6)<sup>16</sup>. A two-tailed paired Student's t-test was used to determine if the synthetic image's  $\beta$  values were significantly different from those of the human images. If the  $\beta$  values of the synthetic images were shown not to differ significantly from those of the human images, with an assumed statistical significance of  $p < 0.05$ , the images were deemed acceptable to use as training images for the model observer under development. The programs used to calculate the NPS and  $\beta$  values for both the human and synthetic images can be seen in Appendix C.

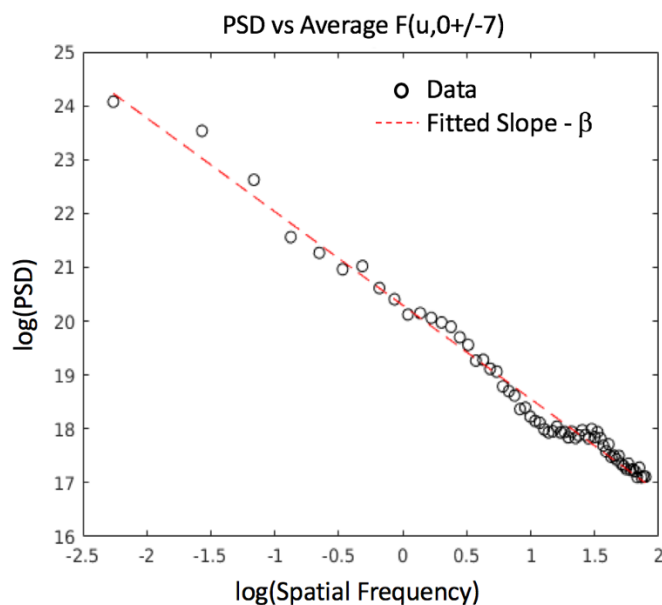


Figure 4-6: Log-log plot of 1D PSD data with a fitted linear regression. The slope of the linear regression is the desired  $\beta$  value.

### 4.3.2 Results and Discussion

Two ROI numbers and sizes were considered for each modality: 15 ROIs at 128 x 128 pixels and 9 ROIs at 256 x 256 pixels for DBT. While 11 ROIs at 16 x 16 pixels and 2 ROIs at 32 x 32 pixels for MBT. For both modalities, the smaller ROI areas were chosen for the analysis over their larger counter parts due to the reduced uncertainty in the resulting averaged NPS. The placement of the ROIs can be seen for each modality in Figure 4-7, a maximum overlap of 50% was permitted. Table 4-1 gives a comparison of the overall average  $\beta$  values for human images vs the synthetic images. It should be noted that there is a decent amount variability in the  $\beta$  values of the human images. The variability is to be expected and was shown by Burgess<sup>16</sup>. Of the 2000 synthetic images created for each modality, 1600 DBT images and 1700 MBT images were kept as training images based on the results of the two-tailed Student's t-test.

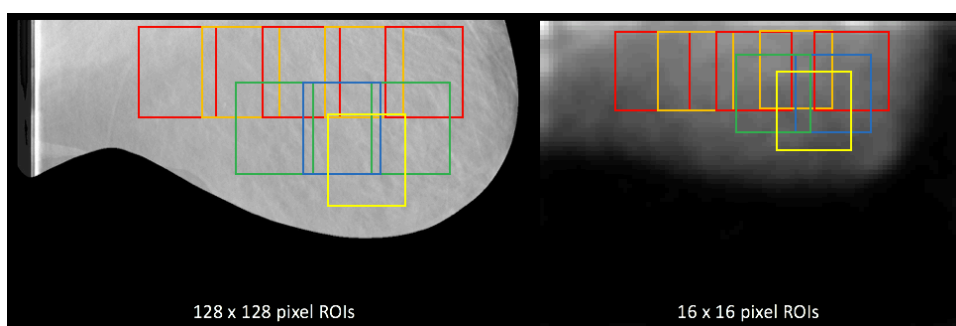


Figure 4-7: Depicts the areas the ROIs were selected for each modality. 15 – 128 x 128 pixel ROIs were used for each slice in the DBT images and 11 – 16 x 16 pixel ROIs were used for each slice in the MBT images.

Table 4-1: Comparison between Human Imaged mean  $\beta$  values vs those of the total synthetic image sets.

	X-ray Recons 128 x 128 ROI		Gamma Recons 16 x 16 ROI	
	Mean $\beta$ -value	Standard Deviation	Mean $\beta$ -value	Standard Deviation
<b>Human Images</b>	1.57	0.11	3.73	0.09
<b>Synthetic Images</b>	1.53	0.06	3.71	0.04

It is important to note that more confidence can be put in the analysis of the x-ray images due to the resolution of the x-ray detectors. The higher resolution allows for better sampling of the object. This allows for reduced uncertainty in the PSD. Unfortunately, nuclear medicine detectors tend to be low resolution when compared to x-ray detectors. Beyond the resolution of the detectors the imaging task of a nuclear medicine system is fundamentally different than that of x-ray. Instead of imaging anatomy, the cellular function is being imaged via radiopharmaceutical distribution. Due to this, nuclear medicine images tend to have less high frequency components causing the PSD analysis to be less reliable. It became a worry when testing the gamma images that correlated low-frequency noise from the reconstruction of the

MBT images would be the dominate driver in the  $\beta$  value. To test if the effect of the reconstruction and detector setup on the  $\beta$  value, two flood phantoms were scanned and reconstructed (Fig. 4-8). The flood phantoms underwent the same PDS analysis (with ROIs indicated in figure 4-8) as the breast images. A low  $\beta$  value would indicate the correlated noise caused by the reconstruction is not the driving factor behind the  $\beta$  values acquired from the PSD analysis of the human and synthetic breast images. Flood A (Fig. 4-8a) had an average  $\beta$  value of 1.23, while flood B's (Fig. 4-8b) average  $\beta$  value was 1.55. These  $\beta$  values suggest the correlated noise caused by the reconstruction and other low frequency noise components are not the driving factors behind the human and synthetic images  $\beta$  values.

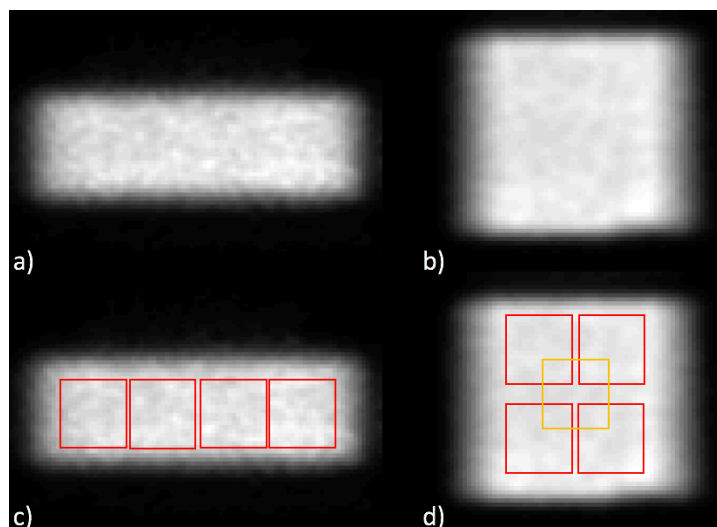


Figure4-8: a) and b) display the central slices of each flood taken. c) and d) display the areas the ROIs were taken for each image for the NPS analysis.

#### 4.4 Addition of Lesions to Synthesized Images

A training set of images for a model observer requires both signal absent and signal present images. Up to this point, only signal absent synthetic images have been discussed. This was necessary due to the need of a realistic background before a signal could be added. The goal of the model observer will be to correctly identify malignant masses within a DMT image set. Therefore, the signal added to the synthetic images is required to be as realistic as possible. The discussion that follows will describe the first-generation lesion addition methods for the DBT and MBT synthetic images. These methods will be built upon to create more realistic lesions and more advance image blending techniques in the future.

There are many techniques used for creating sets of isolated tumors<sup>22-25</sup>. One method uses mathematical modeling to create lesions which are added into the images projection views or into the reconstructed volumes<sup>22</sup>. Another method is to use physical phantoms designed with specific materials and shapes to mimic that of real tissue or radiopharmaceutical distribution<sup>26,27</sup>. Lastly, a real lesion is segmented from human data and inserted into new images with post processing<sup>22</sup>. All of these techniques have been shown to be reliable; however, choosing the correct method can depend on the modality type. For example, segmenting a lesion out of a CT data set is more realistic then segmenting a lesion out of a gamma image. This is mainly due to

the resolution of the CT system. Blurring of the lesion in the gamma image can make it difficult to correctly segment the lesion. For this reason, lesion modeling for the DMT images is split by modality. For MBT images, lesion phantoms were used, while for DBT images a simplified tumor segmentation method was used.

Figure 4-9 is a flow chart describing the method used for insertion of lesion phantom images into the MBT synthetic tomosynthesis images. The lesions were created using two acrylic spheres, 0.8 cm and 1.2 cm, in diameter were filled with 10  $\mu\text{Ci}$  of Tc-99m – pertechnetate solution. Each sphere was then imaged separately under the same protocol as the human image, described in chapter 3. Several image sets were taken of the spheres at different locations in the camera field of view creating multiple lesion positions. Each set of projection images was reconstructed using the same reconstruction algorithm and parameters as the human images. An example of reconstructed lesion slices can be seen in figure 4-10. The reconstructed lesions were then inserted into a subset of the synthetic breast tomosynthesis images via a weighted summation (Fig. 4-11)<sup>24</sup>. By altering the weights of the lesion or synthetic images allows for a variety of lesion intensities to be simulated.

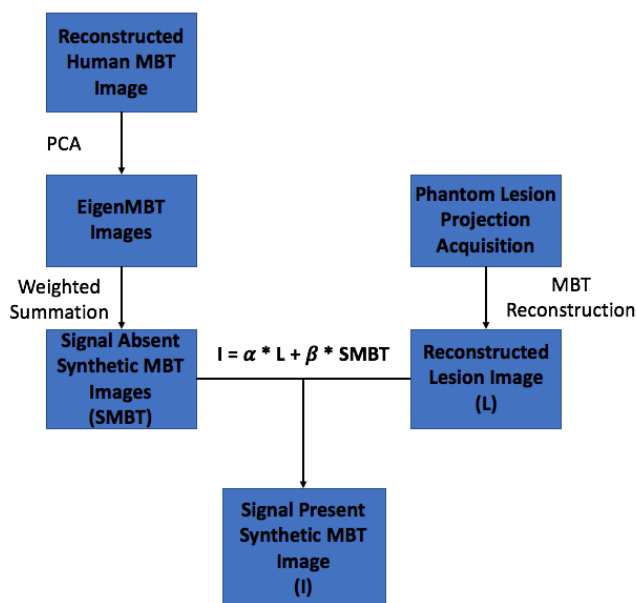


Figure 4-9: Workflow for creating signal present synthetic MBT images. Here spherical acrylic lesion phantoms were used to mimic the shape and size of true lesions. These lesion phantoms were then scanned and reconstructed under the same protocols as the human images then added to synthetic MBT images.

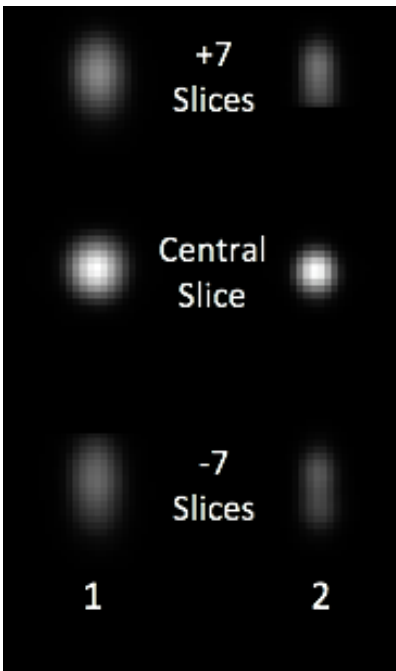


Figure 4-10: Displays different slices of the reconstructed lesion phantoms. 1) depicts the 1.2 cm diameter lesion, while 2) depicts the 0.8 cm lesion. The central (lesion in focus) slice of each lesion is displayed along with two slices depicting the residual blurring of the lesion outside its true location.

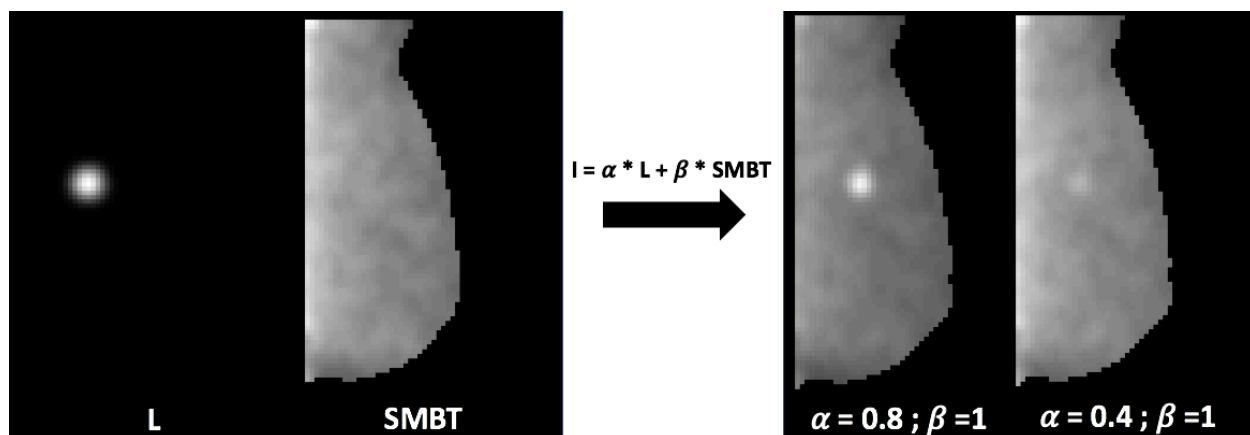


Figure 4-11: Displays the central slice of a lesion phantom (L) and a synthetic MBT (SMBT) image pre and post lesion insertion. The signal present synthetic MBT images created show how different weights can create more visible or subtle lesions.

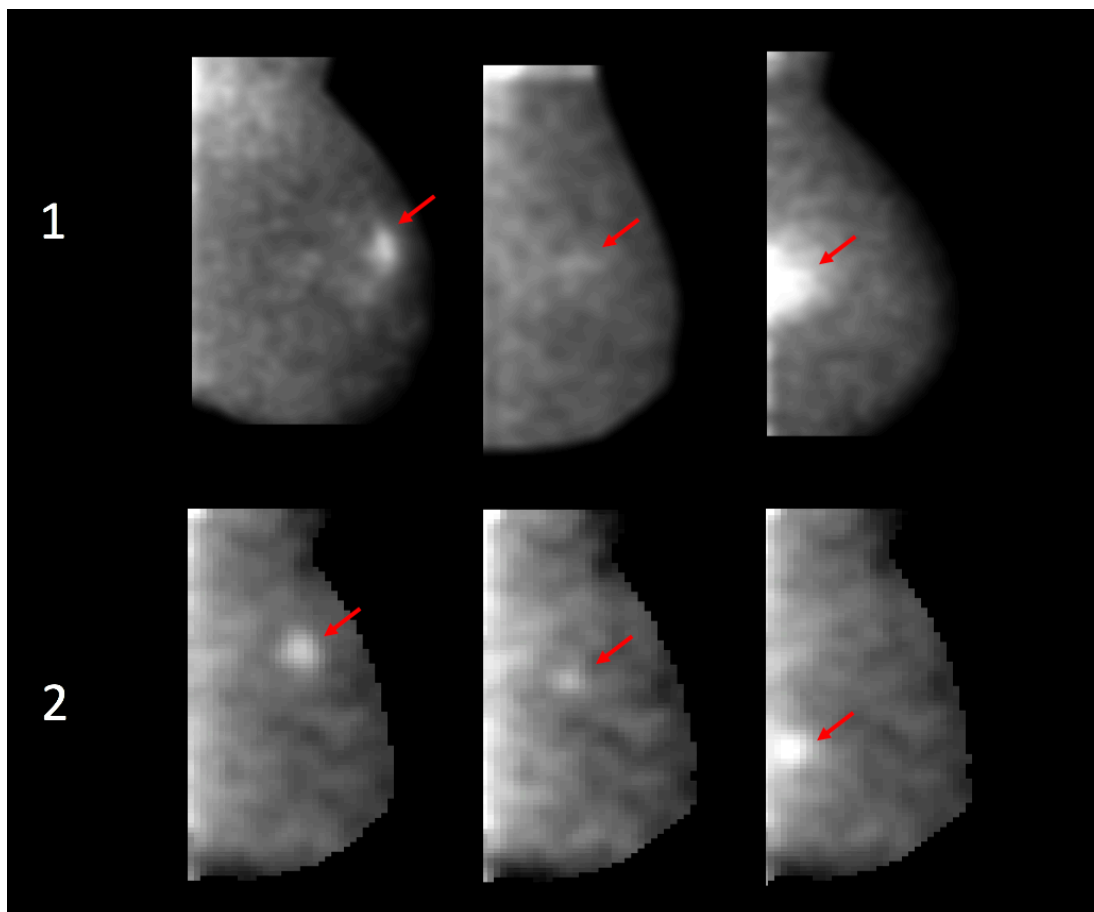


Figure 4-12: Images in row 1 are central slices of lesions in human MBT images depicting differences in lesion sizes, locations, and intensities. Row 2 depicts the central slices of signal present synthetic MBT images created to mimic the human lesions.

Lesions for the DBT synthetic images were biopsy proven masses taken from the set of DMT human images. A flow chart of the method can be seen in figure 4-13. In many cases, a real tumor will be segmented from reconstructed data<sup>24,25</sup>. This is not optimal in tomosynthesis data sets due to the residual blur of the lesion and surrounding breast tissue outside the slices of interest<sup>28</sup>. It becomes difficult to segment the lesion and its blurring without taking background noise and structure with it. To get around this issue, the lesions were segmented via pixel-value thresholding from the projection views of human images<sup>24</sup>. The thresholds were chosen by examining each projection view and measuring the mean pixel values on the edge of the tumor. High-density tumors were chosen to allow for more consistent lesion isolation. The isolated lesion projections were then reconstructed using the same reconstruction algorithm and parameters as the human images. Similar to the MBT images, the lesions were inserted in the synthetic DBT images via a weighted summation. Examples of an isolated lesion can be seen in figures 4-14. Figure 4-15 compares a couple signal present human DBT images with signal present synthetic DBT images.

With the addition of tumors to the synthetic DMT images, a complete model observer training set has been created.

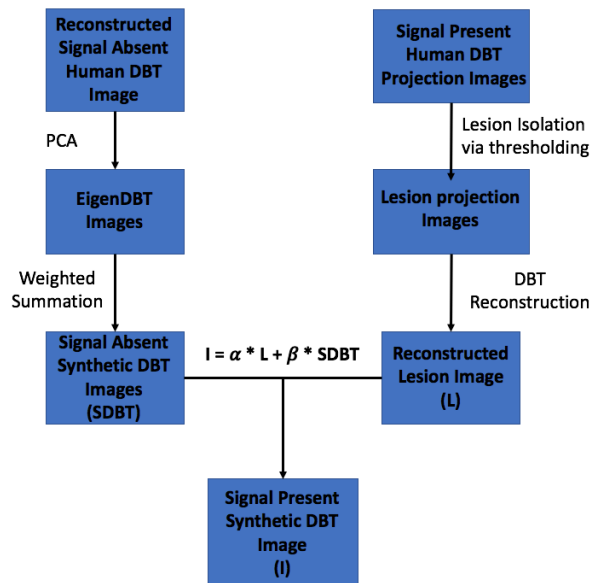


Figure 4-13: Workflow for creating signal present synthetic DBT images. Here lesions are isolated using a threshold method from signal present human DBT projection images. The isolated lesion projection images are then reconstructed and added to synthetic DBT images.

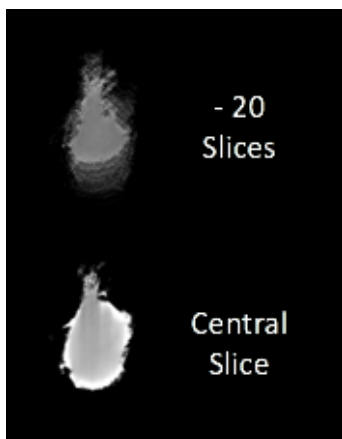


Figure 4-14: Displays a human tumor isolated via pixel thresholding.

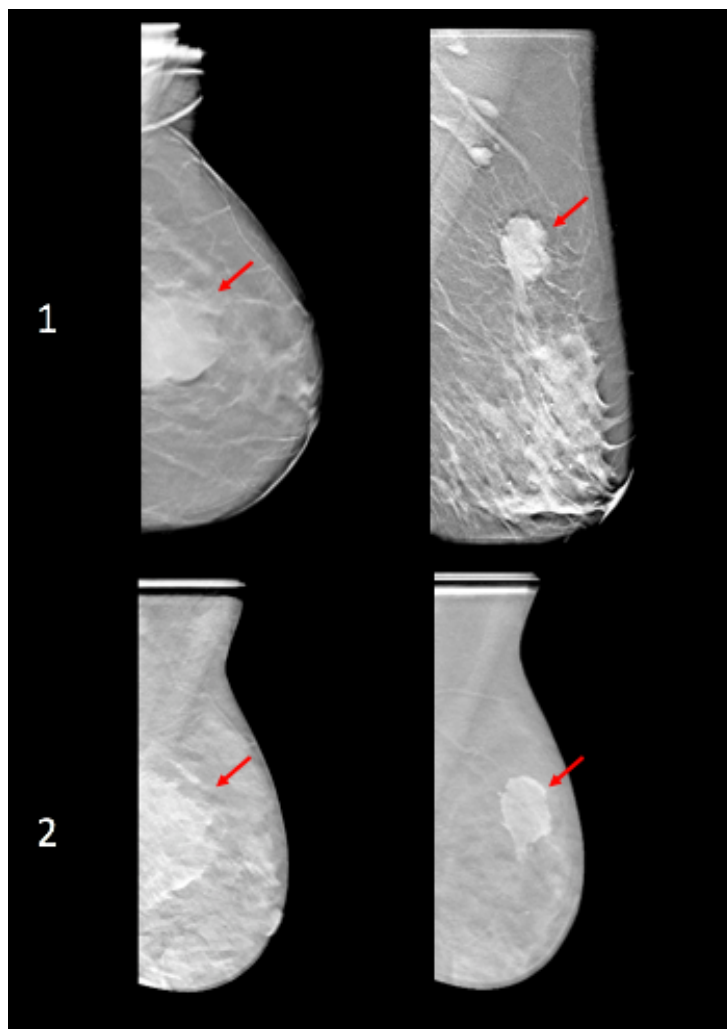


Figure 4-15: Images in row 1 are central slices of lesions in human DBT images. The lesions from row 1 were isolated from the human images and inserted into synthetic DBT images, seen in row 2.

## 4.5 Conclusion

A training set of realistic synthetic images were created for use with model observers under development in our lab. The background noise and structure of the images mimic those of the human data taken with the DMT scanner, with a subset of those images having inserted lesions. However, these are first generation synthetic images. Future work can improve upon a couple aspects. First, different shape and sized eigenimages can be created using image deforming mathematical models (such as finite element analysis), as opposed to using image masking. This would allow the model observers to be trained with a data set that simulates the true variability in human breast size and shape. Second, more sophisticated lesion segmentation methods could be utilized to acquire more subtle and complicated lesion types for the DBT data. Similarly, more complicated phantoms could be used for the MBT images. These phantoms could be larger and irregular in shape to represent linear or more diffuse lesion types.

## References

- 1 Barrett HH, Yao J, Rolland JP, Myers KJ. Model observers for assessment of image quality. *PNAS* 1993;**90**:9758–65.
- 2 Myers KJ, Barrett HH. Addition of a channel mechanism to the ideal-observer model. *J Opt Soc Am A, JOSAA* 1987;**4**:2447–57. <https://doi.org/10.1364/JOSAA.4.002447>.
- 3 He X, Park S. Model Observers in Medical Imaging Research. *Theranostics* 2013;**3**:774–86. <https://doi.org/10.7150/thno.5138>.
- 4 Barrett HH, Myers KJ. *Foundations of Image Science*. John Wiley & Sons; 2013.
- 5 Park S, Zhang G, Myers KJ. Comparison of Channel Methods and Observer Models for the Task-Based Assessment of Multi-Projection Imaging in the Presence of Structured Anatomical Noise. *IEEE Transactions on Medical Imaging* 2016;**35**:1431–42. <https://doi.org/10.1109/TMI.2016.2515027>.
- 6 Burgess AE, Jacobson FL, Judy PF. Human observer detection experiments with mammograms and power-law noise. *Med Phys* 2001;**28**:419–37. <https://doi.org/10.1118/1.1355308>.
- 7 Jolliffe I. Principal Component Analysis. *International Encyclopedia of Statistical Science*. Springer, Berlin, Heidelberg; 2011. p. 1094–6.
- 8 Abdi H, Williams LJ. Principal component analysis. *Wiley Interdisciplinary Reviews: Computational Statistics* 2010;**2**:433–59. <https://doi.org/10.1002/wics.101>.
- 9 Taylor J. *Introduction to Error Analysis, the Study of Uncertainties in Physical Measurements, 2nd Edition*. 1997.
- 10 Sirovich L, Kirby M. Low-dimensional procedure for the characterization of human faces. *J Opt Soc Am A, JOSAA* 1987;**4**:519–24. <https://doi.org/10.1364/JOSAA.4.000519>.
- 11 Turk M, Pentland A. Eigenfaces for Recognition. *Journal of Cognitive Neuroscience* 1991;**3**:71–86. <https://doi.org/10.1162/jocn.1991.3.1.71>.
- 12 Berks M, Caulkin S, Rahim R, Boggis C, Astley S. Statistical Appearance Models of Mammographic Masses. Presented at the International Workshop on Digital Mammography.
- 13 Rose CJ, Taylor CJ. A Statistical Model of Texture for Medical Image Synthesis and Analysis. *Medical Image Understanding and Analysis 2003*. BMVA; 2003.
- 14 Sturgeon GM, Park S, Segars WP, Lo JY. Synthetic breast phantoms from patient based eigenbreasts. *Medical Physics* n.d.;**44**:6270–9. <https://doi.org/10.1002/mp.12579>.
- 15 Williams MB, Mangiafico PA, Simoni PU. Noise power spectra of images from digital mammography detectors. *Med Phys* 1999;**26**:1279–93. <https://doi.org/10.1118/1.598623>.
- 16 Burgess AE. Mammographic Structure: Data Preparation and Spatial Statistics Analysis. Presented at the Medical Imaging 1999: Image Processing.
- 17 Cockmartin L, Bosmans H, Marshall NW. Comparative power law analysis of structured breast phantom and patient images in digital mammography and breast tomosynthesis. *Medical Physics* n.d.;**40**:081920. <https://doi.org/10.1118/1.4816309>.
- 18 Metheany KG, Abbey CK, Packard N, Boone JM. Characterizing anatomical variability in breast CT images. *Medical Physics* n.d.;**35**:4685–94. <https://doi.org/10.1118/1.2977772>.
- 19 Bakic PR, Zhang C, Maidment ADA. Development and characterization of an anthropomorphic breast software phantom based upon region-growing algorithm. *Medical Physics* n.d.;**38**:3165–76. <https://doi.org/10.1118/1.3590357>.
- 20 Kiarashi N, Nolte AC, Sturgeon GM, Segars WP, Ghate SV, Nolte LW, *et al*. Development of realistic physical breast phantoms matched to virtual breast phantoms based on human subject data. *Medical Physics* n.d.;**42**:4116–26. <https://doi.org/10.1118/1.4919771>.
- 21 Dolly S, Chen H-C, Anastasio M, Mutic S, Li H. Practical considerations for noise power spectra estimation for clinical CT scanners. *Journal of Applied Clinical Medical Physics* n.d.;**17**:392–407. <https://doi.org/10.1120/jacmp.v17i3.5841>.

- 22 Pezeshk A, Petrick N, Chen W, Sahiner B. Seamless Lesion Insertion for Data Augmentation in CAD Training. *IEEE Transactions on Medical Imaging* 2017;**36**:1005–15. <https://doi.org/10.1109/TMI.2016.2640180>.
- 23 Peskin AP, Dima AA. Modeling Clinical Tumors to Create Reference Data for Tumor Volume Measurement. Presented at the International Symposium on Visual Computing.
- 24 Robins M, Solomon J, Sahbaee P, Sedlmair M, Choudhury KR, Aria Pezeshk, *et al*. Techniques for virtual lung nodule insertion: volumetric and morphometric comparison of projection-based and image-based methods for quantitative CT. *Phys Med Biol* 2017;**62**:7280. <https://doi.org/10.1088/1361-6560/aa83f8>.
- 25 Chen B, Leng S, Yu L, Yu Z, Ma C, McCollough C. Lesion insertion in the projection domain: Methods and initial results. *Medical Physics* n.d.;**42**:7034–42. <https://doi.org/10.1118/1.4935530>.
- 26 Doshi NK, Basic M, Cherry SR. Evaluation of the detectability of breast cancer lesions using a modified anthropomorphic phantom. *J Nucl Med* 1998;**39**:1951–7.
- 27 Carton A-K, Bakic P, Ullberg C, Derand H, Maidment ADA. Development of a physical 3D anthropomorphic breast phantom. *Medical Physics* n.d.;**38**:891–6. <https://doi.org/10.1118/1.3533896>.
- 28 III JTD, Godfrey DJ. Digital x-ray tomosynthesis: current state of the art and clinical potential. *Phys Med Biol* 2003;**48**:R65. <https://doi.org/10.1088/0031-9155/48/19/R01>.

## Chapter 5

# Characterization of Low Profile 20 x 25 cm NaI(Tl) Gamma Camera for Dedicated Breast Tomosynthesis

### 5.1 Introduction

Over the last 20 years, research has demonstrated the value of compact high resolution gamma cameras for dedicated nuclear medicine breast imaging as a means of mitigating the lack of resolution and sensitivity of standard large cameras<sup>1-5</sup>. Three main types of gamma cameras are currently being implemented: scintillation cameras with position sensitive photomultiplier tubes (PSPMTs) for PET and SPECT, scintillation cameras using silicon photomultipliers (SiPMs) for PET, and solid state direct-conversion semiconductor cameras for PET and SPECT. PSPMT based gamma cameras for breast imaging typically contain a pixelated array of sodium iodide (NaI) or cesium iodide (CsI) crystals, in which confinement of the scintillation light to individual crystals allows for a smaller dead space at the chest wall edge of the detector compared to single-crystal designs<sup>2,6</sup>. SiPMs are high gain integrated arrays of parallel avalanche diodes that operate in Geiger mode and are compact alternatives to bulkier PMTs. They have been successfully used in dedicated breast PET applications in which the 511 keV annihilation photons result in a large number of light photon from the crystal. However their larger electron multiplication gain variance and resulting poorer energy resolution compared to PMTs has limited their application in lower energy single gamma systems to date<sup>7-9</sup>. The most commonly used solid-state semiconductor is cadmium zinc telluride (CZT). CZT arrays exhibit good gamma ray detection efficiency and have been shown to have very good energy resolution<sup>5,10-12</sup>, but suffer from low energy tailing due to hole trapping. CZT systems are currently available from a small number of sources at a great cost for low-defect samples.

The PSPMT-based scintillation camera described here was developed as a replacement for a gamma camera used in a dual modality tomosynthesis system (DMT). The DMT system consists of an x-ray transmission component and a gamma-ray emission component, each performing limited angle tomographic imaging and sharing a common breast immobilization system allowing for unambiguous correlation between radiotracer distribution and anatomic structures in the breast (Figure 5-1). The main design considerations for the new gamma camera were to a) increase the field of view (FOV) from 15 cm x 20 cm to 20 cm x 25 cm, in order to better match the 23 cm x 29 cm FOV of the DMT system's x-ray detector, b) improve system sensitivity and overall imaging performance, and c) decrease the camera thickness, allowing for better camera positioning and patient comfort.



Figure 5-1: Dual Modality Tomosynthesis system (DMT). X-ray tube, gamma camera, and x-ray detector are on a single gantry arm which rotates around an independent breast compression system. This allows for x-ray and gamma image registration. The gamma camera shown in this photo is the older, thicker one.

## 5.2 Methods

### 5.2.1 Camera Design

The low profile (LP) gamma camera contains a pixelated NaI(Tl) scintillator with a crystal size of 1.95 mm by 1.95 mm and 6 mm thick with a crystal pitch of 2.2 mm. The overall active area is 250.5 mm x 199.9 mm. The crystal array's 6.5 mm thick window is optically coupled to a 4 x 5 array of 5 cm x 5 cm Hamamatsu H8500C PSPMTs. In order to compensate for gain variations among the PSPMTs, reduce the number of data channels necessary for readout, and add signal amplification, the manufacturer-provided connector board of each PSPMT was replaced with customized gain matching X-Y conversion board (Figure 5-2a) (Ray Visions, Inc., Yorktown, VA USA). Each customized board contains a gain-matching resistor matrix based on the manufacturer-provided gain map of each PSPMT. The board reduces the 64 channel readout of the 8 x 8 electrode anode array of each H8500C to 16 channels (8X and 8Y) by connecting the rows and columns of the PSPMT anodes. The custom boards reduce the total height of each PSPMT module from 37.7 mm to 27.8 mm (Figure 5-2b). The final total height of the PSPMTs, matrix/gain matching boards, and amplifier/summing board with connectors comes to 37.8 mm, almost exactly the same as the original raw PSPMT height. This is a reduction of almost 2 cm (30%) from our previous PSPMT/electronics configuration.

The X and Y outputs of each board are connected in a lattice framework that is read out along two edges of the camera (40 X by 32 Y) and coupled to an amplifier/summing board. Each signal goes through a low-noise pre-amplification stage followed by a second amplification stage and then sent out of the detector head on shielded ribbon cables. All of 40 X signals are also summed and, after discrimination, used as detector trigger. The signals on the shielded ribbon cables are sent to MDU40-GI32 multichannel integrating ADCs (AiT Instruments, Newport News, VA), see (Figure 5-3a,b). The camera employs a parallel hole collimator with a hexagonal hole height of 18.4 mm, septal thickness of 0.26 mm, and face-to-face diameter of 1.9 mm (Figure 5-

3c). Before characterization, the LP gamma camera went through a calibration process consisting of measuring the pedestals of each ADC channel, mapping the locations of the pixelated crystals in the raw images, and obtaining crystal-specific pulse height spectra to produce a gain correction lookup table. To determine the ADC pedestals, triggers were generated with the PSPMT high-voltage supply turned off. This was repeated multiple times to test pedestal stability. For crystal mapping a high statistics raw image was obtained using a Tc-99m source (Figure 5-4). Once the crystals were mapped, the energy calibration was completed. Characterization of the system's imaging properties was performed according to both NEMA NU-1 standards and commonly published gamma camera characterization methodologies<sup>1,2,13</sup>.

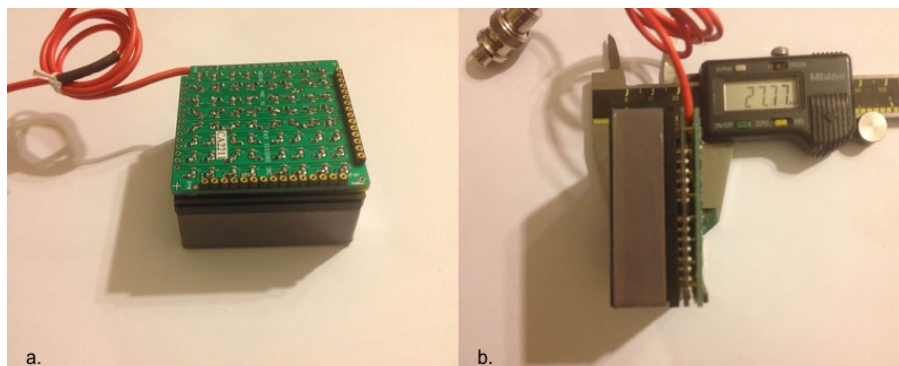


Figure 5-2: a) H8500C PSPMT with customized circuit board attached. b) Total thickness of final PSPMT module is less than 3 cm.

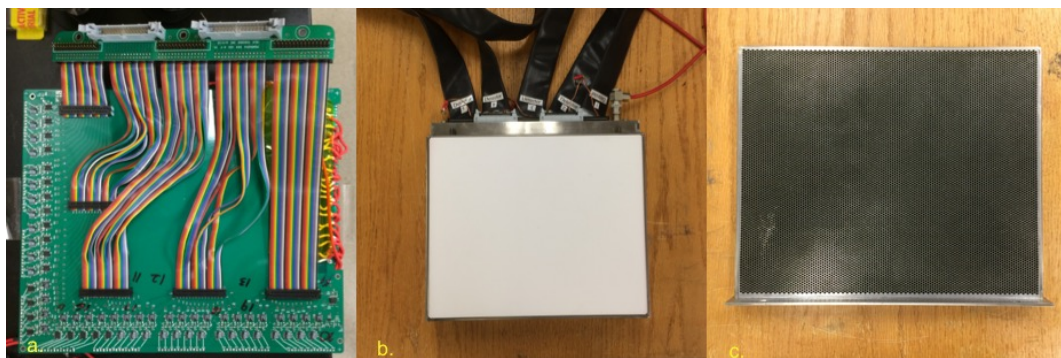


Figure 5-3: a) Camera circuit board showing readout of the 72 X and Y outputs and conversion to ribbon cables. b) Final LP gamma camera assembly. c) LP gamma camera parallel hole collimator.

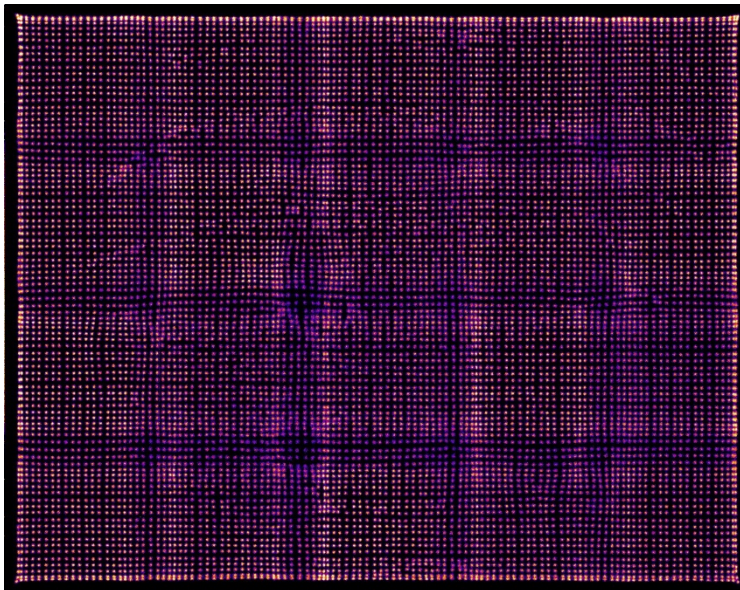


Figure 5-4: Raw flood image used for crystal mapping.

## 5.2.2 Energy Resolution

Good energy resolution permits sensitive rejection of scattered gamma-rays. The energy resolution is dependent primarily on the light output of the scintillator array and the quantum efficiency and gain characteristics of the PSPMTs. To measure the energy resolution a Tc-99m point source at a distance of 125 cm from the camera face was used to flood the entire field of the gamma camera (with the collimator removed) for a sufficient period of time for an individual pulse height distribution to be obtained for each crystal. In each crystal's spectrum the 140 keV photopeak was identified and used to create a lookup table of relative gains. The combined energy spectrum was obtained by summing the individual crystal spectra after normalization by the relative gain factors so that the centers of the photopeaks fell in the same spectral bin (Figure 5-5a). This experiment was then repeated with a Co-57 and Am-241 source. A plot of peak energy versus bin number was created and fit linearly to find a calibration factor (keV per bin) (Figure 5-5b). The energy resolution is reported as the full width at half maximum (FWHM) of the photopeak in bins multiplied by the calibration factor then divided by the center photopeak energy of Tc-99m of 140.5 keV<sup>13</sup>.

$$\text{energy resolution} = \frac{(FWHM * CF)}{140.5 \text{ keV}} \quad (5-1)$$

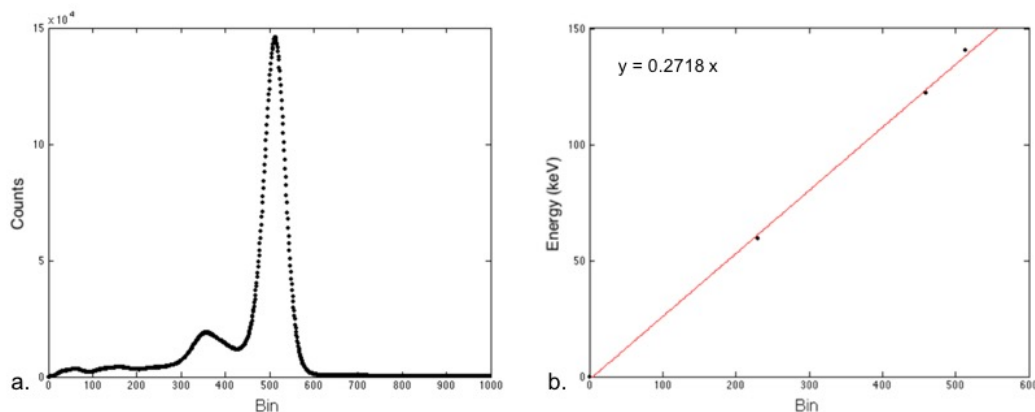


Figure 5-5: a) combined and corrected for non-uniformity energy spectrum for Tc-99m source. b) plot of the energy spectrum's peak bin number versus the known photon energies of Am-241 (59.4 keV), Co-57 (122.1 keV), Tc-99m (140 keV), and the fitted linear regression used to calculate the energy calibration factor.

### 5.2.3 Intrinsic Uniformity

Mapped gamma camera images are corrected for spatially dependent camera sensitivity non-uniformities using a high-statistics correction image obtained under conditions of uniform gamma ray fluence. To correct sensitivity non-uniformities, the raw image is divided on a pixel-by-pixel basis by the high statistics flood image, which has been normalized by dividing each pixel value by the average pixel value. The correction image is acquired with a minimum of 10,000 counts per channel, in order to minimize the effect on the corrected image of added statistical noise. The NEMA protocol requires that the uniformity of both the useful field of view (UFOV) and the central field of view (CFOV) are reported. The UFOV for this gamma camera is 250.5 mm x 199.9 mm (the full active area of the crystal array). The CFOV is defined as the central 56.3% of the UFOV area (75% of each UFOV dimension), which in this case is 187.8 mm x 149.9 mm. To test the camera's intrinsic uniformity, the collimator was removed and a Tc-99m point source was placed at a distance of 125 cm from the camera.

For both the UFOV and CFOV both integral and differential non-uniformity were calculated and are reported in accordance to the NEMA protocol. To calculate the integral uniformity, the maximum and minimum pixels for each FOV are found. The integral non-uniformity is defined as the difference between the maximum and minimum pixel values, divided by the sum of the maximum and minimum pixels and it is reported as a percentage (Eqn. 5-2). Differential non-uniformity is calculated by finding the largest difference between any two pixels within a set of 5 contiguous pixels in a row or column. The differential uniformity is then defined has the same form as equation 5-2; however, the maximum and minimum pixel values are selected with in the 5 contiguous pixels as opposed to the entire FOV. This is done for both the X and Y directions for each column and the maximum value is reported for each direction <sup>13</sup>.

$$Integral\ Uniformity = \frac{(p_{max} - p_{min})}{(p_{max} + p_{min})} x \pm 100 \quad (5-2)$$

The integral and differential uniformity only report the largest non-uniformities in an image. To gain an understanding of the trends in the non-uniformities over the entire FOV, the magnitudes of all the differential uniformity measurements were plotted.

## 5.2.4 Intrinsic Geometric Linearity

The primary source of geometric non-linearity in detectors with tiled PSPMTs is biasing of the measured scintillator light centroid position due to the way that the scintillation light is shared between more than one PSPMT near PSPMT edges. Additional distortions are caused by truncation of the amplified charge pulse near the PSPMT perimeters. Figure 5-4 shows a high-resolution raw image made with a uniform gamma ray illumination. The clustering of the detected events is caused by the light piping effect of the individual crystals. The clusters do not lie along straight row and column lines because of the light sharing and charge truncation effects. However, these distortions can be corrected by mapping the events of each cluster onto a regular matrix corresponding to the known locations of each crystal in the array, leaving only a few small non-linearities associated with any array imperfections (Figure 5-6). The residual geometric distortions following crystal mapping were measured with a 0.5 mm slit created using a lead mask. The slit was placed in the center of the UFOV and was positioned at a 45-degree angle<sup>2</sup>. A Tc-99m point source was placed at a distance that permitted illumination of the entire slit. The spatial differential linearity was calculated by fitting a linear regression to the peak points of the data and the original data points were then subtracted from the fitted line.

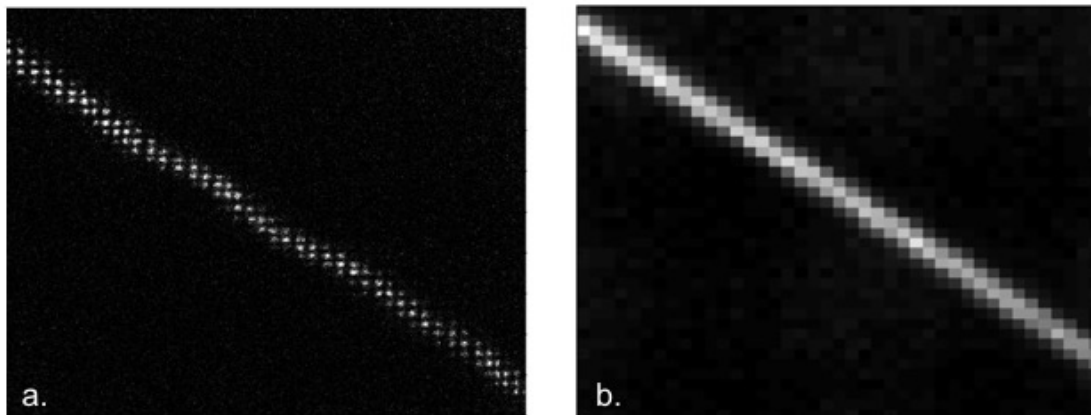


Figure 5-6: a) Raw image of the slit before crystal mapping. Here the non-linearities due to the clustering of the detected events can be seen. b) Corrected image after crystal mapping.

## 5.2.5 Spatial Resolution

### 5.2.5.1 Intrinsic

The lower limit on the intrinsic (no collimator) spatial resolution of gamma cameras with pixelated crystals gamma cameras is set by the crystal pitch, however, the resolution is degraded by gamma-ray scattering, which can deposit energy in more than one crystal. Resolution is also degraded by optical crosstalk between crystals and by the spatial resolution of the photomultipliers. To measure the intrinsic spatial resolution a 0.25 mm wide, 4 mm thick lead slit placed directly on the detector input surface was used. The gamma camera was irradiated with a Tc-99m point source positioned at a distance of 125 cm. The slit was oriented at a slight angle with respect to the crystal array matrix so that the offset between the line source midline and the crystal centers varied along the length of the slit source. By subsampling profiles extracted along rows, and shifting them to align the centers of the slit image, the profiles could be summed to yield a spatially averaged line spread function (LSF)<sup>2</sup>. The averaged LSF was fitted with a Gaussian curve, using MATLAB's gauss fit function, and the FWHM and FWTM were reported<sup>13</sup>.

### 5.2.5.2 Extrinsic

Due to the collimator's geometric spatial resolution the extrinsic resolution (with collimator) of the gamma camera is lower than the intrinsic resolution. Because, unlike the intrinsic resolution, the collimator resolution varies with the source-to-collimator distance, the extrinsic spatial resolution was measured as a function of the source-to-collimator separation. In accordance with the NEMA protocol the resolution both with and without scatter were measured. For the resolution without scatter, a small diameter capillary tube (inside diameter of 0.9 mm) filled with a Tc-99m solution was moved away from the collimator in 1 cm steps for 10 cm. For each source-to-collimator distance the capillary tube was moved laterally at 2 mm steps for 10 mm. For each height, the FWHM and FWTM of each of the lateral positions were found via Gaussian fits and averaged to obtain the average spatial resolution. To obtain a measurement of spatial resolution including the effects of scatter a 10 cm block of acrylic was placed between the source and the collimator. Only one source distance was measured for this resolution, but as before the source was moved laterally at 2 mm steps over 10 mm with the final resolution reported as an average of the FWHM of the lateral positions <sup>13</sup>.

### 5.2.6 System Sensitivity

The largest factors affecting the camera sensitivity are the geometric collimator sensitivity, the absorption efficiency of the crystal material, the open area fraction of the crystal array, and dead time created by the system's electronics and acquisition software. The sensitivity was measured according to the NEMA protocol. The bottom of a 138 mm diameter petri dish was filled with 2 mm of water. A Tc-99m saline solution, whose activity was such that the total count rate was below 30,000 counts per second, was added to the petri dish. A 20% energy window centered at 140 keV was used. The petri dish was placed 10 mm away from the collimator surface at the center of the FOV and over 4 million counts were obtained. There was no scatter material present. For each data set, all the counts in the image were summed and the decay-corrected count rate was found. The decay-corrected count rate was then divided by the total activity in the petri dish

<sup>13</sup>.

### 5.2.7 SNR Experiment

Gelatin breast phantoms were used to compare the detectability, under the Rose criterion, of a range of lesions sizes between the new LP camera and the original camera. A gelatin mixture of 25 g of gelatin powder and 700 ml of water were uniformly mixed with a Tc-99m water solution to create the phantom background. The background was poured into a breast mold and put into a freezer for curing (Fig. 5-7). Three lesions were created using water absorbing beads made of a silicon polymer. These beads allow for custom lesion sizes to be made and allow for the elimination of the thin acrylic barrier, a source of scatter, typically used with fillable lesions. The lesion volumes used were 0.5, 0.25, and 0.125 ml (Fig. 5-7). Each lesion was designed to have a 20:1 lesion-to-background ratio (LBR) based off of MBI studies performed at the Mayo Clinic <sup>14,15</sup>. Before the gelatin phantom fully cured the three lesions were placed in the gelatin phantom. Once cured the gelatin phantom was placed on a rotational stage and simultaneously scanned with both cameras. Two data sets were taken the first scan was 2 minutes per position (to simulate a human scan) and the second 10 minutes per position (for higher counting statistics). The phantom was rotated from +20-degrees to -20-degrees in 10-degree steps in both data sets to simulate a human scan.

The images were then reconstructed using the same ML-EM reconstruction algorithm used to reconstruct the human images<sup>16</sup>. SNR values were calculated for both 2D projection view and 3D reconstructed data sets and were calculated as defined in chapter 2. Lesion counts were obtained from circular ROIs with diameters matching the known diameter of each lesion. The counts were obtained in the central slice of each lesion in the 3D data sets.

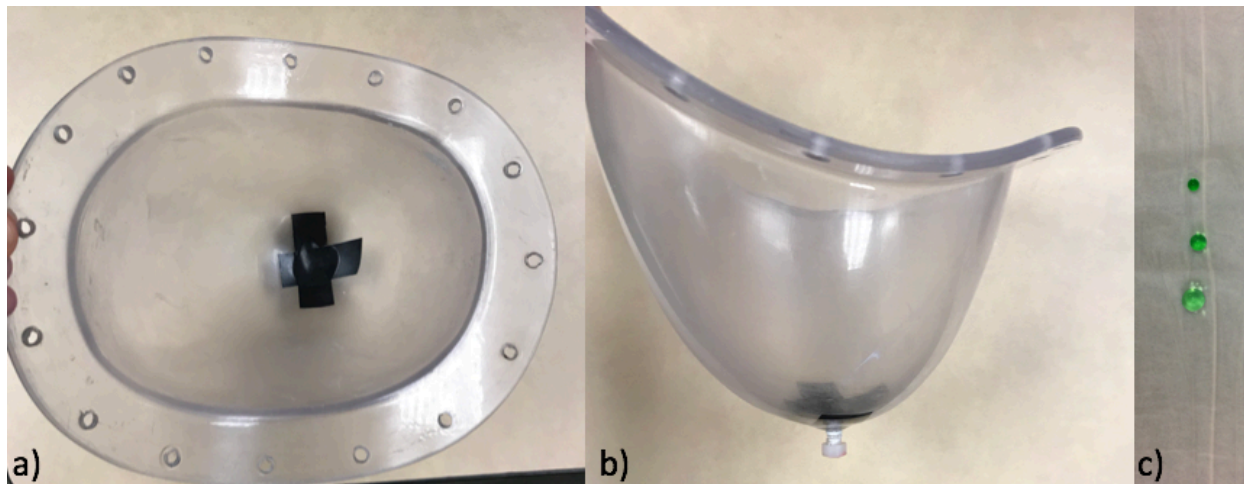


Figure 5-7: a) and b) shows a top view and side view of the breast mold. c) shows the 3 different sized lesions used. The volumes from top to bottom are: 0.125 ml, 0.25 ml, and 0.5 ml.

### 5.3 Results

Table 5-1: Results obtained for energy resolution, intrinsic uniformity, intrinsic spatial resolution, and system sensitivity.

Parameter	
<b>Energy Resolution:</b>	10.8%
<b>Integral Non-Uniformity:</b>	
UFOV	$6.7 \pm 0.4\%$
CFOV	$6.7 \pm 0.4\%$
<b>Differential Non-Uniformity:</b>	
UFOV-X direction	$4.7 \pm 0.1\%$
UFOV -Y direction	$4.1 \pm 0.6\%$
CFOV-X direction	$4.7 \pm 0.1\%$
CFOV-Y direction	$4.1 \pm 0.6\%$
<b>Intrinsic Spatial Resolution:</b>	
FWHM	$2.3 \pm 0.1$ mm
FWTM	$4.2 \pm 0.1$ mm
<b>System Sensitivity:</b>	$240 \pm 8$ cps/MBq

The results obtained for the energy resolution, intrinsic uniformity, intrinsic spatial resolution, and system sensitivity tests are summarized in Table 5-1. The results for the geometric linearity test are displayed in Figure 5-8. There was a maximum deviation from the theoretical straight line of 0.52 mm. The results of the extrinsic spatial resolution test are displayed in Figure 5-9. Both the FWHM and FWTM are displayed, along with the scatter resolution at 10 cm source-to-collimator distance.

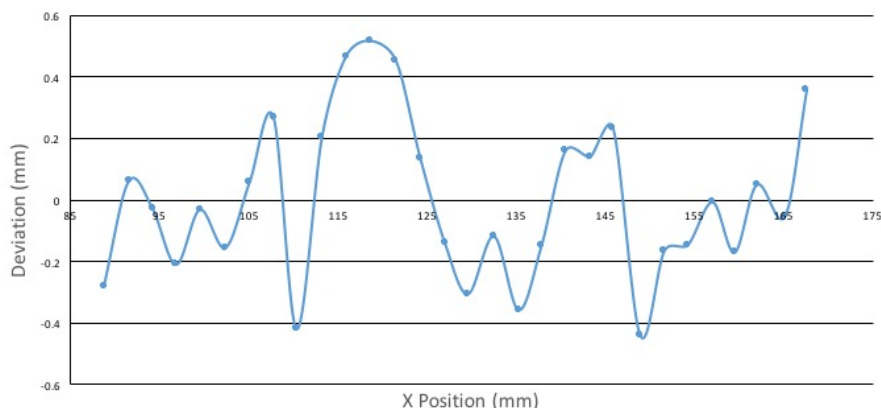


Figure 5-8: Deviation from linear fit of the image of the slit.

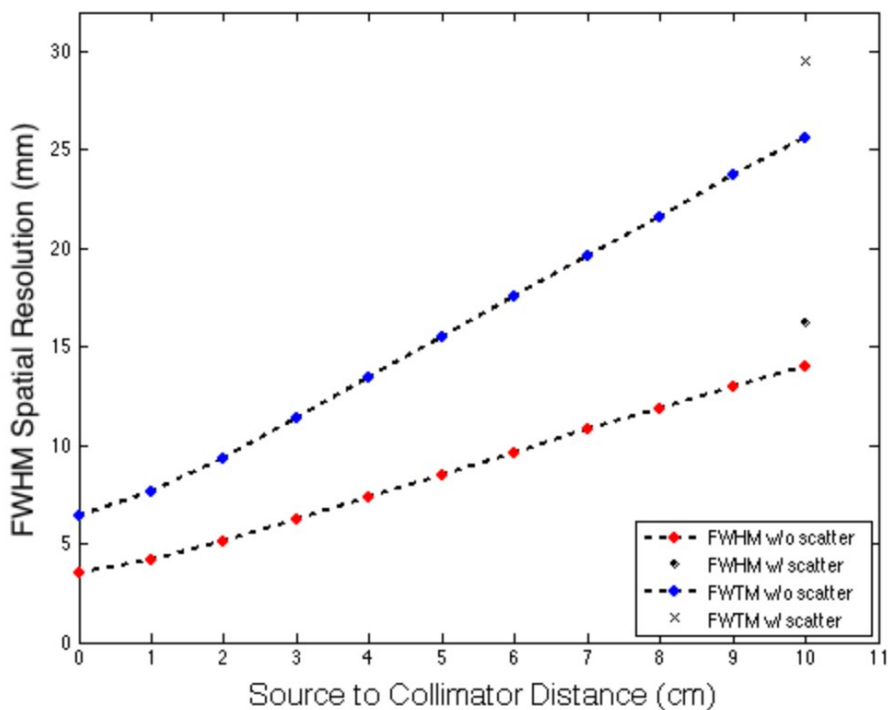


Figure 5-9: Results of extrinsic resolution. Source-to-collimator data was taken over 1 to 10 cm from the face of the collimator. Both the FWHM and FWTM can be seen here along with their corresponding resolutions with a 10 cm scatter phantom.

As seen in table 5-1, the max differential non-uniformities were the same for both the UFOV and the CFOV meaning the area with the largest non-uniformity lies in the COV. To better visualize this a 3D surface plots were created of the differential non-uniformities in the x-direction over the UFOV (Fig. 5-10).

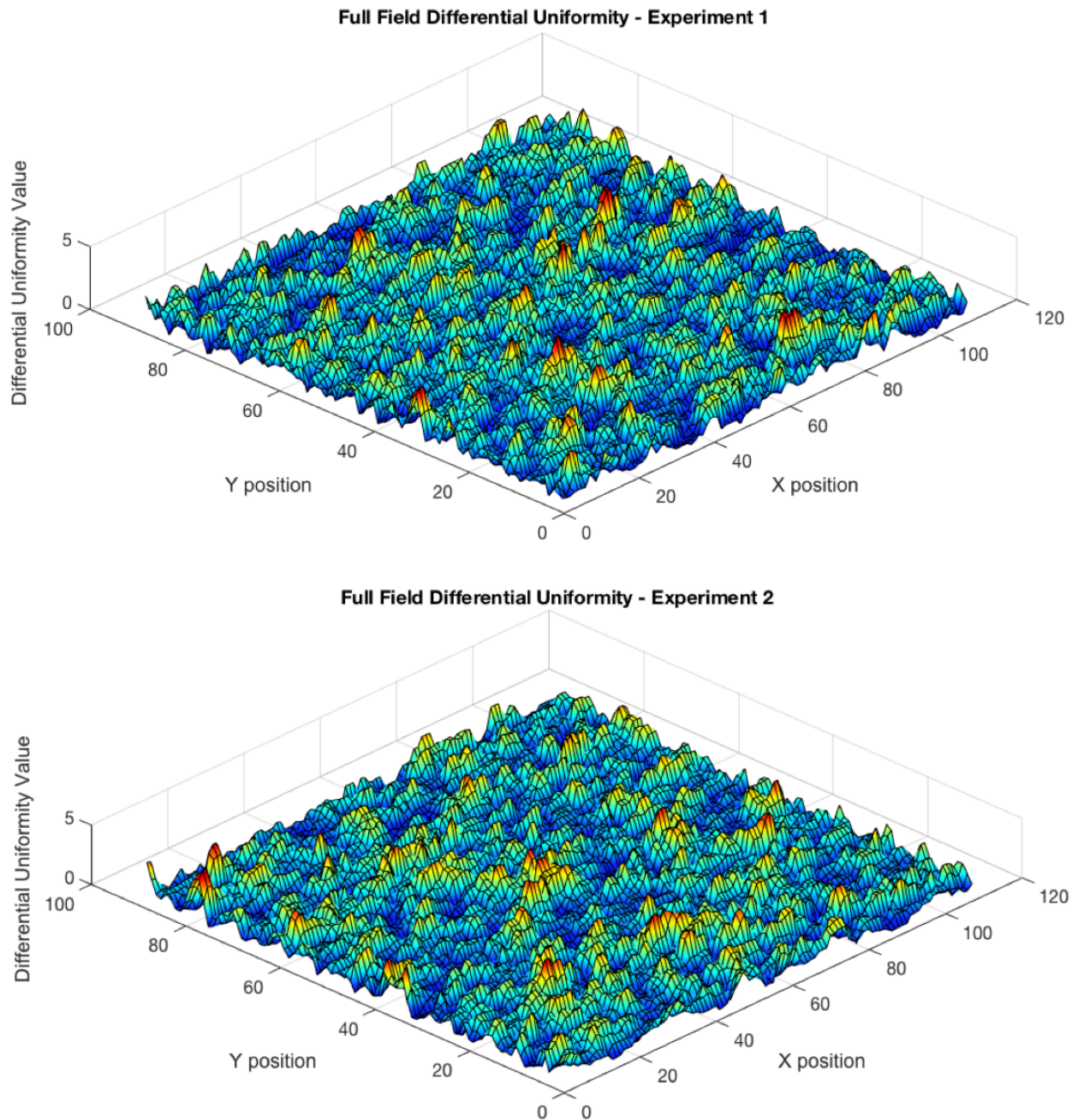


Figure 5-10: Surface plots for two of the differential non-uniformity experiments. Note the change in the positions of the peak non-uniformities.

Figures 5-11 shows the 2D 0° view projections of the SNR phantom for both cameras. Similarly, Figure 5-12 shows the central slice of the 3D reconstructions for both cameras. Table 5-2 lists the projection view calculated SNR values for the LP and original cameras along with the ratio between the LP camera and original cameras SNRs. Table 5-3 reports the same values as table 5-2 but for the central slice of the 3D data set.

Table 5-2: SNR values and SNR ratios for LP camera vs original camera 2D projection views.

	Lesion Size (ml)	2 min Scan			10 min Scan		
		0.5	0.25	0.125	0.5	0.25	0.125
SNR	LP Camera						
	0° projection	4.31	6.31	4.82	10.58	5.06	5.56
	10° projection	4.55	5.12	3.18	7.80	3.37	2.32
	20° projection	4.40	6.36	5.20	7.67	4.36	5.45
	Original Camera						
	0° projection	2.45	3.21	2.25	6.25	2.42	2.61
10° projection	2.62	2.98	1.33	4.79	1.57	1.15	
20° projection	2.57	3.05	2.26	4.05	2.08	2.60	
SNR <sub>LP</sub> /SNR <sub>old</sub>	0° projection	1.76	1.97	2.14	1.69	2.28	1.78
	10° projection	1.73	1.72	2.39	1.63	2.15	2.02
	20° projection	1.71	2.08	2.30	1.89	2.09	2.09

Table 5-3: SNR values and SNR ratios for LP camera vs original camera 3D data set.

	Lesion Size (ml)	2 min Scan			10 min Scan		
		0.5	0.25	0.125	0.5	0.25	0.125
SNR	LP Camera	39.39	35.58	34.74	36.73	35.41	32.35
	Original Camera	22.25	19.97	15.33	20.23	15.46	14.84
	SNR <sub>LP</sub> /SNR <sub>old</sub>	1.77	2.09	2.26	1.82	2.29	2.18

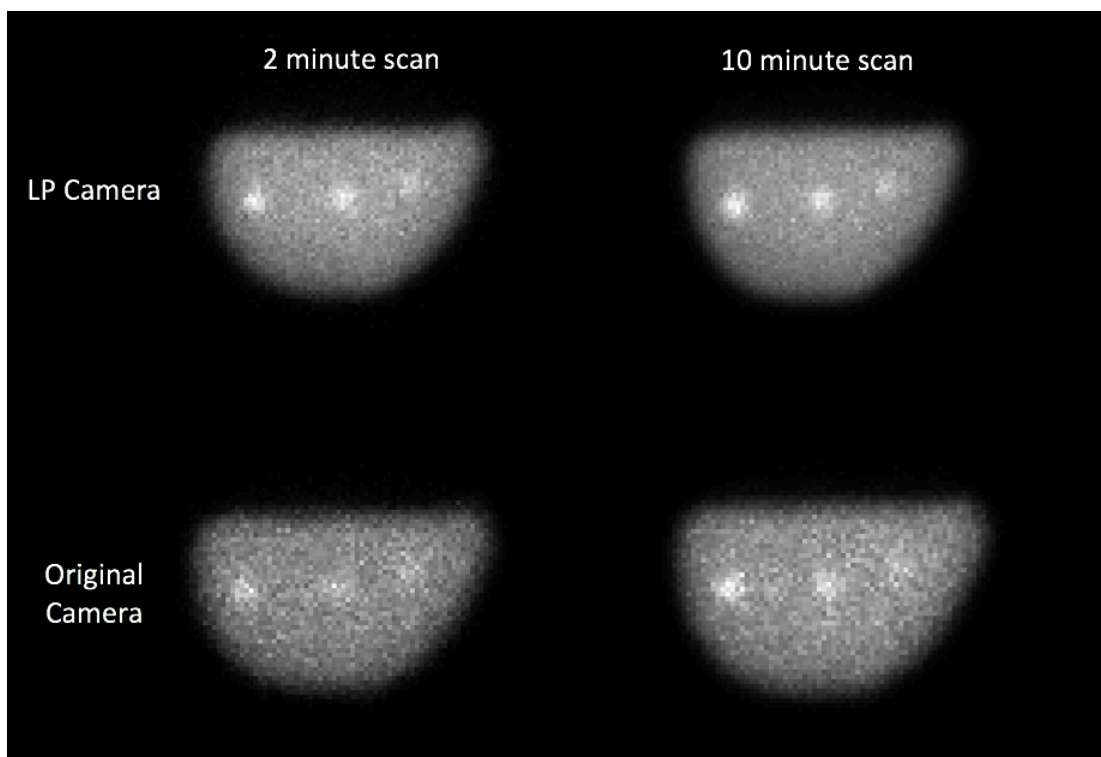


Figure 5-11: Images of the  $0^\circ$  projection view from the LP camera (top) and original camera (bottom).

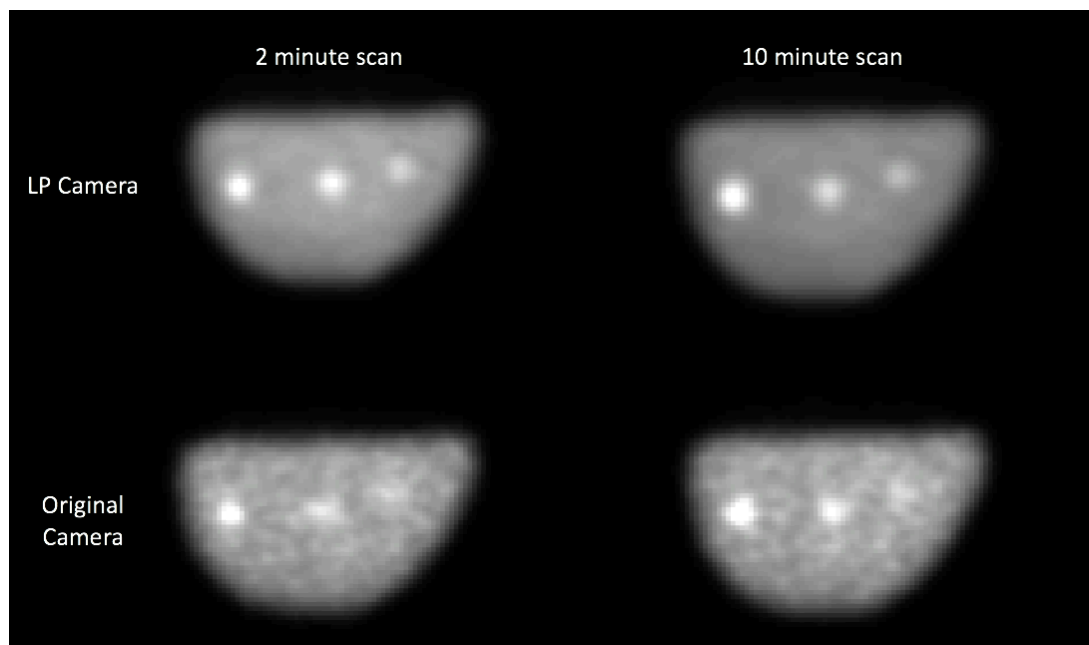


Figure 5-12: Images of the reconstructed central slice from the LP camera (top) and original camera (bottom).

## 5.4 Discussion

The new LP gamma camera was designed to be a superior alternative to the older thicker camera currently used on the DMT system in terms of overall size and imaging performance. Table 5-4 summarizes the comparison between the thicker gamma camera's and the LP gamma camera's dimensions and collimator parameters, while Table 5-5 summarizes the comparison between the cameras' primary imaging performance metrics: energy resolution, intrinsic spatial resolution, and system sensitivity.

Table 5-4: Comparison of thicker gamma camera and LP gamma camera dimensions and collimator parameters.

	Field of View (cm x cm)	Collimator hole length (mm)	Collimator hole diameter (mm)	Collimator septal thickness (mm)
<b>Thicker Camera</b>	15 x 20	21.5	1.9	0.3
<b>LP Camera</b>	20 x 25	18.4	1.9	0.26

Table 5-5: Comparison of imaging characteristics of the current thicker gamma camera and the new LP gamma camera.

Parameter	Thick Camera	LP Camera
<b>Energy Resolution:</b>	13.5%	10.8%
<b>Intrinsic Resolution: FWHM</b>	2.4 mm	2.3 mm
<b>System Sensitivity:</b>	142 cps/MBq	240 cps/MBq

The extrinsic resolution of the new camera was also compared to that of the older camera as reported by Gong et al<sup>17</sup>. Figure 5-13 shows the spatial resolution of both cameras plotted versus source-to-collimator distance. The shorter hole length for the LP camera results in slightly worse spatial resolution for large source-to-collimator distance but provides a factor of ~1.7 improvement in sensitivity.

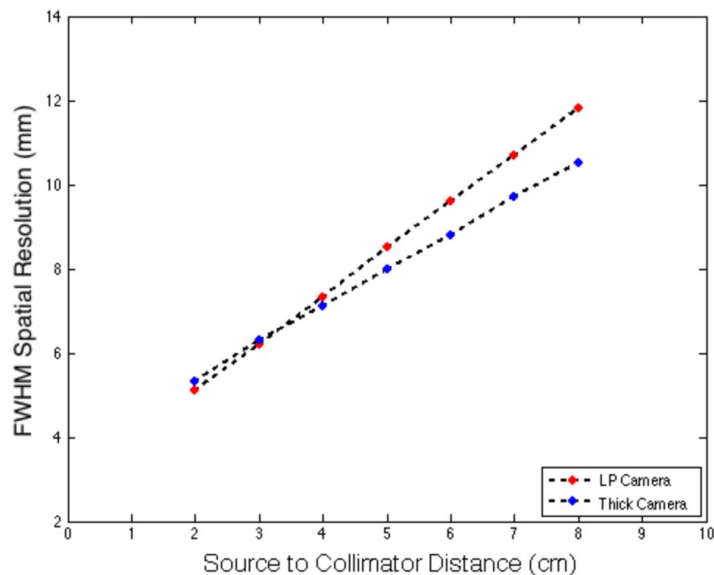


Figure 5-13: Comparison of extrinsic resolution between thicker camera and the LP camera.

Since SNR is proportional to the square root of the sensitivity, it is reasonable to expect an increase in SNR of at least 1.3x (for the LP camera over the original camera). The results show an increase of at least 1.6x in SNR for the LP camera compared to the old, but in many cases, it shows an increase of over 2x. This increase is most likely caused by variability in inter-PSPMT sensitivity in the older camera. Figure 5-14 shows two profiles taken through a row of crystals in raw flood images for each camera. It can be seen that there is roughly a 33% loss in sensitivity in crystals at points where two PSPMTs meet. This loss is even greater in areas where the corners of 4 PSPMTs meet. The sensitivity profile of the LP camera is more stable. This will lead to an increase in the cameras overall sensitivity and SNR ratio.

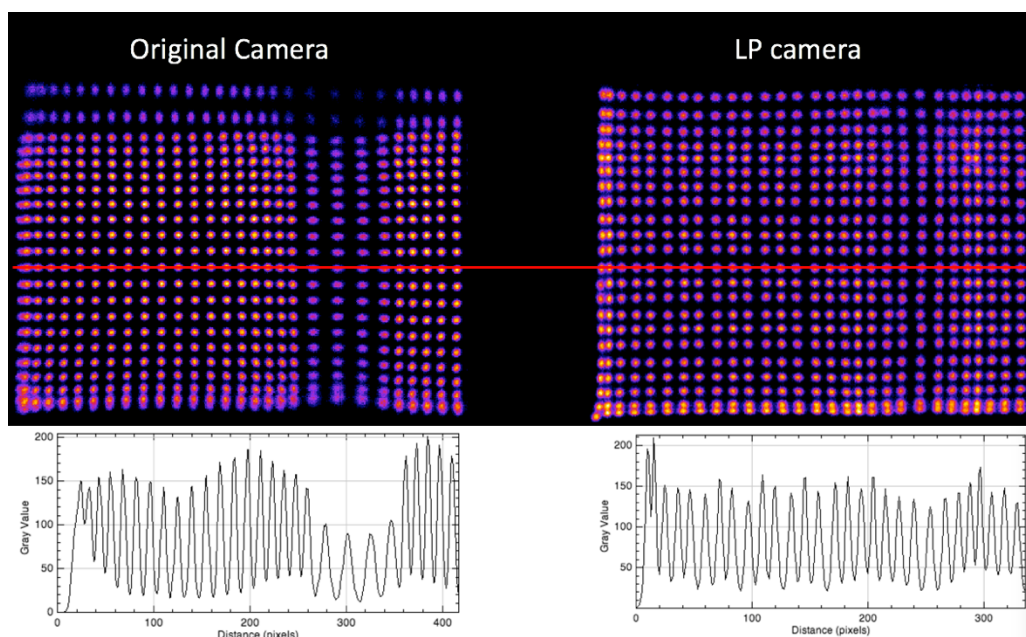


Figure 5-14: Profiles taken through raw data of flood image. Count loss is observed in the old camera due to low sensitivity between PSPMTs.

In addition to improved imaging performance in several aspects, the LP camera provides a thinner profile (8.3 cm thick versus 12.3 cm for the older camera) that permits better camera positioning and greater patient comfort (for example not needing to have the head turned to the side during imaging with the camera above the breast). Also, in addition to the larger nominal imaging FOV of the new camera, the clearer separation of the individual crystal locations in the raw image (see Figure 4) permits crystals all the way to the FOV periphery to be resolved, thus making a larger fraction of the nominal FOV usable. With these improvements in the useful FOV, the new camera permits a reconstructed molecular breast tomosynthesis volume that is similar in size to that of the x-ray tomosynthesis (DBT) component of the DMT scanner. This is important because the smaller of the two volumes sets the upper limit on the amount of breast tissue that can be visualized in the combined structural/functional image.

## References

- 1 Gruber GJ, Moses WW, Derenzo SE, Wang NW, Beuville E, Ho H. A discrete scintillation camera module using silicon photodiode readout of CsI(Tl) crystals for breast cancer imaging. *IEEE Transactions on Nuclear Science* 1998;**45**:1063–8. <https://doi.org/10.1109/23.681979>.
- 2 Williams MB, Goode AR, Galbis-Reig V, Majewski S, Weisenberger AG, Wojcik R. Performance of a PSPMT based detector for scintimammography. *Phys Med Biol* 2000;**45**:781. <https://doi.org/10.1088/0031-9155/45/3/315>.
- 3 Majewski S, Kieper D, Curran E, Keppel C, Kross B, Palumbo A, *et al.* Optimization of dedicated scintimammography procedure using detector prototypes and compressible phantoms. *IEEE Transactions on Nuclear Science* 2001;**48**:822–9. <https://doi.org/10.1109/23.940170>.
- 4 Moadel RM. Breast Cancer Imaging Devices. *Seminars in Nuclear Medicine* 2011;**41**:229–41. <https://doi.org/10.1053/j.semnuclmed.2010.12.005>.
- 5 Long Z, Connors AL, Hunt KN, Hruska CB, O'Connor MK. Performance characteristics of dedicated molecular breast imaging systems at low doses. *Medical Physics* 2016;**43**:3062–70. <https://doi.org/10.1118/1.4950873>.
- 6 More MJ, Goodale PJ, Majewski S, Williams MB. Evaluation of Gamma Cameras for Use in Dedicated Breast Imaging. Presented at the 2004 IEEE Nuclear Science Symposium Conference Record.
- 7 Dolgoshein B, Balagura V, Buzhan P, Danilov M, Filatov L, Garutti E, *et al.* Status report on silicon photomultiplier development and its applications. *Nuclear Instruments and Methods in Physics Research Section A: Accelerators, Spectrometers, Detectors and Associated Equipment* 2006;**563**:368–76. <https://doi.org/10.1016/j.nima.2006.02.193>.
- 8 Eckert P, Schultz-Coulon H-C, Shen W, Stamen R, Tadday A. Characterisation studies of silicon photomultipliers. *Nuclear Instruments and Methods in Physics Research Section A: Accelerators, Spectrometers, Detectors and Associated Equipment* 2010;**620**:217–26. <https://doi.org/10.1016/j.nima.2010.03.169>.
- 9 Degenhardt C, Prescher G, Frach T, Thon A, Gruyter R de, Schmitz A, *et al.* The Digital Silicon Photomultiplier #x2014; A Novel Sensor for the Detection of Scintillation Light. Presented at the 2009 IEEE Nuclear Science Symposium Conference Record (NSS/MIC).
- 10 Verger L, Gentet MC, Gerfault L, Guillemaud R, Mestais C, Monnet O, *et al.* Performance and perspectives of a CdZnTe-based gamma camera for medical imaging. *IEEE Transactions on Nuclear Science* 2004;**51**:3111–7. <https://doi.org/10.1109/TNS.2004.839070>.
- 11 Verger L, Boitel M, Gentet MC, Hamelin R, Mestais C, Mongellaz F, *et al.* Characterization of CdTe and CdZnTe detectors for gamma-ray imaging applications. *Nuclear Instruments and Methods in Physics Research Section A: Accelerators, Spectrometers, Detectors and Associated Equipment* 2001;**458**:297–309. [https://doi.org/10.1016/S0168-9002\(00\)00874-3](https://doi.org/10.1016/S0168-9002(00)00874-3).
- 12 Abe A, Takahashi N, Lee J, Oka T, Shizukuishi K, Kikuchi T, *et al.* Performance evaluation of a hand-held, semiconductor (CdZnTe)-based gamma camera. *Eur J Nucl Med Mol Imaging* 2003;**30**:805–11. <https://doi.org/10.1007/s00259-002-1067-z>.
- 13 *Performance Measurements of Gamma Cameras*. n.d. URL: <https://www.nema.org/Standards/Pages/Performance-Measurements-of-Gamma-Cameras.aspx> (Accessed 9 June 2016).
- 14 Hruska CB, O'Connor MK. Effect of Collimator Selection on Tumor Detection for Dedicated Nuclear Breast Imaging Systems. *IEEE Transactions on Nuclear Science* 2006;**53**:2680–9. <https://doi.org/10.1109/TNS.2006.879824>.

- 15 Hruska CB, Weinmann AL, O'Connor MK. Proof of concept for low-dose molecular breast imaging with a dual-head CZT gamma camera. Part I. Evaluation in phantoms. *Medical Physics* 2012;**39**:3466–75. <https://doi.org/10.1118/1.4718665>.
- 16 Gong Z, Klanian K, Patel T, Sullivan O, Williams MB. Implementation and evaluation of an expectation maximization reconstruction algorithm for gamma emission breast tomosynthesis. *Medical Physics* 2012;**39**:7580–92. <https://doi.org/10.1118/1.4764480>.
- 17 Gong Z, Williams MB. Comparison of breast specific gamma imaging and molecular breast tomosynthesis in breast cancer detection: Evaluation in phantoms. *Medical Physics* 2015;**42**:4250–9. <https://doi.org/10.1118/1.4922398>.

## Chapter 6

# Characterization and Pilot In-Human Trial of Dedicated Breast Ring PET System

## 6.1 Introduction

Whole body PET (WPET) using the radiotracer FDG has shown promise in breast cancer diagnosis and staging; however, due to limitations in scanner spatial resolution, tumor sensitivity is low for tumors less than 1 cm in size<sup>1,2</sup>. Positron emission mammography (PEM) was the first attempt to use more compact dedicated breast PET systems to improve tumor sensitivity for smaller lesions<sup>3,4</sup>. The first PEM systems, developed in the mid 90s, consisted of two opposing planar gamma cameras between which the breast was compressed. The available lines of response (LORs) with this type of geometry resulted in limited angle acquisition leading to asymmetric image volumes with higher resolution in the plane parallel to the camera faces<sup>5-7</sup>. PEM has been shown to have an increased sensitivity for detection of small lesions when compared to WPET<sup>8,9</sup>; however, it suffers from poor spatial resolution in the direction of compression, has poor signal-to-noise ratio for regions of the breast near the chest wall, and cannot image large breasts adequately<sup>6,10</sup>.

To improve the spatial resolution of PEM systems, several new dedicated breast PET designs were created. Wu *et al* improved upon the early PEM design by placing the two opposing planar gamma cameras on a rotational stage allowing the cameras to move around the pendant breast of a prone subject thereby eliminating the limited angle acquisition of the 2-camera PEM system at the cost of increased scan time<sup>11</sup>. Shimadzu developed a full ring PET system and a C-shaped PET system, both designed to eliminate the limited angle acquisition of PEM while improving photon sensitivity<sup>12</sup>. The full-ring detector contains two rings, while the C-shaped scanner has three rings. Both have 12 detector modules per ring<sup>12</sup>, however the C-shape scanner was designed as a 14 module full ring with two side-by-side modules removed to create a gap for improved breast placement for better visualization of the posterior tissue<sup>12,13</sup>. Characterization of the C-shaped system has shown spatial resolution and image contrast at the center of the volume of view (VOV) is comparable to that of the full ring; however, both spatial resolution and contrast are degraded sharply with decreasing distance from the 2-module gap in the ring<sup>13</sup>. Ultimately the C design was abandoned by the company. Two commercial systems have recently been developed; the MAMMI system by Oncovision and a prone dedicated breast PET system by Shimadzu<sup>14,15</sup>. Both systems have multi-ring configurations with 12 detector modules per ring<sup>14-16</sup>.

All of the above systems utilize position-sensitive photomultiplier tubes (PSPMT)<sup>11-15</sup>. While all of these systems were successful at improving the spatial resolution in detecting breast cancers compared to the larger WPET systems (Table 1)<sup>11-15</sup>, only the C-shaped system was specifically designed with the goal of improving posterior tissue visualization compared to other dedicated breast PET systems<sup>12</sup>.

Table 6-1: Depicts the FWHM axial resolution at the center of the VOV of several dedicated breast PET scanners.

Author	System	Center VOV Axial Resolution (mm)
Wu <i>et al</i>	2-camera PET	2.17
Furuta <i>et al</i>	Shimadzu C-PET	1.00
Moliner <i>et al</i>	MAMMI PET	1.60
Miyake <i>et al</i>	Shimadzu Full-Ring PET	1.60

Recent studies have proven that the visualization of posterior breast tissue is a continuing issue for dedicated breast PET. In a study of 230 subjects undergoing both whole body PET (WBPET) and MAMMI PET, with WBPET findings used as ground truth, the MAMMI system had a lesion detection sensitivity of 88.9%, however, when tumors outside the scanner's VOV (near the chest wall) were excluded from the analysis, the sensitivity increased to 98.6%<sup>17</sup>. In a similar study of 69 subjects, comparing WBPET to both Shimadzu's full-ring O scanner and to their C-shaped scanner, showed sensitivities of 82% and 83% for the O and C scanners, respectively, for all tumors. However, excluding all tumors outside of the O and C VOVs the sensitivities increased to 93% and 90%, respectively<sup>18</sup>. The authors of this study noted that all tumors outside of the field of view were located close to the chest wall in the posterior breast tissue<sup>18</sup>.

In an attempt to improve the visualization of the posterior breast tissue compared to previous dedicated breast PET scanners, the breast ring PET (BRPET) system was developed and tested in a joint venture between the University of Virginia, West Virginia University, and Jefferson Lab. The BRPET system is a single full-ring system designed with 12 detector modules based on PSPMTs and LYSO crystal arrays. The crystal array of each module is optically coupled to its PSPMT using a fiber optic plate with trapezoidal cross-section to permit the crystal array to be positioned at a higher vertical location than the PSPMT (Fig. 6-1). This patented slanted light guide approach permits the scintillation crystal arrays to be positioned with their upper portions extending into the hole of the prone table, and thus positioned more posteriorly than the PSPMTs, which are entirely below the table<sup>19</sup>.

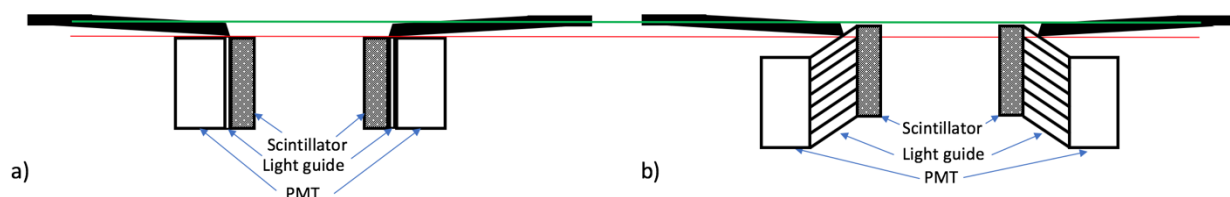


Figure 6-1: Illustrates the theory behind the slanted light guides. Setup a) depicts a classic detector module where the height of the crystal is restricted by the position of the PMT, while the slanted light guides allow for the crystals to be positioned higher into the exam table's opening. The crystal's elevation increase is highlighted by the green line.

The following sections present the characterization of the BRPET imaging performance, as well as the results of a pilot human study of the BRPET system. There are currently no testing standards for this type of dedicated breast PET scanner; however, most developers of dedicated breast PET systems have used modified performance evaluation protocols based on the National Electrical Manufacturers Association (NEMA) NU-4 protocol, which was developed for uniform evaluation of small animal PET scanners<sup>14,15,20</sup>. In addition to the NEMA tests, the energy resolution of the scanner was evaluated and signal-to-noise ratio (SNR) breast phantom experiments were performed to characterize PET image quality. A pilot human study enrolling 10 subjects was carried out to compare the tumor sensitivity and specificity of BRPET to that of contrast-enhanced breast MRI.

## 6.2 Methods

### 6.2.1 System Design

The BRPET scanner contains a single ring of 12 detector modules (Fig. 6-2). Each module is made up of three physical components. The first is a Hamamatsu H8500 Position Sensitive Photomultiplier (PSPMT), with an active area of 49 mm x 49 mm, a bialkali photocathode, and an 8 x 8 anode array. Each BRPET PSPMT has the manufacturer-provided high voltage distribution and strip channel readout connector boards integrally attached with the photomultiplier<sup>21</sup>. A home-made (Jefferson Lab) resistive readout circuit board is attached to the factory provided boards, which includes a single pre-amplification stage followed by a resistive X-Y directional position encoder and secondary amplifiers<sup>21</sup>. The readout board converts the factory provided strip readout into four channel output. The second module component is a 5 cm x 5 cm x 1 cm scintillator array of LYSO crystals with crystal dimensions of 2 mm x 2 mm x 10 mm thick, and a crystal pitch of 2.065 mm. Lastly, between the array and the PSPMT there is a slanted fiberoptic light guide made of a 22 x 22 glued bundle of tightly packed round 2mm diameter plastic polystyrene-based core lightguide fibers (refractive index = 1.60) (Saint-Gobain BCF-98), and PMMA cladding (refractive index = 1.49) to maximize total internal reflection of the scintillation light. The inter-fiber gaps are filled with optical cement from Saint-Gobain which has a transmission of > 98% for wavelengths above 400 nm in order to keep the fiber bunch mechanically together, maximize scintillation light propagation in the fibers, and minimize cross talk between fibers (Saint-Gobain Crystals, OH, United States). The slanted light guide gives the scintillation crystal array a 12 mm vertically upward offset relative to the PSPMT.

The 12 detector modules are placed in a tight ring at evenly spaced angles (30 degrees) resulting in an inner ring diameter of 20.5 cm. The ring is mounted below a modified Lorad breast biopsy table (Hologic, Connecticut, USA). The signal outputs from each detector module have an X and Y format (two per coordinate, four total)<sup>21</sup>. The separate original X and Y spatial coordinates are encoded in the relative amplitudes of the signals coming from the resistive 4 channel readout resistive network<sup>21</sup>. In addition, the summed signal for generation of an energy discrimination pulse and trigger to the Analog to Digital digitizer module is also provided, along with the four X and Y coordinate signals. The X and Y coordinate data from all 12 modules (48 total) are sent to a 64-channel integrating analog-to-digital converter (ADC) (AiT Instruments, Newport News, VA), while the summed signals are passed through a Mesytec MCFD-16 fast 16 channel constant fraction discriminator (Putzbrunn, Germany) to produce a confidence trigger per each detection event. When a coincidence occurs (simultaneous arrival of the summed signals of two modules in the ring within a set timing window), a trigger pulse is sent to the AiT ADC module to initiate digitization of the delayed and shaped 48 (12 modules x 4

signals/module) signals. This trigger timing is adjusted to record full energies of the two coincident signals.

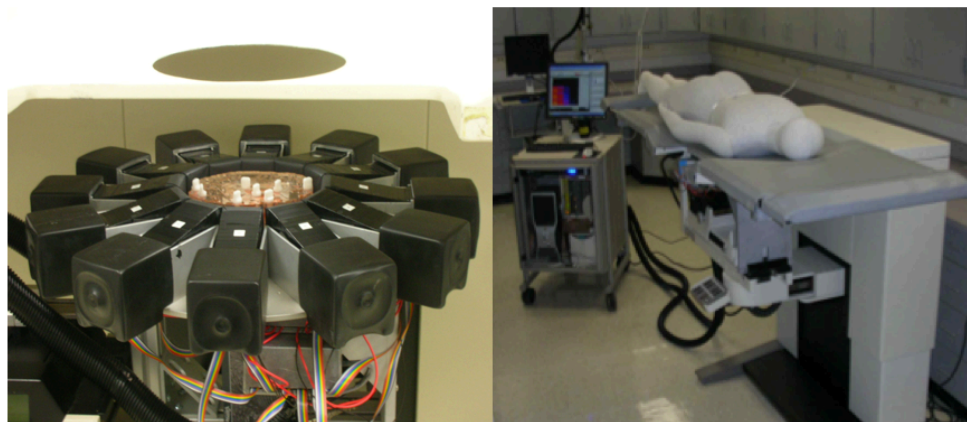


Figure 6-2: The photo on the left shows the BRPET ring. Notice the slanted light guides and increased elevation of the scintillation crystals relative to the PSPMTs. The photo on the right shows the modified Lorad biopsy table. The BRPET ring is attached below the table. A manikin is seen positioned as a patient would be.

## 6.2.2 Energy Resolution

A line source phantom was filled with 500  $\mu\text{Ci}$  (18.5 MBq) of FDG and placed in the center of the VOV. Counts were acquired for 30 minutes. Due to the pixelated nature of the BRPET LYSO crystals, an energy histogram from each individual crystal of each crystal array is recorded (total of 5,808 crystals). Each energy histogram is normalized using the energy look-up table created during energy calibration (Section 2.3.1). The resulting normalized energy histograms are then averaged. The photopeak of the average energy histogram was then fitted to the sum of two Gaussian curves, utilizing MATLABs “gauss2” fit function. The energy resolution was calculated as the full-width at half max (FWHM) of the Gaussian centered on the photopeak divided by the Gaussian peak location (511 keV), and expressed as a percentage<sup>22-24</sup>.

## 6.2.3 Spatial Resolution

To obtain the spatial resolution, the following modified NEMA NU-4 protocol was used<sup>14,15,25</sup>. A 1 mm in diameter Na-22 source with an activity of 10  $\mu\text{Ci}$  (0.37 MBq) was used. Two data sets were taken; one at the central plane of the ring and one in a plane located midway between the central plane and the edge of the axial VOV. For each plane, data was acquired for 5 minutes at 5 different radial distances from the center of the VOV: 0 mm, 20 mm, 40 mm, 60 mm, and 75 mm. Each image was reconstructed using a MLEM algorithm with 10 iterations. The reconstructed voxel size was  $1 \times 1 \times 1 \mu\text{m}^3$ . This voxel size is also used for reconstruction of human breast images. The response function was measured along the axial, radial, and transverse directions. For each direction, the response function is formed by summing over contiguous slices in a direction perpendicular to the direction of response function measurement. Summing is to be performed over all slices that lie within at least two times the FWHM of the response function as measured in the orthogonal direction<sup>25</sup>. In a small departure from the parabolic interpolations used in the NEMA protocol, the profiles were fitted to a

Gaussian curve, again utilizing MATLABs “gauss2” fit function, and the spatial resolution is defined as the FWHM of the fit.

#### 6.2.4 System Sensitivity

System sensitivity in PET imaging is defined as the background-subtracted coincidence rate for a given source strength and branching ratio<sup>25</sup>. Once again, a modified NEMA NU-4 protocol was used<sup>14,15,25</sup>. The same Na-22 point source used in the measurement of the spatial resolution was again used. The source was placed in the centers of the transaxial and axial VOVs and scanned till at least 10,000 true events were counted at which point the time was noted (195 seconds). The source was then stepped in the axial direction from the middle of the axial VOV to the top edge of the axial VOV in 2 mm steps. It was then placed in the center again and the same process was repeated stepping the source to the bottom of the axial VOV. The source was then removed, and a background scan was acquired. Each acquisition was taken over the same time period as used for the center scan.

Single-slice rebinning was used to create transverse 2D sinograms from the raw 3D data. In each row (i.e. each angle in the transverse plane) of the resulting 2D sinogram, all pixels greater than 1 cm away from the largest pixel value in that row were set to zero. The total pixel values in each row were then summed together and divided by the acquisition time to get the count rate per row ( $R_i$ ). The sensitivity per slice,  $S_i$ , is then defined as<sup>25</sup>:

$$S_i = \frac{R_i - R_{bkg,i}}{A}, \quad (6-1)$$

where  $R_{bkg,i}$  is the background count rate per slice in counts per second determined after rebinning and masking the background scan data, and  $A$  is the source activity as measured using a dose calibrator, in Bq. The absolute system sensitivity,  $S_{A,i}$ , is calculated by dividing  $S_i$  by the branching ratio of Na-22 (0.9060), it is then presented as a percentage<sup>25</sup>. Finally, the total system absolute sensitivity,  $S_A$ , is calculated by summing over all transverse slices in the axial VOV, as

$$S_A = \sum_{All\ i} S_{A,i}. \quad (6-2)$$

#### 6.2.5 Count Rate and Scatter Fraction

Large numbers of scatter and random photons lead to count losses at high count rates and the degradation of the SNR<sup>26</sup>. Count rate measurements define the scanners ability to handle high activity sources and is typically measured in terms of the noise equivalent count rate (NECR), which estimates the number of true coincidences per second exempt of scatter, random, and background coincidences<sup>25</sup>. The NECR is a useful figure of merit for image quality because it is proportional to the square of the image SNR<sup>27</sup>. The scatter fraction is the ratio of the scattered coincidences to the true coincidences. It depends on the spatial distribution of the radioactive source, the volume of scattering material in the subject, the mode of operation (e.g. 2D versus 3D), and on the ability of the scanner to reject scattered photons via energy discrimination. The measurements of both the NECR and scatter fraction follow the NEMA NU-2 and NU-4 protocol but used a modified phantom that is more appropriate for dedicated breast imaging.

The NEMA NU-2 and NU-4 protocols follow the same methodology, but each was written for different scanner sizes. NEMA NU-2 is written for whole body PET scanners while NEMA NU-4 is written for small animal scanners. It follows that the most appropriate phantom sizes are scaled to the size of the scanner. Due to the unique size of the dedicated breast

system a phantom was created to fit the scanner. This phantom was based on similar phantoms used in literature<sup>11,14-16</sup>. The phantom is a high-density polyethylene cylinder 165 mm in length, 65 mm in diameter (Fig. 6-3). A 3.2 mm hole is drilled parallel to the phantom's long axis and offset radially from it by 10 mm. Both the NECR analysis and the scatter fraction analysis are performed using the same data sets.

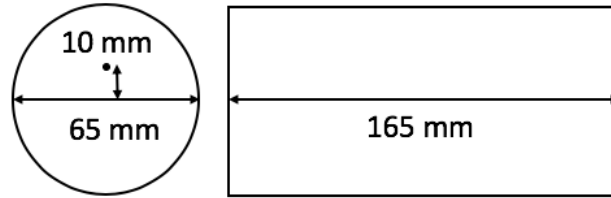


Figure 6-3: Count rate phantom dimensions. The hole 10 mm off center has a diameter of 3.2 mm.

Clear flexible tubing with an outer diameter of 3.2 mm was filled with a known activity of FDG and inserted into the 3.2 mm diameter hole. For these studies this activity was varied from 2.3 mCi to 8 mCi. The reasoning behind the change in activity levels will be discussed shortly. The filled phantom was placed at the center of the VOV such that the transaxial mid-plane bisected the center of the cylindrical phantom. An initial 10 minute scan,  $t_{acq}$ , at time equals zero,  $t_0$ , was acquired followed by a sequence of 10 minute scans every 25 minutes afterwards till the activity was under 100  $\mu$ Ci (to guarantee counting losses of less than 1 percent of the true event rate as dictated by the NEMA protocols). The phantom was then removed, and a 10 minute scan was taken to obtain the background count rate.

Analysis of the data followed the NEMA NU-4-2008 protocol for performance measurement for small animal PET scanners<sup>25</sup>. The data underwent single-slice rebinning to create a set of transaxial sinograms. All sinogram pixels further than 8 mm outside of the phantom edges were set to zero. For each projection angle (i.e. each row of the sinogram), the brightest pixel was identified, and each row of the sinogram was then shifted to align the brightest pixel with center of the histogram. Next all projections in the aligned sinogram are summed to generate a 1D profile. Using linear interpolation, the count values 7 mm to the left,  $C_{L,i,j}$ , and 7 mm to the right,  $C_{R,i,j}$ , of the peak are calculated<sup>25</sup>. These counts are averaged, and the average is multiplied by the number of pixels within the 14 mm wide strip defined by the  $\pm 7$  mm cutoffs. This value is then summed with the counts in the pixels outside the strip to obtain the number of random plus scatter events,  $C_{r+s,i,j}$ <sup>25</sup>. The total counts,  $C_{tot}$ , are then the sum of all pixels in the summed projection.

The low-activity acquisitions, in which the contributions to  $C_{r+s}$  and  $C_{tot}$  from randoms and count rate losses can be considered negligible, are used to estimate the scatter fraction. The scatter fraction (SF) is calculated for each transaxial slice as:

$$SF = \frac{\sum_i \sum_j C_{r+s,i,j}}{\sum_i \sum_j C_{tot,i,j}}, \quad (6-3)$$

where the sum is over the low-activity acquisitions of the final data sets, in which the count loss rates and random event rates are below 1% of the true event rate<sup>25</sup>. It is assumed that at these counts,  $C_{r+s}$ , have a negligible number of random events, therefore contains contributions only from scattered events<sup>25</sup>.

The total ( $R_{tot,i,j}$ ), true ( $R_{t,i,j}$ ), random ( $R_{r,i,j}$ ), and scatter ( $R_{s,i,j}$ ) count rates for each slice  $i$  and each acquisition,  $j$ , are calculated as shown below<sup>25</sup>.

$$R_{tot,i,j} = \frac{C_{tot,i,j}}{t_{acq,j}} \quad (6-4)$$

$$R_{t,i,j} = \frac{(C_{tot,i,j} - C_{r+s,i,j})}{t_{acq,j}} \quad (6-5)$$

$$R_{r,i,j} = R_{tot,i,j} - \frac{R_{t,i,j}}{1 - SF_i} \quad (6-6)$$

$$R_{s,i,j} = R_{tot,i,j} - R_{t,i,j} - R_{r,i,j} - R_{bkg,i,j} \quad (6-7)$$

Where  $R_{bkg,i,j}$  is the background count rate. The NEC rate for each acquisition,  $R_{NEC,i,j}$ , is then calculated as <sup>25</sup>:

$$R_{NEC,i,j} = \frac{R_{t,i,j}^2}{R_{tot,i,j}} \quad (6-8)$$

The Mesytec MCFD-16, allows the user to define which detector module pairs can create a trigger pulse when an event is detected by each within the preset timing window (Fig. 6-4). The above measurements of the counting rates were repeated with several different MCFD-16 configurations, varying the allowed detector pairs and the width of the timing window with the goal of maximizing the system NECR. The configurations tested are summarized in Table 6-2.

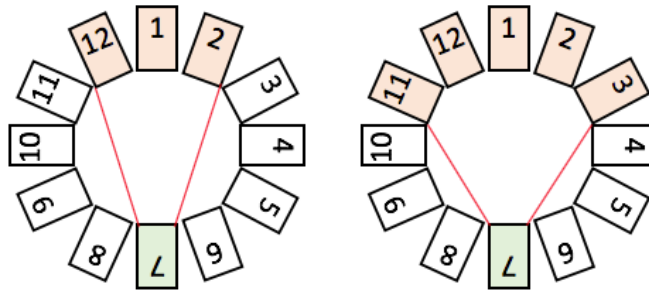


Figure 6-4: Depicts a couple of detector configurations allowed by the Mesytec MCFD-16. In these examples, any given detector module, in this example module 7, can be allowed to create trigger pulses if a coincident event occurs between that module and any of the opposite highlighted modules. Decreasing the number of allowed detector coincidence pairs helps lower the number of triggers caused by random and scatter events, at the expense of reduced sensitivity.

Table 6-2: Mesytec MCFD-16 configurations tested. The first column represents the number of detector modules allowed to create a coincidence event across from a single module, while the second column is the timing window within which two events can be considered a coincidence.

Number of Detectors	Timing Window (ns)
3	8
	10
	12
5	8
	10
	12
7	8

### 6.2.6 Image Quality for Posterior Tissue Imaging

Two unique experiments were designed to observe how high into the 3.35 mm thick examination table's breast positioning hole the BRPET scanner's field of view extends (note that the padding usually on the top surface of the table was removed for these experiments). The experiments used line sources to measure the maximum vertical position that a high contrast source could be positioned and imaged.

The first experiment used five capillaries (1.6 mm outer diameter) vertically spaced at 5 mm (center-to-center) with the top capillary 1.9 mm from the bottom of an acrylic plate laid across the top of the scanner table (Fig. 6-5a). There was a 4 mm distance from the bottom plane of the acrylic plate to the bottom plane of the table. Each capillary tube was filled with ~ 10  $\mu$ Ci of FDG. The phantom was scanned for 10 min. The image was reconstructed using an MLEM algorithm with  $1 \times 1 \times 1 \text{ mm}^3$  voxels. Profiles were taken through the center of the reconstructed image and the locations of the capillary peaks in the profiles were used to calculate the depth below the bottom surface of the acrylic of the topmost visualizable capillary tube.

The second high contrast experiment used two capillary tubes placed at a 43.6 degree angle relative to each other with their intersection point placed at the top surface of the scanner table (Fig. 6-5b). As in the previous experiment, each capillary tube was filled with ~ 10  $\mu$ Ci of FDG. The phantom was scanned for 10 min. The image was reconstructed using an MLEM algorithm with  $1 \times 1 \times 1 \text{ mm}^3$  voxels. A profile running through the center of both capillary tubes was extracted and the distance between the peak points in the profile was used along with the known angle between the capillaries to calculate the distance from the top of the examination table.

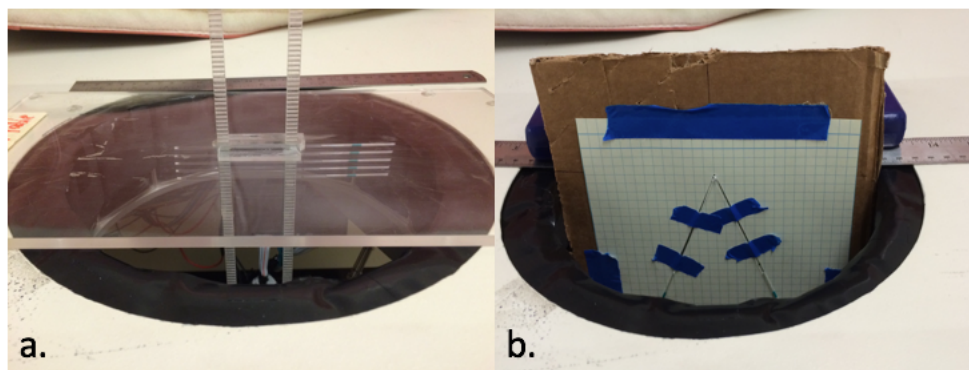


Figure 6-5: Experimental set up of two high contrast vertical position experiments. Image a) is a photo of the capillary phantom with 5 parallel capillary tubes spaced 5 mm from each other center-to-center. Image b) shows the two capillary phantom, with the angle between them 43.6 degrees and their vertex located in the plane of the table's top surface.

Lastly, to characterize the scanner's useful vertical (z-dimension) field of view under more realistic breast imaging conditions with low contrast lesions, a fillable breast phantom containing simulated lesions was used to assess the lesion detectability, based on Rose's criterion, of multiple lesion sizes and activity concentrations, with a variety of z-locations (Fig. 6-6)<sup>26,28</sup>. For any given lesion size and activity concentration, the uppermost lesion position within the scanner's volume of view for which Rose's criterion for SNR (taking SNR = 3 as the limit of detectability) was met, was taken as the upper axial (z-dimension) limit of the useful VOV.

Two lesion sizes were assessed, 0.8 cm and 1.2 cm in diameter. Each lesion was filled with FDG and placed in the center of a fillable cylindrical phantom that was also filled with a background activity of FDG. For each lesion size two lesion-to-background ratios (LBRs) were assessed, 2:1 and 3:1 (Table 6-3). These LBRs were chosen to replicate the low end of observed lesion-to-background uptake ratios for breast cancer reported in the literature<sup>29,30</sup>. The phantom was then placed at the center of the VOV of the BRPET ring with the lesion fully in the axial VOV of the detector ring. The BRPET ring was then translated downwards at 2 mm increments, taking 5 min acquisitions at each position, until the lesion was completely out of the scanner's VOV. The images were reconstructed using the same MLEM algorithm and voxel size as was used in the spatial resolution measurements described above. The images were reformatted to provide sagittal (y-z plane) slices through the center of the lesions. The SNR was calculated, as described in chapter 2, for the sagittal and coronal (x-y) planes. Reconstructed slices illustrating the ROIs used for calculating the SNR can be seen in figure 6-7.

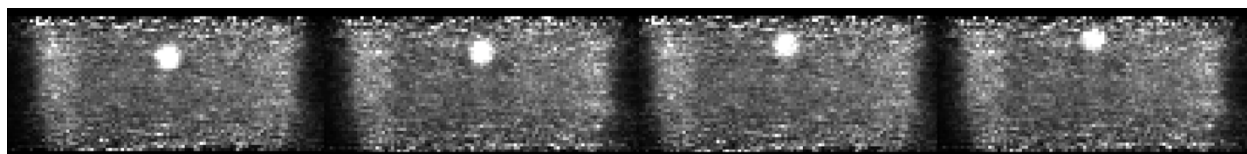


Figure 6-6: From left to right, x-z slices from images obtained with the ring positioned at 2 mm intervals in the z-dimension. The image resulting from the topmost ring position is at the far left.

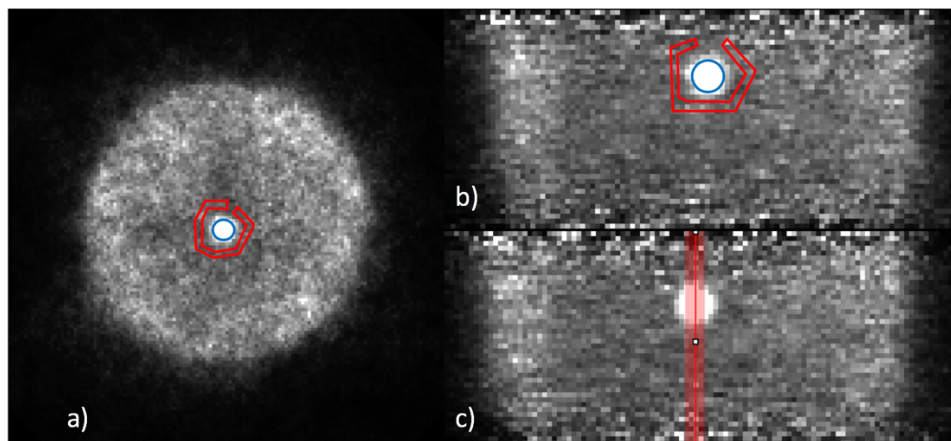


Figure 6-7: ROIs used to calculate the SNR. The average lesion counts are calculated from the ROI in blue in figures a) and b), while the average background counts are calculated from the ROI in red. Figure c) shows the profile used to measure the z-position of the lesion within the VOV.

Table 6-3: Activity concentrations used in SNR Phantom experiments.

Lesion Diameter (cm)	Lesion Concentration ( $\mu\text{Ci/mL}$ )	Background Concentration ( $\mu\text{Ci/mL}$ )	LBR
1.2	3.06	1.03	3:1
1.2	2.04	1.02	2:1
0.8	3.50	1.13	3:1
0.8	2.17	1.03	2:1

\*Lesion-to-Background Ratio

### 6.2.7 Pilot Human Study

To begin to understand the clinical usefulness of the BRPET scanner, a pilot human study was completed comparing clinical contrast enhanced MRI (CE-MRI) and the BRPET system in terms of lesion sensitivity and specificity. In this study, females 18 years of age or older who were not pregnant, not breast feeding, and who were scheduled for a clinical CE-MRI breast scan, or who had had a recent CE-MRI breast scan, were eligible. The clinical CE-MRI includes the following sequences: axial T1 weighted spin echo, axial fat-suppressed T2-weighted spin-echo, and pre- and post-contrast axial T1 weighed fat-suppressed 3D gradient-echo. The contrast study was conducted with 10 ml of Gadavist contrast agent. For the BRPET study subjects were scanned under a protocol approved by the institutional review board of the University of Virginia's School of Medicine. Every subject provided informed consent. All subject information was handled in compliance with the rules and regulations of the Health Insurance Portability and Accountability Act. A total of 10 subjects were scanned with a total of 11 biopsied lesions. Two subjects had no findings in the clinical CE-MRI scan. The histological results of the biopsies can be seen in table 6-4.

Table 6-4: Histological and Imaging Results of Lesions Biopsied

<b>Tumor Status and Type</b>	<b>Number of Lesions</b>
<b>Benign</b>	
Lobular Carcinoma in situ	1
Fibroadenoma	1
Stromal Fibrosis	1
Fat Necrosis	1
<b>Malignant</b>	
Infiltrating Ductal Carcinoma	5
Infiltrating Lobular Carcinoma	2

After consent, each subject was intravenously injected with approximately 6 mCi (222 MBq) of F-18-FDG, resulting in a total body effective dose of 4.2 mSv<sup>31</sup>. A 45 minute uptake time was allowed post injection. The subject was then positioned on the examination table. Two scans were performed, one for each breast, starting with the suspicious breast. To cover the entire breast, the PET ring was positioned as close to the chest wall (i.e. as far vertically upward) as possible and then was moved down in 3 cm steps until the entire breast was covered. The somewhat conservative step size of 3 cm was selected to allow a 2 cm overlap of the 5 cm axial fields of view, thereby facilitating visualization of small or low-uptake lesions in the low sensitivity regions near the axial boundaries of the volume of view. Data were acquired for 5 minutes at each ring position. The injected activity, number of ring positions, and total scan time for each subject can be seen in table 6-5. Once the scans were completed the PET images for each ring position were reconstructed using the same MLEM algorithm and 1 x 1 x 1 mm<sup>3</sup> voxel size used in the system characterization experiments, and the reconstructed volumetric images for each position were stitched together using a weighted linear summation to form a single reconstructed image. The final BRPET images were interpreted by two board-certified nuclear medicine radiologists who were blinded to all background clinical information, while the CE-MRI results were read by a breast radiologist, Mammography Quality Standards Act (MQSA) certified and fellowship trained in breast imaging with 5 years of experience. Each reader was asked rank the image quality of each data set ranking the images as: 1) Not Adequate, 2) Barely Adequate, 3) Adequate, 4) Good, 5) Excellent. Readers were then asked to localize any suspicious findings in the data set and score each finding on a linear 1-5 suspicion scale (1 – Definitely Benign, 2 – Probably Benign, 3 – Indeterminant, 4 – Probably Malignant, 5 – Definitely Malignant). Reader results were used to calculate sensitivity and specificity for each lesion, taking biopsy results as ground truth for malignancy. The reader interpretation form can be viewed in Appendix D.

Table 6-5: Injected activity, ring positions, and total scan time for each case.

Case Number	Injected Activity (mCi)	Right Breast		Left Breast	
		Number of Ring Positions	Total Scan Time (min)	Number of Ring Positions	Total Scan Time (min)
1	4.27	3	15	3	15
2	6.31	4	20	4	20
3	5.5	Not Imaged	Not Imaged	5	25
4	6.23	3	15	3	15
5	7.6	3	15	3	15
6	5.07	4	20	3	15
7	5.3	4	20	4	20
8	5.2	3	15	3	15
9	5.63	5	25	5	25
10	6.57	3	15	4	20

## 6.3 Results

### 6.3.1 Energy Resolution

Figure 6-8 depicts the average corrected energy histogram of the system along with the double Gaussian fitted curve. The calculated energy resolution was 21.2 % FWHM.

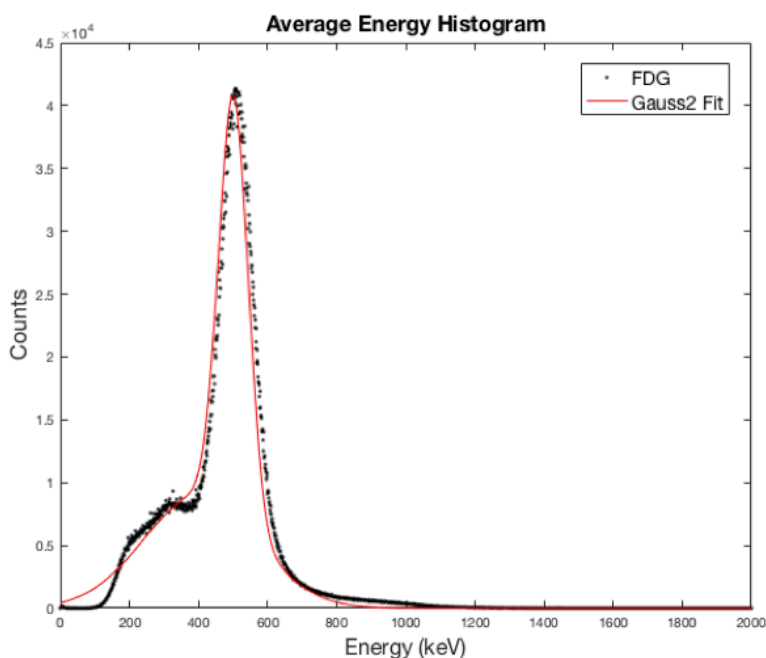


Figure 6-8: Average corrected energy histogram.

### 6.3.2 Spatial Resolution

Figure 6-9a shows an axially central slice from the scan of the 1 mm Na-22 point source when it was positioned at the center of the transaxial VOV, i.e. at the ring isocenter. Figure 6-9b

is the response function for this slice. Response functions were also generated for each of the other source radial positions, located at radial distances of 20, 40, 60, and 75 mm from the center of the VOV. The measured response function FWHMs in three directions are shown in Table 6-6 for the point source in a plane at the axial center of the VOV, for and a plane one-fourth of the axial VOV from the center of the axial VOV. Figure 6-10 contains plots of response function FWHM versus radial source position. The plots show that the spatial resolution is in general degraded towards the periphery of the transaxial VOV compared to the center.

Table 6-6: Spatial resolution measurements in mm.

Radial Distance (mm)	FWHM (mm) - ½ Detector height			FWHM (mm) - ¼ Detector height		
	Axial	Radial	Tangential	Axial	Radial	Tangential
0.0	1.8	1.7	1.9	2.0	1.6	1.7
20.0	2.1	2.5	2.1	2.1	2.1	2.0
40.0	2.2	2.7	2.0	2.2	3.0	2.5
60.0	2.4	3.0	2.5	2.1	3.4	2.4
75.0	2.4	3.1	2.7	1.9	3.6	2.3

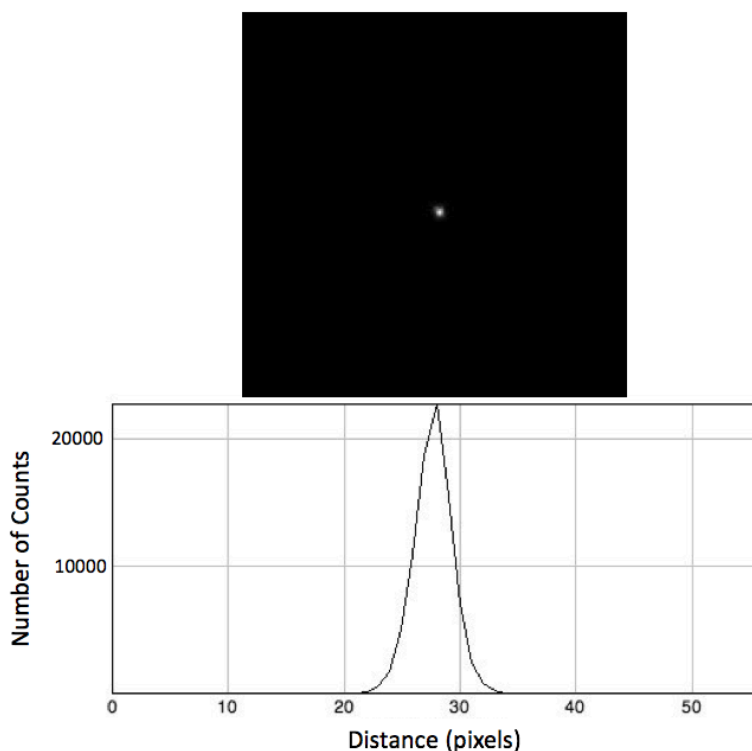


Figure 6-9: The top image is the central slice of the BRPET scan of a 1 mm Na-22 point source located at the center of the transaxial VOV. The resulting profile of the point source can be seen in the bottom image. The profile fitted and its FWHM in the axial, radial, and tangential directions were calculated.

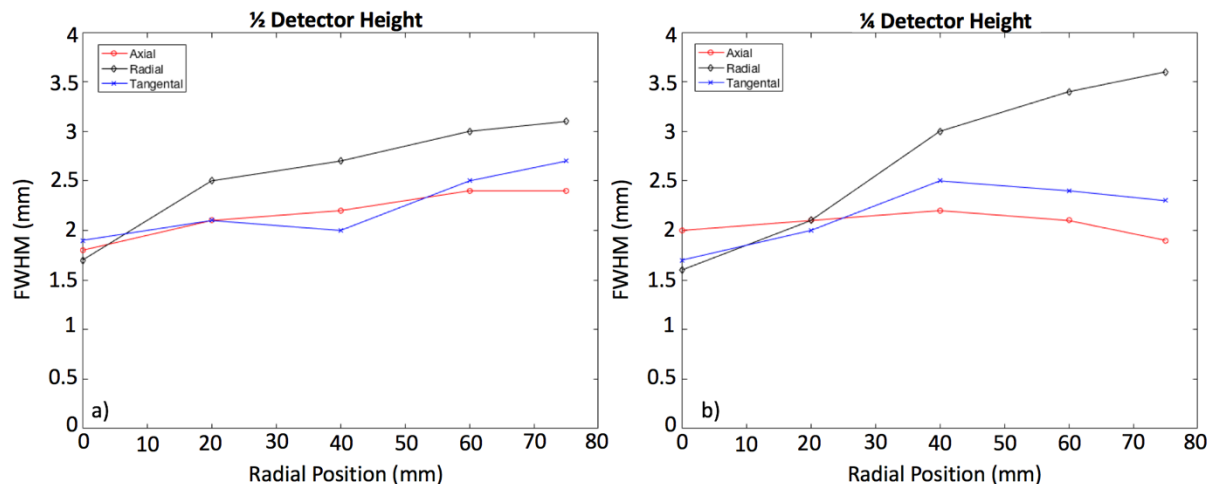


Figure 6-10: Plots showing the degradation of the spatial resolution as the point source is moved from the center of VOV to the edge of the VOV.

### 6.3.3 System Sensitivity

Figure 6-11 shows the absolute sensitivity per slice of the BRPET system with an energy window of 20% (460 keV – 562 keV). At the center of the axial VOV, the peak absolute sensitivity is 0.97%. The total system absolute sensitivity, calculated by summing over all transverse slices in the axial VOV, is 19.3%.

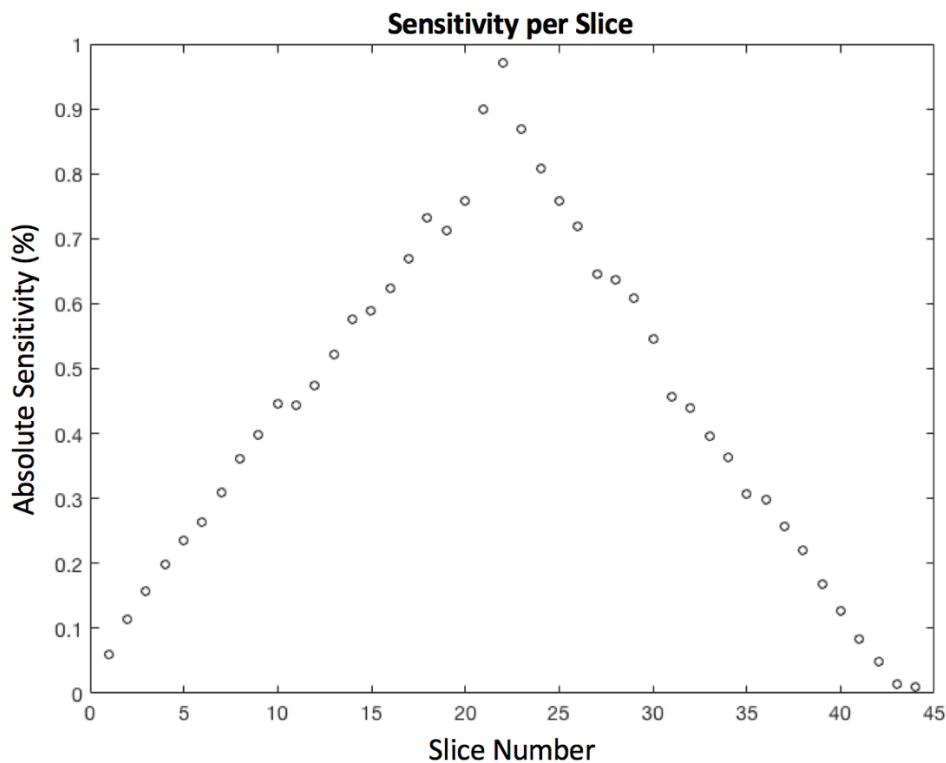


Figure 6-11: Axial absolute sensitivity along z-direction of BRPET scanner.

### 6.3.4 Count Rate and Scatter Fraction

Figure 6-12 shows the results of a single counting rate experiment. This figure depicts the relationships between the NEC rate and the true, random, and scatter rates as the activity increases. Table 6-7 compares the peak count rates and scatter fractions measured for all the tested MCFD-16 configurations. Figure 6-13 compares the NEC rates among different choices for detector coincidence pair rules and timing window width. Figure 6-13a contains NECR curves using a 3-detector coincidence rule, and Figure 6-13b shows then for a 5-detector rule. As expected, when either the number of allowed detector pairs or the timing window width are increased the NEC rates follow; however, as the count rate increase caused by thin increase in number of allowed detectors or timing window width reaches the count rate limit caused by the system's dead time. This occurred when the number of detectors increased to 7, where a significant drop in the count rates was observed (Table 6-7). The maximum NECR among all parameter settings tested is 5.33 kcps at 21 MBq FDG, which occurs when 5 detectors are used with a timing window of 12 ns. However, as seen in Figure 6-13 b, for activities larger than ~20 MBq the NECR quickly drops off leaving a small range of activities for which it is superior to that found with 10 ns window width. Since the activities at which the system will be utilized in breast cancer PET with FDG are small (roughly 5 % of injected activity, 11 MBq for 222 MBq injected activity) it remains the optimal configuration<sup>32,33</sup>.

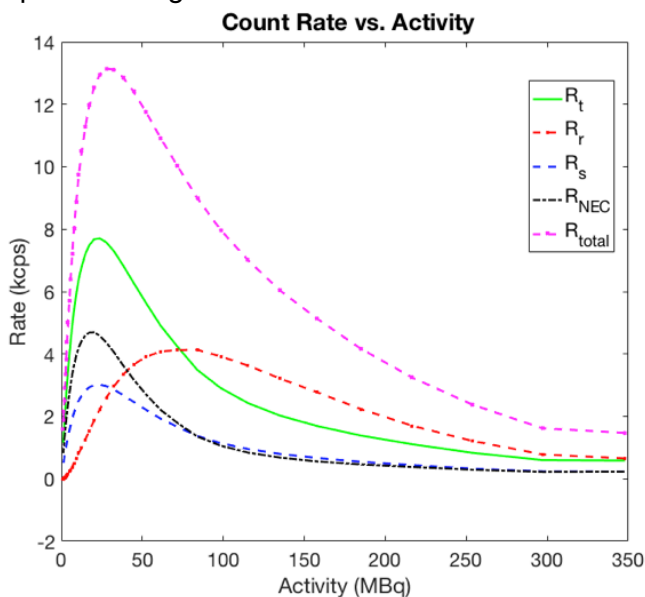


Figure 6-12: Counting rate performance plot as a function of activity for 5 detectors with a timing window of 10 ns.

Table 6-7: Comparison of peak count rates and scatter fractions for all tested MCFD-16 configurations.

Number of Detectors	Timing Window (ns)	Peak NEC Rate (kcps)	Peak Trues Rate (kcps)	Peak Random Rate (kcps)	Peak Scatter Rate (kcps)	Scatter Fraction (%)
3	8	2.77	5.63	6.37	3.66	30.7
	10	3.87	6.70	4.08	2.97	28.8
	12	4.28	7.26	4.25	2.90	39.4
5	8	4.11	6.81	3.88	2.69	28.0
	10	4.69	7.70	4.13	3.02	28.1
	12	5.33	9.02	4.46	3.84	29.8
7	8	1.56	3.29	3.38	1.94	36.8

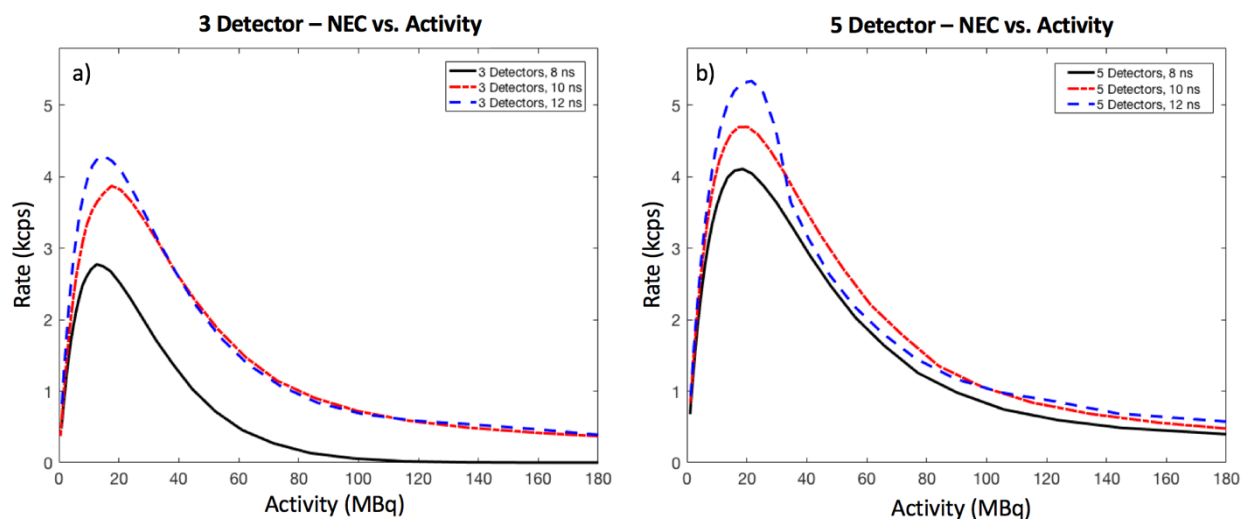


Figure 6-13: NECR curve comparisons for all timing window for 3 detectors (a) and 5 detectors (b).

### 6.3.5 Image Quality for Posterior Tissue Imaging

Figure 6-14 shows reconstructed slices of the two experiments designed to measure the maximum vertical position that can be imaged. Figure 6-15 shows profiles extracted from the slices of Figure 6-14. In the first experiment (Fig. 6-13 a and b), three and a half of the five capillary tubes were visible. The measured peak-to-peak separations for all the visible capillary tubes was 5 mm (5 voxels), which agrees with the physical measurement of 5 mm. Using the physically measured distances between the bottom of the phantom's acrylic plate and the bottom of the table, the known distances between the capillary tubes, and the number of visible capillary tubes, the highest visible point is 6.25 mm below the top of the examination table. Similarly, in the second experiment, the peak-to-peak separation of the two capillary tubes at their topmost visible point was 5 mm (5 voxels). Using the known angle between the capillaries and the height of their vertex, the distance from the top of the table to the topmost plane of the VOV was calculated to be 6.25 mm, agreeing with the parallel capillary experiment.

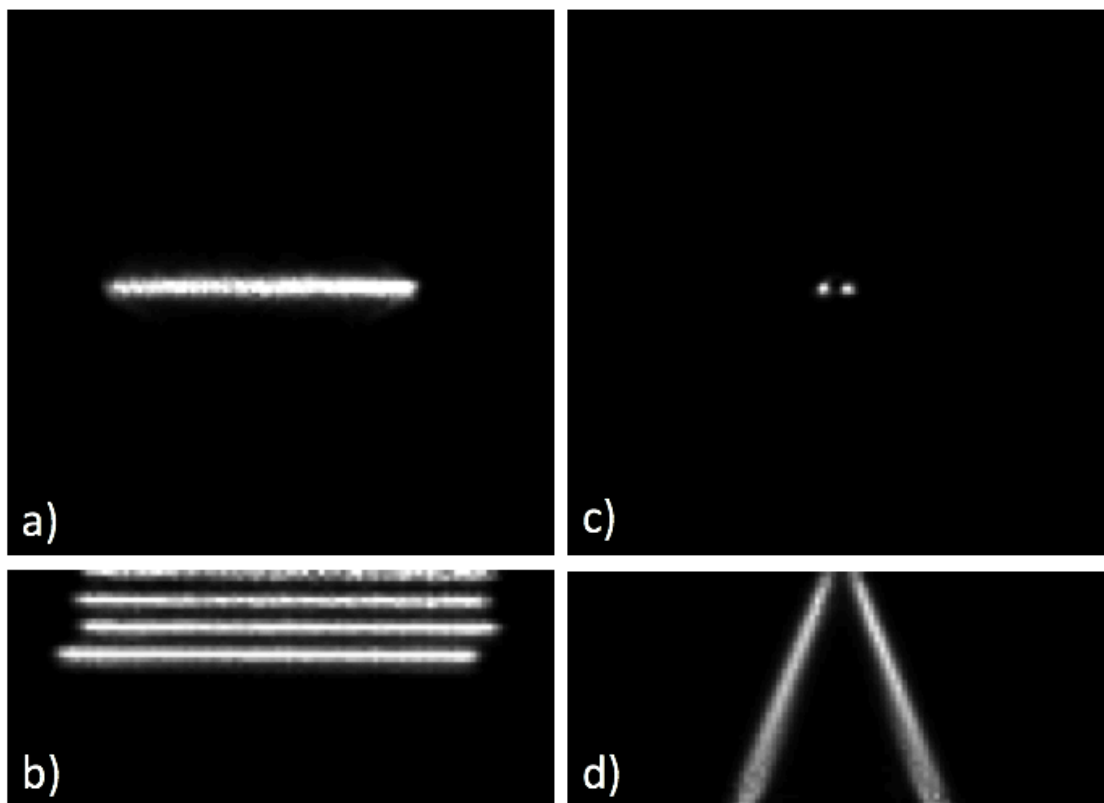


Figure 6-14: Images (a) and (b) are coronal and sagittal slices through the BRPET image of the parallel capillary tube array. Images (c) and (d) are coronal and sagittal slices from the BRPET scan of the angled capillary experiment.

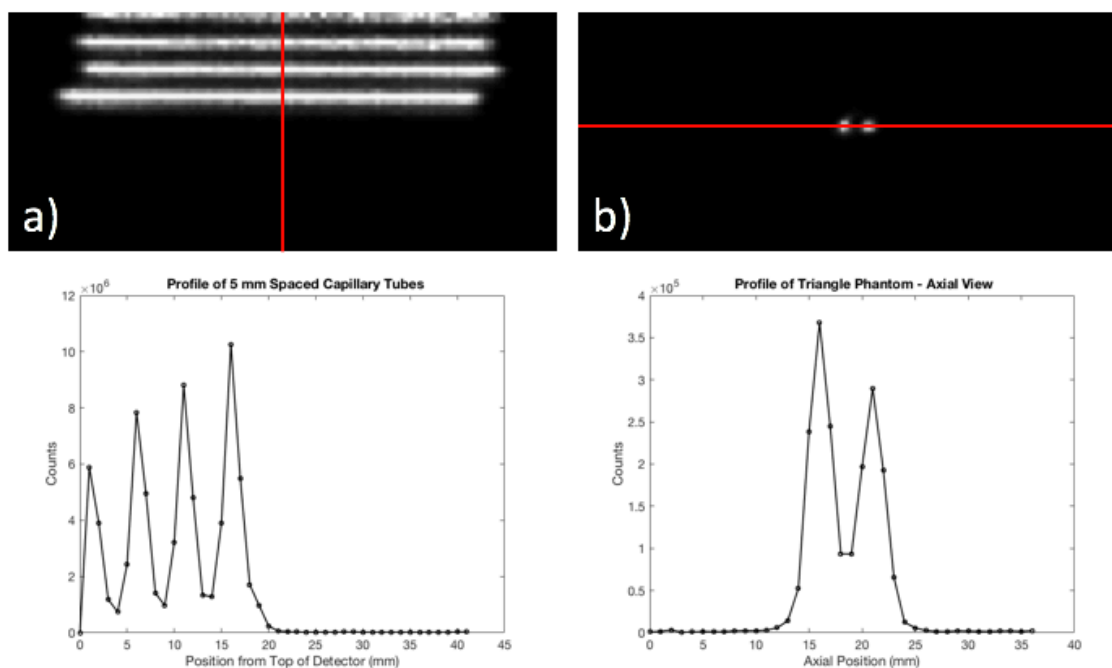


Figure 6-15: Profiles extracted from the parallel (a) and angled (b) capillary images of Figure 6-13. In each case the direction of the profile is indicated by a red line, and the profile is shown below the slice from which it was extracted.

The SNR experiment was performed to ascertain at what distance below the table top the system reliably detects different size lesions with in low contrast conditions. Table 6-8 reports the depth from the top plane going through the uppermost pixelated crystal in the ring at which the SNR is first considered detectable under the Rose criterion. It also reports the SNR of the central slice of the sagittal view of the lesion. For the 1.2 cm lesion both 3:1 and 2:1 LBRs were detectable (SNR  $\geq 3$ ) at a depth of 3 mm. The SNR for the 0.8 mm diameter lesions is  $\sim 3.8$  at 3:1 LBR at a depth of 4 mm, while the SNR was  $\sim 3.0$  at 2:1 LBR at a depth of 11 mm. As expected the SNR rises as the lesion moves from the top of the ring's axial VOV towards the center of the VOV as seen Figure 6-16.

Table 6-8: Depth of highest (vertically) detectable lesion under Rose criterion.

	Highest Observed Detectable Lesion			
Lesion Diameter (cm)	1.2	1.2	0.8	0.8
LBR*	3:1	2:1	3:1	2:1
SNR - Coronal	4.11	4.06	4.28	3.04
SNR - Sagittal	4.84	4.47	3.82	3.08
Lesion Depth (mm)	3	3	4	11
Effective Depth from Top of Table (mm)	9.25	9.25	10.25	17.25

\* Lesion-to-Background Ratio

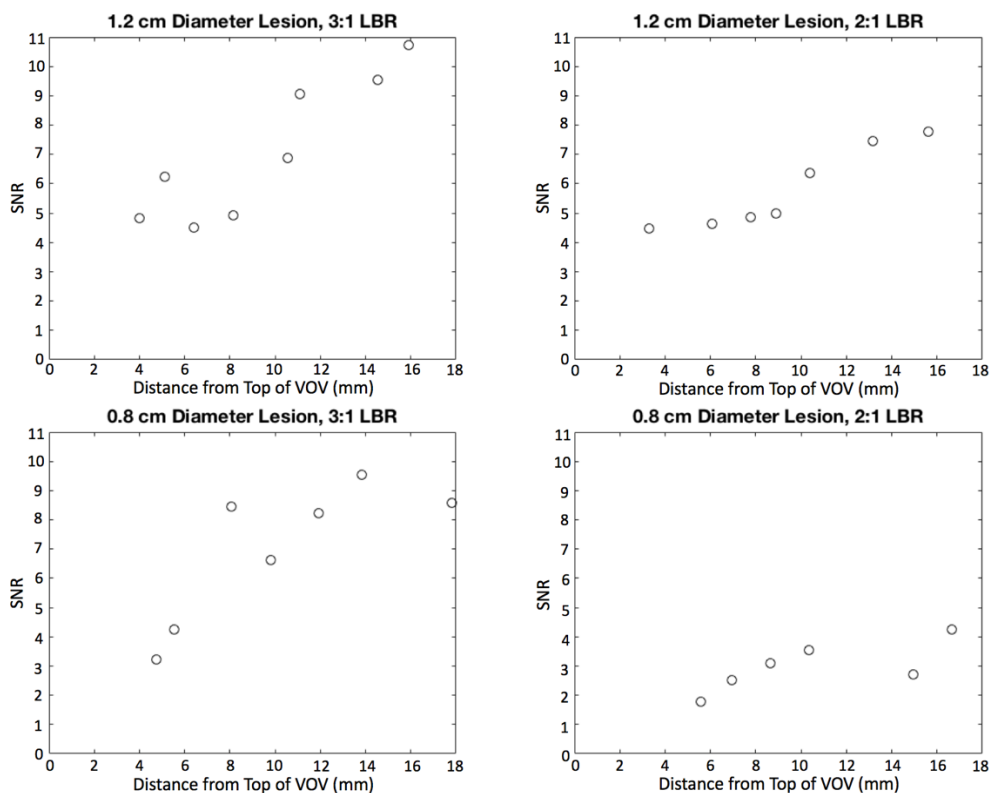


Figure 6-16: SNR values for each lesion and LBR pair as a function of depth from the top edge of the volume of view of the PET ring.

### 6.3.6 Pilot Human Study

Of the 11 biopsied lesions, 7 were malignant and 4 were benign. Table 6-9 shows the sensitivity, specificity, PPV, and accuracy for the BRPET scanner compared those of the CE-MRI under both the conditions that a) lesions rated  $\geq 3$  were considered to be positive findings and b) that lesions rated  $\geq 4$  were considered positive. Figure 6-17 shows a transverse slice of a subject for whom cancer was also detected in the MRI, while Figure 6-18 shows sagittal, transverse, and coronal views of a subject whose biopsy was benign.

Table 6-9: Performance Metrics For BRPET

Metric	Score $\geq 3$ Was Positive			Score $\geq 4$ Was Positive		
	BRPET		MRI	BRPET		MRI
	NM 1	NM 2	BR	NM 1	NM 2	BR
Sensitivity	100	100	100	85.7	100	100
Specificity	100	100	25	100	100	25
PPV	100	100	70	100	100	70
Accuracy	100	100	72.7	90.9	100	72.7

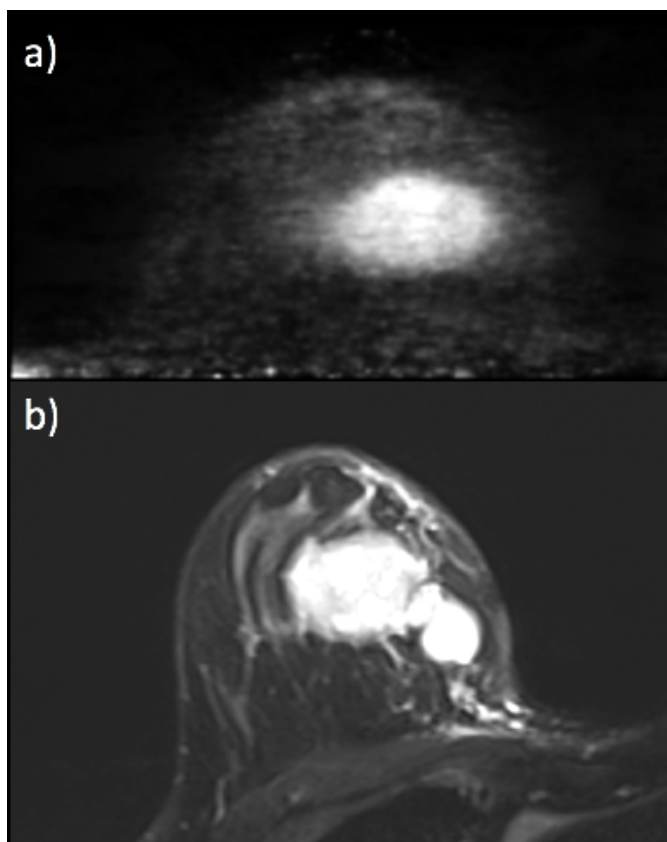


Figure 6-17: (a) BRPET scan of the right breast of a subject with a known malignancy originally seen on a 2D mammogram and then staged with a CEMRI, seen in (b).

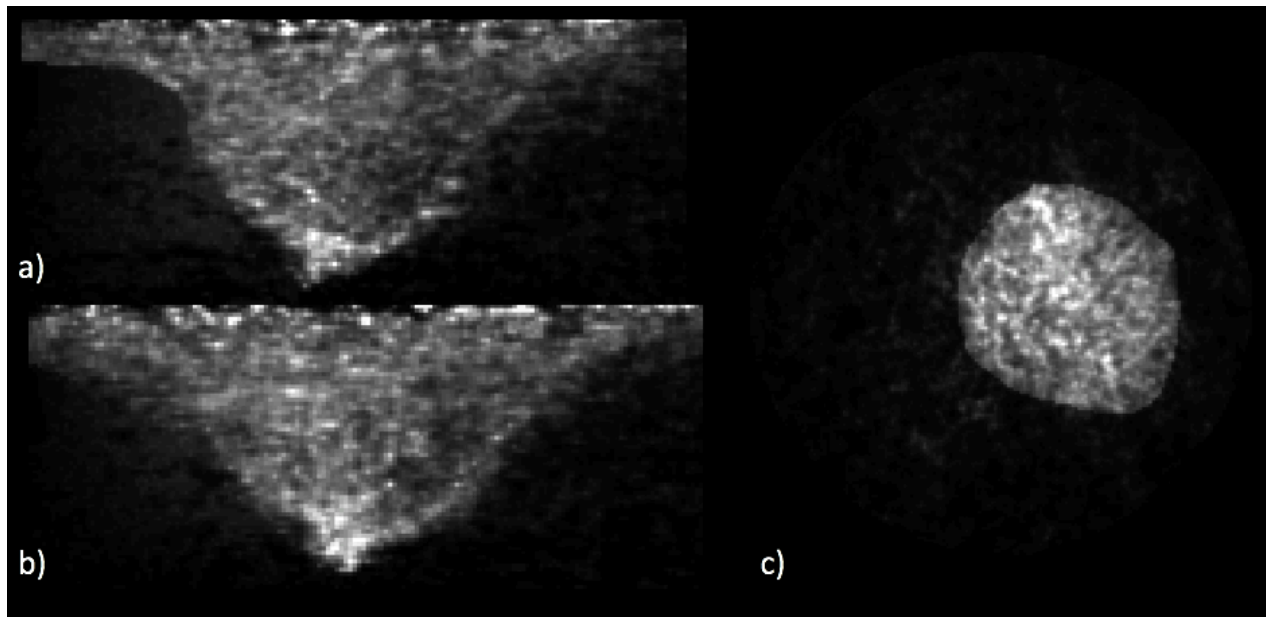


Figure 6-18: Example images of a negative BRPET study. Sagittal (a), transverse (b), and coronal (c) planes are shown.

## 6.4 Discussion

The BRPET system was designed with the main goal of improving the visualization of posterior breast tissue while attempting to also keep the spatial resolution and system sensitivity comparable to those of other dedicated breast PET imagers. The spatial resolution of the BRPET system was found to be comparable to those of commercial dedicated breast PET systems (Table 6-10). This indicates that the main goal of the original dedicated breast PET systems of improving spatial resolution beyond that of WBPET was reached. The full PET rings used in each of the systems of Table 6-10 also enable nearly isotropic spatial resolution, unlike the limited angle PEM systems employing opposed planar detectors.

Table 6-10: Comparison of BRPET spatial resolution and that of commercial systems <sup>14,15</sup>.

System	Resolution at Center VOV (mm)		
	Axial	Radial	Tangential
BRPET	1.8	1.7	1.9
MAMMI	1.6	1.8	1.9
Shidmazu	2	1.6	1.7

The shape of the system sensitivity profile along the ring's axial dimension was as expected, with the peak of sensitivity occurring in the center of the axial dimension. The highest sensitivity in a PET system is at the center of the volume of view, since there the number of geometrically possible lines of response is greatest. Sensitivity falls linearly as a function of the axial distance from the ring's central plane (Figure 6-11). The magnitude of the system sensitivity of the BRPET system was lower than that reported by the MAMMI system (0.97% peak sensitivity and 19.3% total system absolute sensitivity, versus 1.8% peak sensitivity and

20% total system sensitivity for MAMMI) <sup>14</sup>. The similarity between total system sensitivity of the BRPET system and the MAMMI system is at first glance unexpected due to the NECR advantage the MAMMI System has over the BRPET system. The peak NECR for the BRPET system is 5.33 kcps while the MAMMI system's peak NECR is about 25 kcps <sup>14</sup>. However, at low activities, as required by the NEMA protocols, the counting rate capabilities of the systems are similar leading to similar sensitivities <sup>20</sup>.

The BRPET scanner's original trigger circuitry allowed the system to be triggered when a coincidence event occurred between any two modules in the BRPET ring. This led to an extremely high coincidence rate, resulting in low NEC rate due to the accumulation of deadtime. This mode of operation ultimately forced the system counting to halt. The triggering hardware was replaced with the MCFD-16 which allowed for the multiple detector and timing window configurations described above. The configurations tested began with the most stringent trigger set up used (1-3 module pair with 8 ns coincident window). This allowed a coincidence to be made with a module by only the 3 modules directly across from it and the coincidence was only counted if a detection event happened within 8 ns of another detected event. This setup ensured a minimum number of triggers would be caused by random or scattered events, but as seen in table 6-5 it also allowed the lowest total counting rate. Multiple configurations were tested to identify the maximum NEC rate using 5 modules and 12 ns coincidence window width. When the configuration allowed 7 modules the number of coincidence events again led to an accumulation of dead time. This most likely occurs in the triggering system and may require the adaptation of a more specialized triggering system allowing for higher trigger rates.

The results of the high contrast depth experiments showed that under high contrast (e.g. high lesion uptake) conditions the BRPET system is capable of imaging tissue up to within 6.25 mm of the top surface of the examination table. However, lesions in true breast images are likely to result in a lower image contrast. For example, the results of the low contrast lesion experiment showed that a 1.2 diameter spherical lesion with an LBR of 2:1 would have an SNR greater than 3 only for locations greater than 3 mm inside the upper plane of the scanner's VOV, i.e. greater than 9.25 mm below the table top. For an 0.8 mm lesion with the same LBR these distances become 11 mm and 17.25 mm, respectively. Moving to a greater (but still small) LBR of 3:1 had no effect on the depth of detectability for the 1.2 mm lesion, but greatly affected the depth of detectability for the 0.8 mm lesion. The smaller lesion became detectable at a depth within the VOV of 4 mm (10.25 mm below the top of the exam table). Figure 6-16 illustrates the drop in SNR as the lesion is moved toward the edge of the VOV, which is expected due to the drop in sensitivity away from the center plane of the detector ring. It also shows depicts the proportional relationship between lesion detectability near the detector edge and lesion size and LBR. It is important to note that the lesions in this experiment were very low contrast. After analyzing 76 cancers Buck *et al* showed that the mean LBR for ductal breast cancer was 17.3 while for lobular cancer it was 6.5. This would imply that on average the visualizable depth from the top of the exam table for an 0.8 mm lesion would typically be no more than 4 mm. Further study is required to learn how small of a lesion can be reliably detected. To our knowledge no study evaluating the depth of at which dedicated PET systems can reliably image has been completed with similar systems, so, there are no data to which to compare.

The results of the pilot human evaluation of the BRPET system imply that BRPET is both a feasible and accurate means of detecting breast cancer. The sensitivities and specificities for both readers were promising, with only one malignancy being missed if a malignancy is considered a lesion ranked  $\geq 4$ . The CEMRI results showed a very high sensitivity but showed a loss of specificity when compared to the BRPET results. The observed drop in specificity for the CEMRI was due to an increase in false positives. Although the BRPET's performance was encouraging, there were some issues that would need to be addressed. First, is image quality, due to the desire to reduce dose, the count statistics in some of the images was low resulting in

“not adequate” or “barely adequate” image quality scores from the readers. This issue could be solved in several ways. The quickest fix would be to either increase the FDG dose or the increase the scan time. However, it would be advantageous to keep both low, this would then require an improvement in the data acquisition hardware, to improve the count rate capabilities of the system. If the count rate system could be improved the higher sensitivity would allow for the same dose and time to be used. A second way of improving count rates beyond the data acquisition hardware would be the addition of a second PET ring. This would not only allow a higher count rate and sensitivity but would also cut scan time down due to a larger VOV.

The BRPET scanner is a single modality system, so there is an inherent disadvantage when compared to multi-modality systems such as the DMT system. The pre-registered scans of the dual modality scanners allow for quick and accurate co-registration of anatomical and functional images. However, it may be possible to use multi-modality fiducial markers or rigid edges for co-registration of BRPET images with other 3-D image sets. Such markers have been used by Madhav et al. in Duke’s preclinical SPECT/CT system and have been explored with whole body scanners for treatment planning of head and neck tumors<sup>34,35</sup>.

As with other dedicated functional imaging systems, BRPET could potentially be used as an alternative to CEMRI. This type of system has the potential of providing similar cancer detection sensitivity while improving specificity compared to CEMRI. In a recent study of 208 women comparing the Naviscan PEM system to CEMRI, the sensitivity and specificity of PEM were found to be 85% and 75%, respectively, compared to 98% and 48%, respectively for CEMRI.<sup>36</sup> However, it is of note that in that study the number of benign tumors was small so the specificity could not be proven to be significantly different.

Another clinical situation in which the BRPET system may be especially beneficial is in the staging and restaging of patients. This includes the detection of multifocal breast cancers, either ipsilateral or contralateral to a known cancer. Other applications include the characterization of known breast masses, and monitoring patients with a history of breast cancer. In addition, FDG-BRPET could afford the ability to observe relative cellular metabolic rates, making the BRPET system a promising alternative to CT for monitoring early tumor response to therapies. This could be especially valuable in the growing fields of neoadjuvant therapy and personalized medicine. Finally, although it is not in the scope of this project, it is possible that a biopsy system could be integrated into this type of dedicated PET system to permit PET-guided biopsy of lesions that are detectable by PET but occult on typical biopsy guidance modalities such as x-ray or ultrasound. Such a system could also be used for pre-surgical lesion marking for non-palpable lesions.

The characterization and pilot human evaluation of the BRPET system was encouraging; however, the human study was small. The characterization proved the system’s spatial resolution to be comparable to that of a commercial system, but showed it underperformed in count rate performance and system sensitivity. The system was shown to have a small dead area from the top of the exam table due to the unique slanted light guide, but the significance of this could not be verified because none of the study subjects had lesions near their chest wall.

## References

- 1 Wu D, Gambhir SS. Positron Emission Tomography in Diagnosis and Management of Invasive Breast Cancer: Current Status and Future Perspectives. *Clinical Breast Cancer* 2003;**4**, **Supplement 1**:S55–63. <https://doi.org/10.3816/CBC.2003.s.016>.
- 2 Avril N, Adler LP. F-18 Fluorodeoxyglucose-Positron Emission Tomography Imaging for Primary Breast Cancer and Loco-Regional Staging. *Radiologic Clinics of North America* 2007;**45**:645–57. <https://doi.org/10.1016/j.rcl.2007.05.004>.
- 3 Thompson CJ, Murthy K, Weinberg IN, Mako F. Feasibility study for positron emission mammography. *Medical Physics* 1994;**21**:529–38. <https://doi.org/10.1118/1.597169>.
- 4 Weinberg I, Majewski S, Weisenberger A, Markowitz A, Aloj L, Majewski L, *et al*. Preliminary results for positron emission mammography: real-time functional breast imaging in a conventional mammography gantry. *Eur J Nucl Med* 1996;**23**:804–6. <https://doi.org/10.1007/BF00843710>.
- 5 Murthy K, Aznar M, Thompson CJ, Loutfi A, Lisbona R, Gagnon JH. Results of Preliminary Clinical Trials of the Positron Emission Mammography System PEM-I: A Dedicated Breast Imaging System Producing Glucose Metabolic Images Using FDG. *J Nucl Med* 2000;**41**:1851–8.
- 6 Rosen EL, Turkington TG, Soo MS, Baker JA, Coleman RE. Detection of Primary Breast Carcinoma with a Dedicated, Large-Field-of-View FDG PET Mammography Device: Initial Experience. *Radiology* 2005;**234**:527–34. <https://doi.org/10.1148/radiol.2342040654>.
- 7 MacDonald L, Edwards J, Lewellen T, Haseley D, Rogers J, Kinahan P. Clinical Imaging Characteristics of the Positron Emission Mammography Camera: PEM Flex Solo II. *J Nucl Med* 2009;**50**:1666–75. <https://doi.org/10.2967/jnumed.109.064345>.
- 8 Kalinyak JE, Berg WA, Schilling K, Madsen KS, Narayanan D, Tartar M. Breast cancer detection using high-resolution breast PET compared to whole-body PET or PET/CT. *Eur J Nucl Med Mol Imaging* 2014;**41**:260–75. <https://doi.org/10.1007/s00259-013-2553-1>.
- 9 Eo JS, Chun IK, Paeng JC, Kang KW, Lee SM, Han W, *et al*. Imaging sensitivity of dedicated positron emission mammography in relation to tumor size. *The Breast* 2012;**21**:66–71. <https://doi.org/10.1016/j.breast.2011.08.002>.
- 10 Berg WA, Madsen KS, Schilling K, Tartar M, Pisano ED, Larsen LH, *et al*. Breast Cancer: Comparative Effectiveness of Positron Emission Mammography and MR Imaging in Presurgical Planning for the Ipsilateral Breast. *Radiology* 2011;**258**:59–72. <https://doi.org/10.1148/radiol.10100454>.
- 11 Wu Y, Bowen SL, Yang K, Packard N, Fu L, Jr GB, *et al*. PET characteristics of a dedicated breast PET/CT scanner prototype. *Phys Med Biol* 2009;**54**:4273. <https://doi.org/10.1088/0031-9155/54/13/020>.
- 12 Furuta M, Kitamura K, Ohi J, Tonami H, Yamada Y, Furumiya T, *et al*. Basic Evaluation of a C-Shaped Breast PET Scanner. Presented at the 2009 IEEE Nuclear Science Symposium Conference Record (NSS/MIC).
- 13 Kitamura K, Ohi J, Tonami H, Yamada Y, Furumiya T, Furuta M, *et al*. Development of a C-Shaped Breast PET Scanner Equipped with Four-Layer DOI

- Detectors. Presented at the 2008 IEEE Nuclear Science Symposium Conference Record.
- 14 Moliner L, González AJ, Soriano A, Sánchez F, Correcher C, Orero A, *et al.* Design and evaluation of the MAMMI dedicated breast PET. *Medical Physics* 2012;**39**:5393–404. <https://doi.org/10.1118/1.4742850>.
  - 15 Miyake KK, Matsumoto K, Inoue M, Nakamoto Y, Kanao S, Oishi T, *et al.* Performance Evaluation of a New Dedicated Breast PET Scanner Using NEMA NU4-2008 Standards. *J Nucl Med* 2014;**55**:1198–203. <https://doi.org/10.2967/jnumed.113.131565>.
  - 16 Soriano A, Sánchez F, Carrilero V, Pardo A, Vidal LF, Vázquez C, *et al.* Performance Evaluation of the Dual Ring MAMMI Breast PET. Presented at the 2013 IEEE Nuclear Science Symposium and Medical Imaging Conference (2013 NSS/MIC).
  - 17 Teixeira SC, Rebolleda JF, Koolen BB, Wesseling J, Jurado RS, Stokkel MPM, *et al.* Evaluation of a Hanging-Breast PET System for Primary Tumor Visualization in Patients With Stage I–III Breast Cancer: Comparison With Standard PET/CT. *American Journal of Roentgenology* 2016;**206**:1307–14. <https://doi.org/10.2214/AJR.15.15371>.
  - 18 Lima M, Nakamoto Y, Kanao S, Sugie T, Ueno T, Kawada M, *et al.* Clinical performance of 2 dedicated PET scanners for breast imaging: initial evaluation. *J Nucl Med* 2012;**53**:1534–42. <https://doi.org/10.2967/jnumed.111.100958>.
  - 19 Majewski S. High resolution PET breast imager with improved detection efficiency. US7732774B2, 2010.
  - 20 Luo W, Anashkin E, Matthews CG. Performance Evaluation of a PEM Scanner Using the NEMA NU 4 #x2014;2008 Small Animal PET Standards. *IEEE Transactions on Nuclear Science* 2010;**57**:94–103. <https://doi.org/10.1109/TNS.2009.2036847>.
  - 21 Popov V, Majewski S, Weisenberger AG. Readout Electronics for Multianode Photomultiplier Tubes with Pad Matrix Anode Layout. Presented at the 2003 IEEE Nuclear Science Symposium. Conference Record (IEEE Cat. No.03CH37515).
  - 22 Cherry SR, Shao Y, Silverman RW, Meadors K, Siegel S, Chatziioannou A, *et al.* MicroPET: a high resolution PET scanner for imaging small animals. *IEEE Transactions on Nuclear Science* 1997;**44**:1161–6. <https://doi.org/10.1109/23.596981>.
  - 23 Chatziioannou AF, Cherry SR, Shao Y, Silverman RW, Meadors K, Farquhar TH, *et al.* Performance Evaluation of microPET: A High-Resolution Lutetium Oxyorthosilicate PET Scanner for Animal Imaging. *J Nucl Med* 1999;**40**:1164–75.
  - 24 Wang Y, Seidel J, Tsui BMW, Vaquero JJ, Pomper MG. Performance evaluation of the GE healthcare eXplore VISTA dual-ring small-animal PET scanner. *J Nucl Med* 2006;**47**:1891–900.
  - 25 *Performance Measurements of Small Animal Positron Emission Tomographs (PETs)*. n.d. URL: <https://www.nema.org/Standards/Pages/Performance-Measurements-of-Small-Animal-Positron-Emission-Tomographs.aspx> (Accessed 13 January 2017).
  - 26 Cherry SR, Sorenson J, Phelps ME, Methé BM. Physics in Nuclear Medicine. *Med Phys* 2004;**31**:2370–1. <https://doi.org/10.1118/1.1776595>.

- 27 Strother SC, Casey ME, Hoffman EJ. Measuring PET scanner sensitivity: relating countrates to image signal-to-noise ratios using noise equivalents counts. *IEEE Transactions on Nuclear Science* 1990;**37**:783–8. <https://doi.org/10.1109/23.106715>.
- 28 Rose A. Vision: Human and Electronic. *Applied Solid State Physics*. Springer, Boston, MA; 1970. p. 79–160.
- 29 Avril N, Bense S, Ziegler SI, Dose J, al et. Breast imaging with fluorine-18-FDG PET: Quantitative image analysis. *The Journal of Nuclear Medicine; New York* 1997;**38**:1186–91.
- 30 Buck A, Schirrmeister H, Kühn T, Shen C, Kalker T, Kotzerke J, et al. FDG uptake in breast cancer: correlation with biological and clinical prognostic parameters. *Eur J Nucl Med* 2002;**29**:1317–23. <https://doi.org/10.1007/s00259-002-0880-8>.
- 31 ICRP: *ICRP Publication 106*. n.d. URL: <http://www.icrp.org/publication.asp?id=ICRP%20Publication%20106> (Accessed 22 July 2018).
- 32 Brix G, Noßke D, Leche U. Radiation exposure of patients undergoing whole-body FDG-PET/CT examinations. *Nuklearmedizin* 2014;**53**:217–20. <https://doi.org/10.3413/Nukmed-0663-14-04>.
- 33 The 2007 Recommendations of the International Commission on Radiological Protection. ICRP publication 103. *Ann ICRP* 2007;**53(5)**:1–322.
- 34 Madhav P, Crotty DJ, McKinley RL, Tornai MP. Initial Development of a Dual-Modality SPECT-CT System for Dedicated Mammotomography. Presented at the 2006 IEEE Nuclear Science Symposium Conference Record.
- 35 Daisne J-F, Sibomana M, Bol A, Cosnard G, Lonneux M, Grégoire V. Evaluation of a multimodality image (CT, MRI and PET) coregistration procedure on phantom and head and neck cancer patients: accuracy, reproducibility and consistency. *Radiotherapy and Oncology* 2003;**69**:237–45. <https://doi.org/10.1016/j.radonc.2003.10.009>.
- 36 Schilling K, Narayanan D, Kalinyak JE, The J, Velasquez MV, Kahn S, et al. Positron emission mammography in breast cancer presurgical planning: comparisons with magnetic resonance imaging. *Eur J Nucl Med Mol Imaging* 2011;**38**:23–36. <https://doi.org/10.1007/s00259-010-1588-9>.

## Chapter 7

### Conclusions and Future Works

The purpose of this work was to evaluate two novel nuclear medicine based dedicated breast imaging systems designed to improve upon the limitations of current dedicated breast imaging systems. A clinical trial comparing the added benefit of molecular breast tomosynthesis to single view digital breast tomosynthesis using the University of Virginia's novel dual modality tomosynthesis system was completed. To prepare for the development of a model observer designed to test DMT data sets, the first version of synthetic DMT images for use as a clinically relevant training set were created and evaluated. A unique low-profile gamma camera designed to replace the existing gamma camera on the DMT system was evaluated and compared to the current camera. Lastly, a dedicated breast PET system with unique slanted light guides to improve the visualization of posterior breast tissue was optimized and evaluated. A small pilot clinical study was then conducted to discern the if a larger study is warranted.

#### 7.1 Conclusions

The DMT clinical trial imaged 75 women with a total 83 biopsied lesions, 21 of which were malignant and 62 were benign. A nuclear medicine radiologist read through all MBT images ranking any findings on provided reader interpretation sheets. These sheets were later used by a breast radiologist in larger reader session. A single breast radiologist read all 75 cases in a sequential order starting with DBT alone and adding single view 2D mammography followed by MBT images and the nuclear medicine radiologist's consulting sheet. ROC curves of the reader results were created. The analysis of the ROC curves showed the addition of MBT data to the DBT + 2D mammography significantly increased the diagnostic accuracy of single view DMT + 2D mammography. Interestingly, MBT alone was seen to have a significantly higher diagnostic accuracy when compared to that of the single view DMT + 2D mammography. To improve upon the statistical significance of the study a multi-reader analysis should be completed. This would allow for the analysis of inter-reader variability and provide a better understanding of the value of the addition of MBT data.

A set of synthetic images with and without signal were created to be used as a training set for a model observer. These images were created using true human images from the DMT system using principal component analysis to create a set of eigenDBT images and eigenMBT images. The set of eigenimages were then used to create the synthetic breasts via a weighed addition. To be useful as a training set it is essential the synthetic backgrounds created mimic the noise structure of the human images. To test this the human and synthetic images were evaluated by fitting the images' noise power spectrums (NPS) with a power law of form  $P(f) = A/f^\beta$ , where  $f$  is radial frequency. This analysis of the NPS results with a two-tailed paired Student's t-test showed the background noise characteristic were not significantly different from those of the human images.

The new low-profile gamma camera was designed to improve upon the older camera's sensitivity and with the goals of minimizing the overall thickness of the camera while increasing the field of view (FOV) and maximizing the system's sensitivity. The camera met all of these design goals and evaluation of the system showed the increased intrinsic sensitivity coupled with a higher sensitivity collimator allows for the camera to have an improved signal-to-noise ratio. The addition of this camera to the DMT system will improve the MBT systems image

quality when using the current imaging protocols. Due to the superior performance, it is worth examining different imaging protocols, such as dose reduction.

The BRPET system was designed to improve the visualization of the posterior breast tissue, without losing the benefit of high spatial resolution dedicated systems were originally built for. The characterization of the system showed the system resolution was comparable to similar commercial devices. The systems sensitivity was observed to slightly underperform compared to the same devices. This is most likely due to the system's count rate capabilities. The system originally performed with a suboptimal constant fraction discriminator configuration. Optimization of these configurations resulted in a final peak NEC rate of 5.33 kcps. However, this count rate is still roughly 5 times lower than the commercial systems. Experiments were conducted to examine the amount of space between the top of the exam table and the PET ring that is out of the system's field of view. The results showed this system could reliably detect very low contrast 1.2 cm lesions located 9.25 mm below the top of the table. While smaller lesions were shown to be visible, the lesion-to-background ratio of these lesions greatly affected the depth at which they were visible.

A pilot human study comparing the BRPET system to CE-MRI included 10 subjects with a total of 11 biopsied lesions, of which 7 were malignant and 4 were benign. Two experienced nuclear medicine radiologists read all 10 BRPET cases and scored any findings, while an MQSA certified breast radiologist read all 10 CE-MRIs and scored any findings. The results were then compared to biopsied truth and the sensitivities and specificities were calculated. The resulting sensitivity and specificity for the BRPET system were both 100% for both readers when rankings  $\geq 3$  were considered positive, while the sensitivity of reader 1 dropped to 85.7% when rankings  $\geq 4$  were considered positive. Comparatively, the resulting sensitivity and specificity for the CE-MRI were 100 and 25, respectively. This showed a possible advantage in specificity for the BRPET system over that of CE-MRI. None of the imaged subjects had biopsy proven malignancies near the chest wall, so it was not possible to verify the effectiveness of the slanted light guides in human subjects. These results are encouraging and warrant the pursuit of a larger reader study to determine clinical feasibility of the system.

## 7.2 Future Works

### 7.2.1 Dual Modality Tomosynthesis and Low-Profile Gamma Camera

The work presented in this dissertation showed the advantages the LP gamma camera has over the DMT system's original gamma camera. The next step in the development of the DMT system is to replace the original gamma camera with the LP camera, this process has been started. With the implementation of the LP camera, a new set of studies can begin. Beyond the physical advantage of a larger field of view and lower profile, the LP camera provides a higher sensitivity which will allow for the testing of new imaging protocols. Recent literature has shown low dose 2D gamma imaging to be reliable in both phantom and patient evaluation<sup>1-3</sup>. With the higher sensitivity of the LP gamma camera it will be possible to lower the injected dose while keeping the image quality similar to what was obtained by the original camera. The higher sensitivity of the camera could also allow for shorter data acquisition per projection view (assuming injected dose is not changed). This could lead to the testing of imaging schemes in which more projection views are acquired in the same overall exam time. More views or larger angular range could increase the spatial resolution, lesion contrast, and lesion SNR in the undersampled direction. There is an inherent tradeoff between both scan time and image quality and injected dose and image quality. Due to this an optimization study will have to be conducted to ensure the reduction of injected dose and modified imaging scheme do not degrade the image quality.

### 7.2.2 Synthetic DMT Images

The synthetic images were designed to be utilized in the training of a model observer. However, this set of images is constrained to a specific breast size and shape. This can be improved upon with the addition of a reshaping algorithm such as finite element analysis<sup>4</sup>. The implementation of such an algorithm would allow for use of all normal DMT breast images. Recall currently only breasts large enough for the breast mask fit in were used. It would also allow for many different breast shapes to be created. This would improve the final training set by more realistically representing the variability in breast size and shape. A more effective tumor isolation algorithm will also be developed. Currently, the tumor is isolated out of the projection views using pixel value thresholding. This works well for solid masses, but many tumors have irregular and spiculated shapes. The creation of a more advanced edge detecting algorithm would allow for more complicated tumors to be isolated and inserted into the synthetic data sets advancing the realism of the training set.

### 7.2.3 Dedicated Breast Ring PET

The BRPET system was shown to have comparable spatial resolution to that of current commercial devices, however lacked in count rate performance. This is believed to be caused by the deadtime limitation caused by the constant fraction discriminator and timing circuit in conjunction with the time delay in digitization of the data from the analog-to-digital converter. By updating these electronics, the overall performance in count rate and subsequently system sensitivity would allow for greater image quality within the detectors FOV. This would improve the detectability of low contrast objects near the top of the detector ring.

The promising results of the pilot clinical trial warrant a larger clinical trial. In this study it would be worth comparing the breast cancer detection efficiency of the BRPET system to other adjunct imaging systems such as CEMRI and US. A secondary focus of the larger clinical trial would be the recruitment of subjects with findings along the chest wall. This is needed to verify the effectiveness of the system to see the posterior breast tissue.

## References

- 1Hruska CB, Weinmann AL, O'Connor MK. Proof of concept for low-dose molecular breast imaging with a dual-head CZT gamma camera. Part I. Evaluation in phantoms. *Medical Physics* 2012;**39**:3466–75. <https://doi.org/10.1118/1.4718665>.
- 2Hruska CB, Weinmann AL, Tello Skjerseth CM, Wagenaar EM, Connors AL, Tortorelli CL, *et al*. Proof of concept for low-dose molecular breast imaging with a dual-head CZT gamma camera. Part II. Evaluation in patients. *Med Phys* 2012;**39**:3476–83. <https://doi.org/10.1118/1.4719959>.
- 3Kuhn KJ, Rapelyea JA, Torrente J, Teal CB, Brem RF. Comparative Diagnostic Utility of Low-Dose Breast-Specific Gamma Imaging to Current Clinical Standard. *The Breast Journal* 2016;**22**:180–8. <https://doi.org/10.1111/tbj.12550>.
- 4Sturgeon GM, Park S, Segars WP, Lo JY. Synthetic breast phantoms from patient based eigenbreasts. *Medical Physics* n.d.;**44**:6270–9. <https://doi.org/10.1002/mp.12579>.

## Appendix A – DMT Clinical Trial Study Sheets

### DUAL MODALITY BREAST SCANNER READER STUDY STUDY INTERPRETATION FORM

#### Digital Breast Tomosynthesis (DBT)

CASE #: \_\_\_\_\_ READER: \_\_\_\_\_ DATE OF REVIEW: \_\_\_\_\_

**A) IMAGE QUALITY:**

1 Not Adequate     2 Barely Adequate     3 Adequate     4 Good     5 Excellent

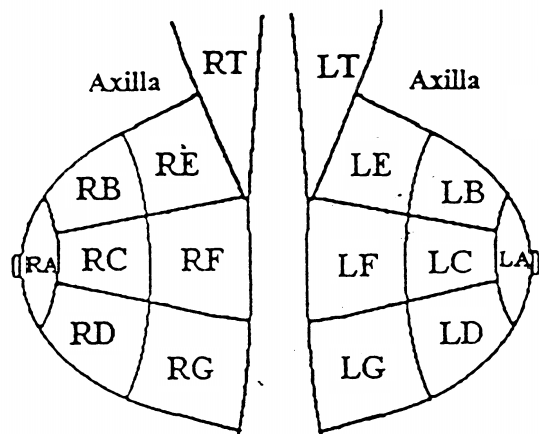
**Positioning:**    Poor    Adequate    Good

**B) BREAST DENSITY:**

1 Fatty     2 Scattered     3 Heterogeneous     4 Dense

**C) Circle findings in the diagram below OR  NO FINDINGS**

MLO VIEW:



**FINDING #1:**  LEFT  RIGHT

Location : \_\_\_\_\_ (i.e. LE) Clock Position: \_\_\_\_\_

Central slice / extent – MLO View: \_\_\_\_\_ / \_\_\_\_\_ – \_\_\_\_\_ Architectural distortion  Focal asymmetryMass – Shape:  round  oval  irregular– Margin:  circumscribed  indistinct  obscured  spiculated  microlobulated– Density:  fat-containing  low density  equal density  high densityCalcifications – Morphology:  coarse heterogeneous  amorphous  fine pleomorphic  Fine linear– Distribution:  Diffuse  Regional  Grouped  Linear  SegmentalRatings –  1- Definitely Benign  2- Probably Benign  3- Indeterminant  4- Probably Malignant 5- Definitely Malignant

Confidence level (of rating): \_\_\_\_\_%

**FINDING #2**  LEFT  RIGHT

Location : \_\_\_\_\_ (i.e. LE) Clock Position: \_\_\_\_\_

Central slice / extent – MLO View: \_\_\_\_\_ / \_\_\_\_\_ – \_\_\_\_\_ Architectural distortion  Focal asymmetryMass – Shape:  round  oval  irregular– Margin:  circumscribed  indistinct  obscured  spiculated  microlobulated– Density:  fat-containing  low density  equal density  high densityCalcifications – Morphology:  coarse heterogeneous  amorphous  fine pleomorphic  Fine linear– Distribution:  Diffuse  Regional  Grouped  Linear  SegmentalRatings –  1- Definitely Benign  2- Probably Benign  3- Indeterminant  4- Probably Malignant 5- Definitely Malignant

Confidence level (of rating): \_\_\_\_\_%

**FINDING #3**  LEFT  RIGHT

Location : \_\_\_\_\_ (i.e. LE) Clock Position: \_\_\_\_\_

**Central slice / extent – MLO View:** \_\_\_\_\_ / \_\_\_\_\_ – \_\_\_\_\_

**Architectural distortion**     **Focal asymmetry**

**Mass – Shape:**  round     oval     irregular

– **Margin:**  circumscribed     indistinct     obscured     spiculated     microlobulated

– **Density:**  fat-containing     low density     equal density     high density

**Calcifications – Morphology:**  coarse heterogeneous     amorphous     fine pleomorphic     Fine linear

– **Distribution:**  Diffuse     Regional     Grouped     Linear     Segmental

**Ratings** –  1- Definitely Benign     2- Probably Benign     3- Indeterminant     4- Probably Malignant

5- Definitely Malignant

**Confidence level (of rating):** \_\_\_\_\_%

**DUAL MODALITY BREAST SCANNER READER STUDY  
STUDY INTERPRETATION FORM**

**MOLECULAR BREAST TOMOSYNTHESIS (MBT)**

CASE #: \_\_\_\_\_ READER: \_\_\_\_\_ DATE OF REVIEW: \_\_\_\_\_

**A) IMAGE QUALITY:**

1 Not Adequate    2 Barely Adequate    3 Adequate    4 Good    5 Excellent

**Positioning:**  Poor    Adequate    Good

**B) BACKGROUND UPTAKE:**

**Left:**    0 no uptake    1 minimal    2 mild    3 moderate    4 intense

homogenous    heterogenous

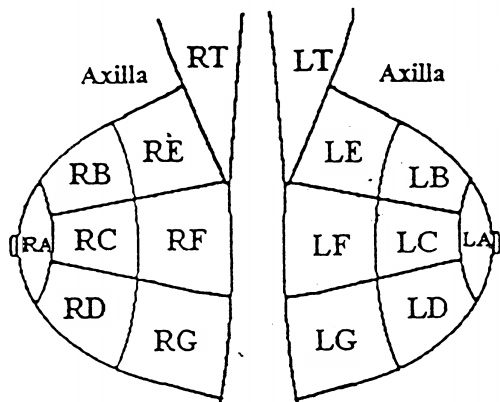
**Right:**    0 no uptake    1 minimal    2 mild    3 moderate    4 intense

homogenous    heterogenous

**Symmetry:**  symmetrical    asymmetrical

**C) Circle findings in the diagram below OR  NO FINDINGS**

**MLO VIEW:**



**FINDING #1:**  LEFT    RIGHT

**Location :** \_\_\_\_\_ (i.e. LE)   **Clock Position:** \_\_\_\_\_

**Central slice / extent – MLO View:** \_\_\_\_\_ / \_\_\_\_\_ – \_\_\_\_\_

**Focus – Number:**  solitary    multiple: \_\_\_\_\_

**Mass – Shape:**  oval    round    irregular

– **Internal uptake patterns:**  homogeneous    heterogeneous    rim uptake

– **Uptake relative to background:**  mild    moderate    intense

**Non-mass uptake – Distribution:**  focal    regional    linear/ductal    segmental    multiple regions    diffuse

– **Internal enhancement patterns:**  homogeneous    heterogeneous

– Uptake relative to background:  mild  moderate  intense

**Ratings** –  1- Definitely Benign  2- Probably Benign  3- Indeterminant  4- Probably Malignant  
 5- Definitely Malignant

Confidence level (of rating): \_\_\_\_\_%

**FINDING #2**  LEFT  RIGHT

Location : \_\_\_\_\_ (i.e. LE) Clock Position: \_\_\_\_\_

**Central slice / extent** – MLO View: \_\_\_\_\_ / \_\_\_\_\_ – \_\_\_\_\_

**Focus – Number:**  solitary  multiple: \_\_\_\_\_

**Mass – Shape:**  oval  round  irregular

– Internal uptake patterns:  homogeneous  heterogeneous  rim uptake

– Uptake relative to background:  mild  moderate  intense

**Non-mass uptake – Distribution:**  focal  regional  linear/ductal  segmental  multiple regions  diffuse

– Internal enhancement patterns:  homogeneous  heterogeneous

– Uptake relative to background:  mild  moderate  intense

**Ratings** –  1- Definitely Benign  2- Probably Benign  3- Indeterminant  4- Probably Malignant  
 5- Definitely Malignant

Confidence level (of rating): \_\_\_\_\_%

**FINDING #3**  LEFT  RIGHT

Location : \_\_\_\_\_ (i.e. LE) Clock Position: \_\_\_\_\_

**Central slice / extent** – MLO View: \_\_\_\_\_ / \_\_\_\_\_ – \_\_\_\_\_

**Focus – Number:**  solitary  multiple: \_\_\_\_\_

**Mass – Shape:**  oval  round  irregular

– Internal uptake patterns:  homogeneous  heterogeneous  rim uptake

– Uptake relative to background:  mild  moderate  intense

**Non-mass uptake – Distribution:**  focal  regional  linear/ductal  segmental  multiple regions  diffuse

– Internal enhancement patterns:  homogeneous  heterogeneous

– Uptake relative to background:  mild  moderate  intense

**Ratings** –  1- Definitely Benign  2- Probably Benign  3- Indeterminant  4- Probably Malignant  
 5- Definitely Malignant

Confidence level (of rating): \_\_\_\_\_%

## Appendix B – Synthetic Image Creation Programs

### Eigenbreast Main Program

Andrew Polemi %  
06/23/17 %

#### Read in image set and set global dimensions

```
M = input('Number of images is:'); % M is number of images to be read
str = input('Type of image is (gamma or xray):','s');
str2 = 'gamma';
type_im = strcmp(str,str2);

if type_im == 1
    % for 3D raw images

    n_x = 66; % # of pixels along x = axis
    n_y = 90; % # of pixels along y = axis
    n_z = 66; % # of slices in image
    n_points = n_x * n_y * n_z;
    % Create average image and Phi images

    [finished_ave]=averageimage3D_gamma(M,n_points); % finished_ave = 1
    then function finished running
else
    % for 3D tomo recons

    n_x = 2007; % # of pixels along x = axis
    n_y = 1120; %1534; % # of pixels along y = axis
    n_z = 66; % 66 now because zeropadding taken away 120; % # of slices in image

    n_points = n_x * n_y * n_z;
    % Create average image and Phi images

    [finished_ave]=averageimage3D(M,n_points); % finished_ave = 1 then
    function finished running
end

clear i f mat str str2 type_im n_x n_y n_z
```

---

#### Create the covariance matrix: L

L = zeros(M);

for i = 1:M

```
f=fopen(['/home/nucmedresearch/DMT/Eigenbreasts/
Final_Eigenbreast_Program/Main_program_results/Recons/
Masked_breast_nzp_gamma_final/phi/phi_' num2str(i) '.raw' ]); % open
image file / '.raw'
mat=fread(f,n_points,'float32','l'); % read image file
```

```

phi1 = mat.';
fclose(f);

for j = 1:M
    f2=fopen(['/home/nucmedresearch/DMT/Eigenbreasts/
Final_Eigenbreast_Program/Main_program_results/Recons/
Masked_breast_nzp_gamma_final/phi/phi_' num2str(j) '.raw' ]); % open
image file / '.raw'
mat2=fread(f2,n_points,'float32','l'); % read image file
phi2 = mat2.';
fclose(f2);

    L(i,j) = phi1 * phi2.'; % the second vector is transposed
    because the we are using row vectors instead of the typical column
    vector
end

fprintf('Percent L completed: %2.f%%\n', i/M * 100)
end

save('L.mat','L')

clear f f2 mat mat2 phi1 phi2

```

---

## Create Eigenimages

```

[finished_uon]=create_eigenbreast3D(M,n_points,L); % finished_uon = 1
then function finished running

```

### Test eigenimages by recreating known image

```

w = zeros(M);
for i = 1:M
    f=fopen(['/home/nucmedresearch/DMT/Eigenbreasts/
Final_Eigenbreast_Program/Main_program_results/Recons/
Masked_breast_nzp_gamma_final/phi/phi_' num2str(i) '.raw' ]); % open
image file / '.raw'
mat=fread(f,n_points,'float32','l'); % read image file
phi = mat.';
fclose(f);

    clear mat f
    [w_test,finished_test]=testeigenimage3D(M,n_points,phi,i); %
    finished_test = 1 then function finished running

    w(i,:) = w_test;

    clear w_test
    save('w_gamma_47eb_final.mat','w')
end

```

---

```
function [finished]=averageimage3D(M,n_points)
% 06/23/17
% Using the image vector create the average image, psi, and the difference
% images, phi.
% NOTE: if you want to output images in figures you need to add n_x, n_y,
% and n_z back into the function.
```

Average face

```
fprintf('starting average breast and phi\n\n')
```

```
sum_v = zeros(1,n_points);
```

```
I = zeros(1,n_points);
```

```
for l = 1:M % create a summed vector of all Image vectors
    f=fopen(['/home/nucmedresearch/DMT/Eigenbreasts/
    Final_Eigenbreast_Program/Main_program_results/Recons/
    Masked_breasts_nzp/originals_nzp/X-Ray_LMLO_masked_'
    num2str(l) '_nzp.raw' ]);
    mat=fread(f,n_points,'float32','l'); % read image file (masked)
    I = mat.';
    fclose(f);

    sum_v = I + sum_v;

    fprintf('Percent average completed: %2.f%% \n', l/M * 100)
```

```
end
```

```
psi = (1/M)*sum_v; % create the average vector psi of all images
```

```
fileID = fopen(['/home/nucmedresearch/DMT/Eigenbreasts/
Final_Eigenbreast_Program/Main_program_results/Recons/
Masked_breasts_nzp/eigenbreast_psi_wmatrix/psi.raw'],'w');
fwrite(fileID,psi,'float32','l');
fclose(fileID);
```

Create Phi

```
phi = zeros(1,n_points); % difference in specific face from average face
```

```
for l = 1:M % create phi
    f=fopen(['/home/nucmedresearch/DMT/Eigenbreasts/
    Final_Eigenbreast_Program/Main_program_results/Recons/
    Masked_breasts_nzp/originals_nzp/X-Ray_LMLO_masked_'
    num2str(l) '_nzp.raw' ]);
    mat=fread(f,n_points,'float32','l'); % read image file (masked)
    I = mat.';
    fclose(f);

    phi = I - psi;

    fileID = fopen(['/home/nucmedresearch/DMT/Eigenbreasts/
    Final_Eigenbreast_Program/Main_program_results/Recons/
    Masked_breasts_nzp/phi/phi_' num2str(l) '.raw' ],'w');
    fwrite(fileID,phi,'float32','l');
    fclose(fileID);
```

```

        fprintf('Percent phi completed: %2.f%%\n' , l/M * 100)
end

finished = 1;

=====

function [finished]=create_eigenbreast3D(M,n_points,L)
% Create Eigenbreast:
% find the eigen vectors of the covariance matrix L
% create eigen vectors, u
% make sure the vectors are orthonormal for the creation of new images

fprintf('starting creation of eigenbreast\n\n' )

[V,D]=eig(L); % D is diagonal matrix of eigenvalues
% V is matrix whose columns are the corresponding right
% eigenvectors

for k= 1:M
    u = zeros(1,n_points);
    uon = zeros(1,n_points);

    for i= 1:M
        f=fopen(['/home/nucmedresearch/DMT/Eigenbreasts/
Final_Eigenbreast_Program/Main_program_results/Recons/
Masked_breast_nzp_gamma_final/phi/phi_' num2str(i) '.raw' ]); % open
image file / '.raw'
        mat=fread(f,n_points,'float32' ,'l' ); % read image file
        phi = mat.';
        fclose(f);

        u = V(i,k) * phi + u; % creation of eigenvectors

    end

    mag = u * u.';
    uon = u/sqrt(mag);

    fileID = fopen(['/home/nucmedresearch/DMT/Eigenbreasts/
Final_Eigenbreast_Program/Main_program_results/Recons/
Masked_breast_nzp_gamma_final/eigenbreast_psi_wmatrix/eigenbreast_'
num2str(k) '.raw' ],'w' );
    fwrite(fileID,uon,'float32' ,'l' );
    fclose(fileID);

    fprintf('Percent eigenbreast completed: %2.f%%\n' , k/M * 100)
end

finished = 1;

=====

function [w,finished]=testeigenimage3D(M,n_points,phi,p)

```

```

% Test the eigenimages by finding weights of original breast and
recreating the breast with the eigenimages

fprintf('testing eigenbreasts\n\n')

w = zeros(1,M);
a = zeros(1,n_points);
w = zeros(1,M);

for i = 1:M
    f=fopen(['/home/nucmedresearch/DMT/Eigenbreasts/
Final_Eigenbreast_Program/Main_program_results/Recons/
Masked_breast_nzp_gamma_final/eigenbreast_psi_wmatrix/eigenbreast_'
num2str(i) '.raw' ]); % open image file / '.raw'
    mat=fread(f,n_points,'float32','l'); % read image file
    uon = mat.';
    fclose(f);

    w(i) = uon * phi.'; % create weighting vector
    a = w(i) * uon + a; % sum weighed eigenbreasts

    fprintf('Percent xray recreation completed: %2.f%%\n', i/M *100)
end

clear mat
clear phi

f=fopen(['/home/nucmedresearch/DMT/Eigenbreasts/
Final_Eigenbreast_Program/Main_program_results/Recons/
Masked_breast_nzp_gamma_final/eigenbreast_psi_wmatrix/psi.raw' ]); %
open image file / '.raw'
mat=fread(f,n_points,'float32','l'); % read image file
psi = mat.';
fclose(f);

clear mat

newI_v = psi + a; % create test image

fileID = fopen(['/home/nucmedresearch/DMT/Eigenbreasts/
Final_Eigenbreast_Program/Main_program_results/Recons/
Masked_breast_nzp_gamma_final/test_images/gamma_'
num2str(p) '_recreated.raw' ],'w');
fwrite(fileID,newI_v,'float32','l');
fclose(fileID);

finished = 1;

```

---

## Eigenbreast Weighting and New Image Program

Andrew Polemi %  
07/12/17 %

```

clc
close all
clear all

```

## Image Input

```

M = input('Number of eigenbreasts is:'); % M is number of images to be read
N = input('\nHow many new synthetic breasts would you like to create?');

```

```

str = input('Type of image is (gamma or xray):','s');
str2 = 'gamma';

```

```

type_im = strcmp(str,str2);

```

```

if type_im == 1

```

```

    % for 3D raw images
    n_x = 66; % # of pixels along x = axis
    n_y = 90; % # of pixels along y = axis
    n_z = 66; % # of slices in image
    n_points = n_x * n_y * n_z;

```

```

else

```

```

    % for 3D tomo recons
    n_x = 2007; % # of pixels along x = axis
    n_y = 1120; %1534; % # of pixels along y = axis
    n_z = 66; %120; % # of slices in image
    n_points = n_x * n_y * n_z;

```

```

end

```

```

clear str str2

```

## Creating new weights if needed

```

fprintf('\nDo we need to create a new weighting matrix? \n')

```

```

str = input('Enter "y" to create new matrix or enter "n" to load a pre-made matrix: ','s');

```

```

str2 = 'y';
new_weights = strcmp(str,str2);

```

```

if new_weights == 1

```

```

    fprintf('\nLoad weight matix from images used to create eigenbreasts \n')
    [filename,path] = uigetfile('*.mat','Please select the weighting matrix for the eigenbreasts');

```

```

    temp = fullfile(path,filename);
    w_temp = importdata(temp); % load test image w-matrix

```

```

    % find average and std dev of test image w matrix
    ave_w = mean(w_temp);
    std_w = std(w_temp);
    two_std_w = 2*std(w_temp);
    w = zeros(N,M);

```

```

    for i = 1:M
        w(:,i) = random('norm',ave_w(1,i),std_w(1,i),N,1); % w-matrix creation
    end

    save('w_matrix.mat','w')
else
    fprintf('\nWeight matrix must be in row format (ie 1 row 10 columns) \nand must be saved as a matrix with
    extention .mat\n \n')

    [temp] = uigetfile('*.*','Please select the weighting matrix for the eigenbreasts');

    N = input('How many weighting sets are there (ie. how many rows of weights): ');

    w = importdata(temp);

end

```

## Creating new images from weights

```

f=fopen('/home/nucmedresearch/DMT/Eigenbreasts/
Final_Eigenbreast_Program/Main_program_results/Recons/Gamma_Imlo/
Eigenbreasts_Psi_wmatrix_mask/psi.raw'); % open image file / '.raw'
mat=fread(f,n_points,'float32','l'); % read image file
psi = mat.';
fclose(f);
clear f mat

for j = 1: size(w,1)

    a = zeros(1,n_points);
    newI_v = zeros(1,n_points);

    for i = 1:M
        f=fopen(['/home/nucmedresearch/DMT/Eigenbreasts/
Final_Eigenbreast_Program/Main_program_results/Recons/Gamma_Imlo/
Eigenbreasts_Psi_wmatrix_mask/eigenbreast_' num2str(i) '.raw' ]); %
        open image file / '.raw'
        mat=fread(f,n_points,'float32','l'); % read image file
        uon = mat.';
        fclose(f);

        a = w(j,i) * uon + a; % creation of weighted eigenbreast sum with new w-matrix
    end

    newI_v = psi + a; % create new synthetic image
    fileID = fopen(['/media/nucmedresearch/Seagate Backup Plus
Drive/gamma_synthetic_images_nzp_041118/gamma_lmlo_synthetic_'
num2str(j) '.raw'],'w');
    fwrite(fileID,newI_v,'float32','l');
    fclose(fileID);

    clear newI_v a
end

```

## Appendix C – NPS Analysis Program

### Noise Power Spectrum Analysis of Clinical and Synthetic Tomosynthesis Reconstructions – 128 x 128 ROI X-ray

Andrew Polemi %

```
% This program is to create regions of interest (ROIs) with in the
% tomosynthesis images create a zero-mean ROI and prepare the resultant
% ROI for the FFT. Once prepared the 2D FFT will be taken to get the NPS
% of the ROI. This will be done for several ROIs with dimensions 128 x 128
% and will be averaged. The average will then be taken and used to create
% a plot of NPS (intensity) vs spatial frequency. It will then be fitted
% with a power-law such that  $NPS = \alpha * f^{(-\beta)}$ .
```

#### Create Global Parameters

```
N = input('\nHow many breasts will be NPS analyzed?'); %46 original nzp images available
M = input('\nHow many slices in the image?');
```

```
fprintf('\nLoad matrix with starting points for the ROI \n')
```

```
[filename,path] = uigetfile('*.*','Please select the starting point matrix');
temp = fullfile(path,filename);
sp = importdata(temp);
```

```
num_ROI = length(sp);
```

```
% for 3D tomo recons
n_x = 2007; % # of pixels along x = axis
n_y = 1120; %1534; % # of pixels along y = axis
n_z = M; % # of slices in image (this is 66 for the masked images)
n_points = n_x * n_y * n_z;
```

```
roi_x = 128; %256; % # of pixels on an edge of the square ROI
roi_y = 128; %256;
```

```
ROI{num_ROI} = zeros(roi_x,roi_y,1); % preallocation of ROIs
zm_ROI{num_ROI} = zeros(roi_x,roi_y,1); % preallocation of zero mean ROIs
```

```
fft_ROI{num_ROI} = zeros(roi_x,roi_y,1); % preallocation of ROIs for fft
```

```
for l = 1:num_ROI
    ROI{l} = zeros(roi_x,roi_y,1);
    zm_ROI{l} = zeros(roi_x,roi_y,1);
    fft_ROI{l} = zeros(roi_x,roi_y,1);
end
```

```
ave_ROI{M} = zeros(roi_x,roi_y,1); % preallocate place holders for average ROIs
```

```
for l = 1:M
    ave_ROI{l} = zeros(roi_x,roi_y,1);
end
```

```
ROI_temp = zeros(roi_x,roi_y,1);
beta = zeros(N,M);
```

```
dx = 0.150; % recon pixel size (x-y dimensions of voxel) in mm
n = roi_x/2;
freq = 1/(dx*n) * (1:n);
```

## Create NPS

```
for l = 1:N
```

```
    f=fopen(['/home/nucmedresearch/DMT/Eigenbreasts/
    Final_Eigenbreast_Program/Main_program_results/Recons/
    Masked_breasts_final/originals_nzp/X-Ray_LMLO_masked_'
    num2str(l) '_nzp.raw']); % open image file / '.raw'
    mat=fread(f,n_points,'float32','l'); % read image file
    I = reshape(mat,n_x,n_y,n_z);
    fclose(f);
```

```
% note in this matrix n_x and n_y flip
```

```
for a = 1:M
```

```
    for b = 1:num_ROI %15 for real data set
```

```
        x = sp(b,1); % the starting pixel coordinates of the ROI
        y = sp(b,2);
```

```
        ROI{b}{:, :, 1} = I(y:y+127,x:x+127,a);
        % The mean of the ROI is taken and subtracted from the ROI
        % to avoid a biased estimate of the zero-frequency of the NPS
```

```
        ave_temp = mean(mean(ROI{b}));
        zm_ROI{b} = ROI{b} - ave_temp;
```

```
        fft_ROI{b} = abs(power(fftshift(fft2(zm_ROI{b})),2)); % NPS Calculation
```

```
        ROI_temp = ROI_temp + fft_ROI{b};
```

```
    end
```

```
% Average the ROI's (FFT) from slice
```

```
ave_ROI{a} = ROI_temp./num_ROI;
```

```
u = [1:64].';
u2 = freq.');
```

```
for i = 1:64
    nps_1d_zero(i) = ave_ROI{a}(65,64+i,1);
end
```

```
for i = 1:64
    for j = 1:7
        temp_nps(j) = ave_ROI{a}(65+j,64+i,1);
        temp_nps_neg(j) = ave_ROI{a}(65-j,64+i,1);
```

```
    end
```

```
        nps_1d_ave(i) = (sum(temp_nps)+sum(temp_nps_neg))/14;
    clear temp_nps temp_nps_neg
end

nps_1d_ave = nps_1d_ave.';
luf = log(u2);
lnps = log(nps_1d_ave);

p = polyfit(luf,lnps,1); % linear fit of log-log NPS data
f = polyval(p,luf);

beta(1,a) = p(1,1); % record beta value from fit

clear p f lnps luf nps nps_1d_ave nps_1d_zero
end
end
```

## Appendix D – BRPET Pilot Clinical Study Reader Sheet

### DEDICATED BREAST RING PET SCANNER READER STUDY STUDY INTERPRETATION FORM

#### Breast Ring PET (BRPET)

CASE #: \_\_\_\_\_ READER: \_\_\_\_\_ DATE OF REVIEW: \_\_\_\_\_

**A) IMAGE QUALITY:**

1 Not Adequate    2 Barely Adequate    3 Adequate    4 Good    5 Excellent

**Positioning:**    Poor    Adequate    Good

**B) BACKGROUND UPTAKE:**

**Left:**    0 no uptake    1 minimal    2 mild    3 moderate    4 intense

homogenous    heterogenous

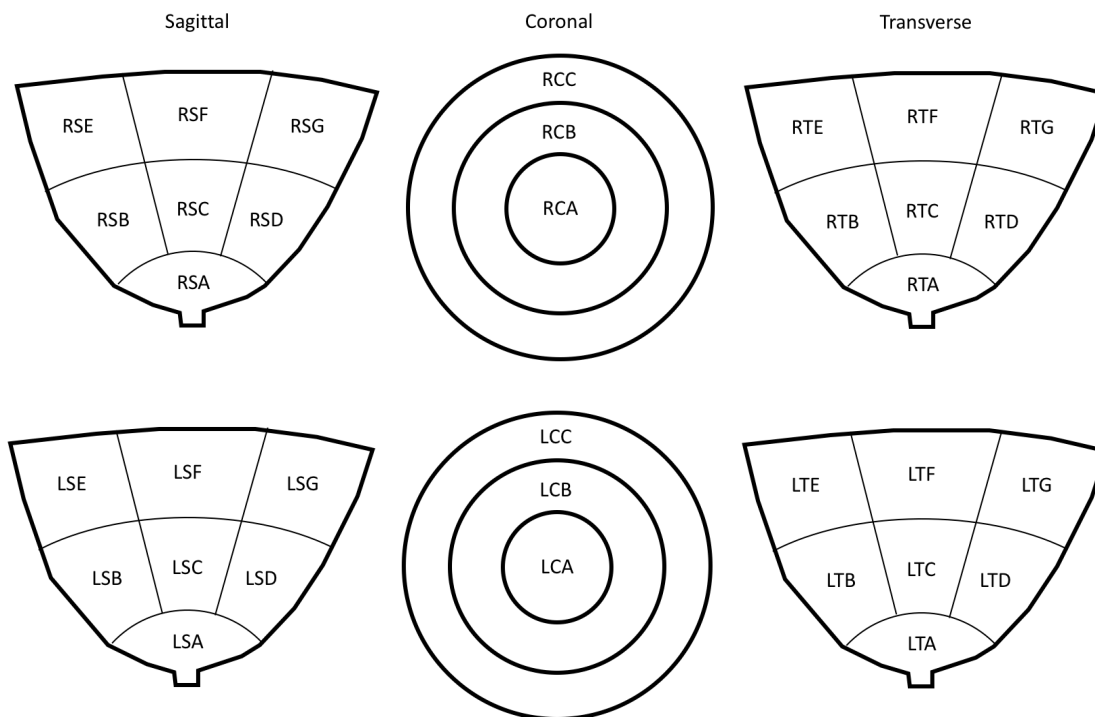
**Right:**    0 no uptake    1 minimal    2 mild    3 moderate    4 intense

homogenous    heterogenous

**Symmetry:**    symmetrical    asymmetrical

**C) Circle findings in the diagram below OR  NO FINDINGS**

**BRPET VIEW:**



**FINDING #1:** LEFT RIGHT

Locations : \_\_\_\_\_ (i.e. LE) Central Slice: S: \_\_\_\_\_ C: \_\_\_\_\_ T: \_\_\_\_\_.

**Focus – Number:**  solitary  multiple: \_\_\_\_\_**Mass – Shape:**  oval  round  irregular– Internal uptake patterns:  homogeneous  heterogeneous  rim uptake– Uptake relative to background:  mild  moderate  intense**Non-mass uptake – Distribution:**  focal  regional  linear/ductal  segmental  multiple regions  diffuse– Internal enhancement patterns:  homogeneous  heterogeneous– Uptake relative to background:  mild  moderate  intense**Ratings** –  1- Definitely Benign  2- Probably Benign  3- Indeterminant  4- Probably Malignant 5- Definitely Malignant

Confidence level (of rating): \_\_\_\_\_%

**FINDING #2** LEFT RIGHT

Locations : \_\_\_\_\_ (i.e. LE) Central Slice: S: \_\_\_\_\_ C: \_\_\_\_\_ T: \_\_\_\_\_.

**Focus – Number:**  solitary  multiple: \_\_\_\_\_**Mass – Shape:**  oval  round  irregular– Internal uptake patterns:  homogeneous  heterogeneous  rim uptake– Uptake relative to background:  mild  moderate  intense**Non-mass uptake – Distribution:**  focal  regional  linear/ductal  segmental  multiple regions  diffuse– Internal enhancement patterns:  homogeneous  heterogeneous– Uptake relative to background:  mild  moderate  intense**Ratings** –  1- Definitely Benign  2- Probably Benign  3- Indeterminant  4- Probably Malignant 5- Definitely Malignant

Confidence level (of rating): \_\_\_\_\_%

**FINDING #3** LEFT RIGHT

Locations : \_\_\_\_\_ (i.e. LE) Central Slice: S: \_\_\_\_\_ C: \_\_\_\_\_ T: \_\_\_\_\_.

**Focus – Number:**  solitary  multiple: \_\_\_\_\_**Mass – Shape:**  oval  round  irregular– Internal uptake patterns:  homogeneous  heterogeneous  rim uptake– Uptake relative to background:  mild  moderate  intense**Non-mass uptake – Distribution:**  focal  regional  linear/ductal  segmental  multiple regions  diffuse– Internal enhancement patterns:  homogeneous  heterogeneous– Uptake relative to background:  mild  moderate  intense

**Ratings** –  1- Definitely Benign  2- Probably Benign  3- Indetermanent  4- Probably Malignant  
 5- Definitely Malignant

**Confidence level (of rating):** \_\_\_\_\_%